Mécanismes fondamentaux du traitement de surfaces par bombardements électroniques pulsés : application aux matériaux métalliques et intermétalliques

Jianxin Zou

To cite this version:

Jianxin Zou. Mécanismes fondamentaux du traitement de surfaces par bombardements électroniques pulsés : application aux matériaux métalliques et intermétalliques. Matériaux. Université Paul Verlaine - Metz, 2007. Français. NNT : 2007METZ018S . tel-01775487

HAL Id: tel-01775487
https://hal.univ-lorraine.fr/tel-01775487

Submitted on 24 Apr 2018

Ecole Doctorale **E**nergie **M**écanique **MA**tériaux

THESE

Présentée à

L'UNIVERSITE PAUL VERLAINE - METZ

Par

Jianxin ZOU

Pour la délivrance du diplôme de :

Docteur de l'Université Paul Verlaine - Metz

SPECIALITE **: Sciences des Matériaux - Physique**

Fundamentals of surface treatments by high current pulsed electron beam : Application to metallic and intermetallic alloys

Soutenu le 8 Juin 2007 à Metz, le jury composé de :

M. Yves PAULEAU	Professeur à l'Institut National Polytechnique de Grenoble, Grenoble, France	Rapporteur
M. Jacques LACAZE	Directeur de recherches CNRS, CIRIMAT-ENSIACET, Toulouse, France	Rapporteur
M. Jean-Marie DUBOIS	Directeur de recherches CNRS à l'Institut de Recherche Jean Lamour à Nancy, Nancy, France	Examinateur
M. Francis WAGNER	Professeur à l'Université Paul Verlaine Metz, France	Examinateur
M. Thierry GROSDIDIER	Professeur à l'Université Paul Verlaine Metz, France	Directeur de thèse
M. Chuang DONG	Professeur à Dalian University of Technology, Dalian, Chine	Directeur de thèse
M. Shengzhi HAO	Professeur Associé à Dalian University of Technology Dalian, Chine	Invité

Laboratoire d'**E**tude des **T**extures et **A**pplications aux **M**atériaux –UMR CNRS 7078
Ile du Saulcy 57045 METZ Cedex 01

Acknowledgement

There are lots of people I would like to thank because they made this thesis possible.

First, I would like to thank Mr. Yves PAULEAU, Professor at the National Polytechnic Institute of Grenoble and Mr. Jacques LACAZE, Director of research at the CIRIMAT-ENSIACET of Toulouse for accepting to be members of the jury and reviewing my PhD thesis. I would also like to thank Mr. Jean Marie DUBOIS, Professor at the Institute Jean Lamour, Mr. Francis WAGNER, Professor at the University Paul Verlaine of Metz and Mr. Shengzhi HAO, associated Professor at the Dalian University of Technology for accepting to be members of the jury.

Many thanks are given to the French Embassy in Beijing for the provision of a "Bourse de co-tutelle" between the Dalian University of Technology and the University Paul Verlaine of Metz. Their financial support makes it possible for me to live and study in France.

Many thanks are due to Prof. Francis WAGNER for his welcome in LETAM.

I would also like to thank my two Ph.D. supervisors, Prof. Thierry Grosdidier and Prof. Chuang Dong. I could not imagine having better advisors and mentors for my Ph.D. Without their broad background knowledge, their inspiration, and their efforts to help me, I would never have finished my experimental work and result analysis concerning my Ph.D subject. They encouraged me and gave me lots of useful ideas throughout the 3 and half years of my Ph.D. The experiences during the past years will benefit me a lot in my future career.

My special thanks are to Dr. Bernard BOLLE for his kind assistance in XRD measurements of D2 steel samples and many useful discussions.

I am indebted to Dr. Nathalie GEY for teaching me how to operate the SEM and EBSD systems and also to do data analysis.

I would also like to thank Dr. Nathalie BOZZOLO for teaching me how to operated TEM and for her helpful assistance in TEM analyses of FeAl samples.

Finally, I take this occasion to thank my colleagues in LETAM and in State Key Laboratory of Materials Modification in Dalian University of Technology, with whom I spent great time with happiness.

This thesis is dedicated to my family especially my wife, my father, my mother, my sister, my father in law and mother in law. They support and encourage me all the time so that I can finish my thesis with great pleasure.

Jianxin ZOU
15 / 04 / 2007

Preface

This manuscript has been written with the goal of reviewing surface modifications of materials by using the high current pulsed electron beam (HCPEB) technique. It gathers results of many previous and present investigations carried out by the author and other scientists who have worked on this specific subject.

The manuscript can be divided into 5 chapters. Chapter I is a general introduction of the high current pulsed electron beam technique. In this chapter, the development and the configuration of the HCPEB system are reviewed.

In Chapter II, physical models have been established to describe many thermal and mechanical processes occurring during the HCPEB treatment of materials, such as melting, diffusion, stress wave propagation and evaporation. Based on the numerical simulations, we have revealed that all the HCPEB treatments can be simply divided into three types: the heating mode, the melting mode and the evaporating mode. This classification is the key to understand many modifications induced by the HCPEB treatment on materials.

Chapter III presents several special phenomena generated by the HCPEB treatment on different materials such as metastable phase formations, special surface morphologies, selective surface purification and texture modifications. Many of them are presented - separately within sub-chapters concentrating on the three different treatment modes - and discussed at the light of the physical models established in Chapter II.

In Chapter IV, the possible applications of the HCPEB technique on metallic and intermetallic alloys have been discussed. These applications includes surface hardening and softening, rapid surface alloying, enhanced diffusion, improving corrosion and wear resistances.

Finally, Chapter V gives the overall conclusions concerning the recent findings and the perspectives on future works that should follow the present thesis.

Index

Chapter III Special phenomena induced by HCPEB treatment……………………24

Appendix – Abstract in Chinese

Résumé

Avec le développement des sciences et des technologies modernes, il est nécessaire de trouver et de développer des matériaux de haute qualité. Un exemple récent est le développement des matériaux nano structurés qui présentent des propriétés très nouvelles et beaucoup d'avantages par rapport aux matériaux conventionnels à gros grains. Par ailleurs, l'amélioration des propriétés des matériaux conventionnels par de nouveaux procédés a également entraîné un vif intérêt. Dans de nombreux de cas, la nature de la surface du matériau est importante. En particulier, la résistance à la corrosion, l'usure et la fatigue sont essentielles pour de nombreuses applications industrielles. Les traitements de surface sont considérés comme des méthodes assez efficaces pour améliorer la qualité des matériaux. Des méthodes de traitement de surfaces conventionnelles, telles que la nitruration et la carburation, ont déjà été appliquées dans l'industrie pour optimiser le comportement de nombreux matériaux. Par contre, ces méthodes sont très coûteuses en énergie et en temps. Les interactions des faisceaux énergétiques tels que les faisceaux d'ions, d'électrons et le laser avec les matériaux ont été étudiées pendant plusieurs décennies. L'application de ces faisceaux énergiques dans l'industrie est très intéressante pour modifier les propriétés de la surface des matériaux métalliques.

La technologie des faisceaux énergiques peut être divisées en deux catégories : les faisceaux continus et les faisceaux pulsés. En plus du traitement des surfaces, les faisceaux continus ont

déjà trouvé des applications dans l’industrie comme le perçage, la découpe et la soudure. Des systèmes à base de faisceaux pulsés sont maintenant aussi en cours de développement pour le traitement de surface des matériaux. La caractéristique principale des systèmes pulsés est la densité d’énergie très élevée transfère vers la surface. Elle induit les cycles thermiques plus rapides.

Parmi les faisceaux énergiques, les faisceaux d'électrons ont été longtemps étudiés et appliqués dans l'industrie. De manière naturelle, il est classique de les diviser en faisceaux d'électrons continus et faisceaux d'électrons pulsés. Les faisceaux d'électrons continus sont connus pour être utilisés dans l'industrie du soudage et d'autres traitements.

Au sein des techniques concernant les faisceaux d'électrons pulsés, la technique ‘High Current Pulsed Electron Beam (HCPEB)’ est assez récente. Elle a été développée à l’institut d'électronique des fortes intensités de Tomsk, en Russie. Au début des années 90, le groupe de recherche mené par le Prof. Proskurovsky a créé une source pulsée à forte intensité de faisceau électronique, qui contient un canon à électrons avec une cathode d'émission et une anode de plasma. La source possède les paramètres suivants : énergie d'électron de 0.5 à 40 keV ; durée d'impulsion de 0.5 à 5 μs ; densité d'énergie de 0.5 à 40 J/cm^2 ; section de faisceau de 10 à 50 cm^2 et fréquence d'impulsion de 0.2 Hz. La technique HCPEB a été étudiée par Proskurovsky et al. pour le traitement d’alliages industriels. Ils ont suggéré que la technique HCPEB peut être une méthode efficace pour la protection thermique, le recuit rapide, le nettoyage et les modifications chimiques de la surface. La source de faisceau d'électrons est la partie principale du système qui produit le faisceau d'électrons pulsé. La figure 1 montre un croquis du canon à électrons. La cathode est faite de graphite. L'anode est en acier inoxydable percée en son centre pour permettre le passage des électrons. Le faisceau d'électron est transporté par le plasma d'anode au collecteur. Pour empêcher le faisceau de converger et de se disperser, un champ magnétique externe - créé par un solénoïde - est appliqué.

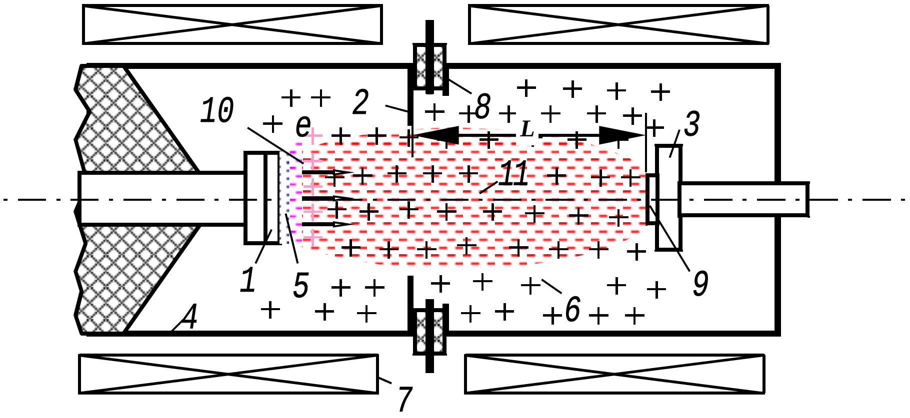

(1) cathode (2) anode (3) collector (4) vacuum chamber (5) cathode plasma (6) anode plasma (7) solenoid (8) spark plasma sources (9) specimen (10) plasma sheath (11)electron beam

Fig. 1 Diagramme schématique de la source de HCPEB.

Quand un faisceau d'électrons avec une densité d'énergie donnée irradie une surface de matériau, plusieurs phénomènes peuvent apparaître à la surface du matériau. Pour le cas du HCPEB, trois zones différentes sont habituellement rencontrées. Une illustration schématique de ces zones est montrée dans figure 2.

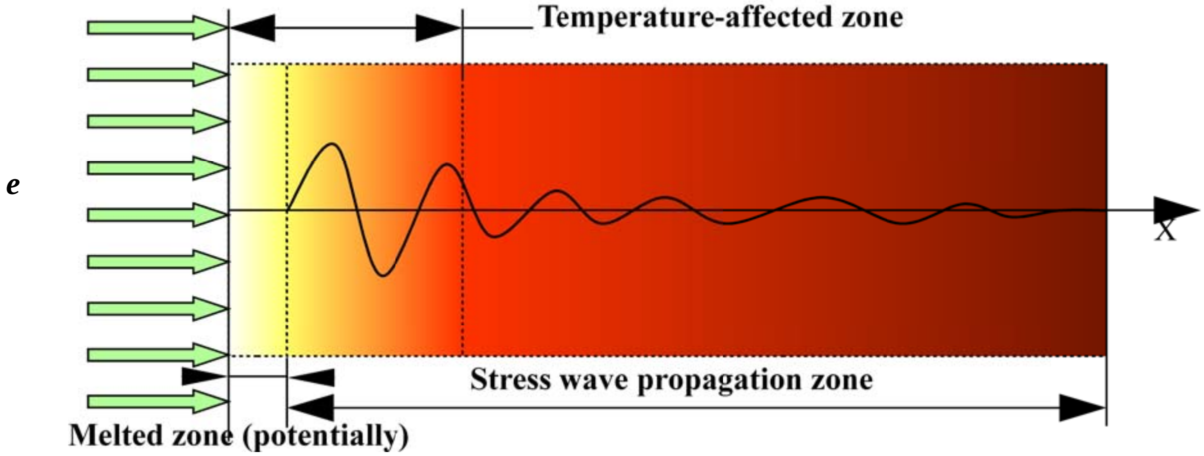

Fig. 2 Des zones différentes dans les matériaux traités par le HCPEB.

Généralement, la zone présentée sur la surface supérieure est une zone qui a été fondue et ensuite solidifiée rapidement. Elle est souvent de quelques μm d'épaisseur mais peut être évitée, en particulier pour les matériaux ayant une conductivité thermique importante ou si l'énergie du faisceau d'électrons est suffisamment réduite. Au-dessous de la zone de fusion, se trouve la zone affectée thermiquement (ZAT), qui se prolonge généralement sur quelques dizaines de μm. Enfin, une dernière zone est présente en raison de la propagation de l'onde de choc et des contraintes thermiques. La dureté du matériau peut également être fortement affectée. Cette zone peut avoir une profondeur beaucoup plus grande que la ZAT. Après un nombre d'impulsions suffisant (en général 15~20), cette zone peut se prolonger jusqu'à quelques centaines de μm sous la surface.

Quand un faisceau d'électrons irradie un matériau, un champ mobile de température est produit dans la couche de surface en raison de l'absorption de l'énergie du faisceau. Le champ de température peut être décrit par l'équation thermique suivante:

$$\rho c(T)\frac{\partial T}{\partial t} = \frac{\partial}{\partial x}(\lambda(T)\frac{\partial T}{\partial x}) + L_v(x,t)$$

(1),

avec les conditions initiales :

$$T(x,0) = T_0$$

(2),

et aux limites:

$$-\lambda(T)\frac{\partial T(x,t)}{\partial x}|_{x=0,x=l} = 0$$

(3).

T est le champ de température alors que ρ, c et λ sont respectivement la densité, la capacité thermique et la conductivité thermique du matériau. L_v est la densité d'énergie de la source de chaleur ; T_0 est la température initiale du matériaux et l l'épaisseur de l'échantillon.

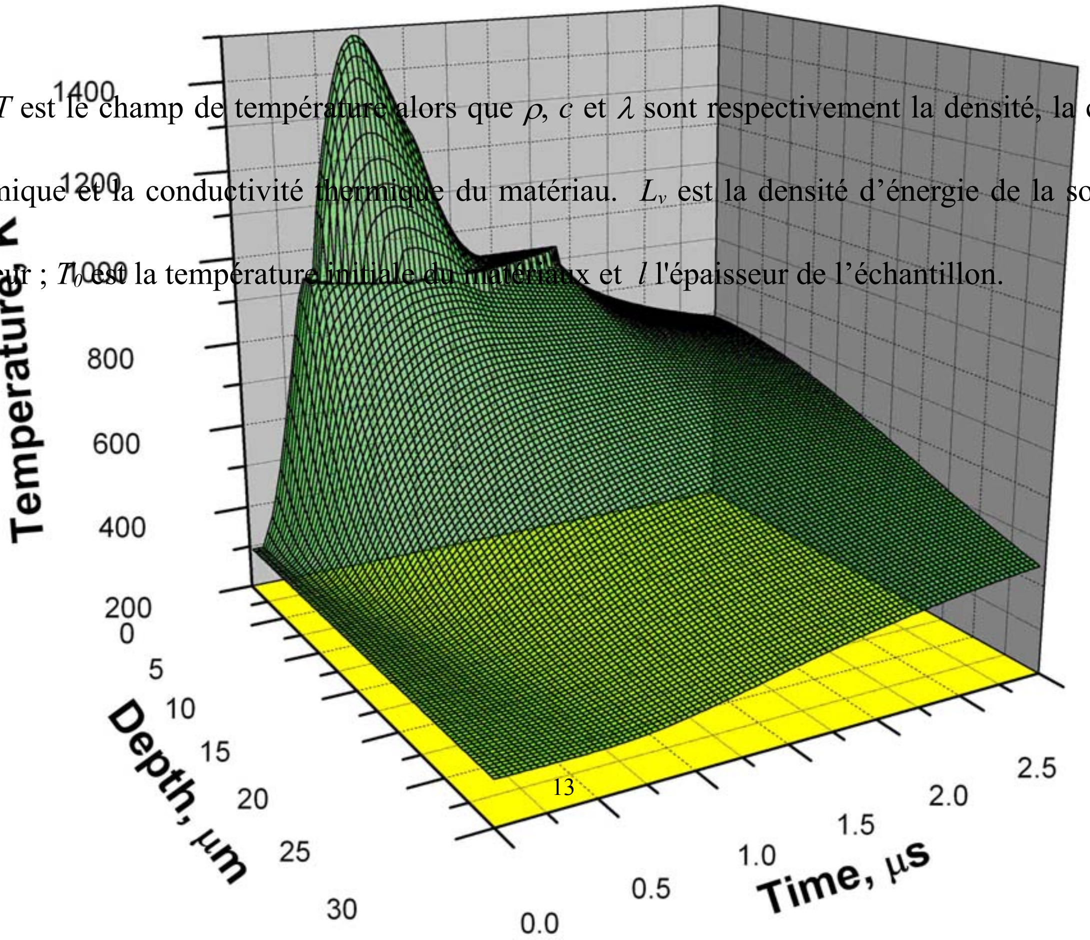

Fig. 3 Distribution du champ de température à la surface d'Al irradiée une fois par HCPEB (densité d'énergie $S \approx 3$ *J/cm*^{2}*,* $\tau \approx 1.5$ *μs).*

Comme exemple, la figure 3 présente l'évolution de la température simulée en fonction du temps et de la profondeur dans le matériau dans le cas d'Al pur traité par HCPEB. La durée d'impulsion est de 1.5 μs ; la densité d'énergie d’environ 3.0 J/cm^2 et la tension d’accélération de 27.8 kV. La modélisation permet d’évaluer un certain nombre de paramètres. Pour avoir un ordre de grandeur, nous avons par exemple dans ce cas les paramètres suivants. L'épaisseur de la zone fondue est d’environ 2~3 micromètres. La vitesse de solidification est de 3~5 m/s, la vitesse de chauffage est d’environ 10^9 K/s, et le refroidissement de 10^8 K/s. En changeant les paramètres de faisceau d'électrons, nous avons aussi constaté que la fusion commençait dans une couche au-dessous de la surface parce que la distribution d'énergie du faisceau d'électrons n’est pas homogène en profondeur et qu’il y a un maximum en sous-couche.

Figure 4 montre les profils de température typiques produits dans la surface supérieure d'un matériau traité par HCPEB avec des densités d’énergies différentes. Comme indiqué dans la figure, pour le traitement à basse densité d’énergie, la température à la surface du matériau ne peut pas atteindre le point de fusion (melting temperature : Tm) pendant le traitement. C’est un mode de traitement que nous appelons le mode ‘chauffage’ (Heating). De même, les modes de traitement pendant lesquels la température à la surface supérieure permet d’atteindre les points de fusion ou d'ébullition (boiling temperature : Tb), s'appellent respectivement les modes de fusion (Melting) et d’évaporation (Evaporating). Cette distinction entre ces trois modes de traitement est, nous pensons, très importante pour obtenir toutes les capacités de cette technique.

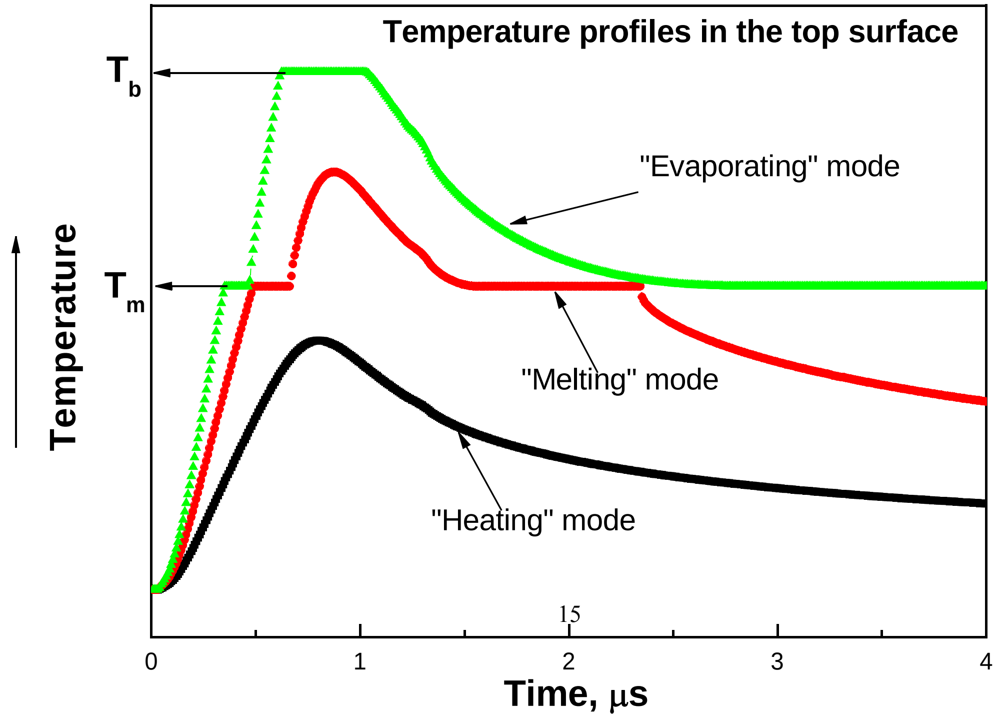

3.0 J/cm^2

2.0 J/cm^2

1.2 J/cm^2

*Fig. 4 Profils de température typiques à la surface d'un matériau (Mg) par traitement HCPEB avec des densités différentes d'énergie (*1.2 J/cm^2, 2.0 J/cm^2, 3.0 J/cm^2*), montrant les trois modes de traitement.*

Pour le traitement par HCPEB sans fusion de la surface, l'effet du champ de contrainte joue un rôle important en déterminant l'état final de la structure. Il y a deux types de champ de contrainte induits par le bombardement sans fusion : les sollicitations thermiques quasi-statiques et les sollicitations thermiques dynamiques.

Les résultats des calculs ont montré que la sollicitation thermique dynamique a généralement une amplitude très faible ; de l'ordre de quelques centaines de kPa. Par contre, la contrainte quasi-statique qui est produite par la différence de dilatation thermique latérale a une amplitude de quelques centaines de MPa. Elle se concentre principalement dans la ZAT et son intensité change avec la distribution du champ de température.

Dans certains cas, le HCPEB peut mener à l'évaporation significative sur les matériaux traités quand leur point d'ébullition est atteint pendant le traitement. Pour les calculs en mode ‘évaporation’, l’Equation 1 a été résolue dans un système mobile afin de tenir compte de la couche évaporée.

Les modifications de surface liées aux différents modes de traitement HCPEB ont été étudiées dans cette thèse. Des techniques telles que le MEB, l’EBSD, le MET, la diffraction de rayons X et le SNMS ont été utilisées pour analyser dans le détail les modifications en surface et en sous couche dans les matériaux traités par le HCPEB. Des phénomènes observés sous les trois modes sont détaillés ci-après.

a) Mode ‘fusion’

Les principaux résultats correspondant aux matériaux traités en mode ‘fusion’ sont :

1. Homogénéisation de la couche fondue.

Le HCPEB est démontré être une méthode efficace pour réaliser l'homogénéisation de la surface de matériaux métalliques qui contiennent des précipités/inclusions. Le traitement induit la formation de cratères par des éruptions initiées aux niveaux de ces secondes phases. En conséquence, on observe une purification sélective de la couche fondue. La réduction de la densité d'inclusion réduit la fréquence des événements d'éruption sur la surface. Finalement, après un nombre suffisant d'impulsions, ceci mène à la formation d'une surface homogène ou la quantité de cratères est très réduite.

2. Formation de grains ultra fins et de nano-structures

Les résultats recueillis ici montrent le potentiel très fort pour la nano-cristallisation de la surface des matériaux, pouvant rendre possible des propriétés améliorées par la technique HCPEB. Pour illustration, la figure 5 donne une image MEB de l'acier D2 traité après 25 impulsions qui montre des grains austénitiques très fins ayant une taille moyenne d'environ 50 à 15

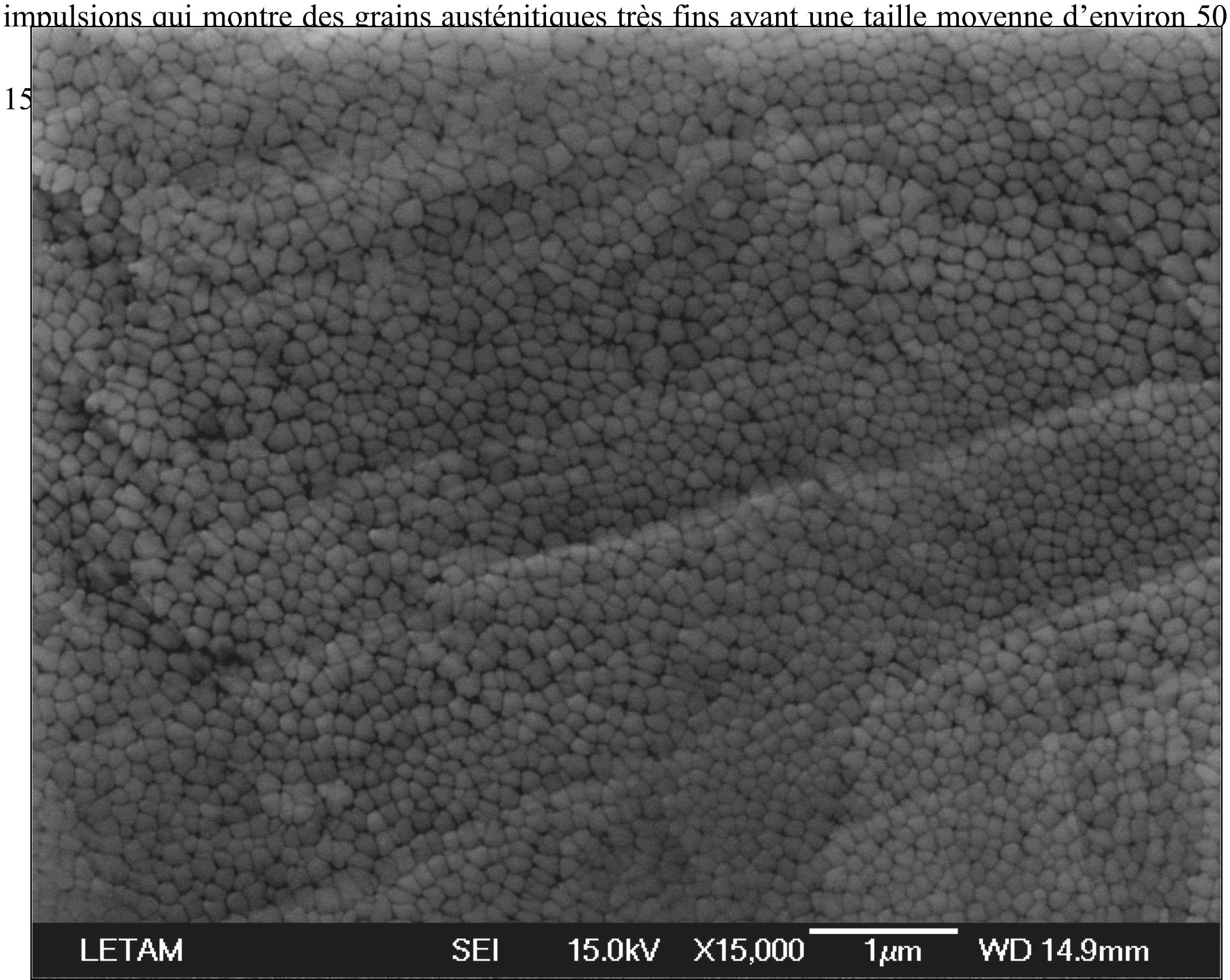

Fig. 5 Micrographique MEB typique de la surface d’un échantillon D2, montrent des grains très fins.

3. Formations de phases métastables.

Les cycles thermiques rapides produits par le traitement HCPEB ont le potentiel de produire des structures métastables, particulièrement dans le cas des aciers. Par exemple, l'austénite a été retenue jusqu’à la température ambiante dans l'acier D2 traité par HCPEB. Ceci a été associé à l’effet des éléments Cr et C et de la taille des grains ultra fins qui inhibent la transformation martensitique. Des transformations différentes ont été observées dans la même couche superficielle quand la composition chimique de la zone fondue n'était pas homogène. Une structure ultra fine de la ferrite mélangée avec de la martensite a été trouvée sur l'échantillon d'acier H13 traité par HCPEB. Ceci illustre l'impact fort de la composition initiale sur la microstructure finale après traitement de HCPEB. Ceci a été confirmé par l’étude de différents aciers au carbone.

4. Formation des textures spécifiques.

Le traitement HCPEB induit à des structures ultra fines ayant des textures de solidification originales. Ceci fut observé pour des couches fondues (i) d'austénite (*fcc*) métastable pour l'acier D2 et (ii) de phase B2 stable dans le cas d'un alliage à mémoire de forme NiTi. Dans les deux cas, la solidification rapide des phases sursaturées a conduit à une texture de fibre mixte <100> (faible) + <110> (forte). A ces textures atypiques ont été associée des densités élevées de joints correspondant à des macles. La formation des joints de macle est vraisemblablement un mécanisme contribuant à la formation de la composante <110> de la texture finale.

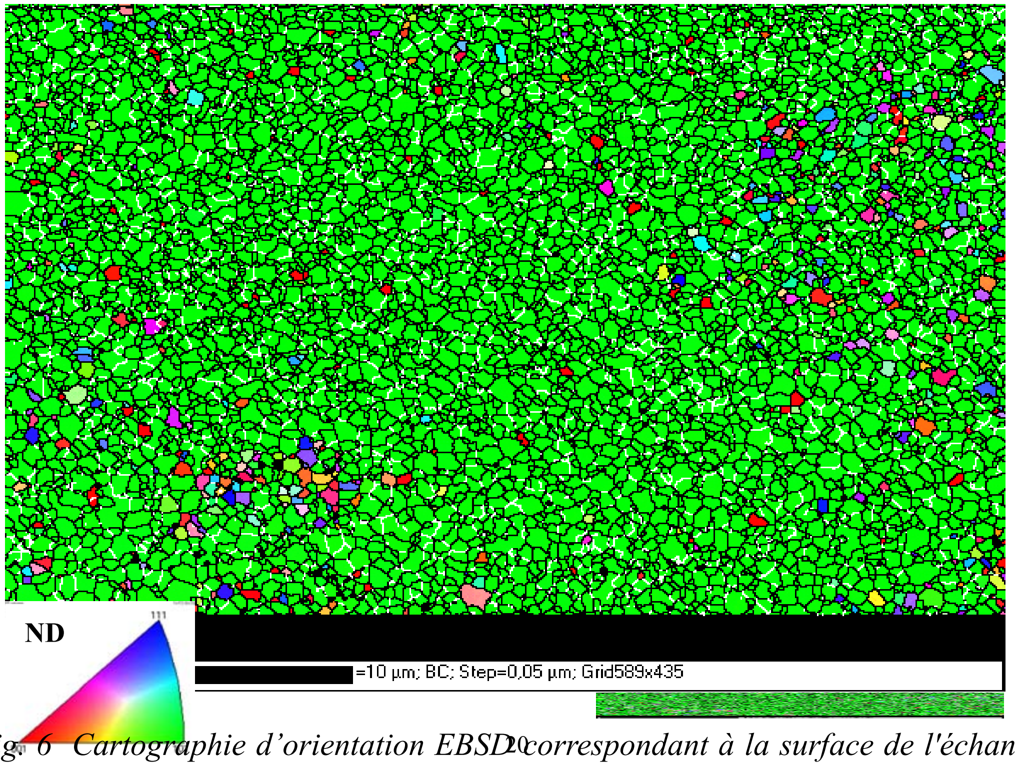

Fig. 6 Cartographie d'orientation EBSD correspondant à la surface de l'échantillon de NiTi traité avec 20 impulsions.

La figure 6 montre une cartographie d'orientation typique obtenue sur l'échantillon Ni (50.6at%)Ti traité avec 20 impulsions en mode 'fusion'. Tous les grains sur la surface ont été classés comme correspondant à la phase austénitique de (B2) NiTi. L'image est presque totalement dominée par des grains verts, qui correspondent aux grains ayant une direction <110> perpendiculaire à la normale de l'échantillon.

5. Formation d'alliage en surface.

La formation d'alliage en surface d'échantillons en utilisant le procédé HCPEB est aussi une manière efficace d'améliorer les propriétés des matériaux. Par exemple, des couches pré enduites déposées à la surface peuvent être rapidement mélangées au substrat pendant la fusion. Ceci peut mener à la modification des phases et des compositions dans la couche superficielle.

6. Durcissement en sous couche.

Basé sur une description des processus thermomécaniques liés au bombardement HCPEB, nous avons pu préciser que les modifications en profondeur sont provoquées par des sollicitations quasi-statiques et d'autres associées à la fusion. L'onde de contrainte intense modifie ainsi la dureté en dessous de la surface sur une profondeur de quelques centaines de μm.

b) Mode 'chauffage'

Sous l'action combinée de la température et des champs de contrainte, il a été montré que des modifications significatives des microstructures et des compositions étaient possible à la surface même sans fusion. Les principaux effets du traitement HCPEB en mode 'chauffage' sont :

1. Efficacité des cycles thermomécaniques.

Il est clair que l'irradiation du HCPEB produit un champ dynamique de température à la surface du matériau. Simultanément à l'effet thermique, l'impulsion crée un champ de contrainte dynamique qui cause un écrouissage intense à la surface du matériau et en sous-couche. La déformation locale dépend de l'orientation des grains et génère des réponses locales différentes. Pour l'acier inoxydable 316L, des macles sont activées dans les grains ayant un axe <111> parallèle à ND. Par contre, des gradients de désorientation assez important créés par l'activité du glissement cristallographique sont observés dans les autres grains. Pour l'intermétallique FeAl, la différence locale de déformation se traduit aussi par le fait que les grains ayant un axe <100> proche de la perpendiculaire à la surface se situent à un niveau inférieur aux autres grains.

2. Modification de la texture et affinement de la taille de grain.

De façon assez remarquable, le traitement HCPEB permet aussi de modifier la texture et la taille des grains en surface d'un matériau sans fusion. Pour étudier les modifications de texture induites par le traitement HCPEB sans fusion de surface, l'alliage intermétallique Fe (40 at%) Al a été choisi. L'échantillon initial a une texture de fibre <110> // ND avec une intensité maximum à environ 6.5 fois l'isotropie. La figure 7 montre une image typique d'orientation d'EBSD de l'échantillon traité avec 20 impulsions sans fusion de la surface. La surface de l'échantillon FeAl caractérisée initialement par une texture de fibre <110> // ND a été modifiée en une fibre <321>. Beaucoup de grains ne montrent plus la couleur verte comme le matériau initial. Figure de pôles de l'échantillon (Fig. 7b) prouve que la texture consiste maintenant en une fibre centrée sur <321> avec une intensité maximale à environ 3 fois l'isotropie. La distribution de désorientation des joints de grains a changé: la fraction des joints de grains de faible désorientation a fortement augmenté. En même temps que l'évolution de texture, nous avons observé un affinement de la taille des grains. Les deux effets sont dû à la formation de nouveaux joints de grains (de faible désorientation) induits par les cycles répétés de la déformation et du restauration / recristallisation dynamiques pendant le traitement HCPEB.

(a)

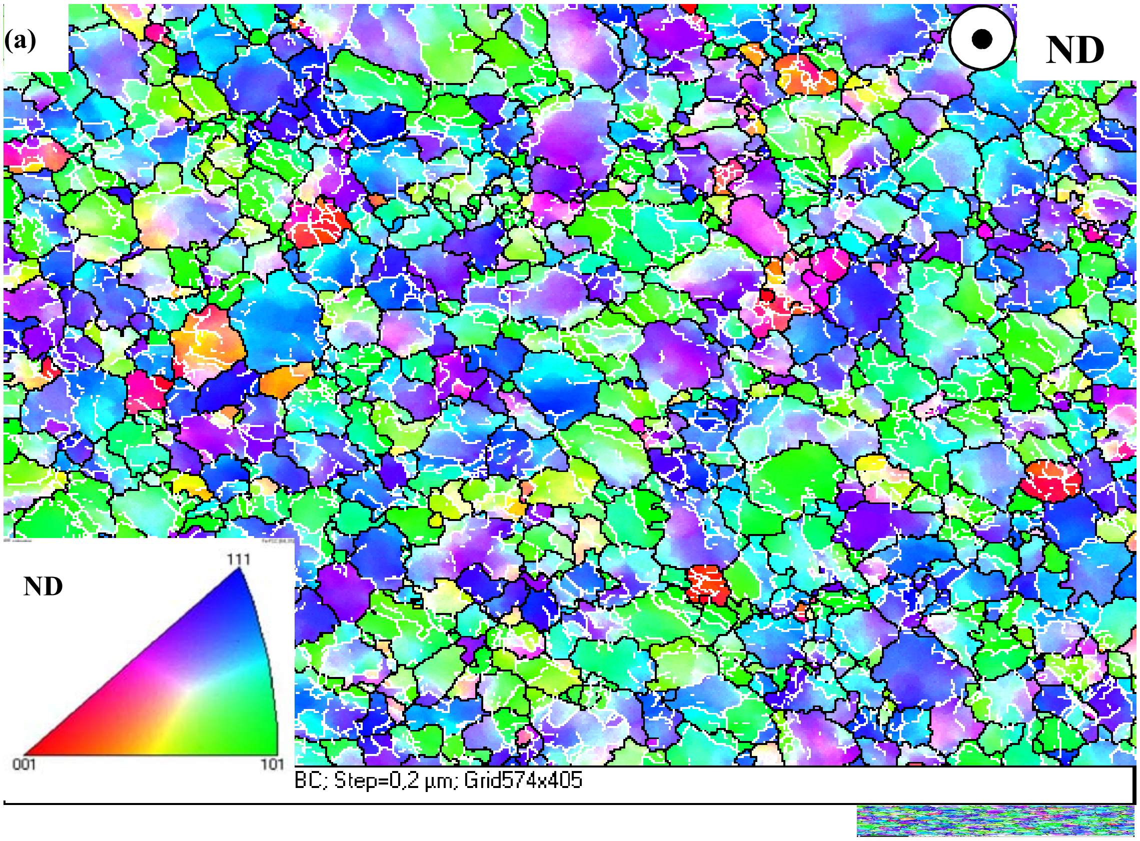
ND
ND
111
001
101
BC; Step=0,2 µm; Grid574x405

(b)

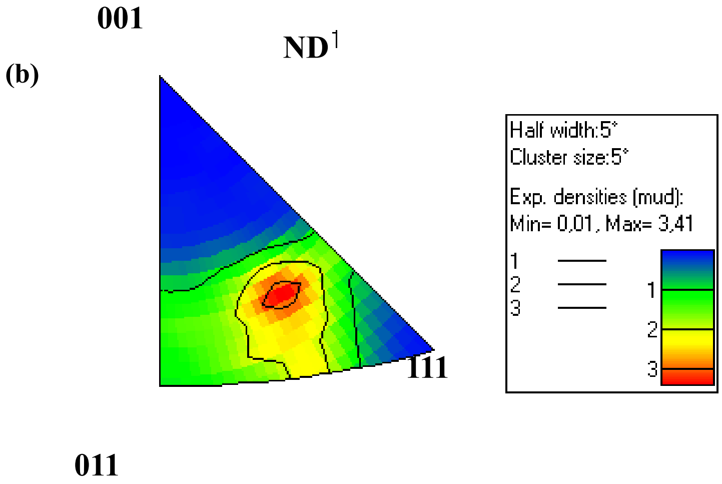
001
ND 1
111
011
Half width:5°
Cluster size:5°
Exp. densities (mud):
Min= 0,01, Max= 3,41
1
2
3
1
2
3

(c)

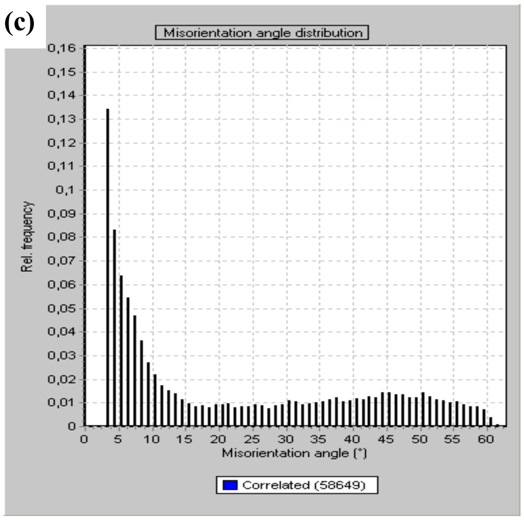
Misorientation angle distribution
Rel. frequency
0,16
0,15
0,14
0,13
0,12
0,11
0,1
0,09
0,08
0,07
0,06
0,05
0,04
0,03
0,02
0,01
0
0
5
10
15
20
25
30
35
40
45
50
55
60
Misorientation angle (°)
Correlated (58649)

Fig. 7 Image d'orientation d'EBSD de la surface de l'échantillon Fe (40at%)Al traité avec 20 impulsions (a), la figure de pôle inverse correspondante (b) et les distributions de désorientation des joints de grain (c).

3. Purification de la surface.

La purification de la surface d'un alliage renforcé par des particules de secondes phases peut également se pr . Dans le cas de l'alliage Fe (40 été enlevées par traitement HCPE

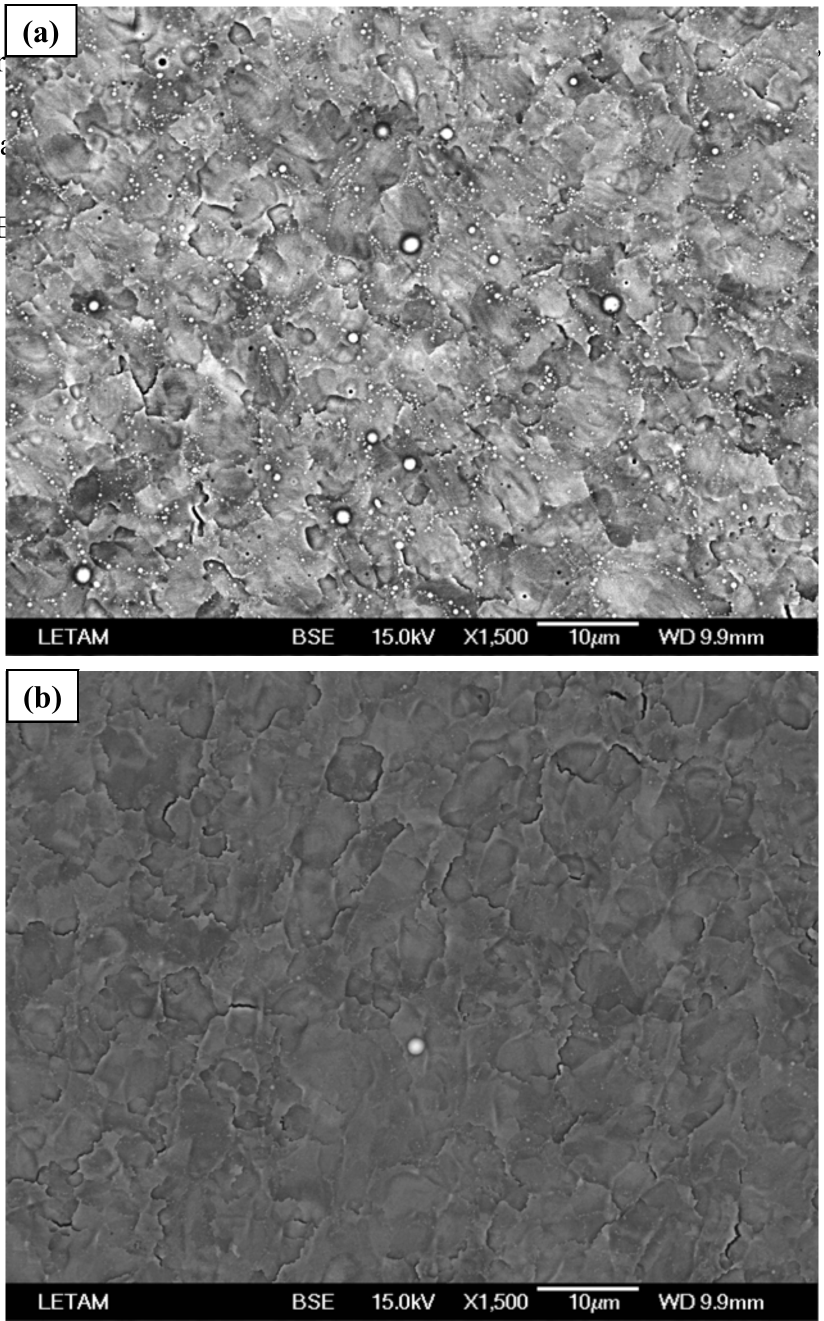

Fig. 8 Micrographies typiques observées sur la surface des échantillons traités avec 5 (a) et 20 (b) impulsions.

La figure 8 montre les micrographies typiques de la surface prise sur les échantillons après 5 et 20 impulsions. Après 5 impulsions, beaucoup de particules sphériques sont présente à la surface (Fig. 8a). Elles sont presque totalement absentes après 20 impulsions (Fig. 8b). Par conséquence, les observations confirment qu'une purification sélective s'est aussi produite sous le mode ‘chauffage’.

c) Mode ‘évaporation’

L'effet du traitement HCPEB pour modifier les surfaces des matériaux sous le mode ‘évaporation’ a été étudié. Des phénomènes d'évaporation significative et de re-condensation sur la surface a été mis en évidence par un modèle physique établi pour rendre compte de l’évaporation. Les caractéristiques principales produites par le mode ‘évaporation’ sont :

1. Modifications de l’aspect de la surface.

L'action du faisceau d'électrons en mode ‘évaporation’ est de modifier la morphologie de la surface et lui donne une forme onduleuse. Cet aspect onduleux est la conséquence de la combinaison (i) de fusion et d'évaporation « locale » sélective et (ii) de la déformation dans la couche fondue sur la surface des alliages.

2. Évaporation sélective.

Le mode ‘évaporation’ peut produire de l'évaporation sélective de certains éléments chimiques à la surface des alliages traités. Le modèle physique proposé pour décrire cette évaporation sélective a donné des profils simulés de composition en assez bon accord avec l'expérience au début du processus d'évaporation.

3. Phénomènes d'évaporation/condensation.

L'effet du mode d'évaporation est plus prononcé après un nombre suffisant d’impulsion et une partie de la vapeur re-condense à la surface. Ceci est clairement montré par (i) la présence de petites protubérances sur la surface ondulée et (ii) des distributions spéciales de composition en extrême surface liée à l’évaporation intensive suivie de cette re-condensation.

4. Modification de la texture spéciale.

Une fibre forte caractérisée par <110> // ND est donc aussi créée dans l'alliage NiTi traité après le traitement HCPEB sous le mode ‘évaporation’. Il existe toutefois des différences marquées par rapport au mode ‘fusion’. En effet, (i) les grains qui ont <110> // ND sont souvent des petits domaines isoles et (ii) lorsqu’ils sont groupés ensemble, ils ne sont pas séparés par des joints de macle.

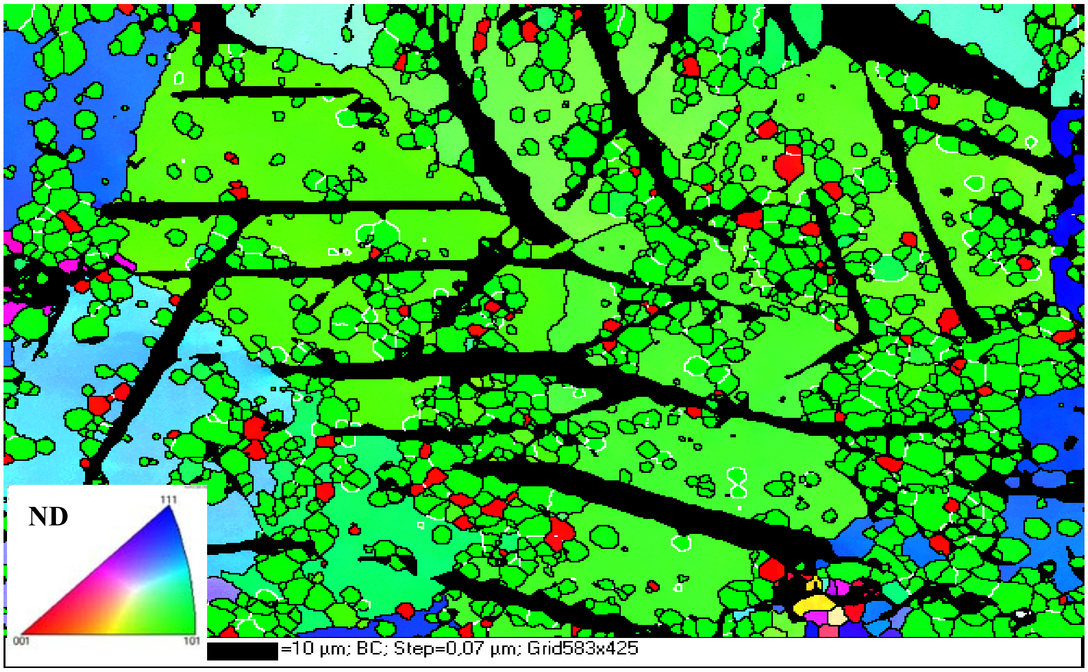

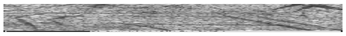

Fig. 9 Cartographie d’orientation typique sur un échantillon NiTi traité avec 10 impulsions en mode ‘évaporation’.

La figure 9 montre une image d'EBSD dans le cas d'un échantillon NiTi traité avec 10 impulsions d'énergie élevée. L’image indique que la plupart des petits grains ont la couleur verte (<110> près de ND) ou rouge (<100> près de ND). En outre, il est intéressant de noter dans la figure 9 que les petits grains ont des couleurs (orientations) indépendantes de celles des gros grains sous-jacents.

Mon document se termine par une revue des applications potentielles de la technique HCPEB pour améliorer les propriétés des matériaux. Sous les trois modes du traitement, on voit que le traitement HCPEB est une manière efficace pour modifier les propriétés des surfaces des matériaux métalliques et intermétalliques. Avec la combinaison des cycles thermiques rapides et des champs dynamiques de contrainte, il est possible de modifier sensiblement les caractéristiques de la surface et, dans beaucoup de cas, d'améliorer les propriétés mécaniques plus rapidement et plus efficacement qu’avec des techniques conventionnelles de traitement de surfaces. Par exemple, la dureté et la résistance à l'usure des surfaces sont efficacement améliorées en raison des formations de structures à grains ultra-fins. L'effet de la purification sélective peut produire des couches de surface aux propriétés améliorées permettent une meilleure résistance à la corrosion. Nous avons proposé d’autres applications du traitement HCPEB pour l'industrie. A titre d’exemple : les surfaces pouvant être durcies ou adoucies.

Il est clair que le potentiel de la technique HCPEB nécessite un bon contrôle des paramètres de traitement pour modifier la surface des matériaux sous le mode de traitement le plus approprié.

Chapter I Introduction

I.1 Development of energetic beams for surface modifications

With the development of modern science and technology, such as aeronautic, atomistic, electronic and biology, there is an increasing requirement of searching and developing high quality materials. One of the recent examples is the world increasing interest of the nanostructured materials which often show novel properties and have many advantages over conventional coarse grained materials [1-3]. On the other hand, methods for treating conventional materials to obtain required properties have also attracted great interest [4-7]. In many cases, the nature of the material surface is of major importance; in particular for corrosion, wear and fatigue resistance properties, which are of interest for industrial applications. The general concept of the surface treatment is to implement a layer at the material surface having different chemistry and/or microstructure in order to obtain certain properties that are necessary for applications. Conventional surface treatment methods, such as nitriding, carburizing, etc., have already been widely used in industry to harden and strengthen several types of work pieces [8-15]. However, these methods are usually time and energy consuming, and in special cases, can not be used or can not meet the requirement of applications.

The interaction of energetic beams such as ion, electron and laser beams with materials has been studied extensively over the past few decades [16-25]. The application of these energetic beams in industry has been of increasing interest to modify the surface of metallic materials [25-30]. Compared with conventional surface treatment methods, these energy beam technologies have their own advantages. They can be applied almost on all kinds of materials with different shapes. They are also clean to the environment and efficient in utilizing the energy. Depending on the continuity of the beams, the energetic beam technologies can be roughly divided into two types: continuous beams and pulsed beams. In addition to surface treatment, high power beams of continuous wave (cw)-system also have a wide field of applications like drilling, cutting and welding [31-37]. In contrast, high power systems involving pulsed beams are now also under development for surface treatment. The main feature of the pulsed systems is the high power density of 10^7-10^{12} W/cm^2 at the target surface, which induces very fast thermal cycles within a narrow depth of the materials' surface layers. A schematic illustration of the working processes of continuous beam systems and pulsed beam systems is shown in the Fig. I-1. For the continuous beam systems, the processing starts and then keeps running during which the vapor generated by beam irradiation may disperse the incident beam energy and reduce the energy utilization rate. Comparatively, the output of pulsed beam systems is discontinuous. The "real" processing starts and finishes usually within a short time. Between two pulses, the surface layer will be rapidly cooled down due to the heat conduction towards the bulk. In addition, the dispersion of beam energy by vapor can be avoided.

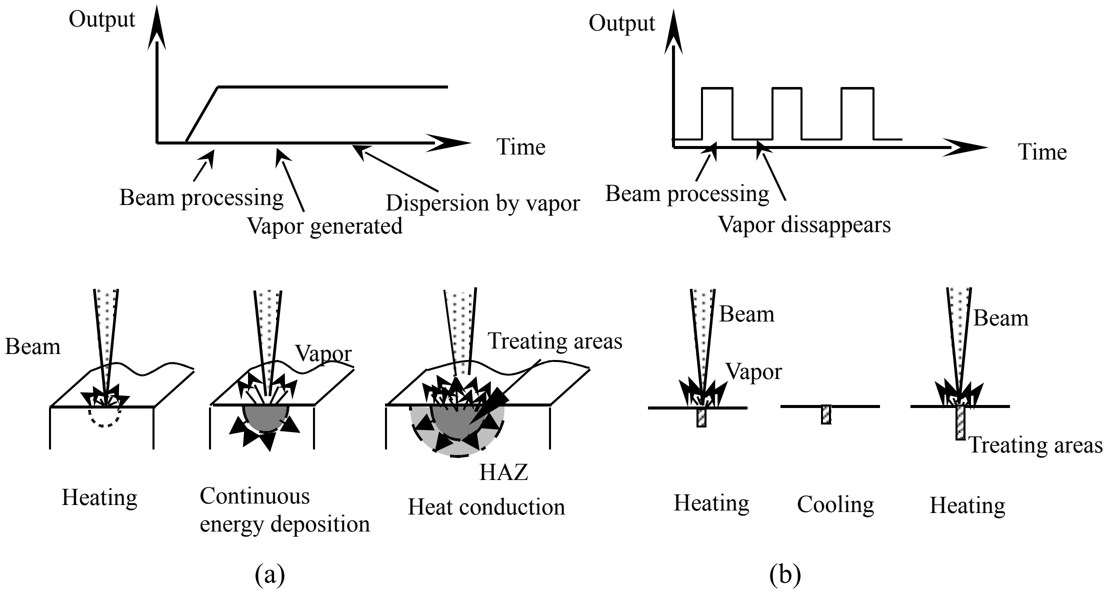

Fig. I-1 Schematic illustration of the surface modification processes with a continuous (a) and pulsed (b) energetic beam.

I.2 Electron beams

As a family member of the energetic beams, electron beams (EB) have long been studied and used in industry [38-40]. Of course, they can be also simply divided as continuous electron beams and pulsed electron beams. Continuous electron beams have long been used in welding industry [31,32]. As for traditional electron beam welding and the more advanced techniques such as surface texturing and surface sculpture processing, electron beams can be also used for many other processing jobs. Several examples are given below:

1) Electron beam evaporation

Electron beams can be used for the evaporation of various metals to produce thin films on numerous different substrates for many industry applications, such as the optical, electronic, aerospace, textile, packaging and electronics industries. These industries produce items such as: capacitors, magnetic devices, semiconductors, metal coated plastics, special photographic products, and multi-layer systems for optical devices. Overlay coating is an equally important industrial area using electron-beam evaporation. For example, coatings of turbine blades with yttrium-stabilized zirconia for thermal barrier coatings.

2) Electron beam melting

High power electron beams can be used to easily process high melting-point metals in vacuum furnaces. By using EB melt processing under high vacuum it is possible to melt and refine metals via the removal of trapped gases and the evaporation of impurities with high vapor pressures. This technology is used to process refractory metals such as tantalum, niobium and molybdenum and reactive metals such as titanium and zirconium, as well as some platinum metals.

3) Electron beam curing

Electron-beam curing of adhesives and resins is a technology which has the potential to provide significant advantages for aerospace/automotive industries and some consumer applications. Unlike traditional thermal curing methods, electron beam curing has: shorter cure times, low energy consumption, reduced volatile emissions, the ability to utilize low-cost tooling materials, and control over curing energy-absorption profile. EB cured materials have been shown to possess excellent mechanical properties, with low molded-in stresses, high glass transition temperatures (Tg) and low porosity content. Electron beam processing offers a number of other benefits over thermal curing. One of the most obvious is cost. Eight independent studies have shown potential manufacturing cost savings of 25-65%. For prototyping alone, this could rise to as much as 90-95%. This is because electron beam processing, as well as greatly speeding up curing time, cures the materials at ambient temperatures, allowing tools to be made from very low cost materials such as foam or wood.

As well as the above uses for electron beam they can also be used for localised in-chamber vacuum brazing, diffusion bonding, heat treatment and many other conventional processing techniques which can be performed under vacuum.

I. 3 Pulsed electron beams

Pulsed electron beam systems were firstly developed in the 50's. For example, the pulsed electron beam system used in Stanford university can provide electron beams with an accelerating voltage of 10 kV, pulse duration 0.5-5 μs, repetition rate 120 s^{-1}, peak current 1 A (current density 6 A/cm^2) [41]. The early work concentrated mainly on the characteristics of the electron beams, such as its stability and controlling parameters [42-44]. It was then used to anneal ion implanted semiconductors [45-50]. Some investigations have revealed that the defects induced by ion implantation in semiconductors can be greatly reduced by exposing the sample to a low energy pulsed electron beam [51-53]. Several new types of pulsed electron sources have been developed later [54-56]. For example, Brau et al. designed a simple pulsed electron gun [54], which can provide an electron beam with an energy of 100 keV, peak current 10 A, pulse duration 7 ns. The application of pulsed electron beams on the treatment of metallic materials started from the 70s' [57,58]. In the 1980s, Follstaedt and Knapp carried out a series of experiments [59,60] on pulsed melting of pure materials as well as a broad spectrum of metallic alloys.

Compared with conventional surface treatment methods, the pulsed electron beam technique has some essential advantages, as described below:

1. Electron beam surface treatment only induces very limited change in the shape of the treated samples. Therefore, it can be used as the final treatment for most of the applications;
2. The necessary time duration for surface treatment can be greatly reduced;
3. Energy consumption can be reduced since the utilization efficiency of the electron beam energy can reach about 90%;
4. In most cases, it does not require a special cooling device;
5. It can be applied to workpieces with complex shapes;
6. The location of the electron beam irradiation areas and the working parameters can be precisely controlled. Thus it is possible to treat a selected area on a workpiece and control the depth of modified layer;
7. The surface modification is finished in a vacuum. Consequently, oxygen, nitrogen and other harmful contaminations are avoided;
8. Rapid surface alloying can be simply achieved by precoating the alloying elements followed by post treatment by the electron beam. This greatly reduces the consumption of the additive elements.

Considering the advantages of pulsed electron beams and their possible applications in industries, different pulsed electron beam systems were developed during the past few decades. These include for examples: gepulste elektronenstrahlanlage (GESA) [61-63], pseudo-spark pulsed electron beam [64-66], high current pulsed electron beam [67-73], etc. They have very different characteristics depending on the electron energy, beam current density, pulse duration and beam cross sectional area. The GESA II system, which is developed through a cooperation between the Efremov Institute St. Petersburg in Russia and the Forschungszentrum Karlsruhe (FZK) in Germany, can produce electron beams with the following parameters: accelerating voltage 200-400 keV, power density up to 6 MW/cm^2, beam diameter 4-6 cm, pulse duration 5-250 μs. It can generate a melted layer with depth more than 100 μm on Fe [62]. Due to the rapid solidification following melting, fine and homogeneous microstructures can be generated in the surface layer. Several investigations have shown that the wear and corrosion resistances of the treated materials can be effectively improved [61]. Surface alloying with Al of steel substrates has also been attempted using the GESA facility for the purpose of improving the corrosion behavior of steels in liquid lead and lead-bismuth [63]. An alloyed layer with depth up to 20 μm could be obtained. Such a thick Al alloyed layer provides a very good corrosion resistance against liquid lead. The pseudo-spark pulsed electron beam can produce pulsed electron beam with accelerating voltage 10–40 kV, power density up to 10^9 W/cm^2. However, the energy concentrates only on a very small area with diameters of few hundreds of micrometers. These systems were proposed to be used in refining the microstructure of the materials surface and surface alloying. A kind of pulsed electron beam generated from the linear inductive accelerator LIU 3000 also exists [74]. It has the following parameters: electron energy 800 keV, beam current 200 A, pulse duration 10^{-7} s, repetition rate 0.5 Hz, beam diameter 20 mm. It has been applied on the modifications of magnetic and transport properties of ferromagnetic materials [74].

I.4 High current Pulsed electron beam technique

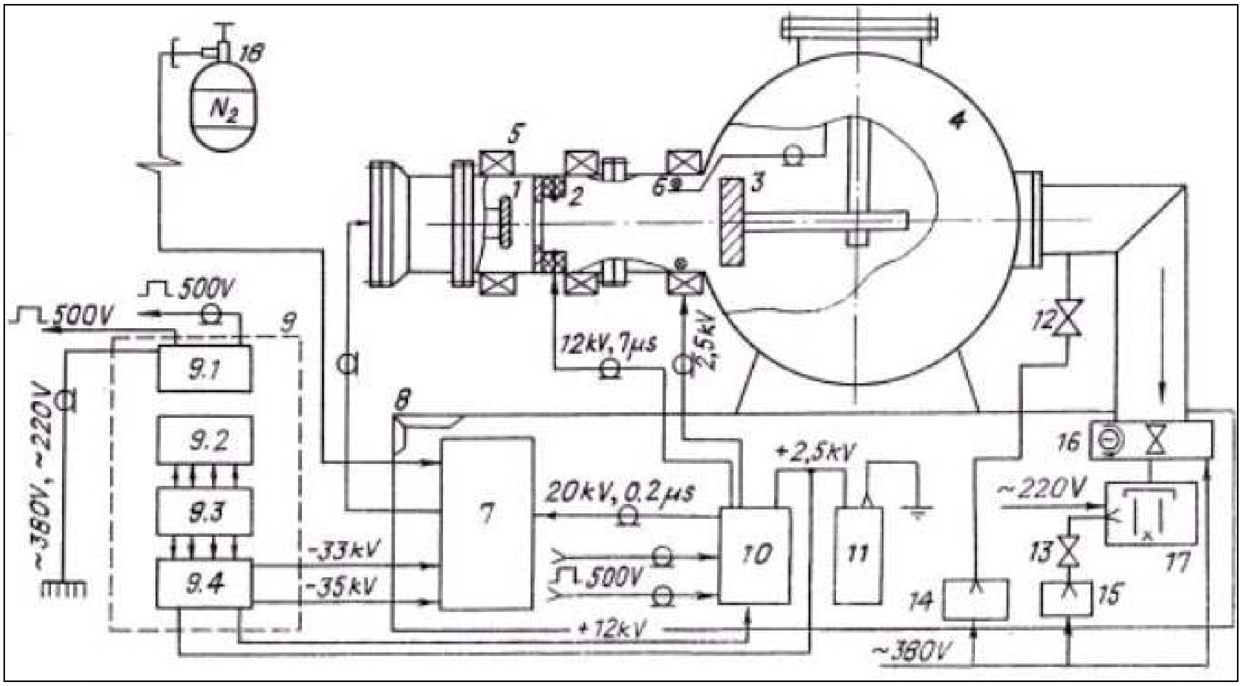

1. cathode, 2. spark source, 3. collector, 4. vacuum chamber, 5. solenoid, 6. rokovsky coil, 7. pulsed high-voltage generator, 8. bracket, 9. electricity controller, 10. pulses trigger, 11. capacitor, 12. 13. manual vacuum valve 1, 2, 14. 15. pump 1, 2, 16. electromagnetism valve, 17. diffusion pump, 18. nitrogen

Fig. I-2 Schematic diagram of the High Current Pulsed Electron Beam (HCPEB) system [67].

Among those pulsed electron beam techniques, the High Current Pulsed Electron Beam technique (HCPEB) is fairly recent [67-70]. It was developed in Russia, institute of high current electronics in Tomsk. In the early 1990s, the research group headed by Prof. Proskurovsky has achieved considerable success in the creation of a high current pulsed electron beam source that contains an electron gun with an explosive emission cathode and a plasma anode placed in a guide magnetic field [67]. The HCPEB source has the following operating parameters : electron energy 0.5–40 keV; The pulse duration 0.5–5 μs; energy density 0.5–40 J/cm^2; beam cross-section area 10–50 cm^2; and pulse repetition rate 0.2 Hz. Proskurovsky et al. have investigated the implications of HCPEB for treating industrial alloys and suggested its potential applications as an efficient method for thermal protection, rapid annealing, surface cleaning and surface alloying [67].

A schematic diagram of the HCPEB system is given in Fig. I-2. It can be divided into four complementary parts: electron beam source, vacuum system, pulsed high power supply and diagnose devices. The electron beam source is the main part of the system which produces the pulsed electron beam. Fig. I-3 shows a detailed sketch of the electron beam gun. The explosive emission cathode is made of porous graphite for its low ionization potential. The anode is made of stainless steel and has a hole in its center through which the beam passes. Graphite cathode spark plasma sources are placed evenly in a circle behind the anode. The electron beam is transported through the anode plasma to the collector. To prevent the beam from pinching and dispersing, an external magnetic field created by a sectioned solenoid is used.

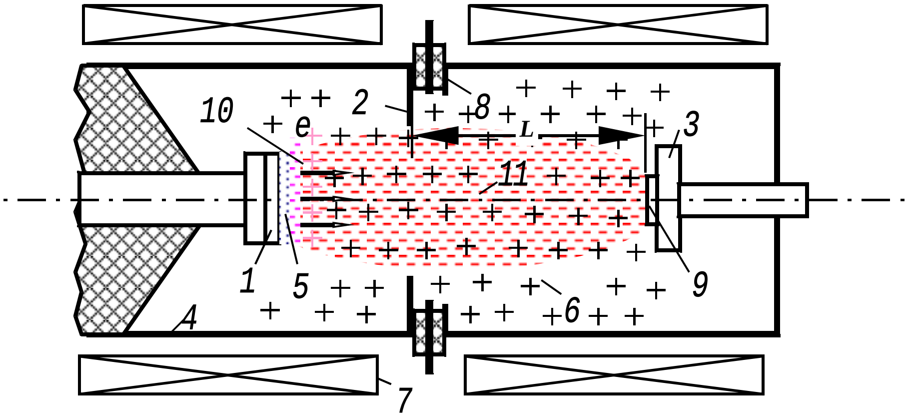

(1) cathode (2) anode (3) collector (4) vacuum chamber (5) cathode plasma (6) anode plasma (7) solenoid (8) spark plasma sources (9) specimen (10) plasma sheath (11)electron beam

Fig. I-3 Schematic diagram of the HCPEB source based on vacuum spark plasma [67].

The explosive electron beam is generated using the following procedures. As the magnetic field reaches its maximum, the spark plasma sources are switched on and the anode plasma fills the chamber. When the anode plasma reaches the graphite cathode, the accelerating voltage produced by a voltage pulse generator is applied to the cathode. This results in the initiation of the explosive electron emission at the cathode and an electron beam is formed in the plasma filled diode. With the use of the magnetic field, the efficiency of the conversion of the energy stored into beam energy is very high, up to 40%. Moreover, the transportation of the beam in plasma permits the anode/treated surface distance to be increased to values as high as 20 cm. Varying the accelerating voltage, magnetic fields intensity and the anode collector distance can control the beam energy density. An image of the HCPEB system is shown in Fig. I-4. One can clearly see the vacuum chamber, the electron gun and the magnetic coils.

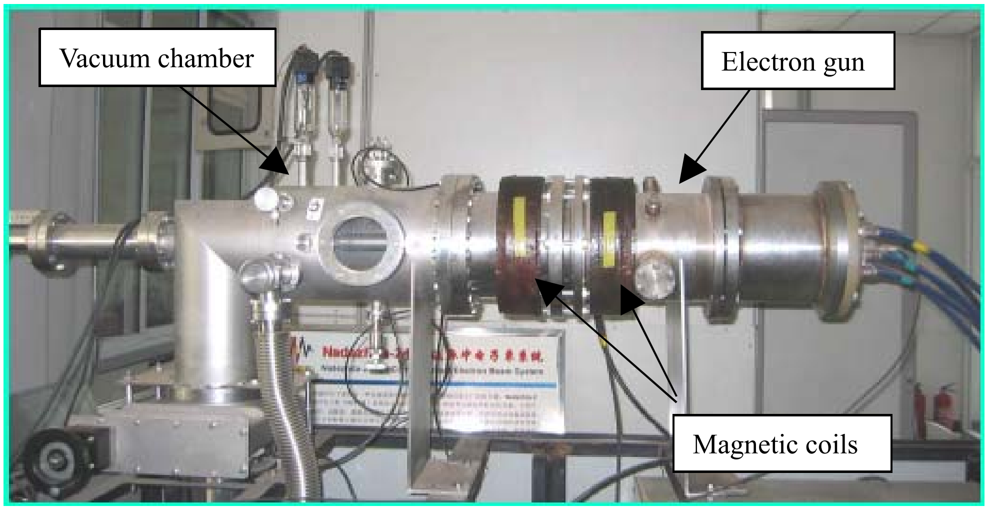

Fig. I-4 An image of the HCPEB system [79].

The simplicity and reliability of this HCPEB technique render special advantages over laser and ion beam treatments, with potential industrial applications [75-78]. The high-density electron pulses of short durations induce dynamic temperature fields in the surface layers giving rise to superfast heating and possible melting. This is followed by a rapid solidification and cooling of the material surface. In addition, a dynamic stress field is formed that causes intense deformation in the material sub-layers [79-81]. As a result, non-equilibrium microstructures can be achieved. This authorizes to form a surface layer with improved physical, chemical and strength properties that are often unattainable with conventional surface treatment techniques [67-69, 77-79]. This is particularly true for corrosion and tribological properties.

Chapter II. Physical foundations of materials surface treatment by HCPEB

II. 1 Interaction of electron beam with materials

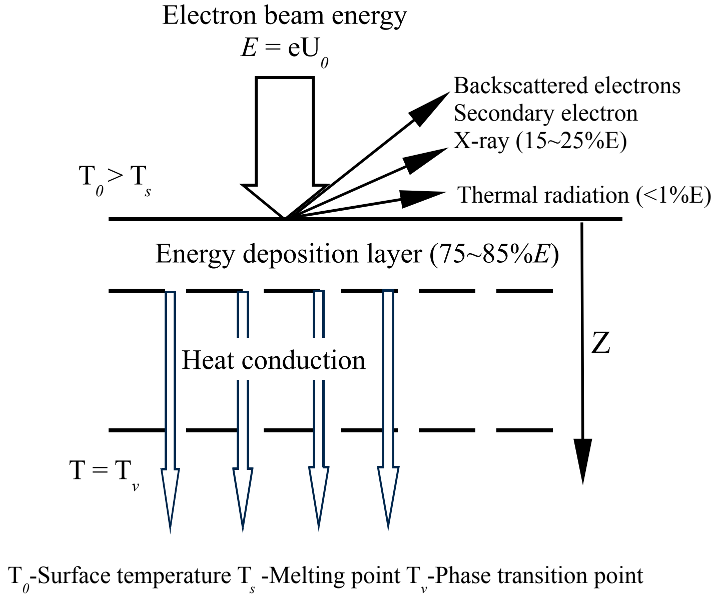

Fig. II-1 Energy transfer in the surface layer of materials during the electron beam bombardment.

When an electron beam having a certain energy density irradiates a target surface, several phenomena take place at the surface layer of the target. These phenomena are of the same type as those induced in electron microscopes [82]. The electron beam can penetrate only a very shallow depth, for instance, about several micrometers when the electron energy is about several tens of keV. Therefore, the energy absorption is limited within this thin surface layer through the interactions of electrons and atoms, and the scattering process mainly converts the electron beam energy into heat. The interactions between the electron beam and target materials are schematically illustrated in Fig. II-1. It should be noted that one of the factors determining the conversion of electron beam energy into materials is the incident angle of the electron beam.

Indeed, the energy deposition profiles of the electron beam inside the target materials can be changed by varying this incident angle [83]. In our case, the incident beam is always set to be perpendicular to the target materials. In the energy deposition layer, about 75% to 85% of the electron energy is transferred into heat and the rest is lost in different ways via the formation of backscattered and secondary electrons, X-ray and thermal radiations [82]. The energy deposition in the top surface layer creates an extremely high temperature gradient. After the shut off of the electron beam, the energy-absorbing layer is cooled down rapidly as a result of the heat conduction through the region adjacent to the heated layer. Depending on different threshold temperatures of a given material, a layered structure can form on the treated material. For example, the top surface is a melted layer if the temperature reaches the melting point and beneath is a heat affected layer where phase transformations may have occurred.

It is well established that three different zones are usually observed in the surface depth of HCPEB treated samples [80,81]. A schematic illustration of these zones created by HCPEB treatment is shown in Fig. II-2.

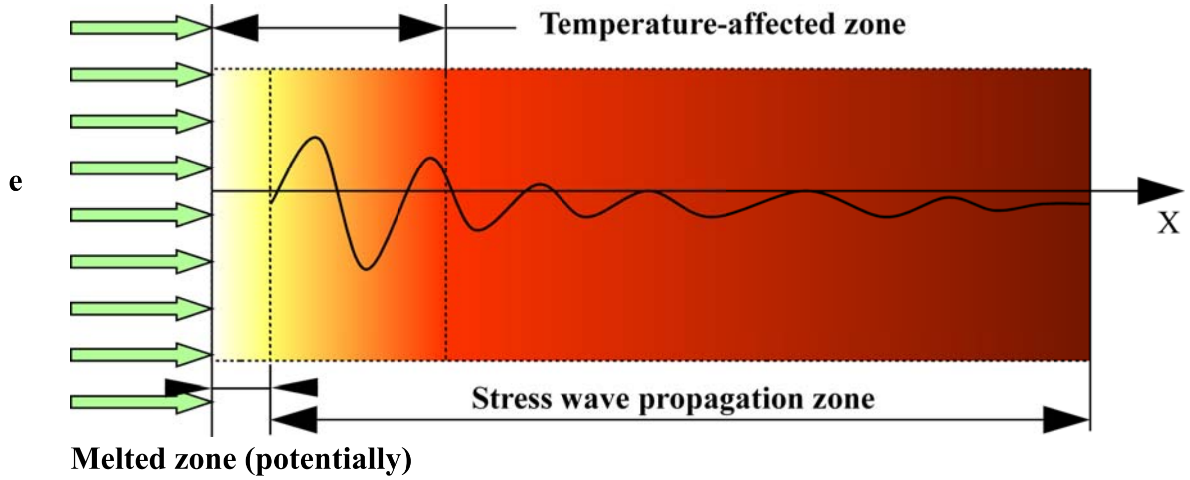

Fig. II-2 Schematic diagram of the different affected zones bombarded by HCPEB treatment.

Generally present at the top surface is a zone that has been melted and subsequently solidified rapidly. It is often a few μm in thickness but can be avoided, in particular for high conductivity alloys, when the energy provided by the electron beam is not sufficiently high. Below is found a heat affected zone (HAZ) that extends generally over a few tens of μm [80]. Finally, a last zone, that is due to the propagation of the shock wave and for which the material hardness can also be strongly affected may be present at depth far exceeding the heat-affected zone. After sufficient number of pulses (typically 15 to 20) of HCPEB treatment, this hardened zone can extend over hundreds of μm [67,84,85].

II. 2 Physical foundations

II. 2. 1Physical model for temperature fields

When an electron beam irradiates a target, a non-stationary temperature field is generated in the surface layer as a result of the absorption of the beam energy. To model the temperature field, the following assumptions are proposed based on the characteristics of the HCPEB technique [81]:

a) the current density of the electron beam is uniform over the total transversal cross-section of the beam;

b) the diameter of the treated material is smaller than that of the electron beam;

c) the initial material is uniform in its physical structure and properties.

The following one-dimensional heat conduction equation has to be solved [76]:

$$\rho c(T)\frac{\partial T}{\partial t}=\frac{\partial}{\partial x}(\lambda(T)\frac{\partial T}{\partial x})+L_v(x,t) \qquad \text{(II-1)},$$

with the initial conditions:

$$T(x,0) = T_0 \qquad \text{(II-2),}$$

and the boundary conditions:

$$-\lambda(T)\frac{\partial T(x,t)}{\partial x}\Big|_{x=0,x=l} = 0 \qquad \text{(II-3),}$$

where T is the temperature field; ρ,c and λ the mass density, the heat capacity and the heat conductivity, respectively. L_v is the volume power density of the heat sources; T_0 is the initial temperature of the material and l is the thickness of the specimen.

The second term on the right hand side of Equ. II-1 can be written as [67]:

$$L_v(x,t) = \frac{j(t)E_0(t)}{r(t)e} f(x,r) \qquad \text{(II-4),}$$

where *j(t)* is the electron current density in the target. *E₀(t)* is the initial electron energy. *r(t)* the extrapolated electron range; *f(x,r)* the depth distribution of the electron energy losses, which can be described as a third-degree polynomial function [67]:

$$f(x,r) = 0.74 + 4.7xr^{-1} - 8.9(xr^{-1})^2 + 3.5(xr^{-1})^3,\ x \in [0,r] \qquad \text{(II-5).}$$

The extrapolated range was found from the formula [67]:

$$r(E_0) = C(E_0/e)^{3/2}/\rho \qquad \text{(II-6),}$$

where C is a constant equal to 10^{-4} kg/(m^{2}V$^{3/2}$) and E_0 is measured in kilo-electron volt.

Based on Equ. II-5, it is known that the beam energy density and its deposition depth in the material will change together with the applied accelerating voltage. As illustrated in Fig. II-3a, the higher accelerating voltage leads to a deeper energy deposition layout in a given material for the case of pure Aluminum. The penetrating range is about 5.5 μm when the accelerating voltage

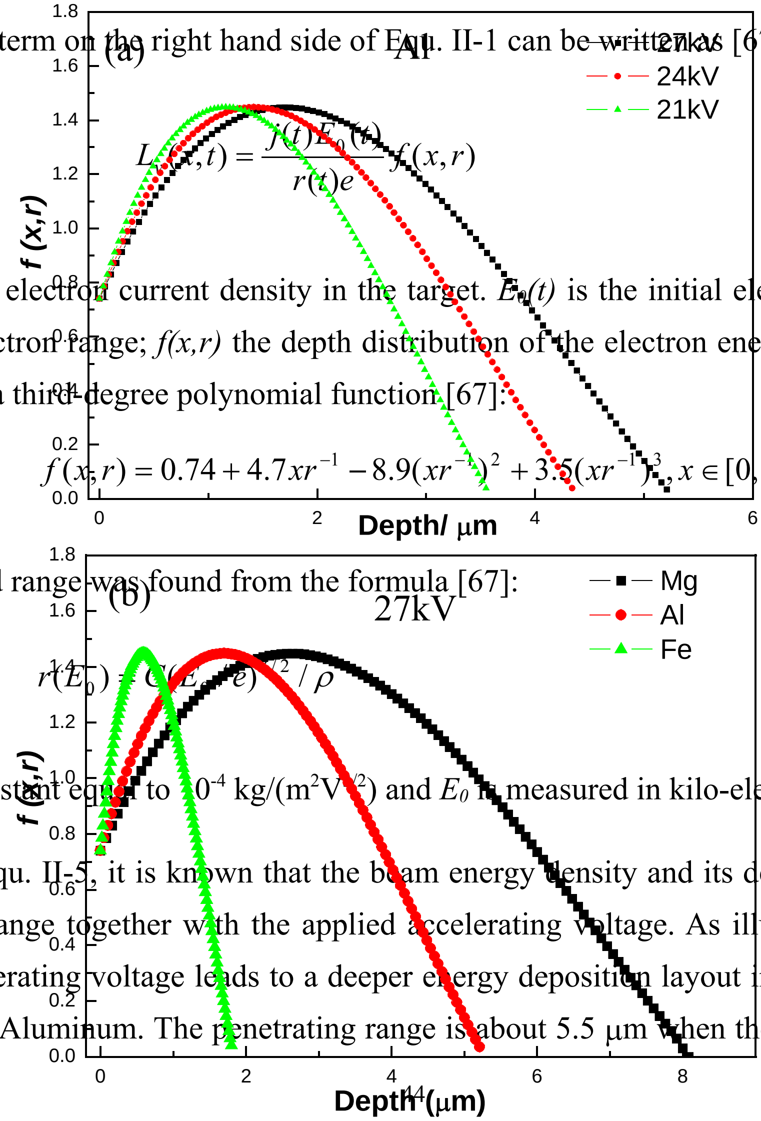

Fig. II-3 The energy deposition profiles of electron beams with different accelerating voltages applied on Al (a) and for different materials under a 27kV accelerating voltage (b).

is 27 kV. Comparatively, it is only about 3.5 μm for 21 kV. Moreover, it can also be seen that the maximum HCPEB energy deposition locates at about one third of the penetrating range. At this depth, this corresponds to the highest heating rate. Fig. II-3b shows that the beam energy density and its deposition depth also change with the treated materials. Under the same accelerating voltage, the electron beam has a deeper penetration depth when the treated material has a lower density. For examples, the penetrating range in Mg is about 8 μm when accelerating voltage is 27 kV, while for Fe, it is only about 1.8 μm.

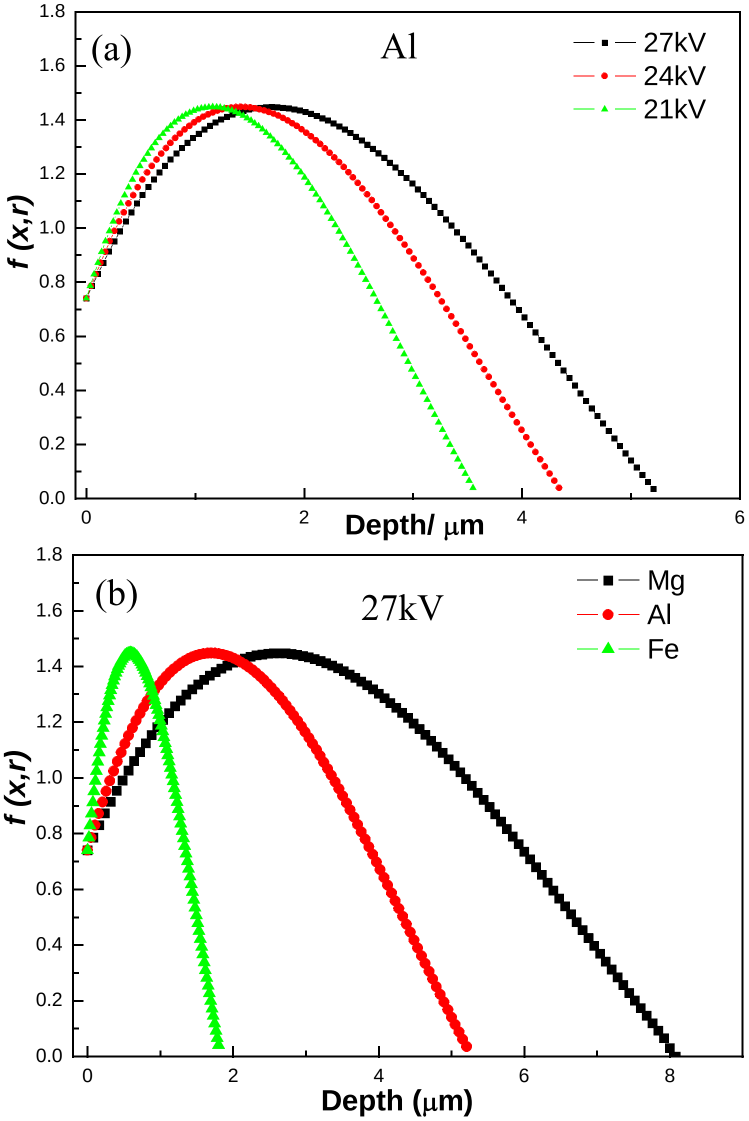

Fig. II-3 The energy deposition profiles of electron beams with different accelerating voltages applied on Al (a) and for different materials under a 27kV accelerating voltage (b).

II. 2. 2 Simulation of temperature field and melting process

Fig. II-4 presents the simulated temperature evolution with time and depth in pure Al treated by HCPEB [81]. The selected pulse duration was 1.5 μs; the energy density about 3.0 J/cm^2 and the accelerating voltage 27.8 kV. The heat-affected zone is localized near the surface, in a depth range of 25-30 μm where T≤ 500 K. Although the maximum energy deposition locates at subsurface, the surface temperature is always the highest because the thermal conductivity of Al is very high. The thickness of the melt is about 2~3 micrometers, which is close to the TEM observation [85]; the melt time is about 1 μs; the velocity of the crystallization front is 3~5 m/s; the heating rate is about 10^9 K/s, and the cooling rate is about 10^8 K/s on average and even higher at the surface.

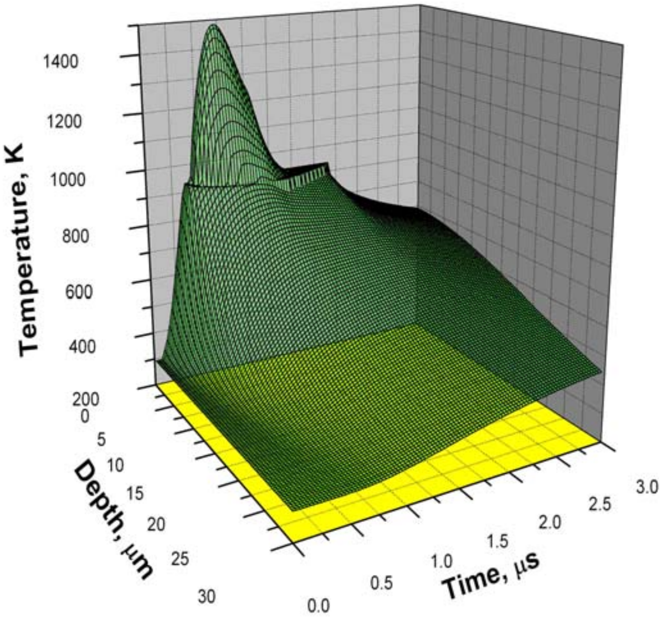

Fig. II-4 Temperature field in the surface layer of Al irradiated by HCPEB, energy density S≈3 J/cm², τ≈1.5 µs.

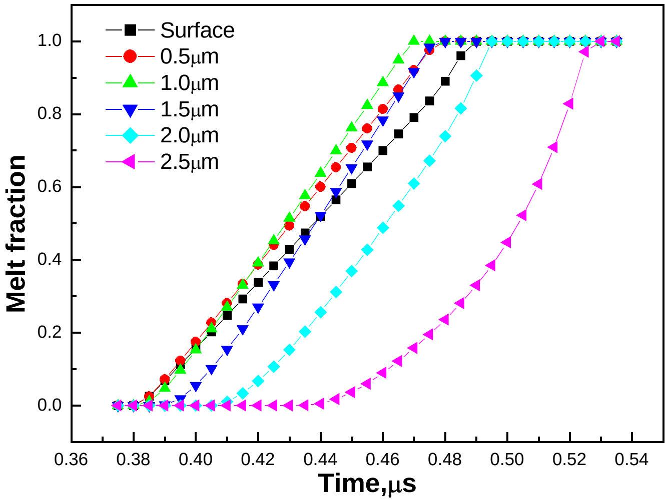

Fig. II-5 Evolution of the melted fraction at different depths, pulse width 1.5 µs, S=3.0 J/cm², E_0=27 keV.

In order to tackle the melting process with calculation, the temperature compensation method given in Ref.[86] is often used. By changing the electron beam parameters, it is depicted that if the pulse is sufficiently short and the energy is sufficiently high, the melting will start in a subsurface layer due to the specific depth distribution of the electron beam energy deposition in the target (see Equ. II-5) and the significantly decreased thermal conductivity near the melting point. Fig. II-5 shows the evolution of the melted fraction at different depths during a heating process. It can be seen in Fig. II-5 that the complete melting first occurs at a depth of about 1~1.5 μm, corresponding to the calculated maximum energy deposition depth (Fig. II-3).

II. 2. 3 Physical model for stress fields

For the HCPEB surface treatment without melting of the surface, besides the effect from temperature field, stress fields will play an important role in determining the final structure and stress strain state. It is already known that there are two kinds of stress fields induced by the bombardment before melting [87] : a quasi-static thermal stress and a dynamic thermal stress. From the theory of thermal-elasticity, it is established that the quasi-static stress is caused by a temperature gradient in the direction of the thickness. It is bisymmetric [87,88]. The dynamic stress is a kind of inertia force associated with super-fast thermal expansion of the solid [87]. It is different from the shock wave induced by a recoil force of gas scattering [89]. Based on the same one-dimensional thermal conductive equation (Equ. II-1), the dynamic thermal stress σ_x and the quasi-static thermal stress $\sigma_{(y,z)}$can be described as the following equations, respectively [88]:

$$\frac{1}{C_S^2}\frac{\partial^2\sigma_x(x,t)}{\partial t^2}=\frac{\partial^2\sigma_x(x,t)}{\partial x^2}-\frac{1+\nu}{1-\nu}\rho a\frac{\partial^2 T(x,t)}{\partial t^2} \tag{II-7}$$,

$$\sigma_y=\sigma_z=-\frac{\alpha E}{1-\nu}T(x,t)+\frac{\nu}{1-\nu}\sigma_x \tag{II-8}$$,

with the initial conditions:

$$\sigma_{x,y,z}(x,0)=0 \tag{II-9}$$,

$$\frac{\partial\sigma_{x,y,z}(x,0)}{\partial t}=0 \tag{II-10}$$,

and the boundary conditions:

$$\sigma(x,t)\,|_{x=0,x=l}=0 \tag{II-11}$$,

$$\sigma_y(t)\big|_{t=0}=\sigma_z(t)\big|_{t=0}=0 \tag{II-12}$$,

where T and σ are the temperature and stress fields respectively; ρ, C_s, ν, E and a are the mass density, the longitudinal sound velocity, the Poisson's ratio, the Young's modulus and the thermal expansion coefficient, respectively. l is the thickness of the specimen.

II. 2. 4 Temperature field and thermal stress wave under non-melting mode

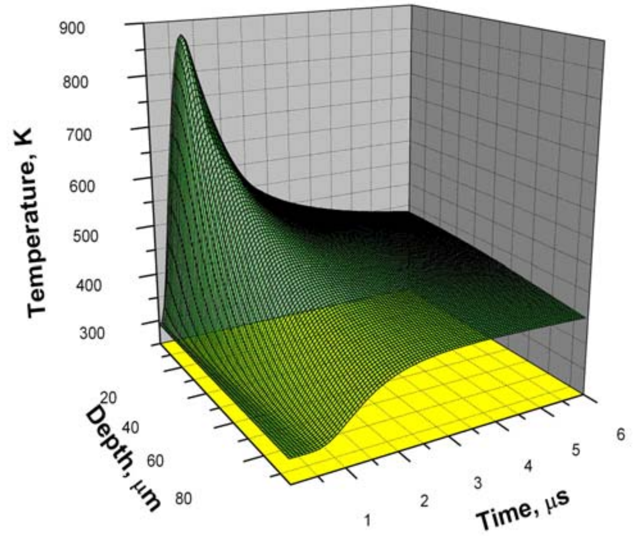

Fig. II-6 Simulated temperature field in the Al sample during HCPEB treatment without melting.

To shov of 1.5μs, an accelerating
voltage of 2 or the simulation of the
temperature 1]. Fig. II-6 shows the
temperature l for a duration of 0-6μs.
The simulati urring in the near surface
layer with a 933K) reached at the top

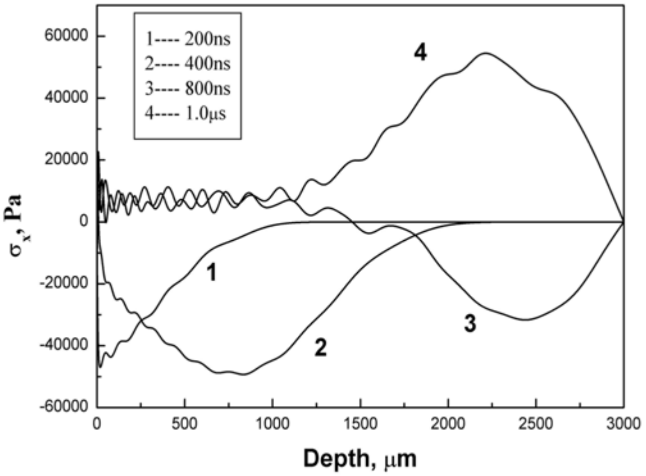

Fig. II-7 Creation, propagation and reflection of the thermal stress wave.

surface within 1 μs.

Fig. II-7 shows the simulated processes of the creation, propagation and reflection of the thermal stress wave in pure Al foil of 3 mm in thickness under the same treatment parameters. Initially a compression stress of long wave with amplitude ~0.05 MPa is formed and then it propagates from the surface into the bulk followed by short waves. The stress wave reverses its polarity when reflected by the rear surface of the target. It interferes with the incoming wave, which makes the absolute value of the long-wave peak slightly higher.

By varying the beam parameters, the long-wave in the thermal stress wave prior to melting was found to obey the following rules [81]:

(1) its amplitude is proportional to the energy density if other parameters are fixed;

(2) its amplitude is inversely proportional to the pulse duration if other parameters are fixed;

(3) its duration is proportional to the pulse duration if other parameters are fixed;

(4) there exists a special distance at which the thermal stress reaches its peak value, being about 20μm for Al.

II. 2. 5 Theoretical analysis of anisotropic thermal stress

The results of the calculations given above have shown that the thermoelastic stress wave has generally a very low amplitude, of the order of several hundreds kPa [80,81]. It can therefore be omitted in the case of severe plastic deformation occurring at the top surface. Comparatively, the quasi-static stress that is generated by the confinement due to the difference of lateral thermal expansion has a higher amplitude. It has a biaxial symmetry and has its direction parallel to the sample surface. It concentrates mainly within the HAZ and changes its intensity with the distribution of the temperature field. Based on Equ. II-8, and considering the anisotropic Young's modulus, the magnitude of the biaxial quasi-static stress imparted to the sample before melting can be estimated by the following equation

$$\sigma_y = \sigma_z = -\frac{\alpha E_{<hkl>}}{1-\nu} \cdot \Delta T(x,t) \qquad \text{(II-13),}$$

where $E_{<hkl>}$ is the Young's modulus along the <hkl> directions. The calculation shows that the magnitude of thermal stress before melting is several hundreds of Mpa, much higher than the yield strength of most metals. It should be noted here that the Young's modulus $E_{<hkl>}$ is also anisotropic in most materials. As a result, the stress amplitude will be different from one grain to another. For a cubic metal, the orientation dependence of the Young's modulus $E_{<hkl>}$ is given by Equ. II-14 [90,91]:

$$\frac{1}{E_{<hkl>}} = S_{11} - 2\{(S_{11} - S_{12}) - \frac{1}{2} S_{44}\} A_{<hkl>} \qquad \text{(II-14),}$$

where $A_{<hkl>} = (h^2k^2 + h^2l^2 + k^2l^2)/(h^2 + k^2 + l^2)^2$, and S_{11}, S_{12} and S_{44} are the compliance coefficients. $A_{<hkl>}$ varies between 0 for the <100> directions, and 1/3 for <111>. Here we define $b=2\{(S_{11}-S_{12})-(1/2)S_{44}\}$ for convenience, which is generally positive. In most *fcc* materials for example, the Young's modulus is the highest along <111> and the lowest along <100> [90]. We notice that, if $A_{<hkl>}=0$ (i.e. for the <100> directions) $1/E_{<100>}=S_{11}$. We can obtain the following equation:

$$E_{<hkl>} = \frac{E_{<100>}}{1 - bE_{<100>}A_{<hkl>}} \qquad \text{(II-15).}$$

Since the Young's modulus of many *fcc* metals shows an nearly linear relation with $A_{<hkl>}$ and $bE_{<100>}A_{<hkl>}$ is quite small, $1/(1 - bE_{<100>}A_{<hkl>}) \approx 1 + bE_{<100>}A_{<hkl>}$. Thus, Equ. II-13 can be written as Equ. II-16:

$$\sigma_y = \sigma_z = -\frac{\alpha E_{<100>}(1 + bE_{<100>}A_{<hkl>})}{1-\nu}\Delta T(x,t) \qquad \text{(II-16).}$$

This equation clearly gives an increased amplitude of quasi-static thermal stress existing from <100> oriented grains to the <111> oriented grains during HCPEB treatment.

II. 2. 6 Quasi-static thermal stress in thin foil

From the theory of thermal-elasticity, the quasi-static thermal stress of a thin foil subject to a temperature distribution *T(x,t)* through the thickness is described by [87]:

$$\sigma_y = \sigma_z = -\frac{1}{1-\nu}\alpha(T)E(T)T(x,t) + \frac{N_T}{l} + \frac{12M_T x}{l^3} \qquad \text{(II-17),}$$

where N_T is a resultant force:

$$N_T = \frac{1}{1-\nu}\int_{-l/2}^{l/2}\alpha(T)E(T)T(x,t)dx \qquad \text{(II-18),}$$

M_T is the bending moment:

$$M_T = \frac{1}{1-\nu}\int_{-l/2}^{l/2} \alpha(T)E(T)T(x,t)xdx. \qquad \text{(II-19).}$$

In this case, the anisotropic effect of stress field is not considered. A thin Al foil was chosen to perform the calculation, the thickness being 150μm [81]. Fig. II-8 shows the evolution of the quasi-static stress with depth and time. The selected electron beam parameters are the same as the calculation of the temperature field. Fig. II-8 shows that the quasi-static compressive stress at the front surface char … ts peak value of about 750MPa at … ar face reaches a value as high as … exceed the yield strength of Al. … ic deformations. Experimental resu … irradiation on Fe reaches about 400

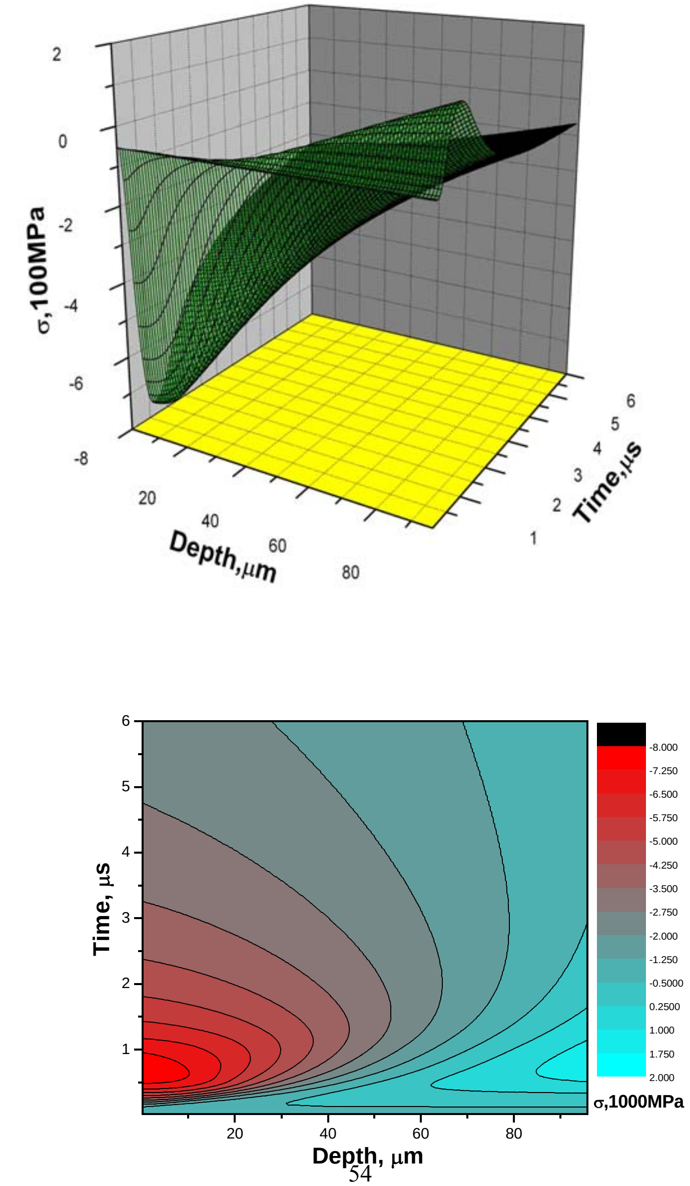

Fig. II-8 (a) Evolution of the quasi-static thermal stress in Al foil during HCPEB treatment. (b) Contour map of Fig. a. Pulse duration 1.5 μs, energy S=1.5 J/cm^2*.*

II. 2. 7 Origin of surface hardening

One of the most important features of the HCPEB treated materials is the hardening of the subsurface layer where the material is not melted [67,78,84]. This is observed in pure Al for which no phase transformations occurred during treatment. Defects created in the materials by HCPEB treatment is regarded as the main reason for the improved mechanical properties. Porgrenjak et al. [92, 93] studied the defect formation in α-Fe treated by an Intense Pulsed Ion Beam (IPIB) and HCPEB. Their results showed that the microhardness of the modified layer is proportional to the local dislocation density. This means that the hardening mechanism under thermal impact treatment is, in fact, a special kind of work hardening.

For Al, the linear expansion factor $\alpha \approx 2.54\times10^{-5}$ m/m•K, while the volume dilatation coefficient equals to 3α. Theoretically speaking, under the two dimensional restraint condition, when the temperature nearly reaches the melting point, the estimated deformation $3\alpha T_m \approx 5\%$, which is the largest deformation for a single-pulse treated Al. This deformation is quite small as compared with normal metal processing, but the deformation process is completed rapidly, within several microseconds, and the deformation rate is estimated to be about $10^{4\sim5}s^{-1}$, much higher than the many conventional processing. According to the theory of work hardening and the experimental results, it is more efficient for thermal impact treatment to increase the microhardness of metals under the same work hardening mechanism [94].

II. 2. 8 Physical model for Diffusion induced by HCPEB treatment

It was already observed that an enhanced diffusion effect could be induced by pulsed electron beam treatment [79,95]. The previous results showed that the pre-coated or implanted elements diffused into a deeper layer by applying several HCPEB pulses [69,77,79]. This effect is not only observed when melting occurred in the surface layer where liquid state mixing played the major role but also as will be demonstrated, under the non-melting treatment condition.

As the pulse duration is very short, and the temperature field and stress fields are transient, the mass transfer during treatment is extremely complicated. Considering the coexistence of the concentration gradient, the temperature gradient and stress gradient during treatment, the diffusion induced mass flow, temperature induced mass flow and stress induced flow must occur simultaneously. Following are the three flows described by Fick's first law :

1.Concentration flow [88]: $J_c = -D\frac{\partial c}{\partial x}$ (II-20),

where c is the concentration of the solute element, D the corresponding diffusion coefficient.

2.Temperature flow [88]: $J_T = -\frac{DQ_a}{RT^2}c\frac{\partial T}{\partial x}$ (II21),

where Q_a is the energy associated with the mass transfer per mole, T the temperature, R the universal gas constant. It should be note here that Q_a can be positive or negative. When it is positive, the solute atoms tend to move towards the colder area. If it is negative, the solute atoms move towards the hotter area during diffusion.

3. Stress flow [88]: $J_\sigma = -\frac{DV_a}{RT}c\frac{\partial \sigma}{\partial x}$ (II-22),

where V_a is the activation volume associated with the mass transfer per mole, σ the stress. Similarly, when V_a is positive, the solute atoms will move towards the area having a lower stress. If it is negative, the solute atoms will tend to move towards the area having a higher stress. Therefore, both the temperature flow and the stress flow can accelerate or suppress the diffusion process.

The total mass flow during treatment will be: $J=J_c+J_T+J_\sigma$ (II-23).

Since $\frac{\partial c}{\partial t} = -\frac{\partial J}{\partial x}$ (II-24),

we therefore obtain the following equation:

$$\frac{\partial c}{\partial t} = D\frac{\partial}{\partial x}(\frac{\partial c}{\partial x} + \frac{Q_a}{RT^2}c\frac{\partial T}{\partial x} + \frac{V_a}{RT}c\frac{\partial \sigma}{\partial x}) \quad \text{(II-25),}$$

where $D = D_0 \exp(-\frac{Q + V_a\sigma}{RT})$. This equation can be used to describe the diffusion processes occurring in materials treated by HCPEB. The initial conditions and the boundary condition may vary depending on the different treating methods.

To solve Equ. II-25 numerically, the differential method described before was also used here. Since the diffusion is combined with the temperature field and stress field, we first calculate the values of stress and temperature in each space and time unit and then put the values into the embedded program for diffusion processes. Finally, we obtain the concentration values at each time and space unit. In order to study the diffusion process induced by HCPEB treatment, a specific system has been selected for calculation. In this case, Al is selected as the diffusion matrix, while Ag is the solute element. This is a typical interstitial diffusion system and has the following parameters: $Q\approx 130$kJ/mol, $Q_a\approx 100$kJ/mol, $V_a\approx 10^{-6}$m^3/mol. The results of calculation show that all three flows have a nonlinear evolution with time and depth; the relative ratio of the three flows is determined to be about: J_c:J_T:$J_\sigma\approx$4:1:10^{-2}. This ratio may change due to the different diffusion systems and treatment parameters. Nevertheless, further calculations show that concentration flow still plays the major role for the diffusion process.

II. 2. 9 Physical model concerning evaporation

In some cases, the HCPEB may lead to significant evaporation on the treated materials when their boiling point is reached during treatment. For calculating the temperature field involving evaporation, the same one-dimensional thermal conductive equation (Equ. II-1) can be still used here. Considering evaporation, Equ. II-1 should be solved in a moving coordinate system, the distance of the moving surface being that of the evaporated layer, which was taken to be the following function of time:

$$X_e(t)=\int_0^t V_e(t)dt \tag{II-26}$$,

where $V_e(t)$ is the moving speed of the surface, $X_e(t)$ the evaporated depth.

For simulating the temperature field involving evaporation, a temperature compensation method is used, which is similar to the calculation of melting process. In each space unit h, during a certain time step τ, the evaporated depth d_k^p can be described with the following equation :

$$d_k^p=\frac{T_k^{p+1}-T_e}{\Delta T_e}h$$

(II-27),

where T_e is the boiling point, ΔT_e the evaporation compensation temperature. $\Delta T_e = H_e/c$, where H_e is the latent heat of evaporation, c the heat capacity of the melt. The whole evaporated depth D^p within the time step τ can be calculated by the following equation:

$$D^p = \sum_{k=1}^{n} d_k^p \qquad \text{(II-28)},$$

where d_k^p is the evaporated depth in space unit k at the time p.

Thus $V_e(t)$ can be described as :

$$V_e(t) = \frac{D^p}{\tau} \qquad \text{(II-29)}.$$

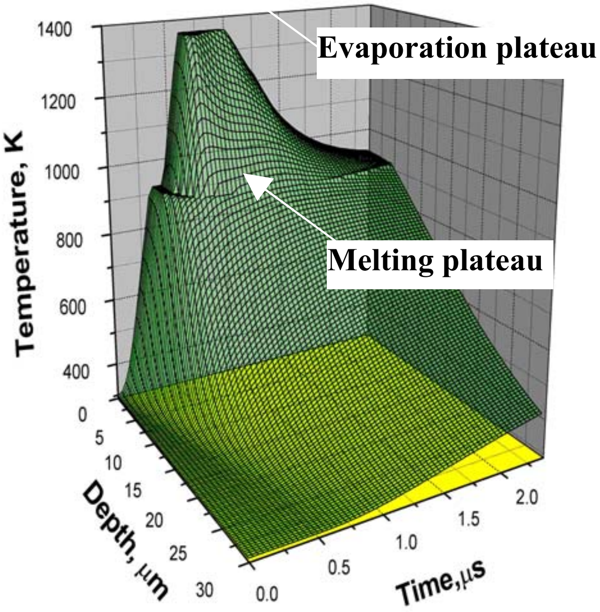

Fig. II-9 Temperature evolution in pure Mg bombarded by HCPEB for an energy density of 3 J/cm^2.

Fig. II-9 shows the temperature distributions in pure Mg over a depth range of 0-30 μm and for a duration of 0-2.5 μs when evaporation occurred during treatment. A pulse duration of 1.5μs and a deposition energy of 3 J/cm^2 were used for simulation. On heating, the presence of a shoulder at 922 K associated with the melting plateau is noticeable. On the top of the graph, another plateau corresp s present. It is the evaporation plateau, within which th ue the evaporation process.

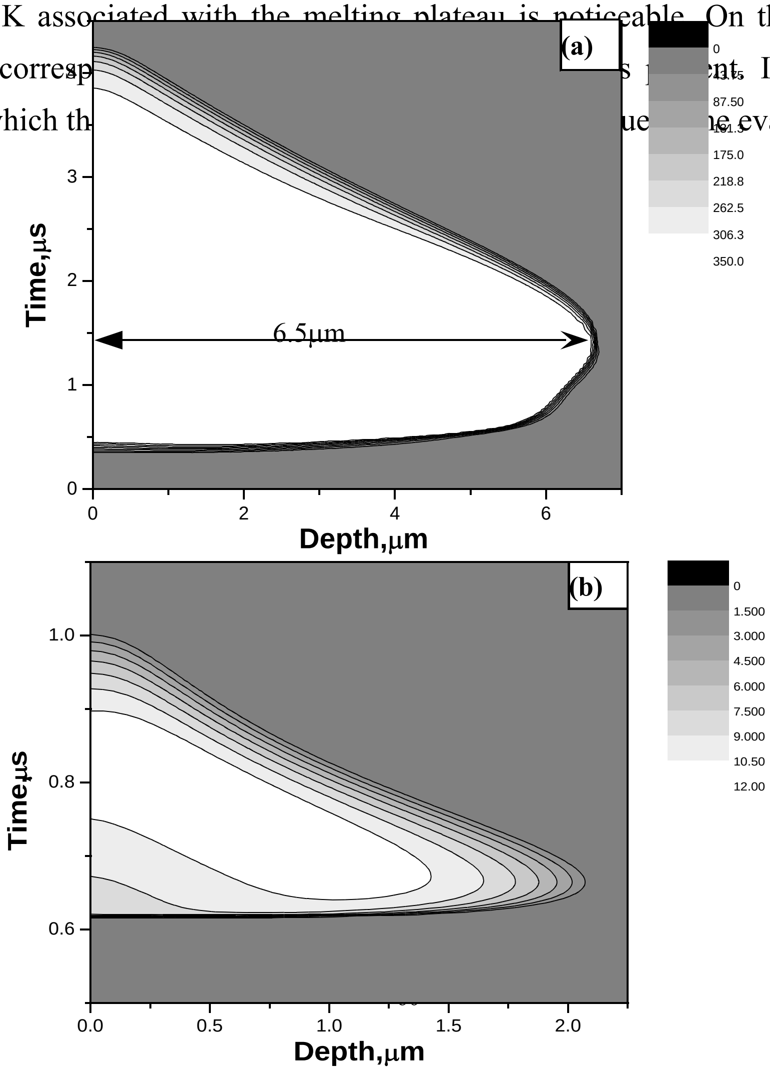

Fig. II-10 Contour plots of melting (a) and evaporation (b) compensation temperatures in pure Mg during the HCPEB treatment for a pulse energy of 3 J/cm^2.

Fig. II-10a and 10b present the depth/time contour plots of the melting and evaporation compensation temperature (arising from the absorption of the latent heat of melting and evaporation), respectively. Fig. II-10a shows that the melting of Mg starts after 0.35μs and the maximum melted depth reaches about 6.5 μm at 1.35 μs. It is interesting to note that the maximum depth of melted layer is reached just before the end of the beam pulse (~1.5 μs). The solidification process starts subsequently and the whole melted layer solidifies within 2.7 μs. The moving speed of the solidification front can reach a value as high as 2.4 m/s. In Fig. II-10b, the evaporation compensation temperature provides with the same kind of graph. However, unlike in the melting process, the evaporation compensation temperature can not be accumulated because the evaporation process makes the material disappear into the vacuum chamber. Therefore, during the calculation, the evaporation compensation temperature is set to 0 before each time step. It is related to the length of space and time step that is selected. From Fig. II-10b, it can be seen that the evaporation starts after 0.62 μs and that the boiling process occurs within a depth of about 2 μm. The maximium of the evaporation regime is located at a depth of about 1.2 μm beneath the surface. This is due to the special energy deposition profile of the electron beam in the materials. After 0.75 μs, the evaporation effect decreases and ends after about 1μs. At that time, the melted layer depth is still increasing. Calculation gives a total evaporated layer of 0.35 μm per pulse in the present case.

It could be suggested that the fast evaporation causes a recoil force into the target. By using a differential method, the recoil pressure *P* can be estimated by using the following equation :

$$P = V_s \rho \sqrt{\frac{8RT_e}{\pi M}} \tag{II-30}$$

(II-30),

where *M* is the molar mass of Mg. According to the calculation results given above, the maximum pressure is less than 0.45 MPa when the maximum energy density is taken at 6 J/cm^2, which is a relatively small stress for metals. If we change the energy density to 3 J/cm^2, which is the normal working parameter, the calculated pressure is even below 0.1 MPa. Therefore, the influence from the evaporation on the deformation process in the solid state Mg present below the melted layer can be omitted. However, the melted surface is likely to be bended under this recoil pressure [96], which, as will be discussed later, can also explain the wavy aspect of the surface observed when the evaporating mode is operating.

II. 3 Three modes of HCPEB treatment

It is clear that the surface properties after HCPEB must be determined by the final structure-phase states generated by this thermo-mechanical treatment [67,79,97,98]. Fairly limited information was available concerning the details of the microstructure modifications at the beginning of my PhD and little was known on the metallurgical phenomena encountered. The mechanisms of structure formations are also of special interest because under HCPEB, phase transformations are likely to take place under non-equilibrium conditions.

To explore the modification of structures and properties under the action of HCPEB, we are illustrating in this thesis some surface effects obtained on several materials. In particular, we detail some of the features observed when treating the top surface with melting, without melting and with partial evaporation. Fig. II-11 shows the typical temperature profiles encountered in the top surface of a material treated by HCPEB with different energy density. As indicated in the figure, under low energy density treatment, the temperature in the top surface of the material can not reach the melting point (T_m) during the whole treating process. Such a treatment mode is called “heating” mode. The treating modes during which the temperature in the top surface reaches melting point and boiling point (T_b) are called the “melting” and “evaporating” modes, respectively. The distinction between these three modes of treatment is, we believe, of the outmost importance to get the full potential of this surface treatment technique. Therefore, the examples of surface modification shown in this work very often are grouped into three different categories: (i) modifications observed in the melted layer (melting mode) and (ii) modification resulting from the so-called heating mode for which the top surface remains in the solid state during the overall treatment (iii) modification under the so-called evaporating mode for which the top surface is partially evaporated during the treatment.

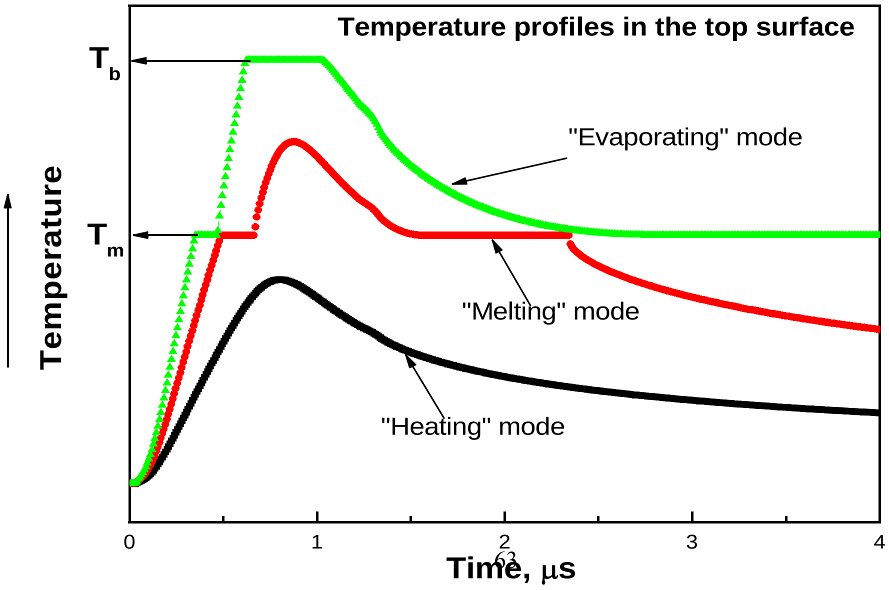

Fig. II-11 Typical temperature profiles in the top surface of a material by HCPEB treatment with different energy density, showing the three treating modes.

Chapter III Special phenomena induced by HCPEB treatment

In the previous chapter, physical models for surface treatments by HCPEB have been established and numerically solved. The results showed that HCPEB irradiation induces dynamic temperature fields in the surface of the material, giving rise to superfast heating, possible melting and even evaporation that is followed by a rapid solidification of the very first surface layer by heat conduction towards the bulk. Concomitant to the thermal effect, it has been shown that the pulsed electron beam creates a dynamic stress field that causes intense deformation at the material surface [80,81]. The combination of these processes makes it possible to modify substantially the surface characteristics and, in many cases, improve the mechanical properties faster and more efficiently than conventional surface treatment techniques [67-79]. In the case of steels for example, it has been established that the hardness, wear resistance or corrosion resistance can be significantly improved by using HCPEB treatment [67-70,98].

Here, we detail, in particular, some of the special phenomena observed when treating materials without melting, with melting and with evaporating of the top surface. These phenomena were observed on many HCPEB treated materials. They can be understood based on the physical foundations established before.

III. 1 Metastable structure formations

HCPEB treatment induces very fast heating, melting, solidification and is followed by rapid cooling of the materials surface layer. These procedures are often performed under non-equilibrium conditions, which render possible formation of metastable phases and microstructures. In particular, phase selection from the melt during rapid solidification and subsequent solid state phase transformation paths during cooling can be affected. These processes need to be studied because they determine the final microstructures and properties of the treated materials. Of course, all the three modes of HCPEB treatment may cause metastable structure formation in the treated materials. In this section, only the melting mode is shown since it is the most important mode and more evidences were observed. We will first show the effect of the HCPEB treatment in different steels (carbon steels, AISI D2 and H13 steels) and then concentrate on a NiTi intermetallic.

III. 1. 1 Carbon steels

Carbon steels have long been studied by scientists and widely used in industry. The phase transformations in steels, especially under non-equilibrium conditions, are still the subject of many recent works [99-101]. Therefore, the study of phase transformations and microstructure modifications in steels induced by HCPEB treatment is of technical and scientific interests. The simple Fe-C system would be ideal for studying metastable phase transformations. In the present work, three steels were investigated. They have different carbon content: ~0.45wt% (45# steel), ~0.77wt% (T8 steel) and ~1.0wt% (T10 steel) which correspond to hypoeutectoid, eutectoid and hypereutectoid steels, respectively. The samples used for HCPEB treatment were divided into two groups: “quenched” and “slowly cooled”. One group of samples was austenitized at Ac_1/Acm +50ºC for 1 hour and quenched in water. They were subsequently tempered at 200ºC for 60min so that all samples consisted of tempered martensite. The other group of samples was austenitized at Ac_1/Acm+50ºC for 1 hour and slowly cooled down to room temperature. In this case, the samples consisted of various amounts of pearlite structure mixed with 42.8% of ferrite for the 45# steel and with 3.9% cementite for the T10 steel. Therefore, each type of steel has two initial structural states. The electron-beam treatment parameters for all type the samples were set as follows: the energy density was about 4 J/cm^2 the accelerating voltage of the electron beam was kept constant at 27 kV and different pulse numbers were used (5 and 10 times).

Fig. III-1 shows the evolution of the XRD patterns of equilibrium treated carbon steels (austenitized and slow cooling down to room temperature) samples with the number of HCPEB pulses. Fig. III-1a is the evolution for the case of 45# steel. The starting material contained in fact two phases : ferrite (α-Fe) and carbide Fe_3C. However, due to the low volume fraction of the carbide, its peaks are not visible in the XRD pattern of the starting material. After the HCPEB bombardment, a fairly weak peak corresponding to γ-Fe is present in the XRD patterns. The peak intensity of the γ-Fe phase decreases after 10 pulses, indicating that the volume fraction of the γ phase detected by XRD decreases. TEM observations show that the austenite formed in the

HCPEB treated 45# steel is nano scaled [102,103]. The formation of the nano-austenite structure might be attributed to the dissolution of the initial cementite present in the pearlite phase and the subsequent stabilization of the γ phase due to the increased carbon concentration. For the case of T8 steel (Fig. III-1b), the initial material contained only pearlite (ferrite+cementite). After the HCPEB treatment, the formation of γ-Fe phase observed from XRD patterns is more pronounced than for HCPEB treated 45# steel. This could be attributed to the higher concentration of C (higher carbide content) in T8 steel than that in 45# steel. Since the γ phase usually nucleates at the ferrite and carbide boundaries during austenitization processes of carbon steels, more carbides in the steel would bring more nucleation sites for the formation of the γ phase. A careful look at the peak corresponding to the {200} plane of the α phase after HCPEB treatment reveals a very weak splitting which indicates the formation of martensite (α' phase) in the surface layer. This means that a part of austenite transformed into martensite during cooling while the rest was retained at room temperature. Size effects and high carbon concentration may contribute to the stabilization of γ phase [101,102]. In the case of the T10 steel (Fig. III-1c), the initial structure is composed of pearlite + cementite. The XRD patterns after HCPEB treatment are also characterized by the presence of γ phase. Comparing the XRD patterns for all the T10 samples and the T8 samples treated with 5 pulses, one can clearly observe that there is more austenite in the surface layer of HCPEB treated T10 steel than that in T8 steel. Of course, this is also due to the higher carbon content in T10 steel than that in T8 steel. On the other hand, the peak splitting of α{200} is also observed.

Fig. III-2 shows the same set of XRD patterns for the same steels but in the quenched and tempered condition. Fig. III-2a gives the evolution for the case of the 45# steel. The quenched and tempered carbon steels contain mainly three phases: tempered martensite (ferrite), carbide (precipitated during tempering) and possible retained austenite (if carbon concentration is high enough). The absence of carbide peaks in the XRD pattern of the starting 45# steel sample is due to the low volume fraction of the dispersed carbides. After the HCPEB treatment, the α{200} peak splitting is clearly observed. EBSD measurements confirmed the formation of martensite in the surface layer [104]. In contrast to the equilibrium 45# steel after HCPEB treatment, no γ phase formation is observed in the quenched 45# steel after HCPEB treatment. Increasing the number of pulses does not bring significant difference here. For the case of the T8 steel (Fig. III-2b) the splitting of the α{200} after HCPEB treatment observed from XRD patterns is more pronounced than that of HCPEB treated 45# steel. This can be attributed to the higher carbon concentration of the martensite formed in HCPEB treated T8 steel. In the case of the T10 steel (Fig. III-2c), the initial structure is composed of ferrite + carbide + residual austenite. After the HCPEB treatment, the splitting of $\alpha\{200\}$ is as high as 2.3º. Of course, this is also due to the higher carbon concentration in the T10 steel than that in the T8 and 45# steels. It can be also observed from the XRD patterns that the austenite content in the surface layer of the HCPEB treated T10 steel increases with the number of pulses. This must be due to the higher dissolution of the carbides after 10 pulses. This hyperthesis is clearly reflected in the increase in the peak splitting of martensite. Indeed, the retained martensite has a higher C content after 10 pulses than 5 pulses of HCPEB treatment.

The comparison of all the above XRD results together with other additional experimental EBSD results gives the following conclusions:

1. For the slowly cooled carbon steels, a part of the austenite induced by HCPEB treatment can be retained down to room temperature. The volume of austenite in the surface layer increases with the carbon concentration of the treated steels and decreases with number of pulses.
2. For the quenched and tempered carbon steels, the austenite formed during rapid solidification transformed into martensite when the carbon content is lower than 0.8 wt%. For high carbon steel (1 wt% C for example), austenite can be retained down to room temperature due to the stabilization effect of C. The martensite formed during the HCPEB treatment shows increased quadraticity (ie. increased carbon concentration of the steels) with increase number of pulses.

3. The different phase transformation paths in the equilibrium and non-equilibrium carbon steels induced by HCPEB treatment can be understood by the ability to homogenize the melt. The very short melt duration does not authorize the “equilibrium” carbon steels to be completely homogeneous because the initial carbides are much bigger than those in their quenched counterpart. Further explanation about the homogenization of the melt during HCPEB treatment can be found in section III.1.2.1.

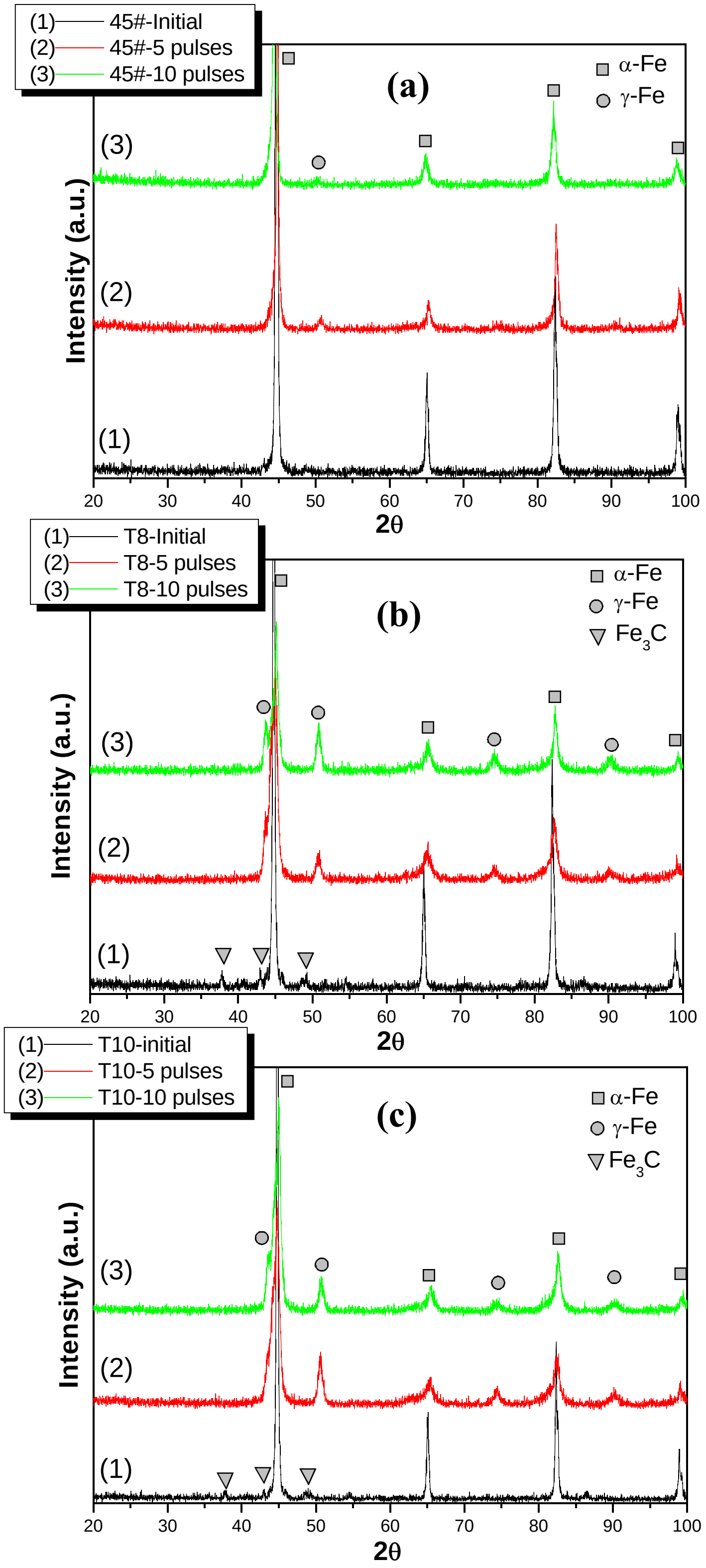

Fig. III-1 XRD patterns of the equilibrium 45# (a), T8 (b) and T10 steels (c) before and after HCPEB treatment.

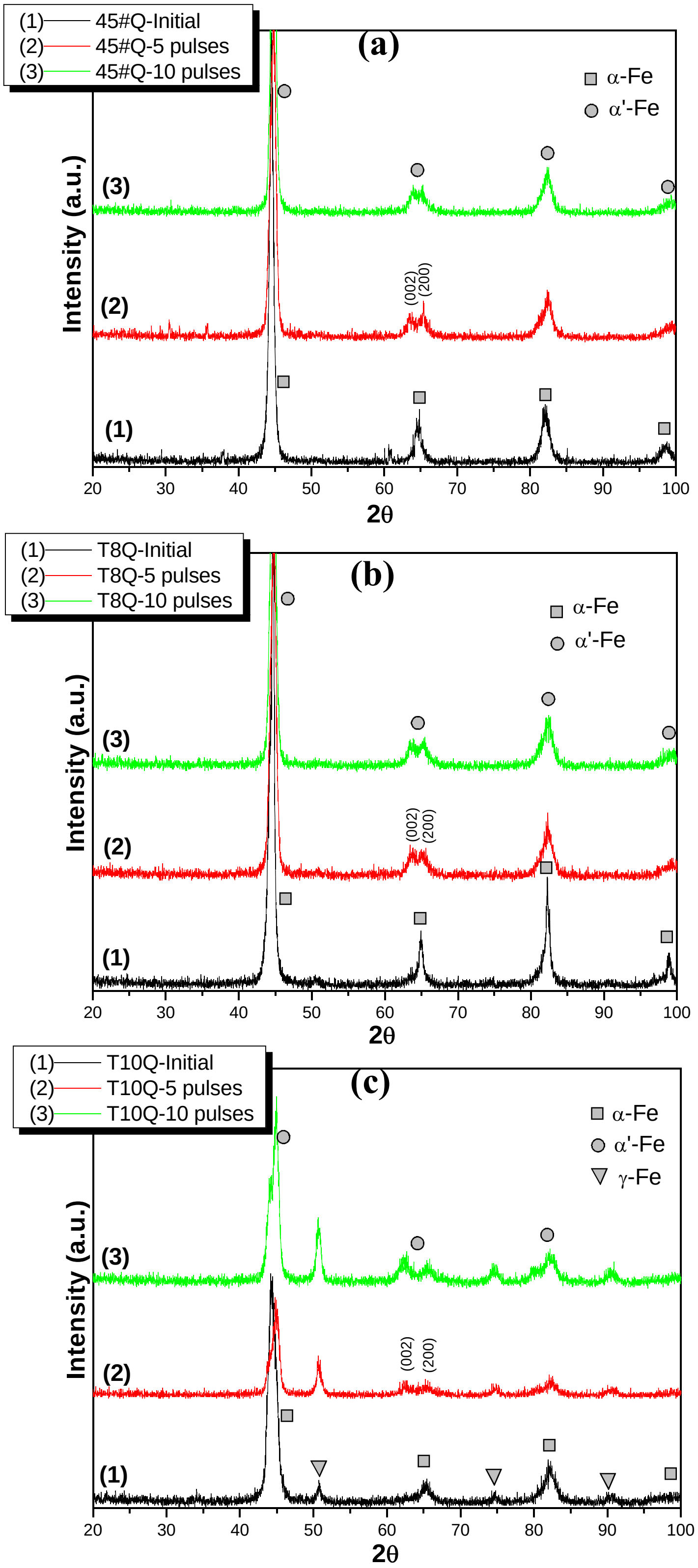

Fig. III-2 XRD patterns of the quenched and tempered 45# (a), T8 (b) and T10 steels (c) before and after HCPEB treatment.

III. 1. 2 Alloyed steels

III. 1. 2. 1 AISI D2 steel

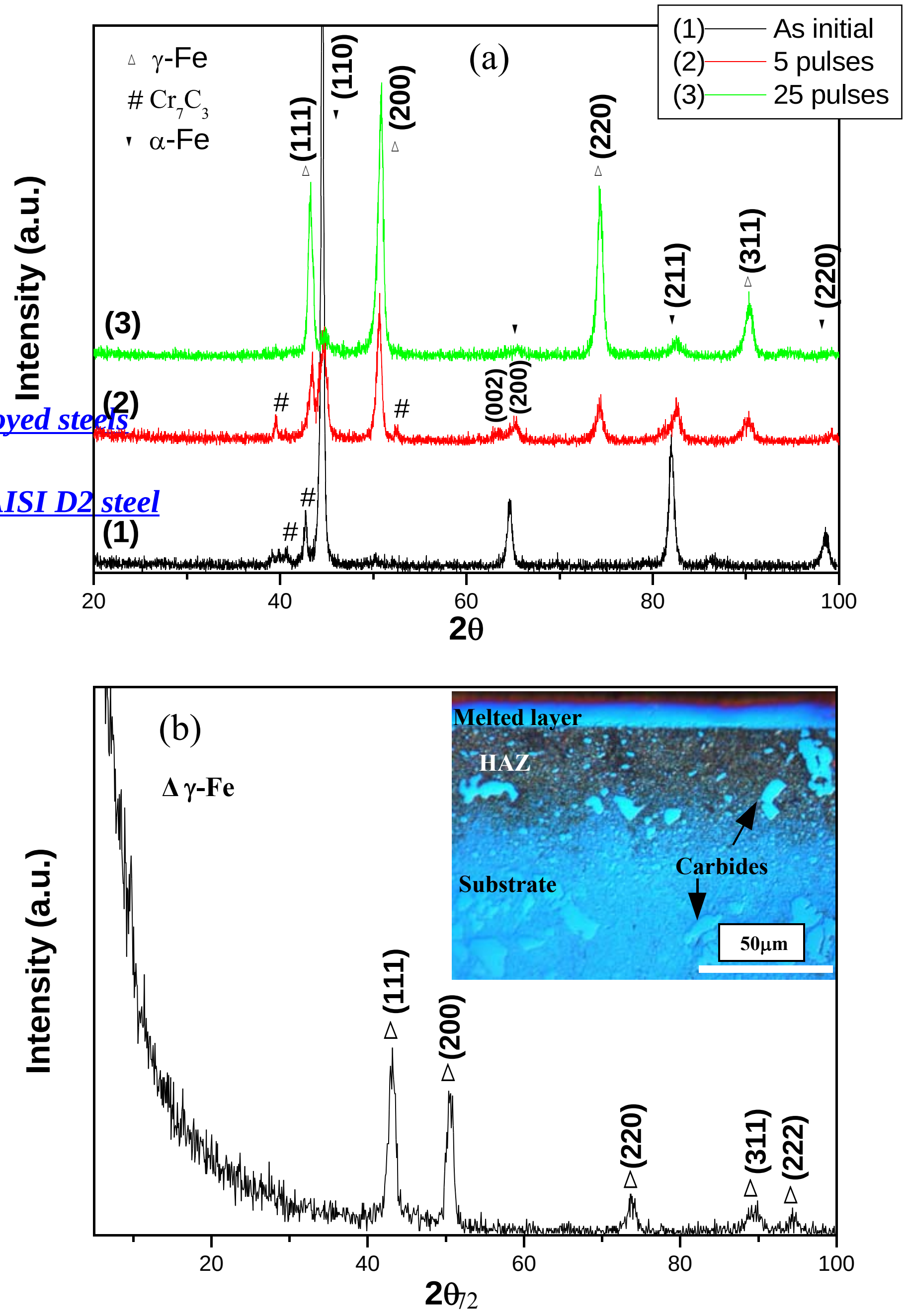

Fig. III-3 (a) XRD patterns of the untreated and treated D2 steel samples. (b) Low incident beam XRD pattern of the 25 pulsed sample, a typical cross sectional OM picture is shown inset.

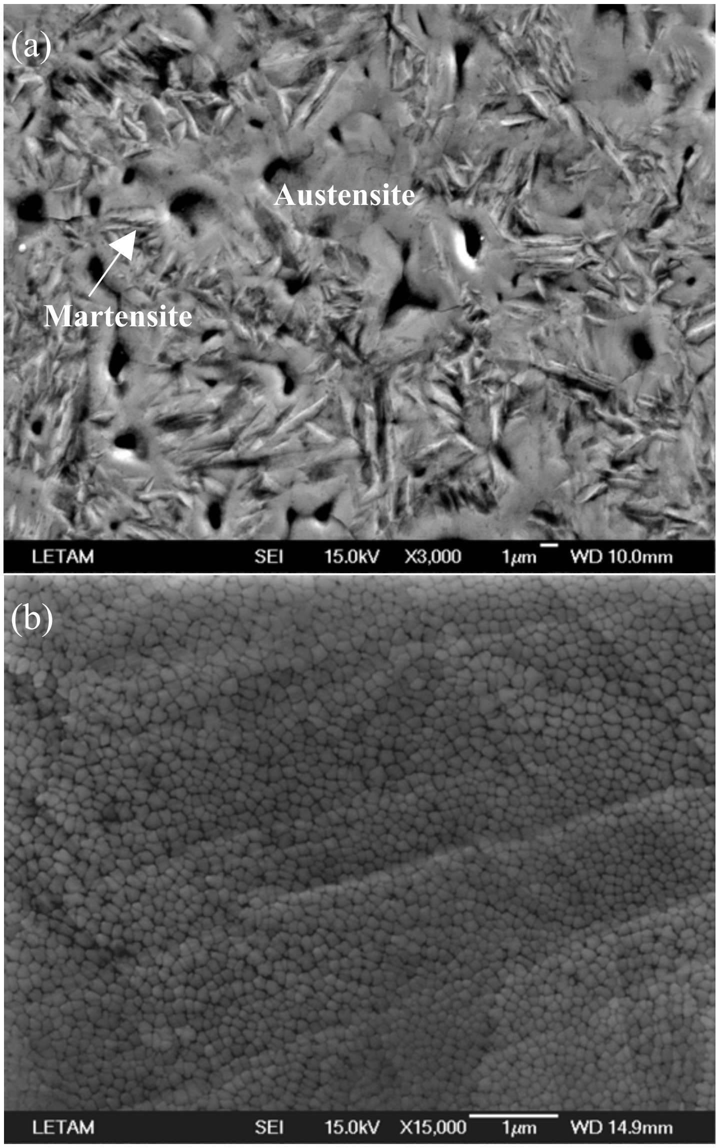

Fig. III-4 A typical SEM surface micrograph on the 5 pulsed D2 sample (a) and high magnification SEM surface micrograph of the sample treated with 25 pulses (b).

The AISI D2 steel (Cr12MoV) is a typical cold worked die steel with high C (~1.5 wt%) and Cr (~12 wt%) concentrations [97]. Fig. III-3a shows the evolution of the XRD traces of HCPEB treated D2 steel samples with the number of pulses. The starting material contained two phases : ferrite (α-Fe) and carbide having the Cr_7C_3 structure. The volume fraction of the carbide is fairly important and the carbide peaks are clearly visible in the XRD trace of the starting material. The intensity of the X-ray diffraction peaks also indicates that the major phase in the initial material was α-ferrite. This phase results from the decomposition of the quenched martensite during the tempering process (tempered martensite). After the HCPEB bombardment, the XRD traces are observed to change somehow dramatically. Concerning the Cr_7C_3 phase, it is clear that the carbide peaks tend to disappear after the HCPEB treatments. As to the α phase, it is interesting to note that some of the peaks in the sample treated for 5 pulses have close neighbours. A splitting of the (200) peak is usually found in newly formed martensite having sufficient amount of C to reveal its quadraticity. It is interesting to note that this peak splitting is no longer observed after 25 pulses of HCPEB treatment. Finally, some new peaks are present in the XRD traces. They were verified to be from the γ-Fe phase. The peak intensity of the γ-Fe phase increases with the number of pulses, indicating that the volume fraction of the γ phase detected by XRD increases.

Fig. III-3b shows the low incidence beam X-ray diffractogram recorded on the sample treated for 25 pulses. It only shows the presence of the γ peaks. This indicates that the surface layer is mainly composed of the γ phase. The typical cross-sectional optical micrograph of the etched sample after the HCPEB treatment for 25 pulses is shown inset of Fig. III-3b. The "white" layer visible on the surface, which appears with a completely different contrast from the rest of the material, corresponds to the melted layer. No carbides or grain boundaries could be observed at the scale of resolution of OM in this layer even after deep etching. Below the melted layer, are the heat affected zone and substrate containing large amount of carbides.

Fig. III-4a shows a typical SEM micrograph taken on the 5 pulsed sample. Some voids are visible on the surface. These voids are generated by the shrinkage associated to the solidification of the melted surface. Fine needle like structures can also be clearly observed, as arrowed in Fig. III-4a. These needles tend to be grouped and connected to each other. It was confirmed by EBSD measurements that those needle like structure is martensite and the rest is austenite. The crystallographic relationship between martensite and residual austenite is found to be Nishiyama-Wassermann (N-W) type [97]. A high magnification SEM image of the 25 pulses treated D2 steel is shown in Fig. III-4b. It reveals very fine austenitic grains or subgrains having a size of about 50~150 nm, which cover the whole surface.

The metastable phases and microstructures formed on the HCPEB treated D2 steel can be understood by considering the effect of the treatment on the dissolution kinetics of the carbides and the ability of the process to homogenize the melted surface. After 5 pulses, the chemical composition in the melted layer is not homogeneous and the martensitic transformation occurred in the Cr and C lean γ grains located away from the craters. Therefore, the microstructure of the melted layers is composed of residual austenite, martensite and un-dissolved carbides. After 25 pulses, most of the carbides in the surface layer are dissolved and a more homogeneous melted layer is formed. As a result, the crater formation is less effective and the microstructure of the melted layers is then composed of ultra fine-grained austenite and nanosized carbides. Even if the cooling rate was very high (~10^7K/s), the martensitic transformation could be completely suppressed after 25 pulses. The stabilization of the γ phase is related to the grain refinement and alloying (Cr and C) of the austenite grown from the melt [99,100,105].

III. 1. 2. 2 AISI H13 steel

AISI H13 steel (4Cr5MoSiV1) is a typical hot worked die steel with lower C (~0.45wt%) and Cr (~5wt%) concentrations compared to the D2 steel [106-108]. Fig. III-5 shows the XRD patterns of untreated and HCPEB treated H13 steel samples. The X-ray diffraction peak indicates that the major phase in the initial material was α-ferrite. This phase results from the decomposition of the quenched martensite during the tempering process. Carbides having the MC and $M_{23}C_6$ structures were detected in the X-ray trace [109]. Because of their low volume fractions, the intensity of the carbide peaks is rather weak.

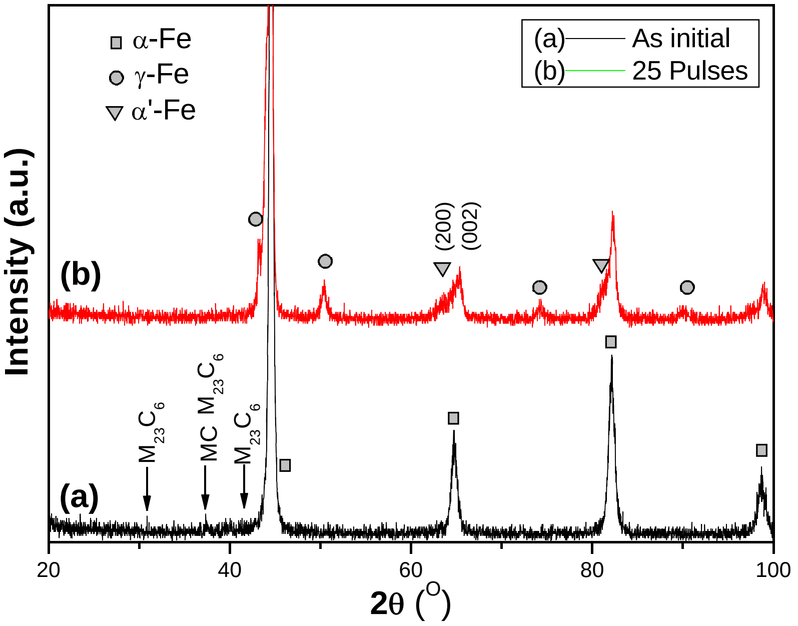

Fig. III-5 XRD patterns of the initial and HCPEB treated H13 steel samples.

After the HCPEB bombardment, the observed XRD pattern has changed quite significantly. As for the other steels, a splitting of the (200) peak is observed after 25 pulses. In addition, some new peaks corresponding to the γ-Fe phase are also present in the XRD traces. The peaks corresponding to the carbides disappeared after the HCPEB treatments, a result of selective purification and dissolution of carbides during treatment [97,98]. Compared to the results obtained in the D2 steel after 25 pulses [97], the relative intensity of the γ-Fe peaks over the α-Fe ones is here much weaker. This indicates that the volume fraction of the γ phase in the surface layer of this H13 steel is lower than the one obtained in the case of the D2 steel.

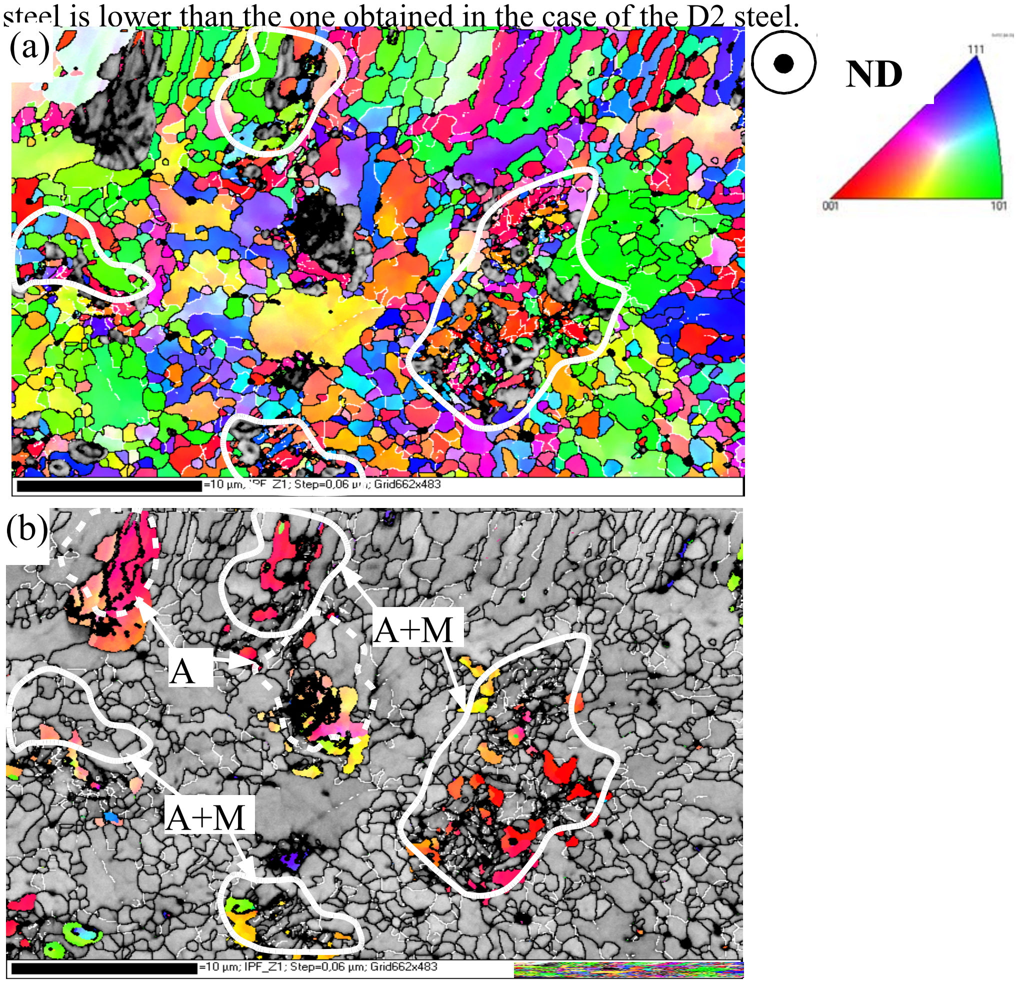

Fig. III-6 Typical EBSD orientation maps measured on the surface of the HCPEB treated H13 steel sample with 25 pulses. The colored grains correspond to the ferrite (a) and the austenite (b) phases.

Fig. III-6a and 6b are EBSD orientation maps taken on the treated H13 steel. The Kikuchi patterns detected by EBSD could be indexed by the ferrite (or martensite) and austenite phases. For the sake of clarity, in Fig. III-6a are colored the areas for which the Kikuchi patterns were indexed as ferrite while the austenite grains are shown in Fig. III-6b. The color of the grains was selected according to the standard color triangle given in the inset of Fig. III-6a. The dark areas in the EBSD maps correspond to the non indexed regions where the Kikuchi patterns are too weak or too blurred to be recognized by the measuring system.

Consistent with the XRD results, the comparison of the two EBSD maps indicates that the ferritic phase is the dominant one at the top surface. From the EBSD map in Fig. III-6a, it can be established that the range of grain size for the ferritic grains is rather fairly broad: from one hundred of nanometers up to a few micrometers. It is also clear that the finer ferritic grains are grouped together and located in specific areas where autenitic grains are also present. These areas are circled and marked with the label (A+M) in both maps of Fig. III-6. In these areas, the γ grains often have the same color (orientation) but are intermixed with α grains having different colors. As confirmed by a detailed EBSD analysis, this type of configuration indicates that a martensitic transformation occurred on cooling; the γ domains having the same color (orientation) corresponding in fact to some retained residual austenite originating from the same large austenitic parent grain [110]. The austenite grains are slightly bigger in this second type of areas and they often stand on their own.

The analysis confirms that the XRD peak splitting visible in Fig. III-5 is due to the presence of martensite and the type of crystallographic relation between the martensite variants and their parent austenite is determined to be the Kurdjumov – Sachs (K-S) type [110]. This relation is different from the N-W type relation observed in D2 steel, which is due to the differences in C and Cr concentrations of the austenite formed on the two steels.

The specific features observed in the H13 steel are compared to the HCPEB treated D2 steel. The major difference between these two steels lies in the different Cr and C concentrations, which change the thermal properties and initial structures of the two steels. Based on the temperature field calculations, it was known that the melted layer depth and melting duration in H13 steel are much lower than those in D2 steel when the same HCPEB parameters were used in the treatment [97, 110]. As a result, the chemical composition in the melted layer of the H13 steel was still not homogeneous after 25 pulses of HCPEB treatment. Under the high temperature gradient and interface velocity generated by the rapid solidification, this heterogeneous chemistry in the melted layer led to the primary solidification of both the (stable) δ and (metastable) γ phases; the γ phase being selected in Cr and C rich areas. The size of the grains of these primary phases was much bigger than the size of the (metastable) γ domains selected from the melt in the D2 steel [97]. This suggests that the undercooling and supersaturation in the melt of the H13 steel during solidification is much lower than those in the melted layer of D2 steel. During the subsequent rapid cooling process, the δ→γ transformation was suppressed and the primary δ phase was retained down to room temperature. On the other hand, partial martensitic transformations occurred in the γ grains. While the analysis of the D2 steel revealed the retention of ultra fine γ grains formed directly from the melt after 25 pulses of HCPEB treatment, the two following phase transition sequences were revealed in the H13 steel : $L\rightarrow\delta$ and $L\rightarrow\gamma\rightarrow\gamma_r+\alpha'$. Therefore, the final structure in the melted layer of the H13 steel consisted of a mixture of δ-ferrite, martensite and residual austenite.

III. 1. 3 NiTi shape memory alloy

The effect of a HCPEB treatment for modifying the surface of an intermetallic shape memory Ni(50.6 at%)Ti alloy has been investigated here to show also the metastable phase and structure formations. The as-received B2 type Ni(50.6 at%)Ti alloy was hot rolled at 750°. This initial material has a recrystallized structure with a very weak (less than two time random) and broad <110> fiber texture // to the rolling direction [111-113]. The grain size was about 10~50μm. For the HCPEB treatment under melting mode, the accelerating voltage and energy density were kept constant at 25 kV and 2.2 J/cm^2, respectively, and different pulse numbers were used, i.e. 5, 10, 20 pulses.

XRD analysis was also carried out on the NiTi alloy samples before and after the HCPEB treatments. Examples of diffractograms are shown in Fig. III-7. For the initial state, the observed peaks correspond to the NiTi (B2 structure) austenite phase and the $NiTi_2$ precipitates. After the HCPEB treatment with 5 pulses, peaks corresponding to the NiTi martensitic phase (B19') are present. In addition, it is also clearly visible that the diffraction peaks of the $NiTi_2$ phase have vanished. This is a consequence of the surface purification effect from precipitates in the surface layer [114]. However, the intensity of the peaks corresponding to NiTi martensite became weaker after 10 pulses and almost disappeared after 20 pulses. This indicates that the fraction of martensite in the surface layer decreases with the number of pulses, a similar case to that observed on the D2 steel samples although the corresponding me[illegible]ferent.

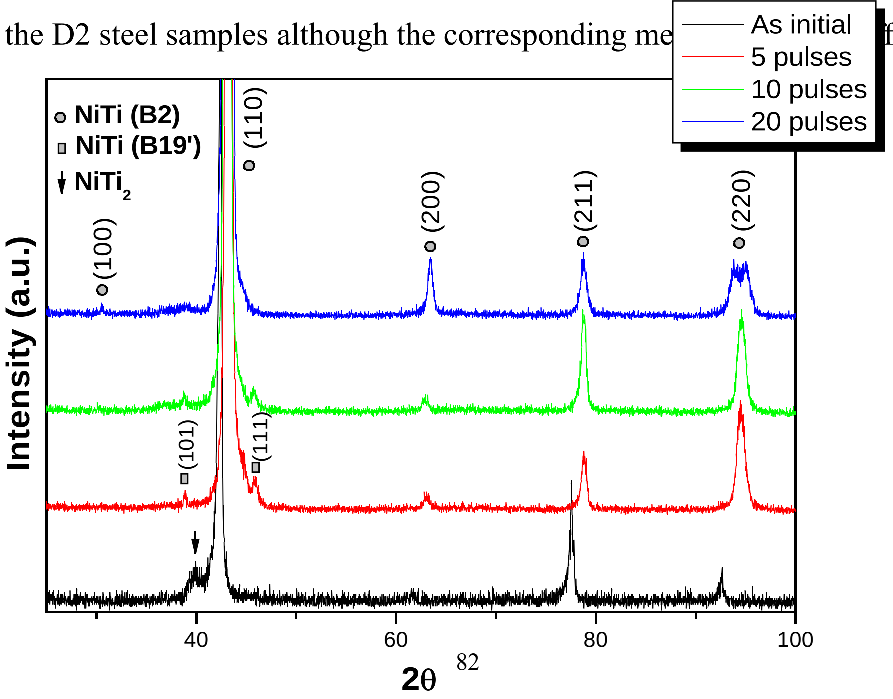

Fig. III-7 XRD patterns of the untreated and treated NiTi alloy samples.

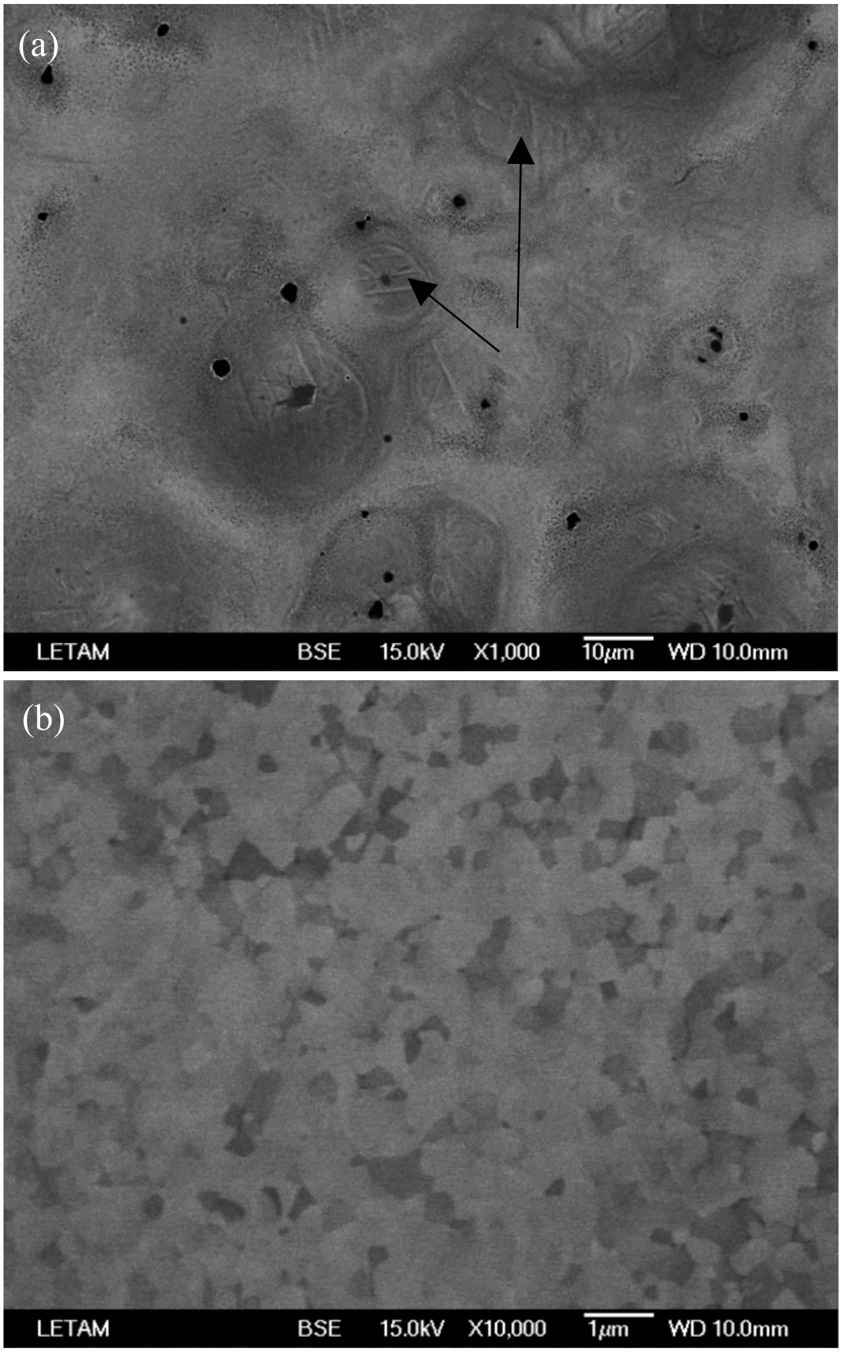

Fig. III-8 Typical BSE surface morphology on the 5 pulsed NiTi sample (a) and high magnification BSE (b) surface morphology of the sample treated with 20 pulses.

To gain more information about the microstructure and texture issued from the solidification of the surface melted zone, FEG-SEM observations and EBSD analysis were carried out at the top surface of the treated NiTi samples. Fig. III-8a shows a typical SEM micrograph of the NiTi sample HCPEB treated for 5 pulses under back scattering condition. Some straight bands having brighter contrast are clearly visible close to the crater formation region. This is reasonable because the martensitic transformation in this alloy was triggered by the high stress field induced by the HCPEB treatment and the stress field near crater formation region is higher due to the shock wave formation [80,111]. The dark spots, often located in the crater centers, are $NiTi_2$ precipitates, which are the initial sites for crater formations. The rest area is covered by fine grains and a network of fine shinkage voids. Much like the 25 pulsed D2 steel sample, a high magnification SEM-FEG image of the 20 pulses treated NiTi (Fig. III-8b) reveals again very fine grains covering the whole surface.

After melting, rapid solidification occurs at rates as high as 10^7K/s due to the rapid heat extraction towards the bulk [80,81]. This leads, in this alloy, to the formation of ultrafine B2 grains at the top surface. At the same time, a quasi-static thermal stress with an amplitude of several hundred MPa forms and causes intense deformations in the material [81]. As revealed by the lath morphology in the SEM image (Fig. III-8a) and confirmed by the XRD traces (Fig. III-7), a martensitic transformation was triggered in the HCPEB treated NiTi with 5 pulses. This martensitic transformation was clearly triggered by the high quasi-static thermal stress and shock waves produced by the HCPEB treatment [111-113]. In cases of D2 steel and NiTi alloy, we have noticed that the evolution of phase transformations with the number of pulses is similar. The martensitic transformation occurred at the early stage of treatment, i.e. 5 pulses. Then it was suppressed by dissolution of carbides or by the grain size constraining effect with sufficient number of pulses. Here, martensitic transformation may also play an important role for the grain refining process. It can divide one grain into some separate blocks and thereby refine the grain. This process occurred again and again during each pulses, until the grain is fine and/or composition is homogeneous enough that martensitic transformation can not occur any more.

III. 2 Special surface morphologies induced by HCPEB treatment

It has already been observed that materials after HCPEB treatment usually show very special aspects of surface morphology [67-71]. For example, crater formation on the HCPEB treated surfaces is a common feature for many materials. It was also observed on the pulsed laser and pulsed ion treated surfaces [115,116]. However, detailed analysis of specific morphologies on different materials with different treating conditions and their corresponding formation mechanisms were still missing. Here, we will classify the features observed on materials under different HCPEB treatment modes as discussed before.

III. 2. 1 Typical surface morphology under heating mode

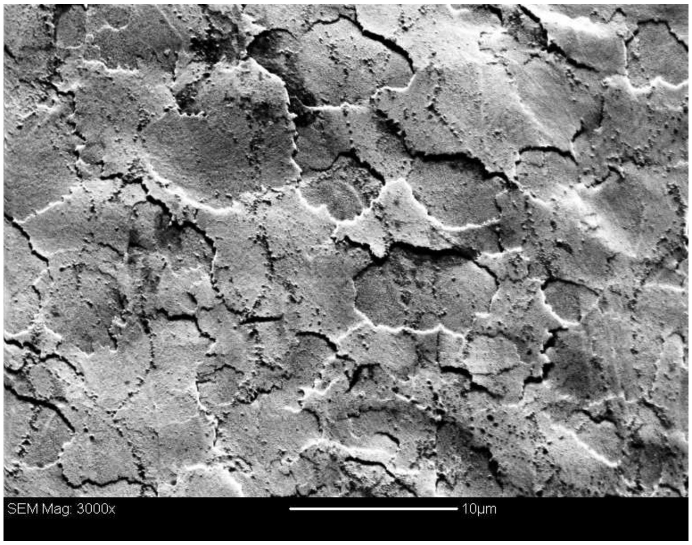

Fig. III-9 Typical SEM micrograph on the 20 pulsed Fe (40 at%)Al sample under heating mode.

The typical surface morphology of materials under heating mode was not studied before. Fig. III-9 shows a typical SEM micrograph on the top surface of a 20 pulses treated Fe (40 at%)Al sample without melting of the surface. It can be clearly seen that the surface is not anymore flat.
Some of the grain rains. This feature is so
important that the g r (Section III.4.1), such a
surface morphology by HCPEB is orientation
dependent [117], wl grains.

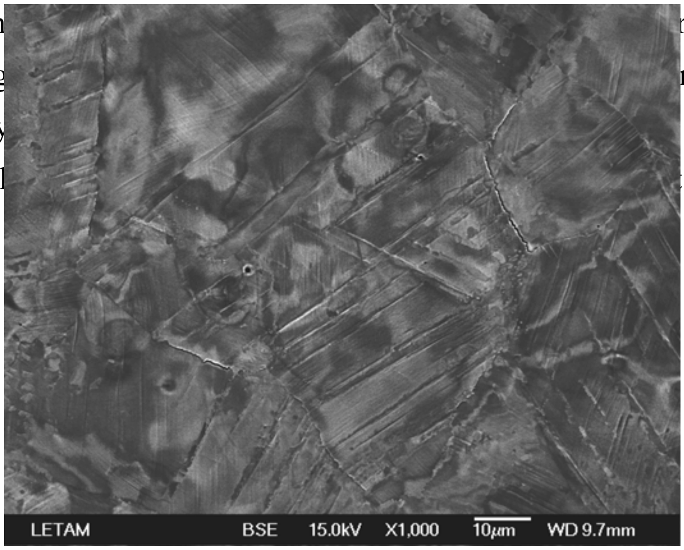

Fig. III-10 Typical SEM micrograph on the 10 pulsed 316L stainless steel sample under heating mode.

Fig. III-10 shows a typical SEM micrograph on the top surface of a 10 pulses treated AISI 316L stainless steel sample without melting of the surface. Two types of traces with different morphology left at the surface are clearly visible. They are also orientation-dependent. As confirmed by EBSD analysis, the wide bands are deformation twins (Section III.4.1). Comparatively, the narrow lines are slip lines.

The above results show that the typical features observed on the materials treated under heating are, in fact, deformation related marks. Those marks are orientation dependent since the thermal stress induced by HCPEB treatment is orientation dependent. Other experiments reveal that those deformation marks became more pronounced with the increasing number of pulses [118].

III. 2. 2 Typical surface morphology under melting mode

It is well established that the HCPEB treatment under melting mode leads to the formation of craters on the surface [67,69,80]. Fig. III-11a and 11b are a set of OM and SEM micrographs allowing to depict clearly the exact crater morphology on quenched and tempered T8 steel sample after 5 pulses (see section III.1.1). They confirm that the whole surface was melted and solidified to a needle like structure (Fig. III-11a). The craters most often have a small hole present in their center. Further observations have shown that: the bigger the hole size, the larger the crater. This can be understood by the fact that, the stronger eruption, the bigger craters. In Fig. III-11a, due to the limitation of depth of field under OM, the different parts of a crater present different focusing because of their different heights. From the SEM image (Fig. III-11b), it can be clearly seen that the edge of a crater is higher than the medium surface level while the center is lower. That is, the craters have a funnel-like morphology. As for other steels or precipitate reinforced alloys, detailed measurements have shown that the crater density on the surface decreases with the increasing number of pulses [98,114].

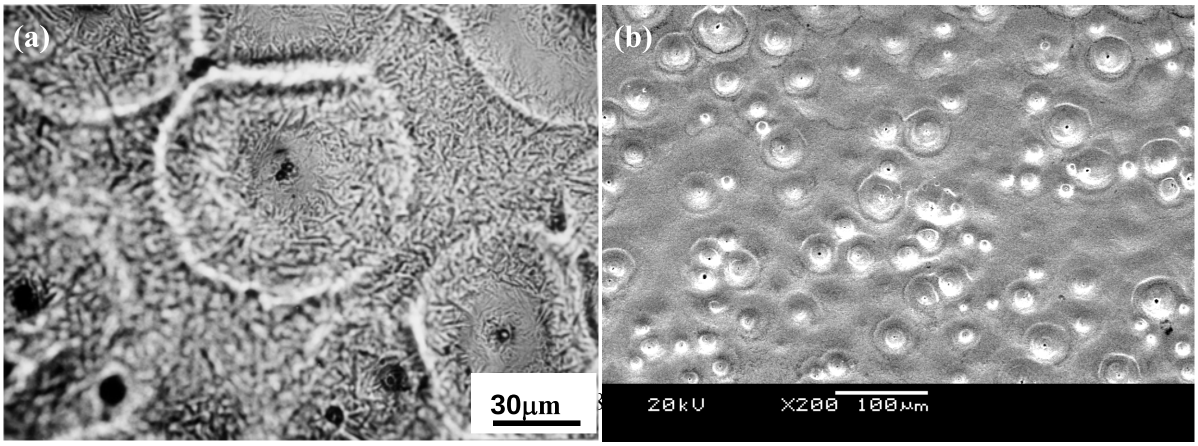

Fig. III-11 Typical surface micrographs of the HCPEB treated T8 (quenched and tempered) sample with 5 pulses.

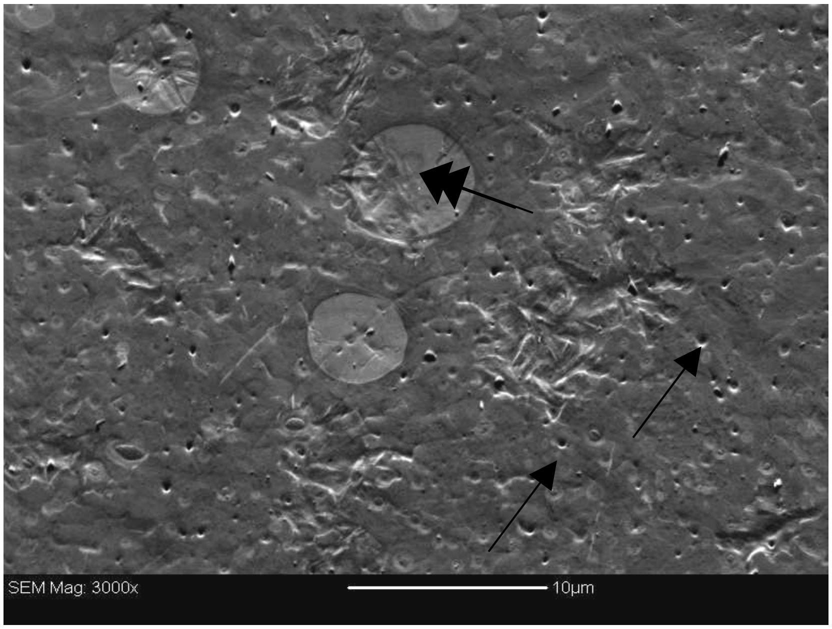

Fig. III-12 Typical SEM micrograph on the 25 pulsed AISI H13 steel sample under melting mode.

Fig. III-12 gives a typical SEM micrograph obtained under secondary electron imaging condition at the surface of the HCPEB treated H13 sample with 25 pulses. Two types of craters can be clearly depicted as the result of the HCPEB treatment. They can be clearly distinguished from their sizes: (i) small ones (arrowed in black) and (ii) bigger ones (double arrowed in black). The big ones have a diameter ranging from several to 10 μms while the size of the small ones is only about 100~200nm. The density of the small craters is much higher than that of the big ones. Detailed analyses revealed that the two types of craters formed on treated H13 steel sample are due to the different eruptions initiating from two types of carbides in this steel [110].

Indeed, as the carbides have lower heat conductivity than their surrounding matrix, they tend to retain the heat generated by the electron beam and, thereby, favor the local formation of subsurface pools of melt [80]. These melted pools will grow in size until internal pressure forces, generated by (i) thermal expansion, (ii) solid/liquid volume change and (iii) possible carbide dissociation + evaporation, make them burst through the thin solid wall separating them from the upper melted surface. Such a crater formation mechanism has been observed in the AISI 316L [98,114] and D2 [97] steels as well as in a NiTi alloy where $NiTi_2$ precipitates served as nucleation sites [114]. Compared to these previous investigations, the interesting results reported here for the H13 steel about the craters is that they have two classes of sizes and two types of shapes. Because of the different types of carbides (large MC and smaller $M_{23}C_6$ carbides) present in the initial H13 sample [110], the local melting process must have resulted in the formation of different types of craters. Indeed, simply from a size effect, the large carbides must have accumulated more heat due to a lower efficiency in heat transfer towards the surrounding metal matrix while, comparatively, the higher surface to volume ratio of the small carbides authorizes to evacuate the heat through their surfaces more rapidly. As a result, higher temperatures and bigger pools of melt are created at the large carbide locations, leading to the formation of bigger and deeper craters. These differences in accumulated energy and depth also explain the two types of shapes: changing from an eruptive shape for the big craters towards a more "bubbling chimney" type for the smaller ones. To some degrees, the crater shapes reported here mimic the shapes of real volcanoes formed on the earth crust. Indeed, depending on energy storage and release procedures, th ’ type characterized by huge sizes towards a ‘ - having much smaller sizes [119,120].

In the present cas e affected also by the different thermal prope r differences in metallic elements and C conce een the two carbides is their Cr, V and C conc uctivity of the carbides. As the MC type of ca at conductivity is lower than that of the $M_{23}C$ f the energy transferred from the electron bean

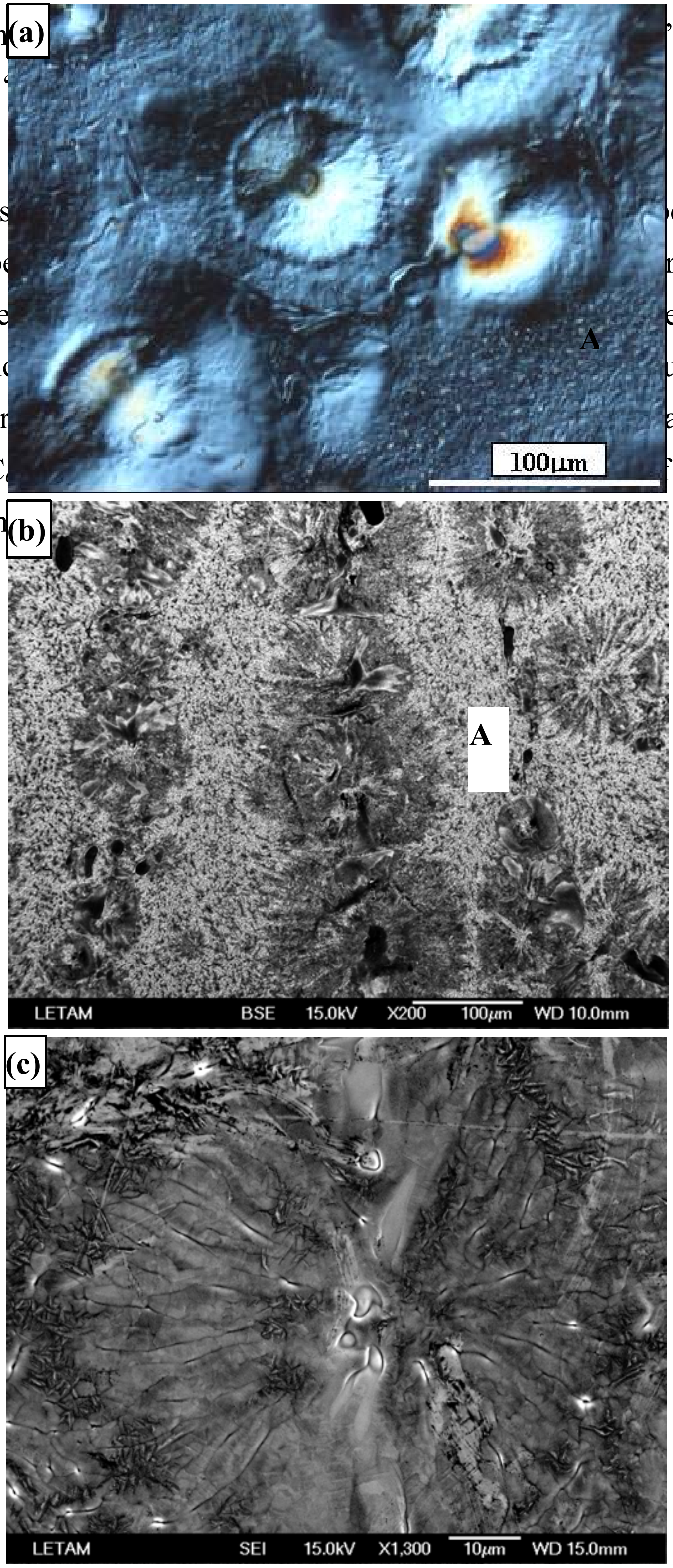

Fig. III-13 Typical optical (a) and BSE (b) surface morphologies of the D2 sample treated with 5 pulses. A typical SEI morphology of a crater is shown in (c).

Crater eruption also plays an important role for surface homogenization [97,114]. An example shown here is also the HCPEB treated D2 steel. Fig. III-13a and 13b show the optical and BSE images of the surface of a sample HCPEB treated for 5 pulses. The craters often display special features. This is particularly visible under the backscattering imaging condition. Firstly, all the craters have an emission like aspect. That is, band like contrasts are radiating from the center of the crater towards its edge. Fig. III-13c is a typical secondary electron image showing the morphology of a crater. A close look at the crater reveals that these bands are, in fact, corresponding to several elongated grains radiating from the central erupted. Shrinkage cavities often formed a linear boundary between two elongated grains. This means that solidification occurred rapidly after the eruption event involved for the formation of the craters. Secondly, the craters display a contrast that is slightly darker (Fig. III-13b) than the one from the flat regions located between the craters (marked A). This suggests that there is a chemical variability at the sample surface. Finally, the black contrast of fairly large carbides can often be observed in the craters. Many of them are located at the crater center and often correspond to erupted carbides. Others, laying on the edge of the craters, are not erupted. These images confirm that in the 5 pulsed sample, (i) the carbide eruption is the reason for the crater formation in this steel and [97] (ii) the eruption events tend to expulse the carbides and break them up into smaller parts. The size of the craters being much bigger than the initial carbides that severed as nucleation site, the eruption events have also the effect of redistributing the carbide chemistry further away and, thereby, reduce the level of segregation in the resolidified layer. However, because of the rapidity of the solidification process, a sufficient number of pulses is needed to reach a fairly homogeneous composition in the melted layer. With the increased number of pulses, more and more carbides have erupted and/or dissolved so that less nucleation sites are available and the crater formation mechanism is less efficient.

Analysis of several precipitate reinforced materials has shown that crater formation on materials induced by HCPEB treatments are related to local melting and eruptions [121] preferentially occur at the structure or composition irregularities, such as carbides in steels [97] or MnS inclusions in stainless steel [114]. Increasing the number of pulses results in the increase of crater density on a certain treated material in the early stage of treatment. However, further increase of the pulse number leads to a decrease of crater density [114] due to the homogenization of the chemistry in the rapid solidified melted layer. It has been demonstrated that this phenomenon can be used to improve the corrosion properties of HCPEB treated materials [114].

III. 2. 3 Typical surface morphology under evaporating mode

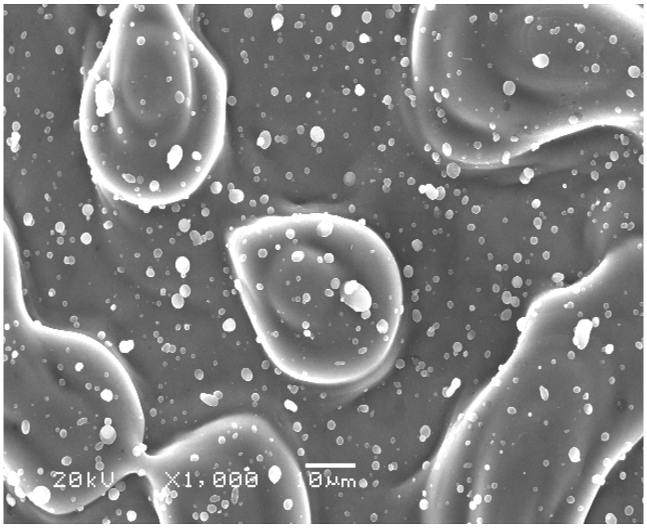

Fig. III-14 Typical surface SEM micrographs of pure Mg after HCPEB treatment under evaporation mode.

The physical model for evaporating mode has been proposed previously in section II.2.9. In alloys, it is expected that the selective evaporation taking place on the surface results in composition changes [111,112,122]. In addition, under intensive evaporating mode, a special surface morphology is observed after treatment [122]. The typical SEM surface micrographs of pure Mg irradiated by HCPEB with an energy density of about 3 J/cm^2 (accelerating voltage 27 kV) are shown in Fig. III-14. Two distinct features can be clearly depicted. The first one is the wavy aspect of the surface. The wavy aspect is due to the succession of hills and valleys at the sample surface, which is different from the common feature of many HCPEB treated metal surfaces (crater morphology). The second feature is the presence of many isolated particles on the surface. These particles are pure Mg and have their size ranging from nanometer to micrometer scales. The shape and the size of these particles suggest that they may have directly condensed from the vapor. Such a phenomenon is so called self-deposition effect, which is usually observed under intensive evaporation mode [111,123].

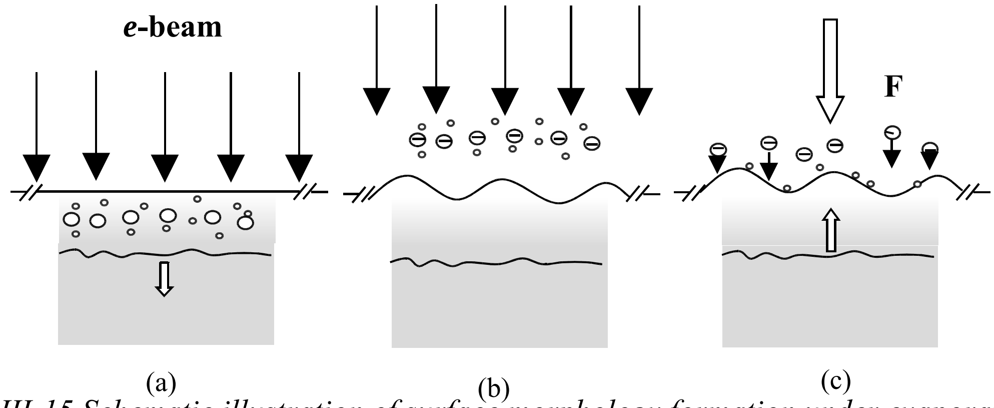

Fig. III-15 Schematic illustration of surface morphology formation under evaporating mode.

Based on the calculation results given before (section II.2.9), the formation mechanism of the special surface morphology of Mg under intensive evaporation mode can be proposed as follows. During the HCPEB process, when the boiling point of Mg is reached, evaporation will occur within a certain depth, as shown in Fig. III-15a. This leads to the formation of evaporating vapor droplets inside the melt. The boiling and the recoil force associated with the evaporation event together with local higher evaporation rate of small droplets lead to the formation of a wavy surface. As the whole evaporation process occurred within the pulse duration, the spilled droplets will be charged in the electron beam, as seen in Fig. III-15b. Since these droplets have the same negative charge as the electrons, they will be attracted back to the surface by electric force. At the same time, the solidification occurs very rapidly and the wavy surface morphology is retained after solidification (Fig. III-15c). All the above processes finally lead to the formation of a wavy surface and the presence of small particles re-deposited on top of it [123].

Another example to show the re-condensation effect is given here in the case of the Ni (50.6 at%)Ti alloy treated with HCPEB under the evaporating mode [107]. The electron-beam treatment parameters were as follows: the accelerating voltage 27 kV, the energy density 3 J/cm^2 and the sample was treated for 10 pulses.

Fig. III-16 shows a typical optical micrograph and a BSE image of the 10 pulses treated sample surface. The aspect of the surface is very different from the one observed on the 5 pulsed sample for which only rapidly solidified fine B2 grains and shrinkage cavities were observed [111]. The wavy aspect of the surface is clearly visible in Fig. III-16a. Another feature is the presence of many straight bands. These are the witness marks associated with the stress induced martensitic transformation taking place in the subsurface of this shape memory alloy [111-113]. From the BSE morphology, the band-like feature is even more visible. In addition, there are many small particles attached on the surface: a very similar case to the surface feature on pure Mg treated under intense evaporating mode.

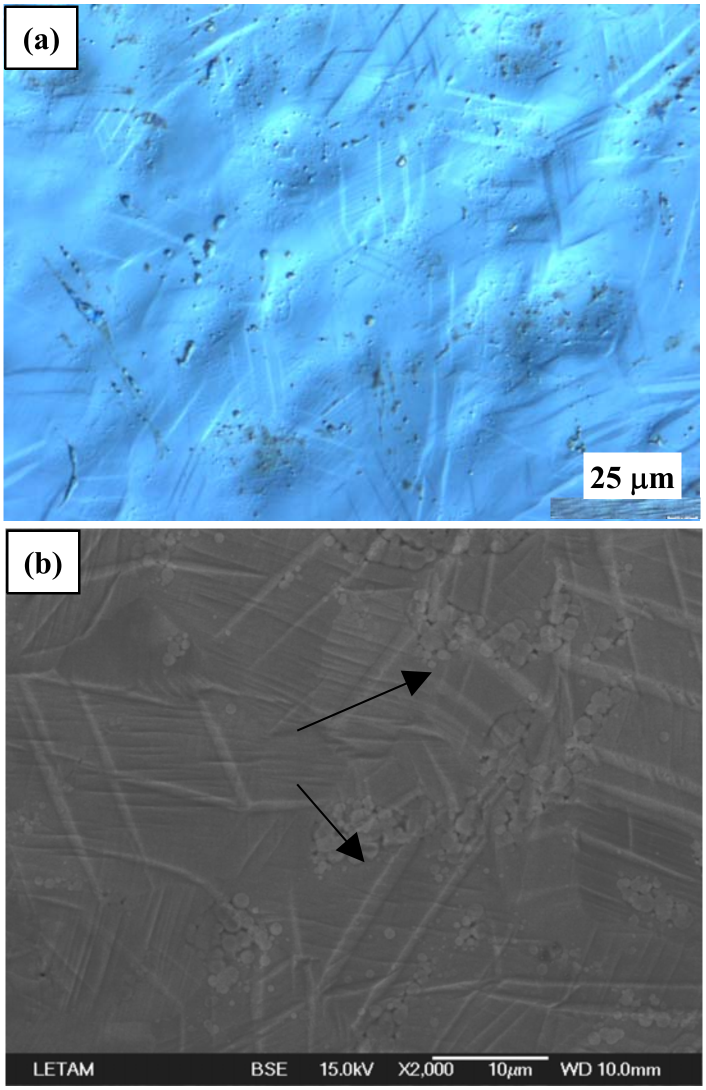

Fig. III-16 Typical optical (a) and BSE (b) micrographs taken on the surface of the 10 pulsed treated NiTi alloy sample under evaporating mode.

In the case of this alloy, the selective evaporation must change the chemistry of the alloy surface. To reveal possible chemical modification after the HCPEB treatment, Sputtered Neutral Mass Spectrometry (SNMS) was carried out on the treated NiTi samples [111,112]. The result of this analysis is shown in Fig. III-17 where the evolution of the amount of Ni and Ti is plotted as a function of the distance from the surface. The chemical variation is clearly visible in the surface layer. The chemical modification starts from a depth of about 4 μm and the Ti content increases until it reaches its maximum value of about 54.5 at% at a depth of 400 nm. Indeed, the vapor pressure of Ni is higher than that of Ti at same temperature. Also, the heat of evaporation for Ti (421kJ/mol) is higher than that of Ni (370.4kJ/mol) [107]. Therefore, a selective evaporation will occur under the HCPEB treatment, giving rise to a more effective evaporation of Ni over Ti. This leads to the increase of Ti concentration in the surface layer. However, within several hundreds of nanometers from the surface the Ti concentration shows a surprising decrease. At the top surface the Ti concentration is only about 50.8 at%. The selective evaporation and re-deposition induced by the HCPEB treatment are responsible for these chemical modifications [111]. The condensation of the evaporated matter is indeed a mechanism that can lead to the formation of 'isolated' particles on the surface. Also, the Ni concentration is higher than Ti concentration in the vapor due to the selective evaporation of Ni in the melt. Therefore, the selective evaporation leads to the increased Ti concentration in the melted surface layer while the re-condensation will result in the decrease of the Ti concentration on the top surface.

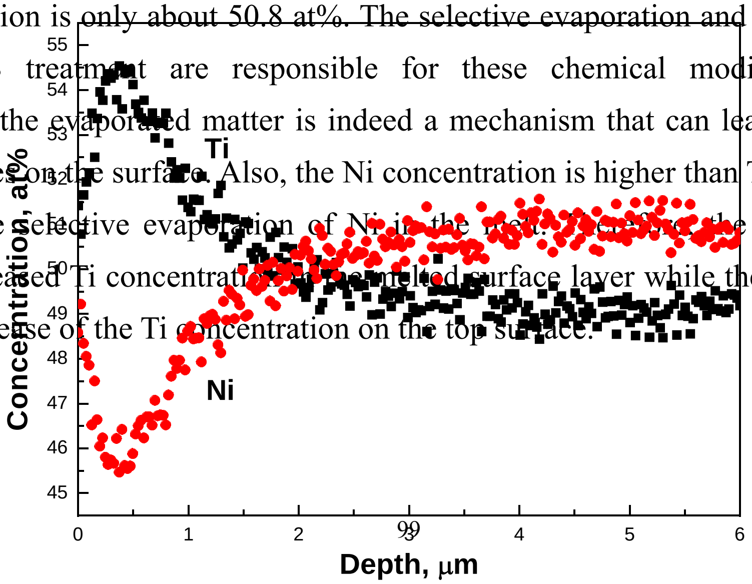

Fig. III-17 SNMS composition profiles of Ni and Ti for the 10 pulses of HCPEB treated Ni(50.6 at%)Ti sample under evaporating mode.

III. 3 Surface homogenization and selective purification

It is established that the compositions in the melted layer of a HCPEB treated material will be homogenized due to the liquid state diffusion and possible convection [67-72,76]. The dissolution of second phase particles or precipitates has been observed on some materials treated by HCPEB [67,69,84]. In these cases, melting is regarded as the major reason for the homogenization. Here, we will present some special phenomena occurring during HCPEB treatment which lead also to the homogenization of the surface layer. It will be demonstrated below that the surface purification can be obtained both under the heating and melting modes.

III. 3. 1 Selective surface purification under melting mode

As just explained, the formation of craters is a common feature on the materials treated by HCPEB. Generally, the craters are regarded as a disadvantage that deteriorates the quality of the materials surfaces [67,69]. Also, the craters result in an increase of the surface roughness, which limit the scope of applications of the treated materials. Here, I will show some advantageous aspects of the crater formation associated with the HCPEB treatment: the selective surface purification via crater eruption on the AISI 316L stainless steel.

Fig. III-18 shows a backscattered electron image of the untreated 316L steel sample. It reveals many tiny inclusions in the austenite matrix of the steel. They are MnS particles that are the consequence of sulfur addition for machinability [124,125]. Unfortunately, these inclusions act as initiation sites for pitting corrosion and, consequently, deteriorate the corrosion resistance [125]. The ideal solution would be to remove the inclusions from the surface after machining.

Fig. III-19a is a secondary electron image of a 316L sample HCPEB treated for 5 pulses. It shows many craters. Fig. III-19b is the corresponding backscattered electron image taken from the same area. It shows that dark spots are often located at the center of some craters, while some other craters do not appear to have any. Elemental line scan analysis, as shown in Fig. III-19b, revealed that the dark spots correspond to the MnS inclusions. As the inclusions' physical properties such as density, heat conductivity, heat capacity and melting point are usually different from those of the matrix phase, they can act as nucleation sites for the subsurface melting [97,114]. Fig. III-19c shows a typical laser 3 dimensional micrograph on the 5 pulses treated 316L sample. A line scan of relative height which crosses 3 craters was done along the gray line in the map. The curve reveals that the crater center has a very deep hole which suggests that some solid matter inside the hole has been pushed out. Fig. III-19d is a cross section image showing details of a crater formed in the same sample. Its diameter is about 50 μm and the depth is maximum in its center (about 5 μm and consistent with the results shown in Fig. III-19c) where a MnS inclusion was located. These two micrographs clearly support that MnS inclusions are the initiation sites for craters in the 316L steel and that an eruption event took place [112].

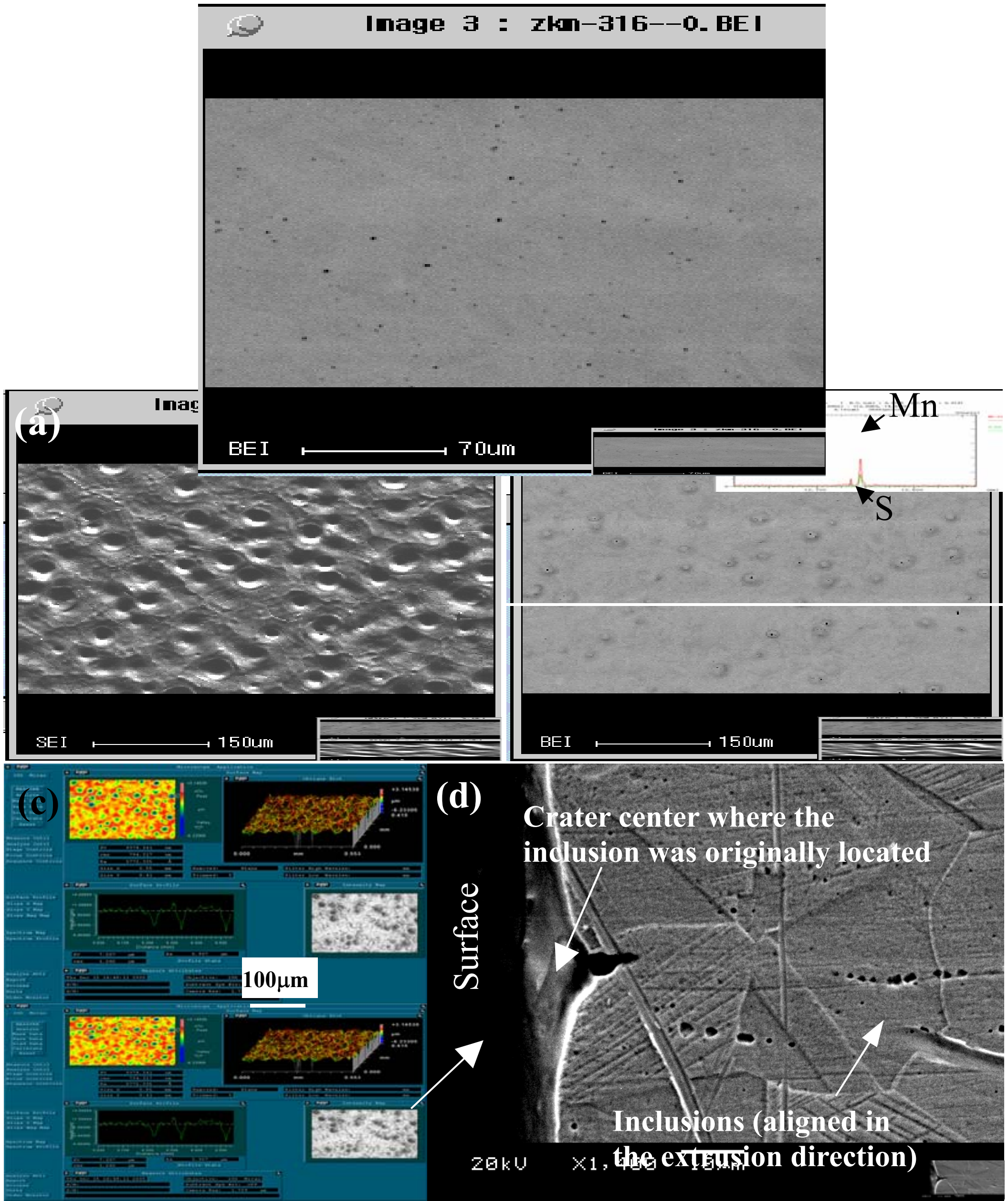
Image 3 : zkm-316--0.BEI
BEI
70um
(a)
Imag
SEI
150um
Mn
S
BEI
150um
(c)
100µm
(d)
Crater center where the inclusion was originally located
Surface
Inclusions (aligned in the extrusion direction)
20kV

Fig. III-19 Secondary electron images (a) and its corresponding backscattered electron images (b) of the 316L sample treated for 5 pulses. The line scans show that the black spots are remnants of MnS. Fig. c shows a typical laser 3 dimensional morphology on the 5 pulse treated 316L sample and a line scan of relative height which crosses 3 craters. Fig. d is a SEM image showing the typical aspect of a crater viewed on cross section of the 316L sample treated for 5 pulses.

Fig. III-20 shows the evolution of the densities of second phase particles and craters as a function of the number of pulses. The inclusion density decreases rapidly for the 5 pulse treatment and reaches a plateau regime after 10 pulses. After 5 pulses, the crater densities are approximately one order of magnitude below those of the inclusions. The crater density decreases substantially. It is clear that the eruption process - or partial eruption - of the inclusions results in the homogenization and purification of the melted surface. In addition, dissolution of the inclusions should also occur at a rate depending on their solubility. MnS has a very low solubility in steels [126], even at elevated temperatures. Calculation of the cooling rate for the top melted layer gave values in the range 10^7 to 10^8 K s^{-1} for the top melted layer [81,121]; the same order of magnitude as chill block melt spinning [127]. Since the solidification front is extremely fast, for example the estimated front velocity was in the range 2 to 10 m/s for 316L [111], solute trapping can occur under rapid solidification [128]. Therefore, the combined effects of eruption, mixing and solute trapping during rapid solidification are also to homogenize melted layer. Thus, with the increased number of pulses, the particle density on the top surface becomes lower. This reduces the number of nucleation sites for craters and, after 20 pulses, the crater density drops down to only about 1/4~1/6 of the highest values. Therefore, at this stage, a homogeneous purified layer (several μm thick) that contains a limited number of craters covers the surface of the steel.

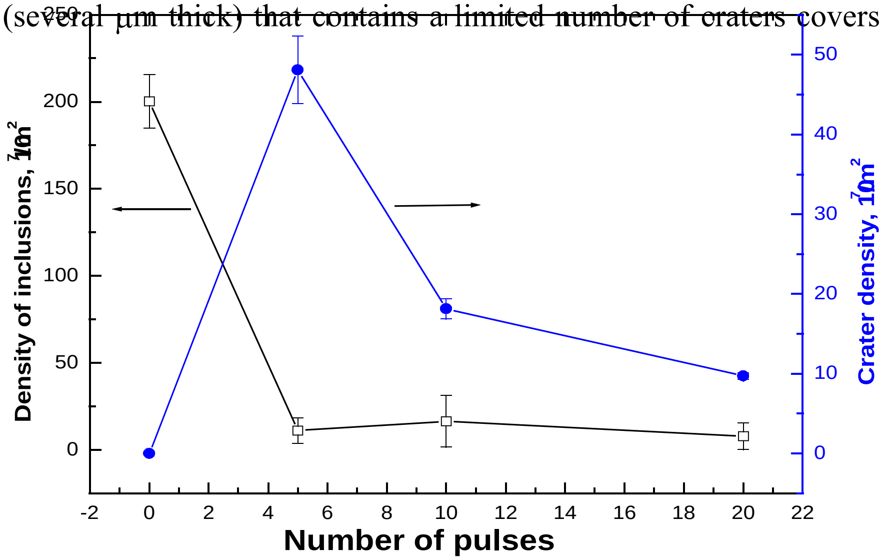

Fig. III-20 Evolutions of the densities of second phase particles and of the crater densities on the surface of the 316L steel samples versus the number of pulses.

III. 3. 2 Surface purification of FeAl under heating mode

As will be shown cle reinforced alloys can also
occur when the materi

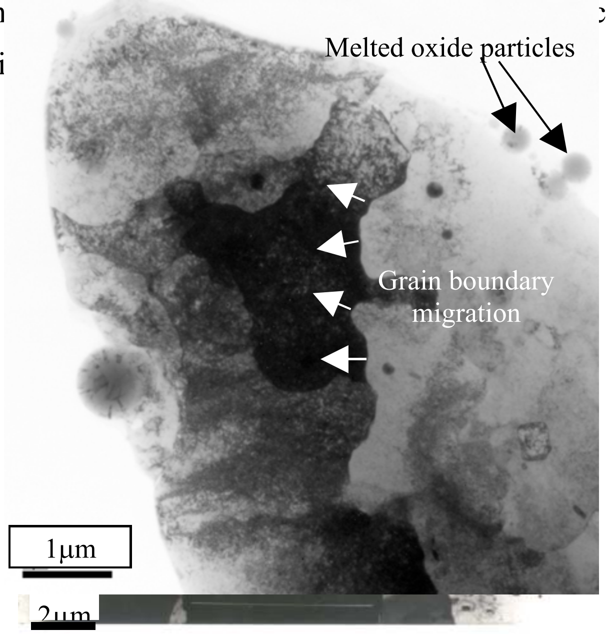

Fig. III-22 A typical bright field TEM micrograph in the top surface layer the 5 pulses treated FeAl sample.

Fig. III-21 A typical TEM micrograph of the untreated FeAl sample.

Fig. III-21 shows a typical TEM micrograph observed in the initial sample of an oxide dispersed strengthened (ODS) B2 Fe (40 at%)Al alloy. The oxide (Y_2O_3) is intentionally added (i) to increase the creep properties and (ii) to reduce the grain size and consequently improve room temperature ductility [129,130]. These oxides may be detrimental if they are located at the surface because the material is notch sensitive and the surface oxides may nucleate cracks. The coarse grained structure with limited dislocations can be clearly observed. Besides, many oxide particles are present. They are distributed fairly homogeneously inside the grains at the grain boundaries. Their size ranges from several nms to about 2 μm.

For the 5 pulsed sample, the typical morphology at the top surface is shown in Fig. III-22. Compared with the initial sample, the microstructure has changed somehow significantly. Three kind of features are clearly seen. Firstly, the dislocation density in grains has increased a lot and is very different from one grain to another. This means that the top surface layer has been heavily deformed and the deformation is not homogeneous. Secondly, there exist many round particles. Their size and shape suggest that they have melted and resolidified during treatment. EDS analysis showed that these particles are rich of Y, Al and O. They are preferentially melted oxide particles. This is not surprising because the oxide particles have a much lower heat conductivity compared with that of the FeAl matrix. Thirdly, the grain boundaries are not anymore as straight as the initial state. Th [illegible] dicates that grain boundary migration has occurre [illegible] ill be discussed in the next section III.5.2.

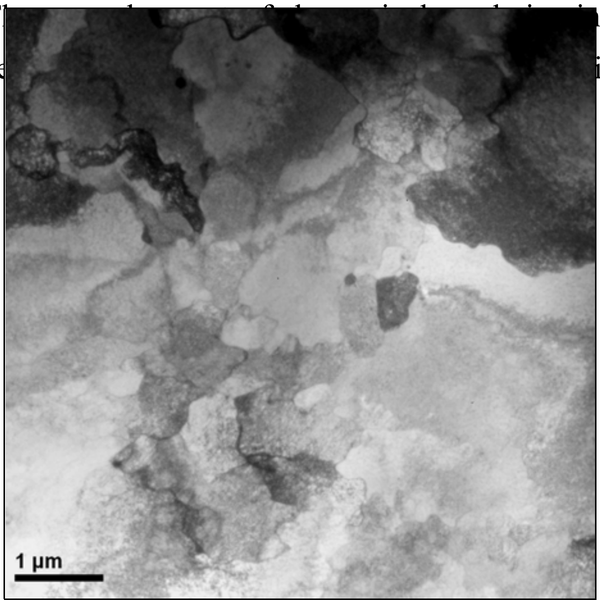

Fig. III-23 TEM observations in the top surface layer of the 20 pulsed FeAl sample.

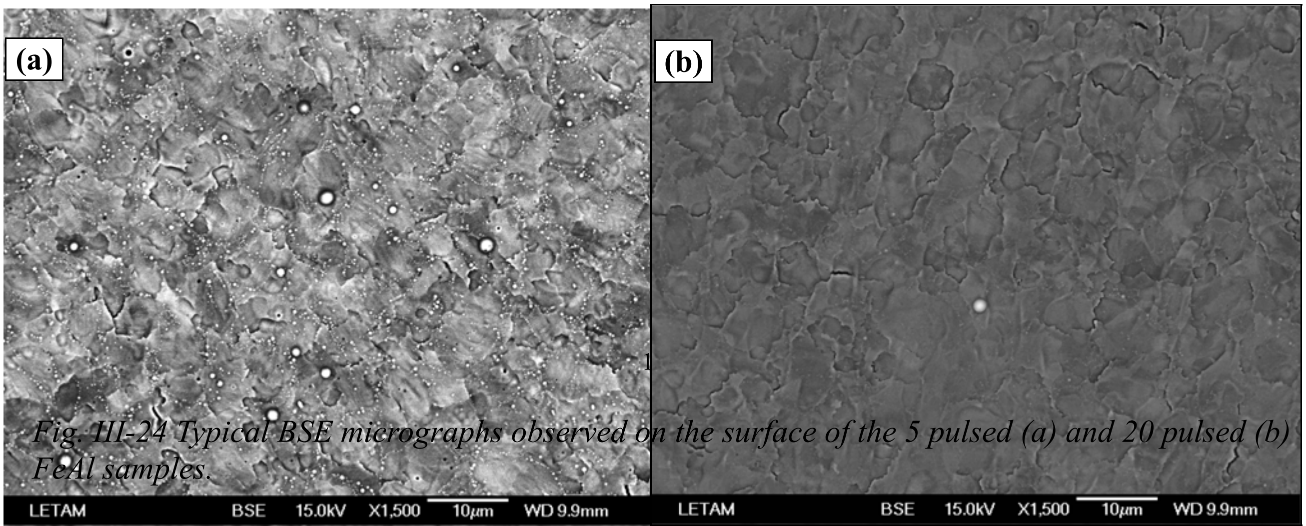

Fig. III-24 Typical BSE micrographs observed on the surface of the 5 pulsed (a) and 20 pulsed (b) FeAl samples.

The typical TEM micrograph taken at the top surface of the 20 pulsed sample is shown in Fig. III-23. Compared with the microstructures in the top surface of 5 pulsed sample, the oxide particles almost disappeared completely. This means that the selective surface purification, which we observed before, is not necessary under the melting mode and via crater eruption mechanism. It can be done through preferentially melting of the impurities that are sputtered off during the following pulses. Fig. III-24 shows the typical surface BSE micrographs taken on the 5 and 20 pulsed samples confirming this mechanism. After 5 pulses, many spherical particles appeared to be attached on the top surface (Fig. III-24a), and they were almost totally removed after 20 pulses (Fig. III-24b). Therefore, both the TEM and SEM observations confirm that a selective purification occurred under heating mode.

III. 4 Stress state and deep modification

III. 4. 1 Orientation dependent deformations induced by HCPEB

As is discussed before (section II.2.5), the stress induced by HCPEB treatment should be orientation dependent. Two examples have been selected here to show the effect of orientation dependent stress on the HCPEB treated materials: Fe (40 at%)Al and 316L stainless steel. The major difference between these two materials is their stacking fault, which is known to be the most important factor determining the type of deformations. Generally, materials having low stacking fault energy are easy to deform via twinning, for examples, Zn, Mg, stainless steels. On the contrary, those materials having high stacking energy tend to deform through extensive dislocation gliding, for examples, Al, Ni or even FeAl.

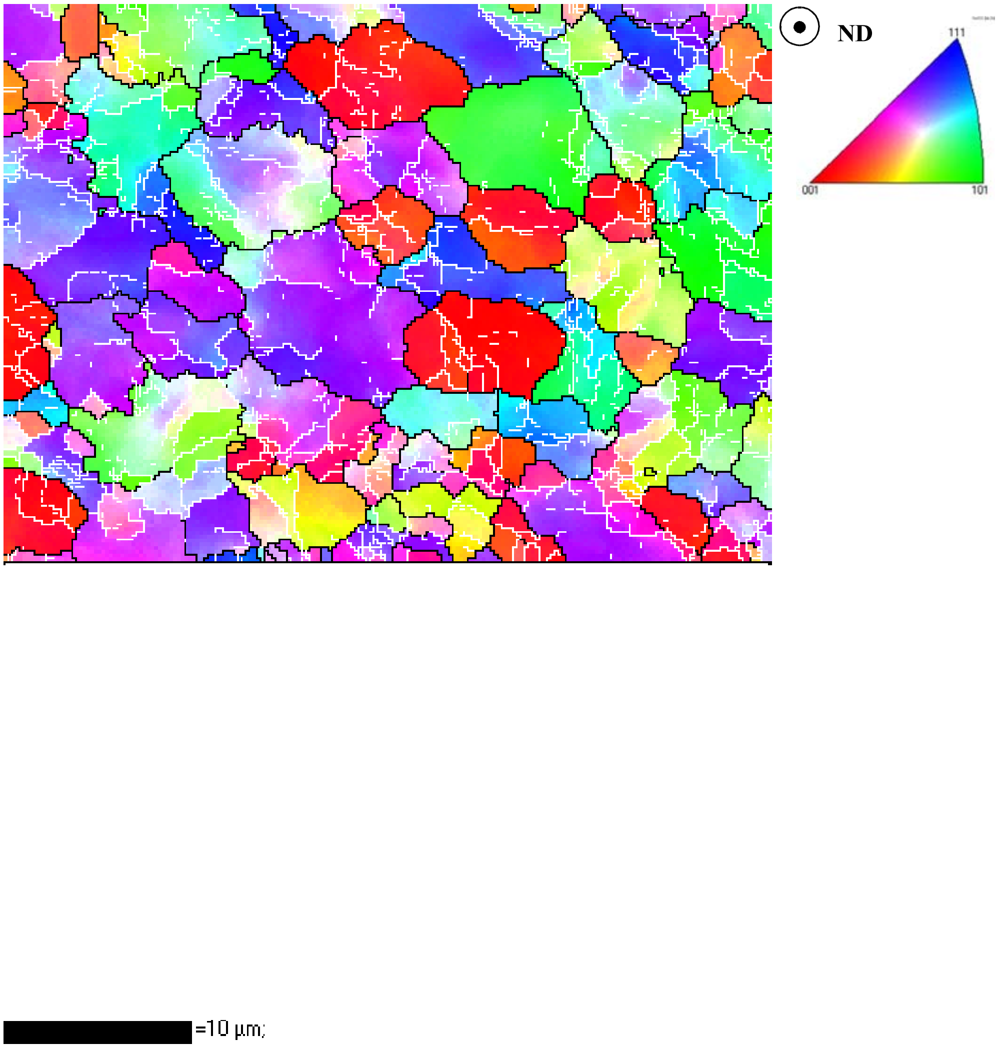

Fig. III-25 An EBSD OIM map taken from the same area as shown in Fig. III-9.

Fig. III-25 is the EBSD OIM map taken from the same area corresponding to Fig. III-9 (section III.2.1). The general aspects of the EBSD analysis on this sample will be discussed later. Here, we focus on the details of orientation dependent deformations. Compare Fig. III-25 with III-9, those grains having a lower depth level than the others always have a red color. This means that they have their <100> direction close to ND. Comparatively, those grains having other colors (orientations) do not show a big difference in height. Considering the orientation dependent stress induced by HCPEB treatment, the above results can be explained as follows. During the HCPEB treatment, the grains will be slightly stretched along ND under the action of quasi-static thermal stress. However, the stress is lower in near <100> oriented grains than that of the other grains, the deformation level is therefore lower in those grains. As will be shown in section III.5.2, the total strain induced after 20 HCPEB pulses could reach a value as high as 152%. Consequently, the accumulated difference in the strain between those grains became so important that it could be observed through the height of grains.

Another example shown here is the AISI 316L stainless steel sample HCPEB treated with 10 pulses under heating mode (section III.2.1). Fig. III-26a gives a typical EBSD orientation map from the top surface of the treated sample. Unlike the case of FeAl, which has a very high stacking fault energy, deformation twins are present in many grains of HCPEB treated 316L stainless steel. Their width ranges from several hundred of nanometers to several micrometers. They are always observed in those grains having their <111> direction close to the sample ND, indicating that the dominant deformation mechanism in those grains during HCPEB treatment is twinning. All of these twins have red or near red color, that is, their <100> direction is closely parallel to ND. This is due to the 60º shearing during twining deformation (the angle between the (111) and (100) planes is 54.7º). Fig. III-26b gives the pole figures of the grain marked by “A” in Fig. III-26a. From the pole figures, it is confirmed that this grain has its <111> direction almost parallel to ND and contains three family of twins having <100> close to ND. A specificity concerning the grains which do not contain twins and for which the significant amount of slip lines are present at the surface is that they often display a wide range of color in the EBSD maps. This indicates that the misorientation within these grains is rather high : a consequence of the intense deformation occurring during the HCPEB treatment. It is also clear that the deformation mode in those grains, especially in grains having their <100> direction close to ND, is dislocation gliding without any twinning. A line scan of misorientation in Fig. III-26c reveals that the misorientation within one grain can reach as high as 12°. Fig. III-27 gives a more general EBSD orientation map taken from the top surface of the same sample. A careful inspection of this micrograph confirms the orientation dependent feature mentioned above.

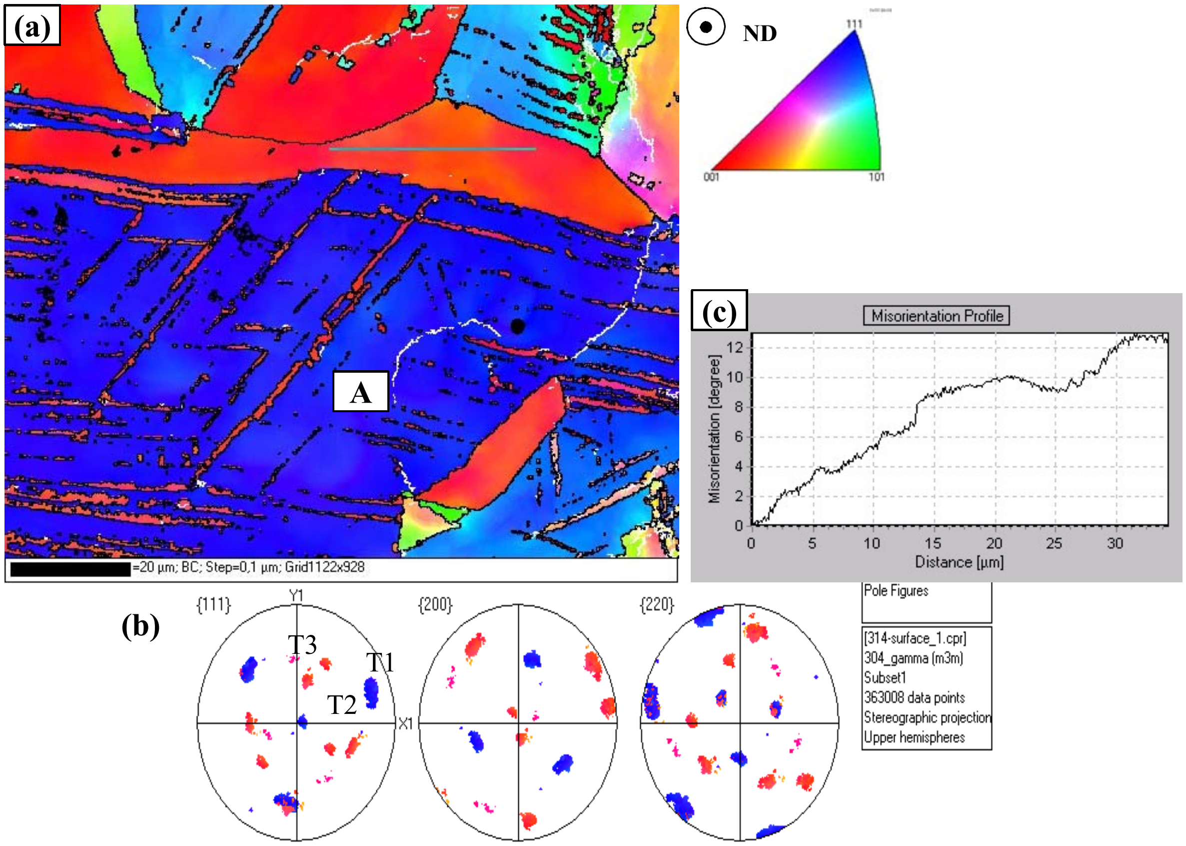

Fig. III-26 Typical EBSD OIM map measured on the 10 pulsed 316L sample (a), pole figures corresponding to the grain marked 'A' (b) and a line scan of misorientation along the marked line (c).

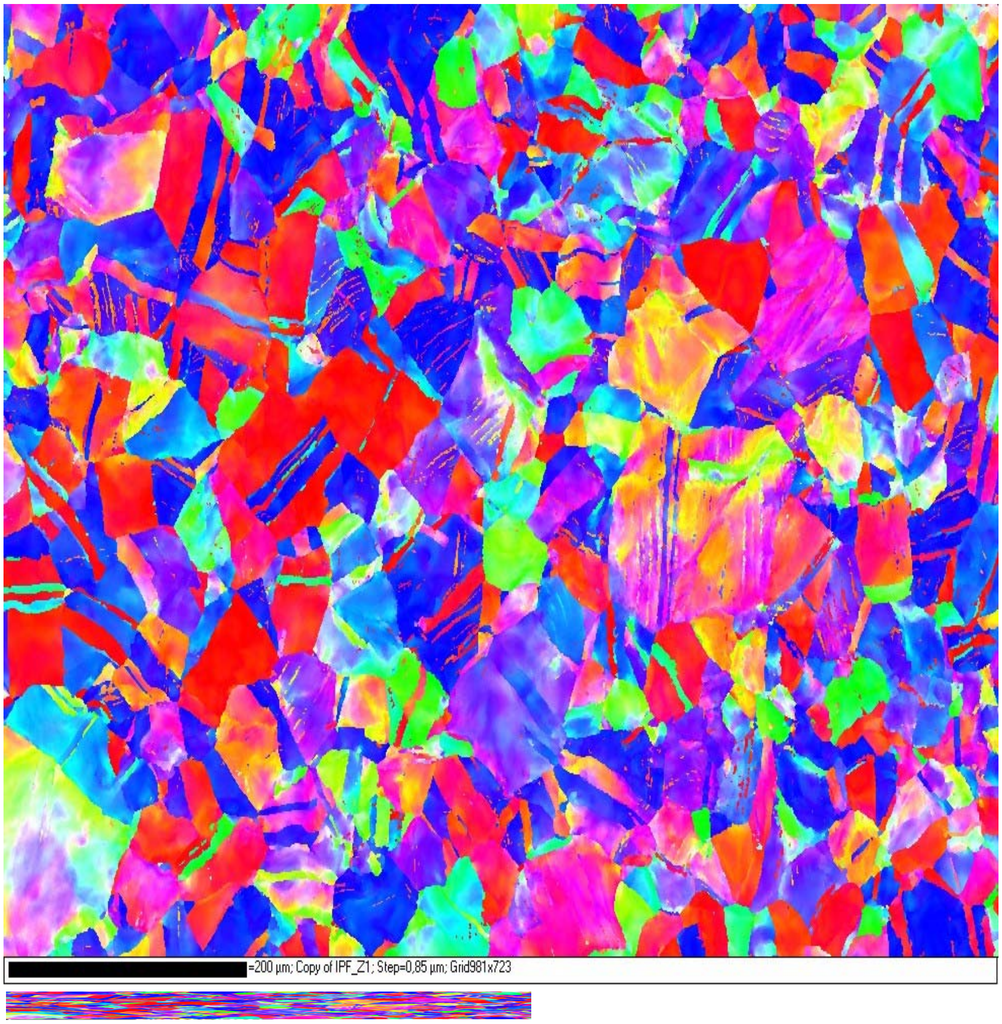
=200 µm; Copy of IPF_Z1; Step=0,85 µm; Grid981x723

Fig. III-27 A general EBSD orientation map measured on the 10 pulsed 316L sample under heating mode.

The present experimental results do confirm a difference in deformation depending on the orientation of the grains and the staking fault energy of the material. Further analysis is now under way to explain quantitatively the triggering of the deformation mechanisms and, thereby, give more experimental information on the exact nature of the stresses generated at the surface of HCPEB treated samples.

III. 4. 2 Shock stress wave after surface melting and deep modification

During HCPEB treatment, due to the drastic temperature change, a steep temperature gradient is generated along the incident direction of the beam [80]. However, due to the lateral confinement along the surface, the thermal expansion in the directions vertical to the beam is strongly restricted, causing the quasi-static thermal stress (Fig. III-28a). As discussed in section II.2.2 and according to Qin et al. [80], a local melting occurred in the subsurface layer when the temperature rises and the melted pools are formed beneath the surface as shown in Fig. III-28b.

Due to the liquid pressure, a resultant force *P* from the quasi-static thermal stress and the liquid volume expanding exerts on the pool of melt and is transmitted by the pool of melt in all directions [80]. The force *P* along the beam direction constitutes the source of the shock thermal stress wave (Fig. III-28b). If the thin outer surface solid layer cannot withstand this pressure, a volcano-like eruption occurs, as shown in Fig. III-28c. The shock stress is then released (Fig. III-28c). The duration of the shock wave pulse is the time interval between the initiation of the sublayer melting and the crater eruption.

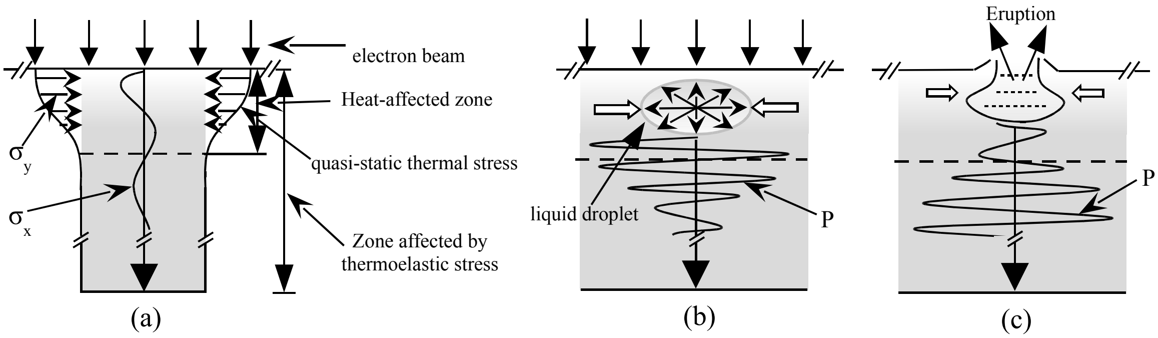

Fig. III-28 Schematic illustration of the formation of a crater via sub-layer eruption and the generation of the shock thermal stress, σ_x the thermoelastic stress, σ_y the quasi-static thermal stress, and P the shock thermal stress.

Calculations on HCPEB treated Al shows that the amplitude of the shock stress wave can be as high as 600 MPa at the top surface [80]. It then decreases when propagating into the bulk due to the attenuation effect of materials upon the stress wave [80].

The shock wave acts with the materials and may change the microstructures and properties in the deep layer [79,80,84,122]. In order to find the direct experimental evidence for the existence of the shock stress wave, we select the Al plates with a diameter of 100 mm, which is larger than the diameter of the electron beam (60 mm), and the beam and the plate are homocentric. Figs. III-29(a–c) show the cross-section distribution of microhardness inside the bombarding zone, at the zone edge and outside the bombarding zone.

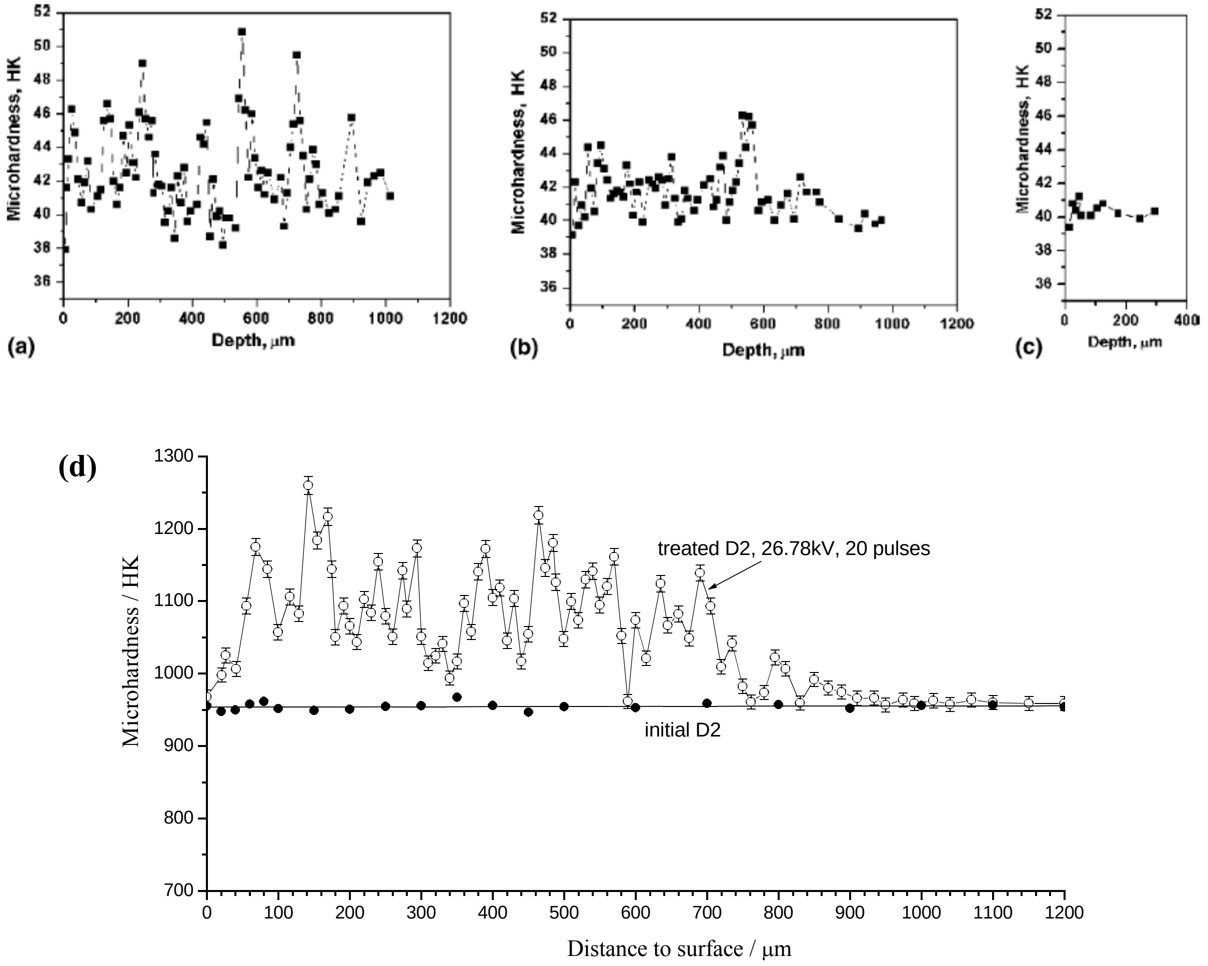

Fig. III-29 Depth distribution of microhardness on the cross-sections of the Al sample bombarded by HCPEB for 15 pulses: (a) 20 mm,(b) 30 mm and (c) 40 mm from the center. Microhardness profile of a treated D2 steel sample with 20 pulses is shown in (d).

The experiment parameters are pulse duration 0.8 μs, energy density 5 J/cm^2, and 15 pulses. The average microhardness (HK46) in Fig. III-29(a) is higher than that (HK42) in Fig. III-29(b). It shows that the higher is the energy density of the electron beam, the deeper is the sublayer melting and the more violently does the melted material erupt. From the SEM observations, it was also found that the density of craters on the surface in Fig. III-29(a) is higher than that in Fig. III-29(b). The microhardness distribution in Fig. III-29(c) is shallower and the amplitude is lower (HK40) than the other two cases. Coincidently, no craters are detected on the surface in the SEM observation. The average microhardness in Figs. 29(a) and (b) is about 15% and 7.5% higher than that in Fig. III-29(c), respectively. The above results confirm that the shock stress wave generated in the eruption region plays a dominant role in the enhancement of the microhardness. Fig.

III-29(d) shows the cross-section distributions of microhardness in the HCPEB treated D2 steel sample, treating parameters being pulse duration 1.5 μs, energy density 3.7 J/cm^2, and 20 pulses. The microhardness amplitude in the modified zone is higher than the average microhardness of the initial steel sample by about 30% (from HK950 up to HK1250). The modified zone extends up to 900 μm. The fact that the beam-affected zone goes far beyond the heat-affected zone is also observed. As calculated, the amplitude of the shock stress wave is several hundreds of MPa during a single pulse. The shock stress decays after transmitting several times. In a real working process the stress wave may be reflected by boundaries, either grain boundaries or the target rear surface. The boundaries further damp the stress wave. Therefore, increased bombardments enhanced the modification effects over increased depth ranges. The direct experimental proof of the existence of the stress wave far below the surface is illustrated in reference [79], where two wave fronts are observed about 0.5 mm beneath the surface of a HCPEB treated pure Al sample.

III. 5 Texture modification

Under the different treating modes, the HCPEB treatment always causes intense heating and deformation. These processes, solely or in combination, have the potential to change the initial grain orientations in the treated surface layers [131]. In other words, the texture in the treated material surface layers can be modified. Before this PhD, the evolution of texture in the surface of HCPEB treated samples was never studied. Here, we will show some recent investigations concerning texture modification in the HCPEB treated material surfaces, covering the effect of all the three treating modes. The analysis of texture development is of interest because the orientation of the grains does control several physical as well as electric and plastic deformation properties.

III. 5. 1 Texture modification under melting mode

Solidification of metallic materials has been studied for several centuries under both equilibrium and non-equilibrium conditions [132]. It is so complicated that many phenomena during solidification, such as dendritic growth, are still fascinating scientists and will still be the topic of many future research works. Rapid solidification of materials is of special interest for scientists and engineers due to the fact that it can often provide fine grain structures with good application properties [133-135]. Several factors may contribute to grain growth behaviours during fast solidification [132]. Among them, the solidification rate and the composition of melts often play the major role in determining various solidification related phenomena, such as phase selection, the solidification texture, the dendritic growth behaviour, etc [136,137]. The emergence of HCPEB treatment authorises a different way of studying fast solidification of metallic materials. Under melting mode of the HCPEB treatment, the surface layer of the treated materials, usually several micrometers in thickness, will be melted and directionally solidified on the solid substrates. This renders the opportunity to investigate the effect of solidification speed, the composition of melts and the substrate on the growth behaviours of different materials. Here, the fast solidification induced special grain growth will be investigated in the cubic system, which is, from crystallography point view, the simplest system to be studied. Two materials were selected in this work, (i) the AISI D2 steel for which the γ (*fcc*) phase was selected from the melt and retained down to room temperature and (ii) the NiTi shape memory alloy where B2 grains formed from the melt. It has to be mentioned here that the NiTi shape memory alloy is an example of material that will undergo the majority effects of either the melting or evaporating processes depending on the energy input provided by the HCPEB system.

III. 5. 1. 1 AISI D2 steel

The texture state of austenite formed in the 25 pulses treated D2 steel sample has been measured by X-ray diffraction [138]. The results indicated the presence of a <100> fiber texture component parallel to the normal direction (ND) of the sample with a large spread around this ideal orientation. In addition, <220> fiber component was also present. These two texture components were rather weak; having maximum slightly above 2 times random.

The presence of the mixed <100> + <110> fiber texture in the rapidly solidified γ layer is rather surprising. It was tentatively explained by the following reasons. Normally, the development of texture during solidification can be influenced at the two stages controlling the solidification process that starts by nucleation and continues with growth. In the case of rapid solidified melt spun ribbons, it is well known that the microstructure consists of randomly oriented grains nucleated at the wheel contact while their competitive growth through the ribbon thickness leads to the development of a columnar dendritic structure accompanied with strong

Fig. III-6. A typical SEM surface micrograph on the 5 pulsed D2 sample (a) and high magnification SEM surface micrograph of the sample treated with 25 pulses (b). Typical TEM image in the melted layer of the 25 pulsed sample (c).

texture effects [139]. Generally, the dendritic trunks grow along the thermal gradient direction following well defined crystallographic directions which, for *fcc* materials, are the <100> directions as shown in many previous works [136,140]. In our case, the nucleation stage can be affected by the material from which the melted layer re-solidifies. However, as the starting material was not textured, it was unlikely that a specific texture could be generated, from epitaxial growth for example, directly from the beginning of the solidification process. A competitive growth of grains must take place in the resolidified layer during which it would be expected that the grains with their <100> axis not oriented in the gradient direction are restrained in their growth. As the melted layer is fairly thin (2~3 μm), this progressive development of favorably oriented grains, by a growth selection process from randomly nucleated grains, can easily explain the presence of a weak <100> fiber texture with a fairly broad distribution around this ideal orientation. The concomitant presence of the <110> texture is much more surprising. Despite the high (45°) misorientation of <110> oriented grains with <100> which would be favorable for solid state grain growth; because of the rapidity of the cooling associated with the HCPEB treatment and , as confirmed by the microstructure revealed by the EBSD analysis [138], a recrystallization process in the as-solidified layer could not be the origin of this double fiber texture. Therefore, like the <100> grains, the <110> oriented grains must have grown from the liquid. Changes in the dendritic growth directions with respect to solidification conditions have been reported in transparent materials [141] as well as in Al alloys [136, 137,140]. In particular, EBSD analysis has revealed that the growth direction can change from <100> to <110> in Al alloys directionally solidified in high thermal gradients [136]. This was considered to be associated with a modification of the atom attachment kinetics when supersaturation is increased. In our case, modeling has shown that the solidification front moves very fast at solidification rates ranging from 1.5 m/s at the early stage of solidification towards 10 m/s at the top surface. These extreme growth rates together with the large supersaturation in C and Cr of the γ phase in our alloy may favor different growth directions. EBSD analysis in the Al alloys has revealed that the <110> orientations could be reached by twinning, the <110> twinned arms being suggested to originate directly from the regular <100> trunks [136].

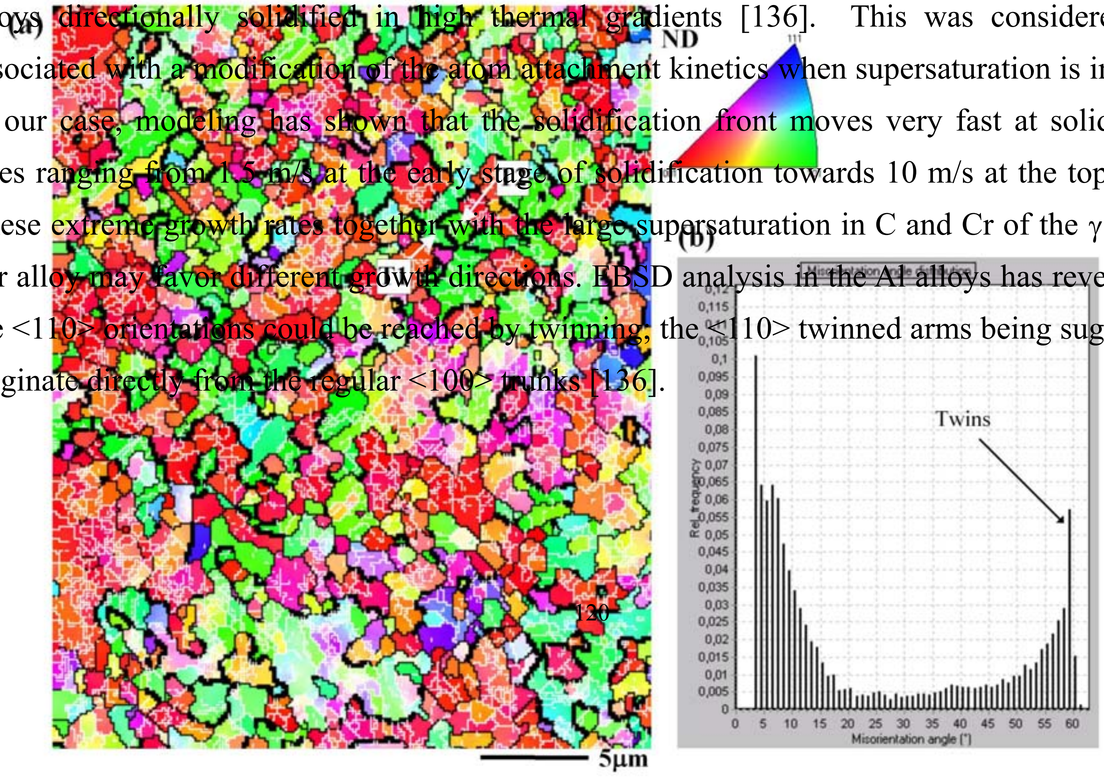

Fig. III-30 Typical EBSD OIM map measured on the top surface of the 25 pulses treated D2 sample (a) and the corresponding grain boundary misorientation angle distribution (b). Grains T1 and T2 are two near <110> domains separated by a (111) twin plane [138].

Fig. III-30 shows the EBSD map obtained from the top surface of the melted layer together with its corresponding chart of grain boundary misorientation distribution. The map clearly shows that the occurrence of Σ3–twin boundaries is also observed in our alloy. As in the Al-based alloys, the (111) twin planes most often separate near <110> oriented domains. Also, the EBSD map provided here clearly shows that (i) the Σ3−twin boundaries are never observed within the near <100> oriented areas and that (ii) they can also separate domains that are rather fairly away from the ideal <110>//ND. These results tend to confirm that the formation of these twins in our alloys is an intrinsic mechanism of the orientation related growth and is not related to subsequent annealing phenomena. Our results also show that, despite the very different processing conditions, the change in growth direction and some of its related mechanism such as twinning previously revealed in Al-based alloys [137], can also occur in the Fe-based metallic system. Recent theoretical and experimental analysis have demonstrated that the growth directions can vary continuously between different crystallographic directions as a function of crystalline anisotropy parameters which are themselves a function of the chemical composition [137]. In particular, a continuous dendritic orientation transition was observed between the <100> and <110> directions when the nominal composition of the alloys varied from about 25 to 60 wt % Zn in Al-Zn alloys. This transition was however reported to be more abrupt (from 10 to 30 wt% Zn) when plotted has a function of the actual composition in the deposited solids [137]. In our coating, as the supersaturation in Cr and C that essentially stabilized the γ phase originates from the fast dissolution of carbides [97], it is very likely that even after 25 HCPEB pulses – as confirmed by some remaining carbides in the melted layer [97] – the chemistry in the layer still presented sufficient local inhomogeneities that could modify substantially the local growth behavior of the melt during the rapid solidification event. Thereby, it could turn out that the HCPEB technique carried out on materials of selected chemistry is a possible effective way to control texture – and related anisotropic properties - at the surface of treated metallic materials.

III. 5. 1. 2 NiTi alloy

The Ni (50.6 at%)Ti alloy investigated in this section has been treated for 20 pulses under a HCPEB power of about 2.2 J/cm^2 with accelerating voltage of 25 kV (section III.1.3). The input power is sufficiently low to avoid significant evaporation. Therefore, the melted layer is thicker than the ones obtained in the NiTi alloys investigated in the next section (evaporating mode). Also, the lower input power should limit the amount of stress induced martensite present in the subsurface. Fig. III-31a and 31b give a typical EBSD OIM map on the 20 pulses treated NiTi sample under melting mode as well as its related pole figures. All the grains on the top surface were indexed as corresponding to the NiTi austenitic phase having the B2 structure and no martensitic phase could be indexed. The map in Fig. III-31a is almost completely dominated by grains having a green color, which corresponds to grains having a {110} plane perpendicular to the ND. Besides, some red colored grains, having their {100} plane perpendicular to the normal direction, are also present. The pole figures (Fig. III-31b), containing rings, depict the mixed fiber texture. Fig. III-31c shows the corresponding grain boundary misorientation distribution. The result reveals a surprising phenomenon: nearly 40% of the grain boundaries are twin boundaries. The rest are randomly distributed within the whole range.

Therefore, the suprising features revealed in the D2 steel are also present in the NiTi shape memory alloy. Clearly, the presence of <110> oriented grains can not be explained by a "conventional" solidification process. The <110> texture component may result from a modification of the atom attachment mechanism during solidification due to the high velocity of the solidification front in the super-saturated liquid and the formation of large amount of twin boundaries should also play an important role for the <110> texture formation during solidification. Further work is now under way to fully elucidate the texture formation mechanisms under the action of HCPEB surface treatment under melting.

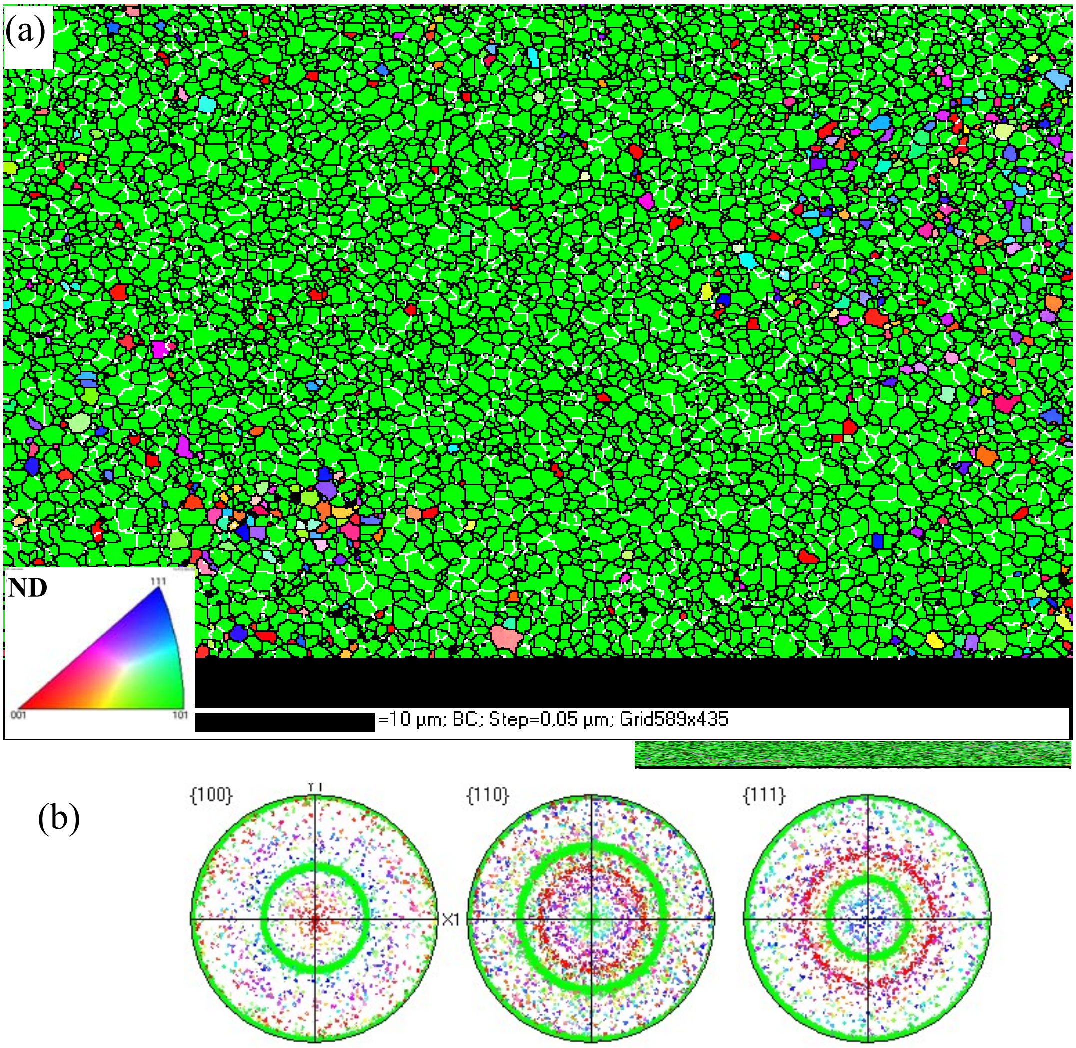

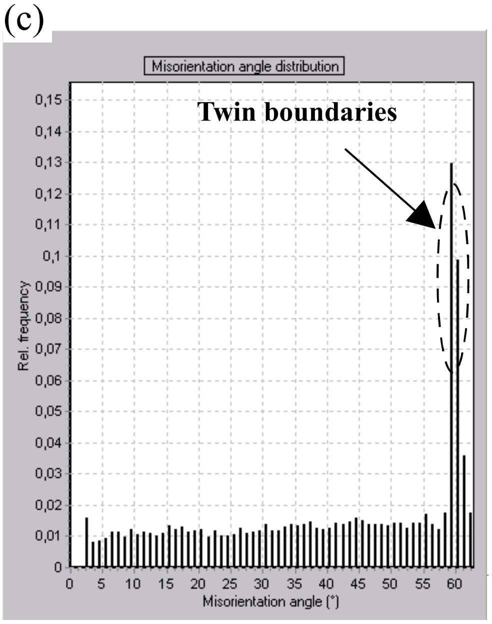

Fig. III-31 Typical EBSD OIM image measured on the surface of 20 pulsed NiTi sample (a), its corresponding pole figures (b) and the grain boundary misorientation distribution (c).

III. 5. 2 Texture modification under heating mode

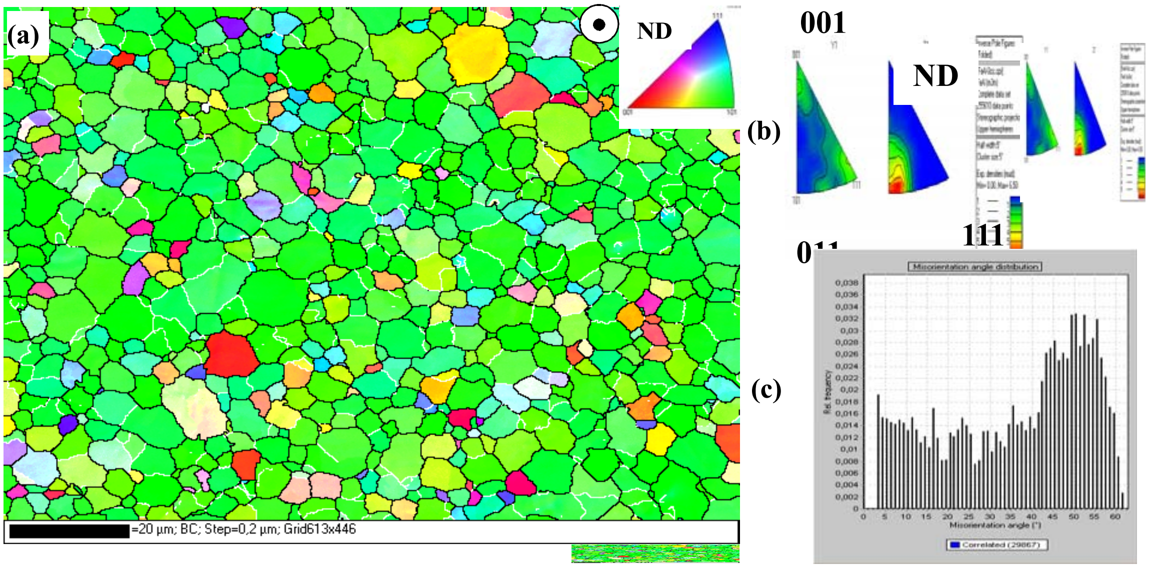

Fig. III-32 EBSD orientation map on the surface of the untreated FeAl sample (a), corresponding inversed pole figures (b) and grain boundary misorientation distributions (c).

In order to study the texture modifications induced by HCPEB treatment without melting of the surface, the Fe (40 at%)Al intermetallic alloy has been selected. The as-received oxide dispersed strengthened (ODS) B2 Fe (40 at%)Al alloy was hot extruded at 1250°C from milled powers [142]. Fig. III-32a shows a typical EBSD orientation map of the initial sample. Grain boundaries having misorientation between 3° to 15° are shown in white while higher misorientation ones are shown in black. The standard color triangle is shown inset. The corresponding inverse pole figure (Fig. III-32b) shows that the initial sample has a <110> fiber texture // to ND, which is the typical texture for extruded bcc (or B2) alloys [142]. The maximum intensity of the texture is at 6.5 times random, consistent with earlier XRD results [142]. The grain boundary misorientation distribution of the initial sample is given in Fig. III-32c.

The HCPEB treatment was carried out below the onset of melting. Figs. III-33a, 33b and 33c show the same type of analysis carried out on the 5 pulsed sample while Figs. III-33d, 33e and 33f are relative to the 20 pulsed sample. It is interesting to note in both maps (Figs. III-33a and 33d) that many of the initially fairly straight high angle grain boundaries have adopted a curved aspect; suggesting that some grain boundary migrations occurred during the HCPEB treatment. The curvature of the grain boundaries was also more pronounced after 20 pulses. This is in consistent with the TEM observations given before (Fig. III-22 and 23). Humphery et al. have studied such a phenomenon called strain induced grain boundary migration [143]. It normally occurred during annealing of deformed materials where the grain boundaries move from grains having lower dislocation density towards the neighbor grains having higher dislocation density. The

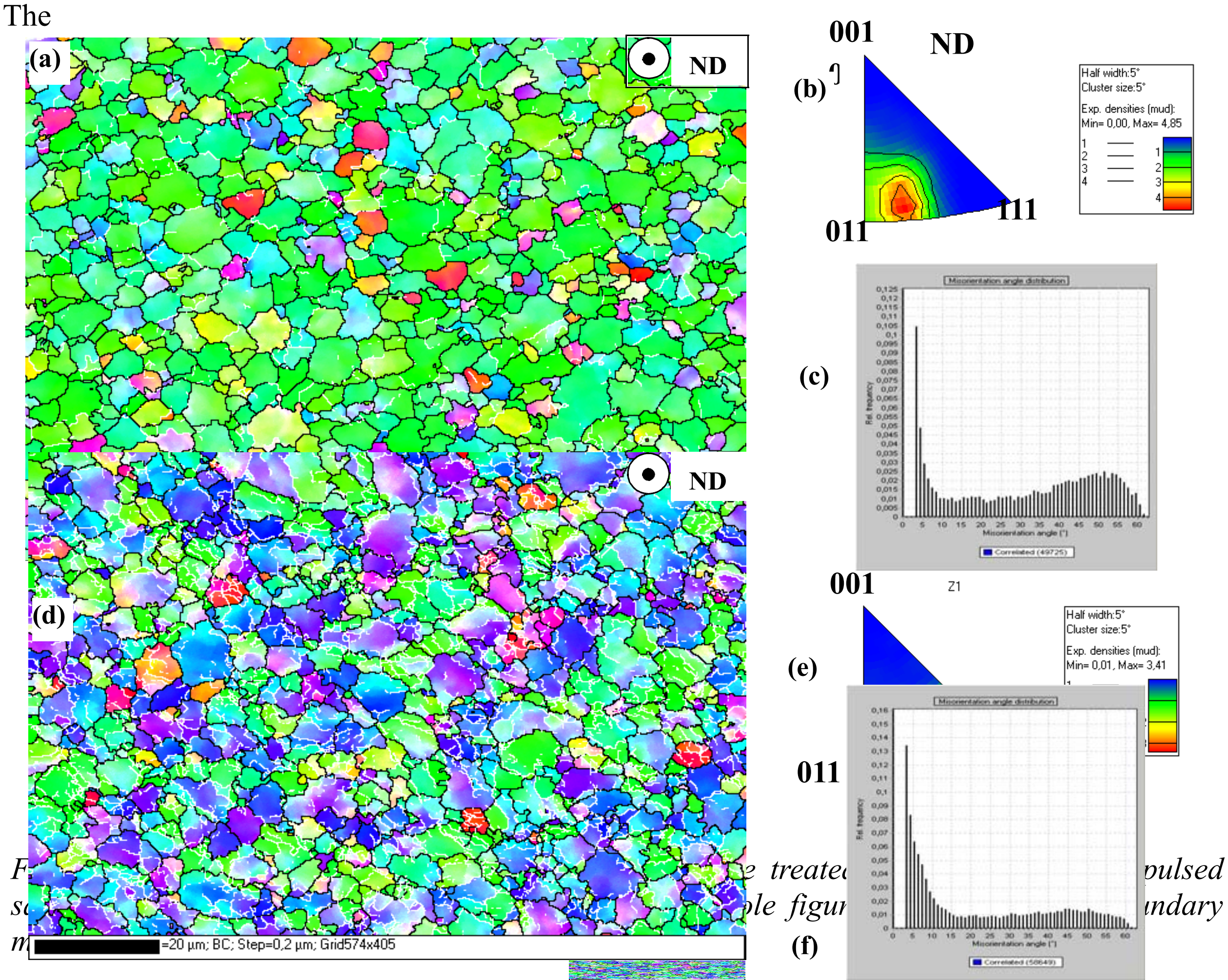

F e treate pulsed
s ole figur ndary
m

ND

process is to reduce stored deformation energy by reducing dislocation density. One of the specific features of this boundary migration is the curvature aspect of the grain boundaries. In this case, during each pulse, the surface layer of the sample was deformed while a dynamic recovery/recrystallization process occurs due to the high temperature field and stored deformation energy from the previous pulse. Also, the degree of deformation is different from one grain to another. The combination of the above processes results in the dramatically increased dislocation density and migration of the grain boundaries. The increased fraction of low angle grain boundaries corresponds to the creation of new sub-grains inside the initial grains. As a result, grains were refined. The determination of the so-called "grain size" by EBSD is dependent on the selection of misorientation angles. If we use a boundary misorientation angle of 5 degrees for the determination of grain size, then the average grain size is about 3.6 μm for the untreated sample. It decreases down to 2.8 μm for the 5 pulsed sample and 1.8μm for the 20 pulsed sample. This clearly shows a microstructure refinement with the increasing number of pulses.

In Fig. III-33b, the texture component of the sample treated for 5 pulses has been shifted to a fiber which is about 7 degrees away from <110> towards <111>. It has an intensity at about 5 times random. The grain boundary misorientation distribution of the 5 pulsed sample shows an increased fraction of low angle boundaries. The inverse pole figure of the 20 pulsed sample (Fig. III-33e) shows that the texture consists now of a broader fiber centered on <321> and having a maximum intensity at about 3 times random. The grain boundary misorientation distribution of the 20 pulsed sample has also changed significantly: the fraction of low angle grain boundaries being increased more substantially.

By using the computer code described in chapter II, we calculated the transient thermal cycle in the present case. The simulation of temperature field reveals a very fast heating and cooling thermal cycle occurring in the near surface layer with a maximum temperature of 1510K reached at the top surface within 0.7 μs. In addition to the surface aspect of the sample that is very different from the melted ones (section III.2), this calculation confirms that the energy provided here by the HCPEB treatment did not lead to the melting of the surface (the melting point of Fe (40 at%)Al is 1653 K). As discussed before, the thermal elastic stress wave can be omitted while quasi-static stress plays the major role in this case. For FeAl, Young's modulus E is temperature dependent, for example E=170 GPa at room temperature and E= 110 GPa at 773 K. The calculations show that the maximum amplitude of thermal stress can reach values as high as 2 GPa, much higher than the yield strength of FeAl. Under the action of the high thermal stress during heating, the grains in the surface layer will be deformed with a very fast deformation rate but for very small values of strain. For Fe (40 at%)Al, the linear expansion coefficient α is temperature dependent and $\alpha \approx 1.483 \times 10^{-5} + 6.7 \times 10^{-9} T$ m/m•K [144], while the volume dilatation coefficient is equal to 3α. Under the two dimensional constraining condition the theoretically estimated deformation $\int_{298}^{1510} 3\alpha(T)dT$ would be 7.6%, when the temperature reaches 1510 K, for a single-pulse of HCPEB treatment on the FeAl sample. After 20 pulses, the total deformation could therefore reach a value as high as 152%. In combination with the heat cycle, this is large enough for modifying significantly the texture state of the material. It is clear from the evolution of the texture and microstructure with the number of pulses given in Fig. III-32 to III-33, that the repeated action of the beam has generated thermal-mechanical cycles, leading to in situ recovery/recrystallization processes that have modified the texture. The process has also reduced the grain size by inducing the formation of low angle boundaries that, under further HCPEB cycles, should transform towards higher angle boundaries. Unlike conventional deformation processes, these changes have been induced by the HCPEB technique without significant changes in the morphology and aspects of the sample. This demonstrates the high potential of the HCPEB technique.

III. 5. 3 Special texture formations under evaporating mode

To gain more information about the microstructure issued from partial evaporation and following solidification of the surface melted zone, FEG-SEM and EBSD were carried out to characterize the top surface of the HCPEB treated Ni (50.6 at%)Ti samples under evaporating mode [111-113]. To this end, the NiTi alloy was HCPEB treated with a higher energy than the one used in the previous section (melting mode).

Fig. III-34 shows a typical SEM image, its corresponding EBSD map and pole figures for the case of a sample HCPEB treated for 10 pulses under high energy. These images reveal the presence of some features that are similar to the ones previously depicted (see section III.1.3): (i) several bands in the SEM image that correspond to martensitic variants, (ii) voids corresponding to shrinkage cavities and (iii) sub-micrometer grains at the surface. The major difference between the samples treated under melting and evaporating modes lies in the distribution of the fine grains and the shrinkage cavities. While the fine grains and cavities are fairly well distributed over the entire sample surface under the melting mode, the pulsed sample surface treated under evaporating mode is characterized by the presence of areas containing no cavities and a very limited numbe ostructure are clearly visible n deformation marks (arrowe iants. The fact that these mar correspond to traces of mart l defects also bridge B2 grai ot show up in Fig. III-34b). ransformation was triggered ssociated with the HCPEB tr s containing a limited numbe d to rounded protrusions att SD OIM map, the small as well as the large grains present at the surface were all indexed as corresponding to the NiTi auste indexed. The OIM map reve (near <100>) colors. Also, it <110> or

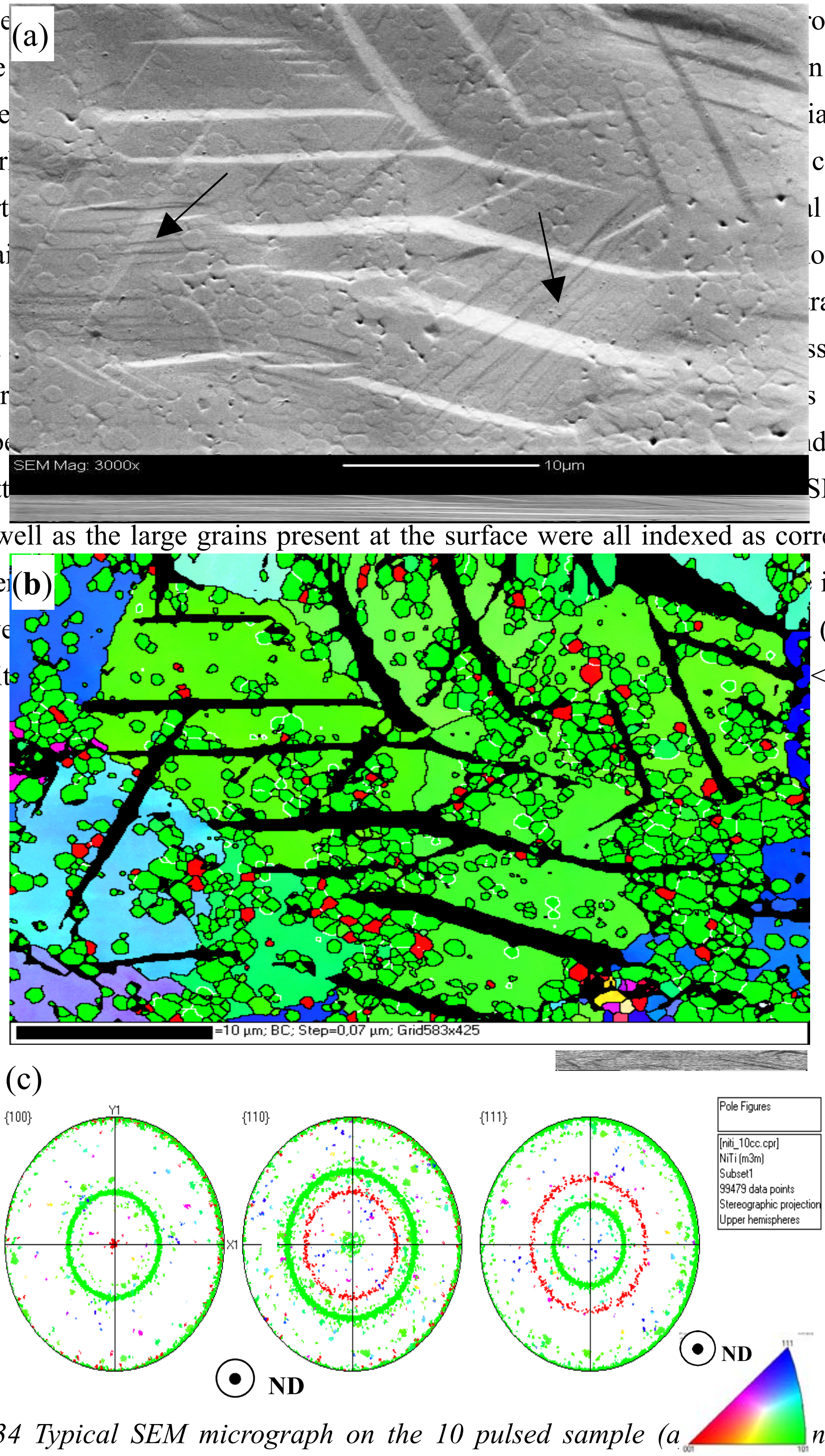

Fig. III-34 Typical SEM micrograph on the 10 pulsed sample (a nding EBSD OIM map (b) and the corresponding pole figures of the small grains (c).

near <100> orientations regardless of the color (orientation) of the large grains present underneath. The pole figures of the small grains (Fig. III-34c) confirm that the texture of the protrusions present on the surface is a fiber texture consisting of a mixture of two components : a strong <110> and a weaker <100>.

After melting and potential evaporation, rapid solidification occurs and leads, in this alloy, to the formation of ultrafine B2 grains at the top surface [80,81]. Under the evaporating mode, the interesting observation revealed in this work is again the presence of the mixed <100> + <110> fiber texture. In the present case where evaporation is operating, the EBSD analysis of the surface does not show the presence of any twin. A mechanism involving twinning is therefore ruled out in this alloy when evaporation is intensive. At some point during the process, the solidification and evaporation mechanism must indeed operate simultaneously. Normally, under solidification the atoms move from the liquid to build up the ordered NiTi solid with preferred growth orientation (<100>) [145]. Concomitantly, the evaporation process creates an atom flux in the opposite direction [146]. The evaporation mechanism is known to lead to an atomic motion having a velocity in the range of several hundred of m.s^{-1} [146,147], which is much faster than the moving speed of the solidification front. Therefore grain growth proceeds in an environment where the evaporation mode creates an important atom transfer along the solid/liquid interface; which may modify drastically the atom attachment conditions during solidification. In addition to a solidification process strongly affected by the concomitant occurrence of evaporation, the fact that some of these grains are isolated (ie. OIM map in Fig. III-34b) suggests that they may even have redeposited directly from the vapor. From the analysis of vapor deposition processes, it is well established that their preferred growth direction can depend on many parameters such as vapor pressure, substrate orientation, deposition temperature, … [148]. Clearly, further theoretical and experimental analysis concerning the HCPEB are required to fully understand the growth mechanisms of these grains; since it is clear that their nature can not be explained by a rapid solidification process only.

Chapter IV Applications of HCPEB treatment

The initial goal of developing HCPEB technique for surface treatment of materials is, in fact, to apply this new technique in industry [67]. For this sake, HCPEB treatment has been attempted on different industrial materials under different treating parameters to see how the treatment can affect the surface microstructures and modify the application properties [67-79]. The investigations carried out in the past decade have clearly shown that the HCPEB treatment can lead to non-stationary temperature and strong stress fields in the surface layers of materials. As a result of those complex processes discussed in the above two chapters, non-equilibrium microstructures can be achieved in the surface of materials. This may lead to the formation of a surface layer with improved physical, chemical and strength properties that are often unattainable with conventional surface treatment techniques. Previous studies did show that the HCPEB treatment leads to a significant improvement in the wear and corrosion resistances of many steels and alloys [149-170]. It could also be established that the final structures and properties of HCPEB treated materials are strongly dependent on the parameters of the electron beam, such as beam energy and number of pulses [98,114]. Based on the physical foundations and special effects given before, we will demonstrate here several possible applications of the HCPEB treatment under different treating modes.

IV. 1 Surface hardening and softening

One of the important effects induced by the HCPEB bombardment on the treated materials is known to be surface hardening [67]. Many factors account for this effect since the harness of a material depends on its structural, phase and stress-strain states. All of these states can be changed by HCPEB treatment as we have discussed before. In fact, the HCPEB treatment can induce both hardening and softening of the surface depending on the response of the treated material and the electron beam parameters used. Here, we will show some examples of surface hardening and softening induced by HCPEB treatments.

Fig. IV-1 shows the evolution of the hardness values obtained on the surface of the D2 steel after 5 and 25 HCPEB pulses (section III.1.2.1). The data were obtained with different loads: 25, 50 and 100 g. The initial harness of the sample is about 500 Hv. It does not vary with the load. After 5 pulses, the hardness increases. It is also interesting to note that the hardness decreases when the load increases. From the phase and structural analysis given in the previous chapter (section III.1.2), it is clear that the increase in hardness after 5 pulses can be attributed to the formation of martensite in the top surface melted layer. The decrease of surface hardness with load for the 5 pulsed sample is due to the fact that martensite is only confined within the top surface melted layer that is about 2 μm thick. Comparatively, the hardness of the 25 pulsed sample is lower than that of the initial and 5 pulsed samples. In addition, the hardness increases when the load is increased. The decrease in hardness after 25 pulses is due to the formation of an homogeneous layer of metastable austenite in the melted surface layer. This austenite is softer than the initial material. The increase in hardness with load is also the correspondence of austenite formation which is only located in the melted surface layer. After 25 pulses, the thickness of this melted layer is only increased up to 3 μm.

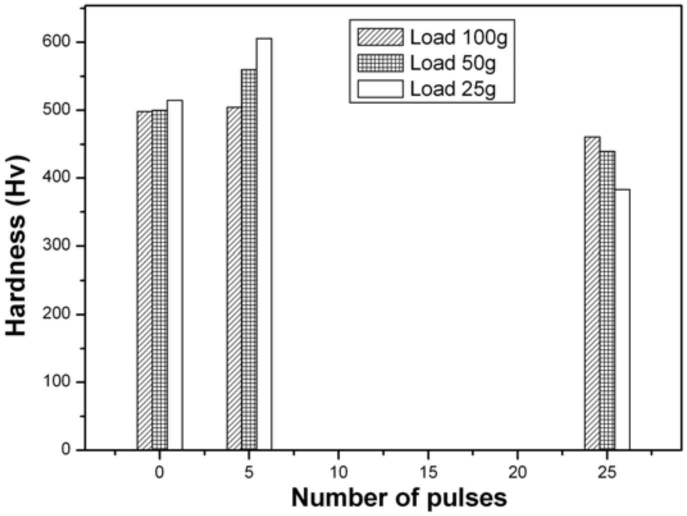

Fig. IV-1 Surface Vicker's hardness of AISI D2 steel samples before and after HCPEB treatments under different loads.

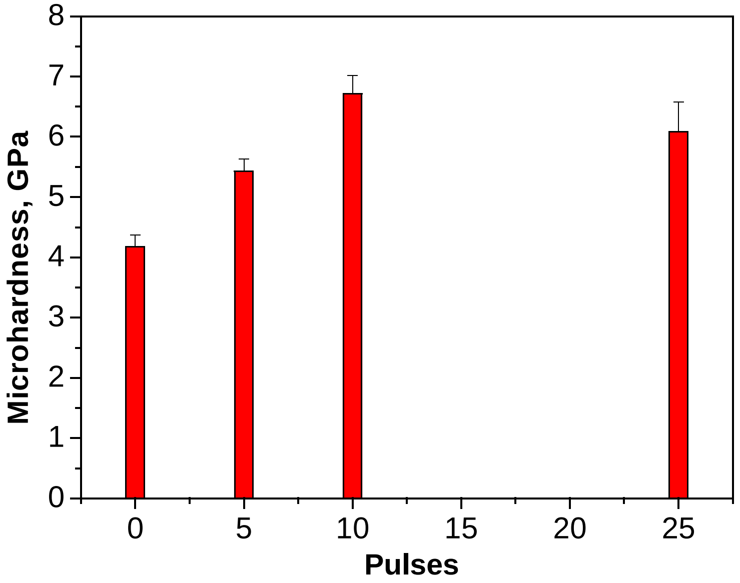

Fig. IV-2 Surface microhardness of the quenched and tempered T8 steel samples before and after HCPEB treatments.

The surface hardness evolution of the quenched and tempered T8 steel with the number of pulses is shown in Fig. IV-2. The initial sample has a hardness of about 4.2 GPa. It increases to 5.3 GPa after 5 pulses and 6.7 GPa after 10 pulses. After 25 pulses, the hardness decreases to about 6 GPa. From the XRD analysis given before (section III.1.1). It can be concluded that the increased hardness after HCPEB treatment is mainly due to the formation of martensite in the surface layer. Comparatively, the slight decrease in hardness from 10 pulses to 25 pulses is a result of the presence of a small amount of austenite after 25 pulses [104].

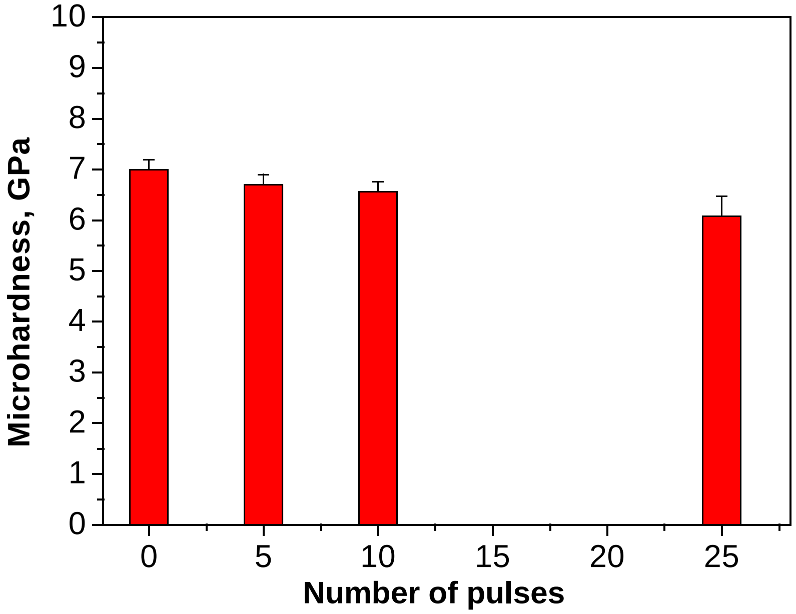

Fig. IV-3 Surface microhardness of the quenched and tempered T10 steel as a function of the number of HCPEB pulses.

In some cases, the HCPEB treatment may lead only to a continuous softening of the surface. This is illustrated in Fig. VI-3 in the case of the T10 steel. Clearly, the hardness keeps decreasing with the number of pulses for the quenched and tempered T10 steel, the decrease in hardness can be attributed to formation of austenite, whose amount increases with the number of pulses (see section III.1.1).

From the above examples, it is clear that the HCPEB treatment can induce both softening and hardening. In the case of steels, phase transformations have a strong effect. The formation of martensite is always associated with hardening while the softening can be the result of austenite formation. Without phase transformation, other factors such as residual stresses, quenched-in vacancies, grain size modification and dislocation densities can also play a role [92,93,149]. For example, Pogrebnjak et al. have shown the dependence of hardness on dislocation densities in pure iron treated by HCPEB [92,93].

IV. 2 Rapid surface alloying

It is already known that HCPEB is a good method for rapid surface alloying. Pogrebnjak et al. have studied the post-treatment of Ta and Mo precoated Fe samples and found the coated elements can diffuse significantly into the materials under transient thermal procedures [77]. They used a “duplex” method, that is film deposition plus HCPEB post-treatment, to treat a low carbon steel [156]. The results revealed that intermetallic compounds were formed during surface alloying. We have also attempted the HCPEB treatment of powder-precoated Al and steels (examples being carbon powder on Al, TiN and Cr powders on D2) [79]. Significant mixing of the precoated powders with the surface layer occurs during the irradiation, resulting in enhanced mechanical properties such as high microhardness and fretting fatigue resistance. Here we will show some typical examples on surface alloying by HCPEB treatment.

IV. 2. 1 Oxidation protection of H13 steel by HCPEB treatment

Al films were deposited on the H13 steel samples and HCPEB was then used to treat the Al-coated specimens [165]. The HCPEB treatments were carried out with parameters including :

accelerating voltage; 27 kV, energy density; 3 J/cm^2, number of pulses; 4 and 15, pulse duration; 1.5 μs.

Fig. IV-4 compares the surface morphologies of the sample precoated with Al using arc
deposition with the … hology of the aluminum-
precoated sample, r … o the presence of large
particles, typical of a … e area is partially melted,
as can be seen in Fig … lmost completely melted
and some spalling p … Al film is porous, so the
mixing process will … ess is below the electron
penetrating range in … X analysis at the electron
energy of 20 keV co … ntent reaches about 22 at
% (~12 wt%), which … tests in air at 750°C, the
oxides on the initial sample are mainly Fe$_3$O$_4$ and Cr$_2$O$_3$, while the coatings of post treated
samples contain dens … ance of about 40 times as
compared with the in

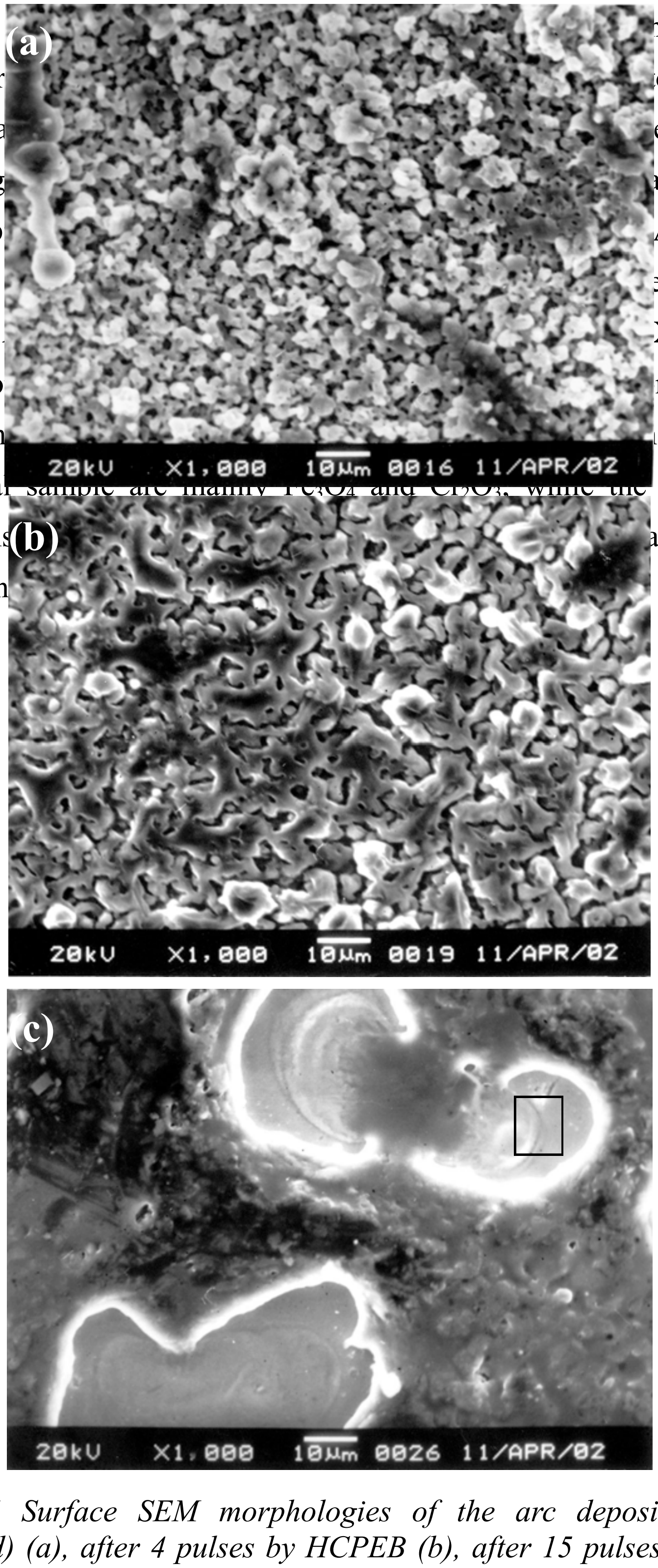

Fig. IV-4 Surface SEM morphologies of the arc deposited Al film (untreated) (a), after 4 pulses by HCPEB (b), after 15 pulses by HCPEB (c). (The EDAX analysis was conducted in the marked area).

IV. 2. 2 Surface alloying of 316L stainless steel with Ti

A thick pure Ti powder layer was pre-coated on the 316L stainless steel sample surfaces by brushing [171]. They were then treated by HCPEB with the following parameters: energy density ~3 J/cm^2, pulse duration ~1.5 μs, number of pulses being 10 and 20.

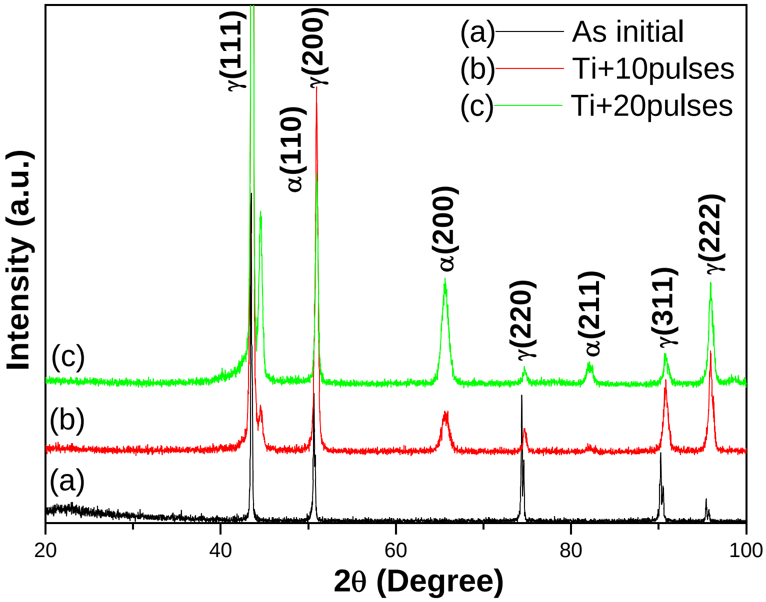

Fig. IV-5 XRD traces of the as received 316L stainless steel (a) and Ti pre-coated samples after 10 pulses (b) and 20 pulses (c) by HCPEB.

The phases in the surface layer of untreated and Ti alloyed samples were identified using the XRD, as shown in Fig. IV-5. It reveals that phase transformation takes place during Ti-alloying. Comparing with the XRD trace of the untreated 316L steel, which shows a single γ-phase structure, α phase was found in the melted layer after irradiation. This means that the alloyed layer contains a mixture of α and γ phases because Ti is an α phase former. The addition of the Ti element into iron favored the formation of α phase. As a result of the HCPEB treatment, the fine Ti powder was melted and dissolved into the substrate. The melted layer re-solidified to form the new phase. The peak intensity of the α phase increases with the increased number of pulses, which is due to the increased depth of the alloyed layer.

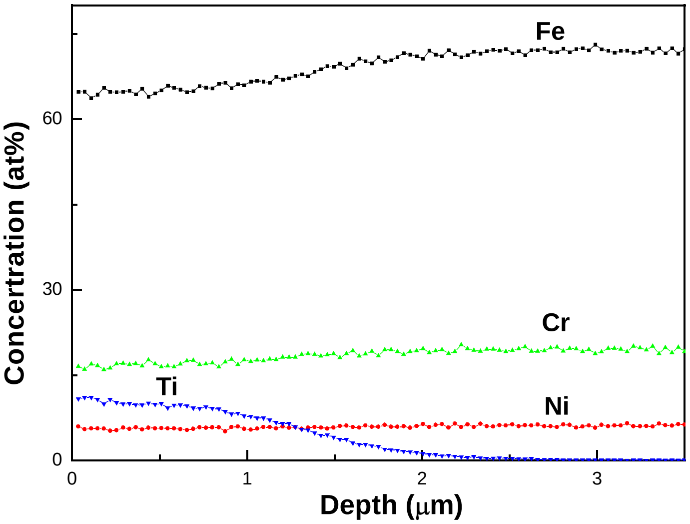

Fig. IV-6 Composition profiles of 316L stainless steel sample after surface alloying by HCPEB with 20 pulses.

To quantitatively reveal the chemical modifications after the HCPEB treatment, SNMS was carried out on the Ti alloyed sample treated for 20 pulses. The result of the analysis is shown in Fig. IV-6, where the evolution of the amount of Ti, Fe, Cr and Ni is plotted as a function of the distance from the surface. On the top surface, the Ti concentration is about 10 at%. It decreases gradually with depth and goes down to 2.5 μm. The beneficial effect of this Ti diffusion layer has been demonstrated for corrosion resistance. Indeed, the potentiodynamic polarization tests of the untreated and Ti-alloyed samples have been carried out in Tyrode's simulated body fluid. In the present study, the Ti-alloyed sample with 10 pulses shows the best corrosion resistance. This was attributed to its better surface state including micro-cracks free and good Ti homogeneity.

IV. 3 Enhanced diffusion

It has been observed that enhanced diffusion effect occurred in a Ti-implanted 9Cr18 steel post-treated with HCPEB irradiations under heating mode [95]. By applying just several pulses, the composition profile of the initial implanted Ti could change significantly. Numerical simulation was carried out to describe the enhanced diffusion effect. It was shown that the reduced diffusion activation energy is one of the main reasons that lead to the enhanced diffusion. This decrease is related to high concentrations of non-equilibrium defects, for instance, vacancies, induced by the HCPEB irradiation post-treatment [92,93].

To study the enhanced diffusion effect, we have also carried out rapid surface alloying on FeAl with carbon, for which a graphite powder was spread onto the sample surface before the HCPEB irradiation. The sample was then treated by HCPEB with 2 pulses. For comparison, a reference sample was also treated with the same condition but without graphite powders on it. Fig. IV-7 shows a cross section hardness profile versus depth. It shows clearly the stronger effect - an increase of more than 100HV - associated with the thermally enhanced solid state diffusion of C on alloying and hardening the surface compared with the directly treated sample. This could be directly due to the diffusion of the C atoms in the FeAl cell, as it is established that C atoms do strengthen the atomic binding [172], or to the precipitation of carbides [173].

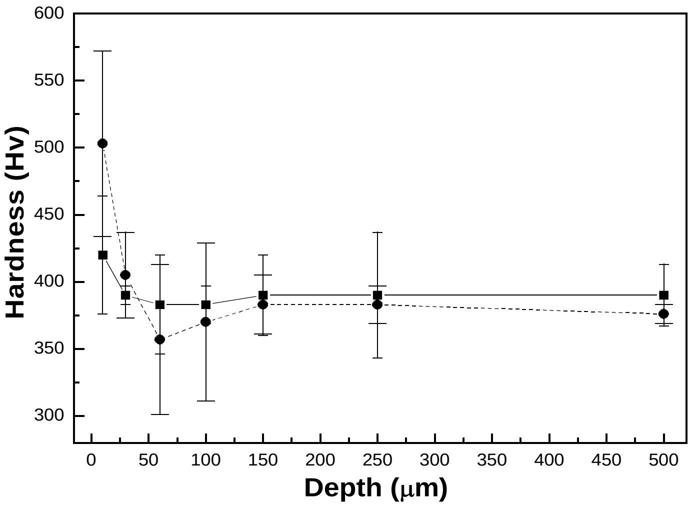

Fig. IV-7 Effect of the HCPEB treatment on hardening the Fe-40Al intermetallic. Samples treated for 2 pulses with (rounded symbols) and without (squared symbols) the presence of a previously deposited graphite layer.

IV. 4 Improving corrosion resistance

It was recently demonstrated that selective purification as well as homogenization in the melted layer generate higher corrosion resistances of the precipitate containing materials [114]. This is for example illustrated in Fig. IV-8 for the case of the 316L stainless steel. The electrolyte solution was the Tyrode's simulated body fluid (TSBF). Clearly, both the open circuit potential (E_{cor}) and the corrosion current density at the passive state (I_p), are improved, showing the better corrosion resistance after the HCPEB treatment.

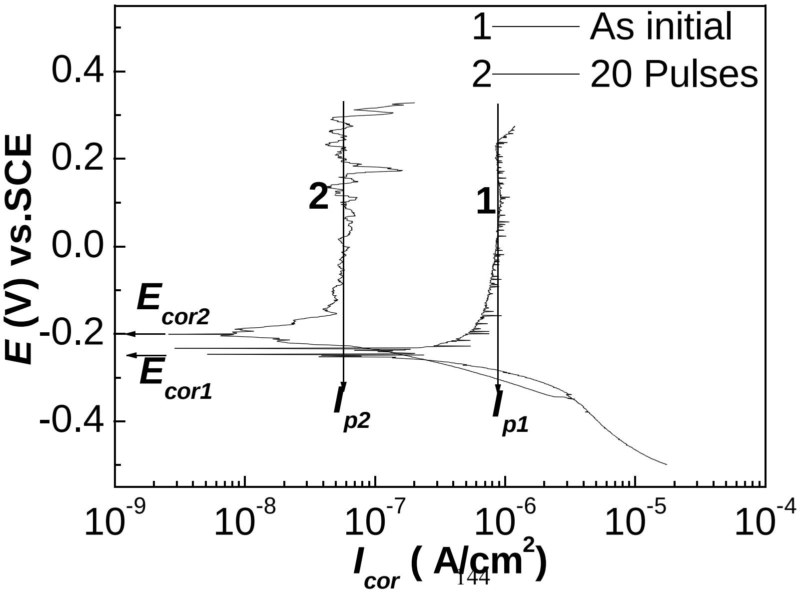

Fig. IV-8 Potentiodynamic polarization curves of 316L stainless steel sample in Tyrode's simulated body fluid before and after HCPEB with 20 pulses.

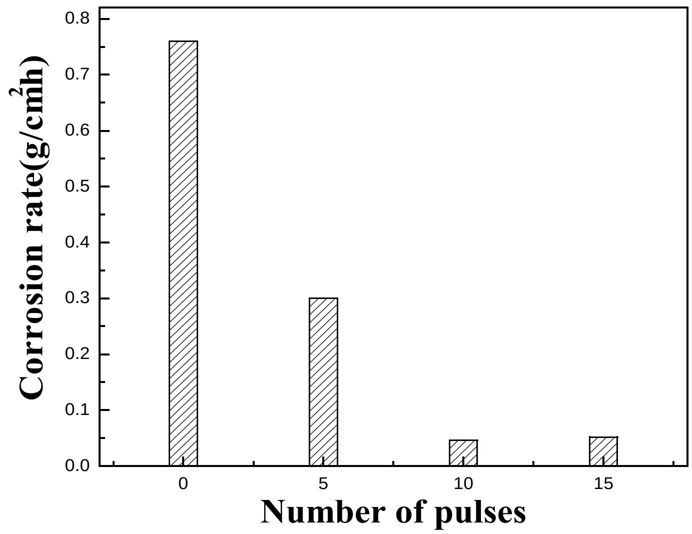

Fig. IV-9 Evolution of the corrosion rate with the number of pulses for the case of HCPEB treated Mg AZ91 HP alloy.

Fig. IV-9 gives the result of 5% NaCl immersion test of a Mg alloy AZ91HP before and after HCPEB treatments [161]. The average corrosion rate decreased after HCPEB treatment and the best corrosion resistance is found for the sample treated with 10 pulses, which is an order of magnitude lower than that of the untreated sample. According to the structural analysis, the existence of dense MgO layer can have a positive effect on the improved corrosion resistance of the treated sample. Also, the disappearance of the second phase $Mg_{17}Al_{12}$ in the melted layer increases Al concentration in surface layer. This over saturated solution favors the formation of a homogenous passive film during corrosion process and thereby improves the corrosion resistance of the treated samples.

As was shown before, HCPEB treatment under evaporating mode can effectively change the surface chemistry of the treated materials [111,112,122]. In the case of NiTi alloy, Ti concentration increases in the surface layer as a result of selective evaporation. Such a modification in surface chemistry may significantly change the corrosion behaviors of the treated materials. As an example, the potentiodynamic polarization curves of the untreated and HCEPB treated NiTi with 5 pulses under evaporating mode in the simulated body fluid are given in Fig. IV-10. An obvious difference lies in the open circuit potential E_{corr} for the samples that have been immersed in TSBF for 30 minutes. For the initial sample, E_{corr}= -0.339 V. It increased to 0 V after HCPEB treatment. Based on the cathodic part of the polarization curve, the corrosion rate is normally proportional to the calculated corrosion current density. In this case, the corrosion current density (i_{corr}) decreased from 1.1×10^{-7} A/cm^2 for the initial sample to 2.78×10^{-8} A/cm^2 for the treated sample. In short, the polarization curves reveal a significant improvement in the corrosion resistance of NiTi after HCPEB surface treatment. The selective evaporation effect, together with surface purification effect, leads to the formation of a Ti over-saturated solid solution layer containing in the near surface layer. These effects contribute to the improved corrosion resistance of the alloy in the simulated body fluid. It should be recalled that the formation of crater on the surface of HCPEB sample has a deterioration effect on corrosion. Therefore, the best corrosion performance are always obtained after a sufficient number of pulses. Indeed, a good balance must be achieved between the favorable and deterioration factors that can be imparted by the HCPEB treatment on the surface.

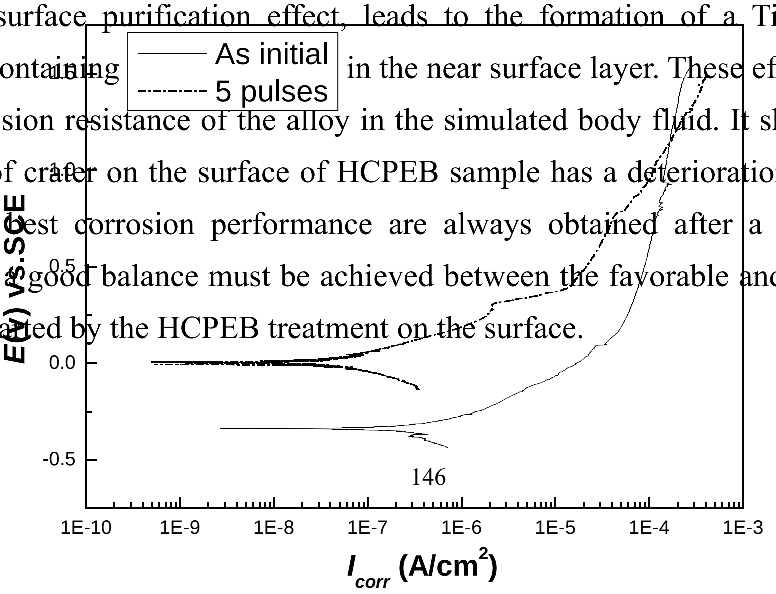

Fig. IV-10 Potentiodynamic curves of the untreated and treated samples in Tyrode’s simulated body fluid.

IV. 5 Improving wear resistance

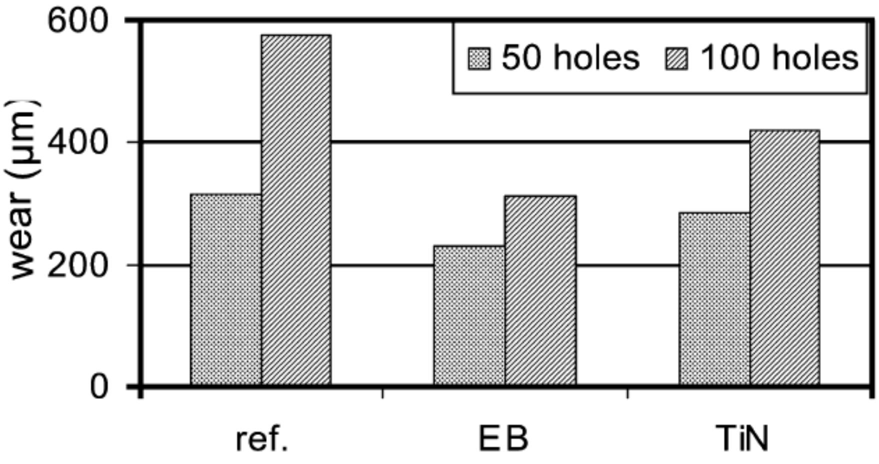

Fig. IV-11 Results of wear resistance of a HCPEB treated S652 steel by drilling tests [152].

It has been already demonstrated in many previous investigations that the wear resistance of various steels and alloys can be significantly improved after HCPEB treatment under melting mode. We have observed that the sliding wear resistance of AISI D2 steel can be improved after HCPEB treatment [79]. In the case of the H13 steel, HCPEB treatments lead also to an improved wear resistance compared to the reference one due to the increased hardness after HCPEB treatment [110]. Ivanov et al. have tested the wear resistance of a HCPEB treated S652 steel by drilling [152]. The results are summarized in Fig. IV-11. The wear resistance of HCPEB treated sample is much higher than that of the reference sample and even lower than that of TiN film coated sample.

Fig. IV-12 gives the evolutions of the friction coefficient measured during fretting wear tests on an untreated D2 steel sample, a sample HCPEB treated with 20 pulses and a sample precoated with Cr powders and HCPEB treated by 10 pulses [174]. A significant difference lies in the starting number of cycles for the severe worn stage can be clearly observed. It can be improved from 60 cycles for the untreated sample to 700 cycles after HCPEB direct treatment and further increased to 1500 cycles after HCPEB surface alloying with Cr. The results revealed a significant improvement in fretting wear resistance of D2 steel after HCPEB treatment.

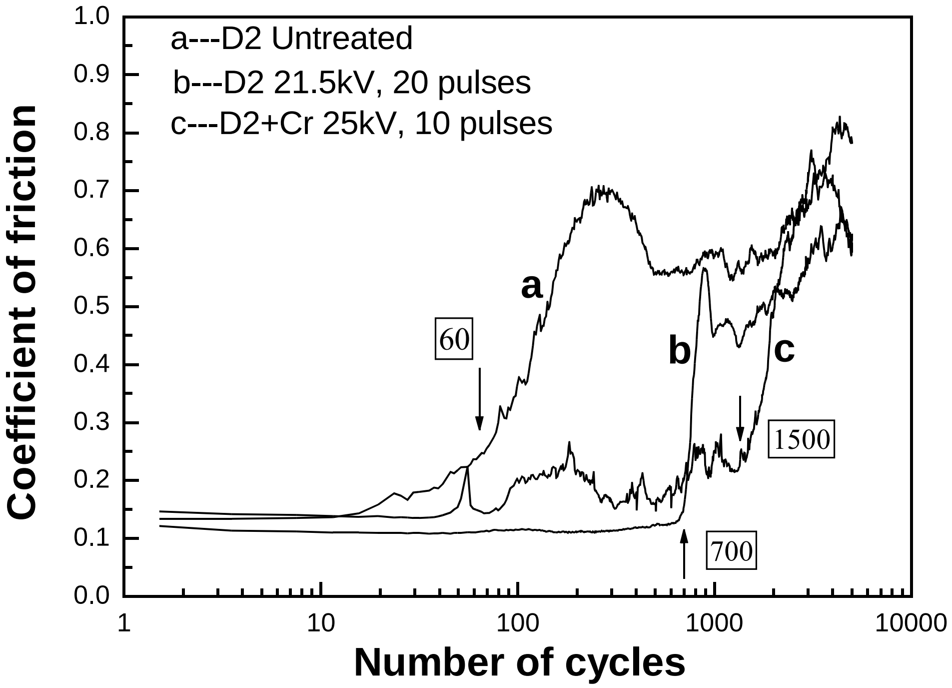

Fig. IV-12 Coefficient of friction vs. number of fretting cycles of the untreated and HCPEB treated D2 steel samples, load : 100N, total number of cycles : 5000, sliding length : 150μm.

Wear tests have also been attempted on a HCPEB treated Mg AZ91HP alloy under melting mode [161]. The sliding wear volume and average friction coefficient were measured for the samples before and after the HCPEB treatment. The results are summarized in Fig. IV-13. The average friction coefficient of the treated samples reduced compared to the original sample. It can be seen that the wear volume reduced from $7.79\times10^{-3}mm^3$ for the untreated sample to $3.29\times10^{-3}mm^3$ for the sample treated with 10 pulses, showing an effective improvement of the sliding wear resistance of Mg alloy AZ91HP after HCPEB treatment. These results can be interpreted as follows: (i) the presence of nanograined MgO on the top surface can have a lubricating effect and improve the wear resistance; (ii) Both the over saturation of Al element in α(Mg) solid solution and deformations in the sub-surface layer induced by stress waves have hardening effects on the surface layers. Because the depth of nanograined MgO is only about tens of nm, it is believed that the increased hardness plays the major role in the improvement of friction and wear properties in this case [161].

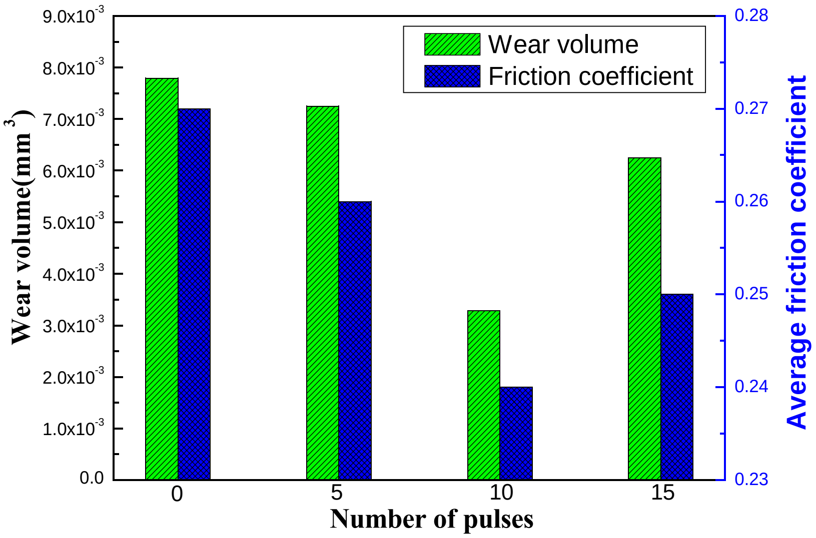

Fig. IV-13 Evolution of the wear volume and the friction coefficient of a HCPEB treated Mg AZ91 HP alloy with the number of pulses.

Under evaporating mode, it is also possible to modify substantially the wear property of the materials. The example shown here is that of a Mg AZ31 alloy [122]. The wear data for the alloy in reciprocating tests are summarized in Fig. IV-14. The wear rate reduces with increasing the number of HCPEB pulses. The difference is quite drastic from the untreated sample to the 10-pulsed treatment. The best result was obtained for the 15-pulsed treatment; with an improvement in wear resistance by a factor of 6.7. Due to the increase in hardness, the friction coefficient values were lowered by more than 20% after the HCPEB treatments. In all cases abrasive wear was encountered but the wear resistance was drastically improved after the HCPEB treatments. The best wear resistance was observed for the 15-pulsed treatment, with an improvement by more than a factor of 6 over the starting material [122].

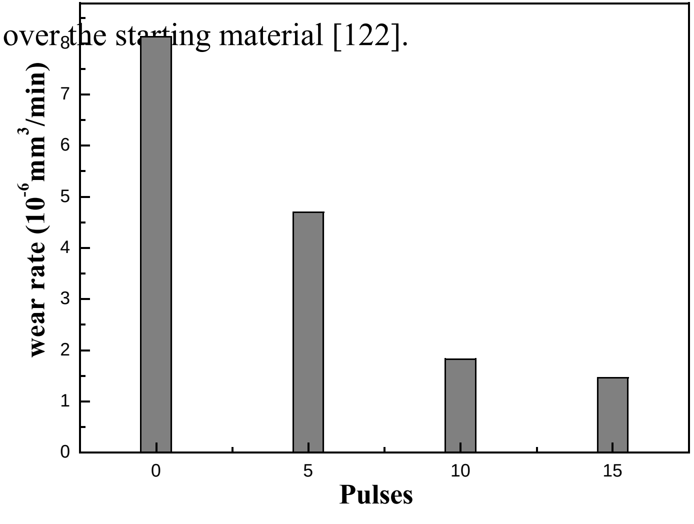

Fig. IV-14 Evolution of the wear volume of a HCPEB treated Mg AZ31 alloy HCPEB treated under evaporating mode as a function of the number of pulses [122].

Chapter V Conclusion and perspectives

V. 1 Summary

Recent development and research work carried out using the fairly recently developed HCPEB technique have been reviewed by underlying its effects under the “melting”, “heating” and “evaporating” treatment modes.

At first, different physical models for the HCPEB treatment of materials under the three different treatment modes have been proposed.

The results of calculations concerning the heating mode have revealed that (i) the quasi-static thermal stress is orientation dependent and has an amplitude of several hundred MPa, which is enough to induce significant plastic deformation; (ii) the amplitude of the thermal stress wave is only about several hundred kPa, which in many cases can be omitted. Thereby, this suggests that the quasi-static thermal stress together with the fast thermal cycle should make it possible to modify substantially the surface layers under the heating mode.

Calculations concerning the melting mode have shown that (i) the melting starts from the subsurface, (ii) the depth of the melted layer – which was in good agreement with the experimental observations - depends on the material properties and input electron beam power and (iii) the melt solidifies at a speed of several m/s. The subsurface melting is one of the factors inducing the formation of craters and shock waves. The rapid solidification authorizes the homogenization of the melted layer and specific grain growth behaviors.

Concerning the evaporating mode, the model can describe quantitatively the whole evaporation process and the depth of evaporated layer. Therefore, these models have been demonstrated to be useful tools to give new insight in the understanding of the phenomena induced by the HCPEB treatment.

Subsequently, the intriguing surface modifications associated with the HCPEB treatment were detailed. Techniques such as TEM, SEM, EBSD, X-ray diffraction and SNMS can be used, in a complementary manner, to analyze accurately the surface and subsurface modifications encountered in the materials. Some of the different features observed under the three modes are in the following 3 parts.

a) The major results corresponding to materials treated under the melting mode are :

1. Homogenization of the melted layer.

The high-current pulsed electron beam is demonstrated to be an effective way to achieve surface homogenization of metallic materials containing precipitates/inclusions. The treatment induces the formation of craters by eruptions of the second phase inclusions that lead to a selective purification of the surface melted layer. The associated reduction of the inclusion density reduces the occurrence of the eruption events on the sample surface. Ultimately, after sufficient number of pulses, this leads to the formation of a homogeneous – almost crater free-surface.

2. Ultra fine grain and nanostructure formations.

The results gathered here show the very strong potential for surface nanocystallization of materials with improved properties by HCPEB technique. The mechanisms were identified to produce ultra fine microstructures from the melted liquid by taking advantage of the rapid solidification from the melt as well as solid state martensitic transformation in steels.

3. Metastable phase formations.

The rapid thermal cycles generated by the HCPEB treatment has the potential of generating metastable structures. This was particularly detailed in the case of different steels. For example, austenite was retained at room temperature in the D2 steel treated by HCPEB due to the stabilization from high Cr and C content and the grain size effect. Different solidification paths and following solid state transformation paths were observed in the same treated surface layer when the chemical composition of the melt was not homogeneous. For example, ultra fine structure of mixed δ ferrite, austenite and martensite were found in the HCPEB treated H13 steel sample. This shows the strong impact of initial composition on the final microstructure after HCPEB treatment.

4. Formation of specific textures.

The HCPEB irradiation has induced ultra fine grain structures with specific texture states in the melted surface layers of both (i) the metastable *fcc* austenite in a D2 steel and (ii) the stable B2 matrix of a NiTi shape memory alloy. In both cases, rapid solidification of the supersaturated phases has led to a mixed <100> (weak) + <110> (strong) parallel to ND fiber texture to which was associated a high portion of twin boundaries. The formation of twin boundaries is likely to play a major role in the growth mechanisms of the highly undercooled melt that determines the presence of the final <110> texture.

5. Surface alloying.

Surface alloying by HCPEB under melting mode is an efficient way for improving the surface properties of materials. For this purpose, other coating techniques were combined with HCPEB post treatments. The material pre-deposited on the surface can be rapidly mixed into the substrate during melting. This led to the modification of structure, phase and compositions in the surface layer.

6. Subsurface hardening.

On the basis of a description of the transient thermo-mechanical processes associated with the HCPEB bombardment, it is pointed out that the deep modification effect are caused by the stress wave originated from the quasi-static stress and sublayer melting. The intense stress wave interacts and modifies the structure and properties over a depth zone of a few hundreds micrometers, far beyond the heat-affected zone.

b) Under the combined action of the temperature and stress fields, significant modification of the microstructures and compositions were also demonstrated to take place at the surface without any melting. The main findings obtained under the so-called heating mode are :

1. Effectiveness of the thermomechanical cycles.

It is clear that the HCPEB irradiation induces a dynamic temperature field in the surface of the material and that, concomitantly to the thermal effect, the pulse electron beam creates a dynamic stress field that causes intense deformation at the material surface and sub-surface. The deformation is demonstrated to be orientation dependent and formed under the biaxial quasi-static thermal stress occurring during the HCPEB bombardment. For the 316L stainless steel, twinning was activated in grains having <111> close to ND while high misorientation deformation gradients were created by intense crystallograplic slip in the other grains. For the FeAl intermetallic, local strain resulted in those grains having <100> close to ND to be at a lower level on the surface than the other grains.

2. Texture modification and grain refinement.

The surface of an initially extruded FeAl sample characterised by a sharp <110> fiber texture parallel to the sample normal direction was modified towards a broader <321> fiber. Together with the texture evolution, a grain refinement effect was observed. Both effects are due to the formation of new (low angle) grain boudaries induced by the repeated cycles of deformation and dynamic recovery/recrystallization during the HCPEB treatment.

3. Surface purification.

Surface purification in particle reinforced alloys can also occur when the material is treated under the heating mode. As shown in the case of a Y_2O_3 oxide strengthened Fe (40at%)Al alloy, the oxide particles were evaporated and removed by HCPEB treatment without any melting of the FeAl matrix.

c) The effect of the HCPEB treatment for modifying the surfaces of materials under evaporating mode has also been clearly established. The occurrence of significant evaporation at the top melted surface and re-condensation was highlighted by a physical model established for modeling the evaporating mode. The main features generated by the evaporating mode are :

1. Surface aspect modification.

In addition to the formation of craters, the action of the electron beam under evaporating mode is also to modify the surface morphology by forming a wavy aspect on the surface. This wavy aspect is the consequence of the combination of (i) melting and subsequent selective "local" evaporation and (ii) deformation in the melted layer operating at the surface of the alloys.

2. Selective evaporation.

The evaporation mode can generate the selective evaporation of some species at the surface of the treated alloys. The physical model proposed to describe this selective evaporation gave simulated composition profiles in fairly good agreement with the experimental ones at the beginning of the evaporation process.

3. Evaporation/condensation phenomena.

The effect of the evaporation mode is more pronounced after sufficient number of HCPEB pulses; a stage at which a part of the vapor often recondenses on the treated surface. This is clearly shown by (i) the presence of small protrusions and/or rounded droplets solidified on the wavy surface and (ii) the special composition distributions along depth after intensive evaporation.

4. Special texture modification.

A strong <110> fiber is created in the treated NiTi alloy after HCPEB treatment under evaporating mode due to the rapid solidification and evaporation/condensation mechanisms. Compared to the melting mode, the <110> oriented grains are often isolated island and, when grouped together, are not twinned.

Finally, the last section of this document has concentrated on potential applications of the HCPEB technique to improve the materials' properties. Under all the three treatment modes, HCPEB treatment is proved to be an efficient way to modify the surface of metallic materials to taylor metallic materials' properties. The combination of super fast thermal cycles and dynamic stress fields makes it possible to modify substantially the surface characteristics and, in many cases, improve the mechanical properties faster and more efficiently than other conventional surface treatment techniques. For examples, as a result of the ultra fine structure formations and strain hardening, surface hardness and wear resistance can be effectively improved. Selective surface purification effect can generate surface layers having improved corrosion properties. Other possible applications of the HCPEB technique, for example rapid surface alloying, have been proposed in the literature.

Overall, this review clearly demonstrate that the high potential of the HCPEB technique can be better achieved by a good control of the processing parameter in order to treat the sample surfaces under the most appropriate mode.

V. 2 Concluding remarks and future challenges

The HCPEB surface treatment technique is very new and promising technique which has potential applications in industry and is of great scientific interests. From the investigations carried out in the present study, future works concerning this technique may involve the following aspects :

a) Explore further the potential of the heating mode. Indeed, this versatile treating mode is very interesting and should receive thorough investigations covering its effect on properties going from hardening towards improvements of fatigue properties.

b) The texture modification induced by the HCPEB treatment under different modes were always rather unusual. However, the detailed mechanisms involved during rapid solidification under melting mode, deformation and recrystallization under the heating mode and condensation under the evaporating mode are still missing. To give more insights towards the determination of the exact mechanisms, analysis of HCPEB treated single crystal having different orientations should be carried out.

c) For some special applications, the HCPEB technique may be combined with other techniques as a pre-treatment or post treatment method. For example, HCPEB treatment may be used as pre-treatment to improve the adhesion strength of the films deposited on a given material.

d) The physical models concerning thermal stress fields induced by HCPEB are still not complete, especial when plastic deformation is considered. In fact, the stresses and related deformation procedures during HCPEB treatment are very complicated due to the rapid thermal cycles and the properties of the treated materials. Further study should consider both the anisotropic aspects of the stresses and the plastic deformations.

e) HCPEB surface treatments should be applied to new materials and its potential to create amorphous phases should be tested.

Generally speaking, there are also many other phenomena induced by the HCPEB treatment remaining unknown or poorly understood. New ideas, theories and other characterization techniques could be helpful to improve our understanding of the technique and to obtain its full potential.

VI. References

[1] H. Gleiter : Nanocrystalline materials, *Progress in Materials Science* 33 (1989) 223

[2] M. A. Meyers, A. Mishra, D. J. Benson : Mechanical properties of nanocrystalline materials, *Progress in Materials Science* 51 (2006) 427

[3] H. Gleiter : Nanostructured materials: basic concepts and microstructure, *Acta Materiallia*, 48 (2000) 1

[4] R. S. Mishra, R. Z. Valiev, A. P. Zhilyaev, A. K. Mukherjee, S. X. McFadden : Low-temperature superplasticity in nanostructured nickel and metal alloys, *Nature* 398 (1999) 684

[5] W. P. Tong, N. R. Tao, Z. B. Wang, J. Lu, K. Lu : Nitriding Iron at Lower Temperatures, *Science* 31 (2003) 686

[6] Y. M. Wang, M. W. Chen, F. H. Zhou, E. Ma : High tensile ductility in a nanostructured metal, *Nature* 419 (2002) 912

[7] X. Y. Liu, P. K. Chu, C. X. Ding : Surface modification of titanium, titanium alloys, and related materials for biomedical applications, *Materials Science and Engineering: R: Reports* 47 (2004) 49

[8] A. S. Korhonen, E. H. Sirvio : A new low pressure plasma nitriding method, *Thin Solid Films* 96 (1982) 103

[9] A. Grill, D. Itzhak : Nitriding of AISI M2 tool steel in an inductive r.f. plasma, *Thin Solid Films* 101 (1983) 219

[10] K. Ozbaysal, O. T. Inal, A. D. Romig : Ion-nitriding behavior of several tool steels, *Materials Science and Engineering* 78 (1986) 179

[11] P. Goeuriot, F. Thevenot, J. H. Driver : Surface treatment of steels: Borudif, a new boriding process, *Thin Solid Films* 78 (1981) 67

[12] K. S. Nam, S. R. Lee, K. H. Lee, S. C. Kwon : A study on plasma-assisted boriding of steels,

Surface and Coatings Technology 98 (1998) 886

[13] K. Q. Zheng, S. Y. Zhang : The influence of laser carbo-nitro-boriding on metallic surface properties, *Materials Chemistry and Physics* 24 (1990) 279

[14] B. S. Suh, W. J. Lee : Surface hardening of AISI 316L stainless steel using plasma carburizing, *Thin Solid Films* 295 (1997) 185

[15] J. M. Baek, Y. R. Cho, D. J. Kim, K. H. Lee : Plasma carburizing process for the low distortion of automobile gears, *Surface and Coatings Technology* 131 (2000) 568

[16] N. A. Vitovskii, T. V.Mashovets, O. V. Oganesyan : Influence of the intensity of electron irradiation on the formation of defects in indium antimonide, *Soviet Physics* 12 (1978) 1277

[17] D. K. Das, A. G. Paradkar, R. S. Mishra : Microstructure and creep behaviour of laser surface alloyed aluminium, *Scripta Metallurgica et Materialia* 26 (1992) 1211

[18] W. Ensinger, H. R. Müller : Surface modification and coating of powders by ion beam techniques, *Materials Science and Engineering A* 188 (1994) 335

[19] V. Vassileva, K. Vutova, G. Mladenov : An investigation of the influence of heat transfer on crystallization processes during electron beam melting and casting of metals, *Vacuum* 62 (2001) 197

[20] J. C. Oh, K. Euh, S. Lee : Hardness improvement of TiB_2/Ti surface-alloyed material fabricated by High-Energy electron beam irradiation, *Scripta Materilia* 39 (1998) 1389

[21] S. J. Kwon, S. H. Choo, S. Lee : Hardness improvement of TiC-reinforced ferrous surface composites fabricated by High-energy electron beam irradiation, *Scripta Materilia* 40(1999) 235

[22] Lyutovich, K. Maile, A. Gusko, Kh. Ashurov, S. Morozov : Characterisation of the generation of ions in electron beam evaporator for the control of metal deposition processes, *Surface and Coatings Technology* 151-152 (2002) 105

[23] Z. G. Song, C. K. Tong, H. Gong : Secondary and backscattered electron yields of polymer

surface under electron beam irradiation, *Applied Surface Science* 119 (1997) 169

[24] A. Belattar, G. A. Stephens, P. D. Cardwell : Ion beam annealing effects of surface amorphous layers produced by Sb implanted <100>Ni using 1.5 MeV Xe^+ and Ar^+ ion beams, *Nuclear Instruments and Methods in Physics Research Section B* 93 (1994) 261

[25] L. Guzman, S. Tuccio, A. Miotello, N. Laidani, L. Calliari, D. C. Kothari : Improvement in mechanical properties by ion implantation of SiC films deposited on steel and copper, *Surface and Coatings Technology* 66 (1994) 458

[26] T. Kwok, K. I. Leong, F. T. Cheng, H. C. Man : Microstructural and corrosion characteristics of laser surface-melted plastics mold steels, *Materials Science and Engineering A* 357 (2003) 94.

[27] H. C. Man, Z. D. Cui, T. M. Yue, F. T. Cheng : Cavitation erosion behavior of laser gas nitrided Ti and Ti6Al4V alloy, *Materials Science and Engineering A*, 355 (2003) 167

[28] Y. T. Xie, X. Y. Liu, A. P. Huang, C. X. Ding, P. K. Chu : Improvement of surface bioactivity on titanium by water and hydrogen plasma immersion ion implantation, *Biomaterials* 26 (2005) 6129

[29] T. Yamada, K. Miura : Water adsorption on electron irradiated NaF(001) surface, *Applied Surface Science* 130-132 (1998) 598

[30] S.J. Kwon, S. H. Choo, S. Lee : Hardness improvement of TiC-reinforced ferrous surface composites fabricated by high-energy electron beam irradiation, *Scripta Materialia* 40 (1998) 235

[31] G. Mladenov, K. Vutova, S. Wojcicki : Experimental investigation of the weld depth and thermal efficiency during electron beam welding, *Vacuum* 51(1998) 231

[32] M. Wykes, C. Punshon, L. Jones : All-position reduced pressure electron beam welding for large fusion containment vessels, *Fusion Engineering and Design* 58-59 (2001) 793

[33] J. C. Ion, H. R. Shercliff, M. F. Ashby : Diagrams for laser materials processing, *Acta Metallurgica et Materialia* 40 (1992) 1539

[34] T. J. Lienert, E. D. Brandon, J. C. Lippold : Laser and electron beam welding of SiCp reinforced aluminum A-356 metal matrix composite, *Scripta Metallurgica et Materialia* 28 (1993) 1341

[35]E. Koleva : Statistical modeling and computer programs for optimization of the electron beam welding of stainless steel, *Vacuum* 62(2001) 151

[36] G. M. S. de Silva, J. A. Leather, J. C. Anderson : The fabrication of foil masks using laser cutting, *Thin Solid Films* 77 (1981) 341

[37] B.S. Yilbas, M. Sami, J. Nickel, A. Coban, S.A.M. Said : Introduction into the electron beam welding of austenitic 321-type stainless steel, *Journal of Materials Processing Technology* 82 (1998) 13

[38] B. A. Movchan, Electron-beam melting and evaporation of metals and non-metals, *Vacuum*, 32 (1982) 567

[39] R. K. Brow : Electron beam reduction of sodium-containing glass surfaces, *Journal of Non-Crystalline Solids* 175 (1994) 155

[40] P. Petrov : Electron beam surface remelting and alloying of aluminium alloys, *Vacuum* 48 (1997) 49

[41] D. K. Winslow : The current in magnetically focused, modulated electron beams, microwave lab. rep. No 380, Stanford university, 1957

[42] J. T. Senise : Note on Positive-Ion Effects in Pulsed Electron Beams, *J. Appl. Phys.* 29 (1958) 839

[43] G. G. Isaacs : High-power pulsed electron beam from a glow discharge, *Electron. Lett.* 3 (1967) 542

[44] P. A. Bokhan, G. V. Kolbychev : Generation of high-current pulsed electron beams in a gas

at intermediate pressure, *Sov. Phys. Tech. Phys*. 26 (1981) 1057

[45] Y. Yamamoto, T. Inada, T. Sugiyama, S. Tamura : Pulsed electron beam annealing of arsenic-implanted silicon, *J. Appl. Phys.* 53 (1982) 276

[46] E. F. Kennedy, S. S. Lau, I. Golecki, J. W. Mayer, W. Tseng, J. A. Minnucci, A. R. Kirkpatrick : Pulsed electron beam annealing of ion implanted Si layers, *AIP Conf. Proc.* 50 (1979) 470

[47] N. C. Schoen : Thermoelastic stress analysis of pulsed electron beam recrystallization of ion-implanted silicon, *J. Appl. Phys.* 51 (1980) 4747

[48] T. I. Kolchenko, V. M. Lomako : Introduction and annealing of defects in n-type GaAs following irradiation with electrons and gamma rays, *Radiation Effects* 37 (1978) 67

[49] M. Zdzislaw, N. Brett, P. Krishnamachar : Effect of scanning electron beam annealing on the reverse current in Ti-GaAs schottky diodes, *Japanese Journal of Applied Physics, Part 2: Letters* 27 (1988) 704

[50] R. G. Little, A. C. Greenwald, J. A. Minnucci : Pulsed electron beams for annealing of ion-implanted silicon, *IEEE Transactions on Nuclear Science* 26 (1978) 1683

[51] A. Kawasuso, M. Hasegawa, M. Suezawa : An annealing study of defects induced by electron irradiation of Czochralski-grown Si using a positron lifetime technique, *Applied Surface Science* 85 (1995) 280

[52] G. Lulli, P. G. Merli : Electron beam annealing of semiconductors by means of a specifically designed electron gun, *Materials Chemistry and Physics* 9 (1982) 285

[53] J. L. Tandon, I. Golecki, M-A. Nicolet, D. K. Sadana, J. Washburn : Pulsed electron beam induced recrystallization and damage in GaAs, *Appl. Phys. Lett.* 35 (1979) 867

[54] C.A. Brau, J. L. Raybun, J. B. Dodge, F. M. Gilman : Simple, pulsed, electron beam gun, *Rev. Sci. Instrum.* 48 (1977) 1154

[55] Lü Chuanxin et al. : A 10^{11}W high current pulse electron beam accelerator, *Nucl. Fus.*

Plasma Phys. 3 (1983) 235

[56] G. A. Mesyats, D. I. Proskurovsky, V. P. Rotshtein, N. I. Lebedeva : Low-energy, high-density pulsed electron beam for surface heating, *Sov. Phys. Dokl.* 25 (1980) 650

[57] S. N. Makeev, S. B. Seleznev, O. I. Shmid : Thresholds and properties of damage produced by pulsed electron beams in piezoelectric ceramic materials, *Sov. Phys. Tech. Phys.* 28 (1983) 847

[58] M. Tholomier, M. Pitaval, M. Ambri, D. Barbier, A. Laugier : Electron microscopy studies of pulsed electron beam annealing in phosphorus-implanted silicon, *J. Appl. Phys.* 54 (1983) 1588

[59] D. M. Follstaedt, W. R. Wampler : Vacancies in Al after pulsed electron beam melting, *Appl. Phys. Lett.* 38 (1981) 140

[60] J. A. Knapp, D. M. Follstaedt : Rapid e-beam heating for studying metastable transitions in Mn, *J. Mater. Res.* 4 (1989) 1393

[61] V. Engelko, B. Yatsenko, G. Mueller, H. Bluhm : Pulsed electron beam facility (GESA) for surface treatment of materials, *Vacuum* 62 (2001) 211

[62] G. Mueller, V. Engelko, A. Weisenburger, A. Heinzel : Surface alloying by pulsed intense electron beams, *Vacuum* 77 (2005) 469

[63] V. Engelko, G. Mueller : Influence of particle fluxes from a target on the characteristics of intense electron beams, *Vacuum* 62 (2001) 97

[64] X. L. Jiang, K. F. Chen, et al. : A New Type of Pulsed Electron and Ion Beam Source with the Duration of Nanoseconds, *Acta Physica Sinica* 32 (1983) 1344

[65] X. L. Jiang, N.Xu : The Multi-Beam Generator With Multi-plate Chamber, *Rev. Sci. Instrum*. 61 (1990) 644

[66] X. L. Jiang, N. Xu : Preparation of Dense Films of Crystalline ZrO2 by Intense Pulsed Eleectron-beam Ablation, *J. Appl. Phys*. 66 (1990) 5594

[67] D. I. Proskurovsky, V. Rotshtein, G. E. Ozur, A. B. Markov, D. S. Nazarov : Pulsed electron beam technology for surface modification of metallic materials, *J. Vac. Sci. Tech. A.* 1694 (1998) 2480

[68] D. I. Proskurovsky, V. P. Rotshtein, G. E. Ozur : Pulsed Electron-beam technology for surface modification of metallic material, *Surface and Coatings Technology* 96 (1997) 117

[69] D. I. Proskurovsky, , V. P. Rotshtein, G. E. Ozur : Physical foundations for surface treatment of materials with low energy, high current electron beams, *Surface and Coatings Technology* 125 (2000) 49

[70] Y. F. Ivanov, V. P. Rotshtein, D. I. Proskurovsky : Pulsed electron-beam treatment of WC–TiC–Co hard-alloy cutting tools: wear resistance and microstructural evolution, *Surface and Coatings Technolog* 125 (2000) 251

[71] A. D. Pogrebnjak, S. M. Duvanov, A. D. Mikhaliov : Surface and near surface structure and composition of high-dose implanted and electron beam annealed single crystal copper, *Surface and Coatings Technology* 89 (1997) 90

[72] A. B. Markov, V. P. Rotshtein : Calculation and experimental determination of dimensions of hardening and tempering zones in quenched U7A steel irradiated with a pulsed electron beam, *Nuclear Instr. And Methods in Phys. Research B* 132 (1997) 79

[73] D. I. Proskurovsky, G. E. Ozur, V. P. Rotshtein : Production and application of low-energy, high-current electron beams, *IEEE International Conference on Plasma Science*, Jun 4-Jun 7, 2000 : 285

[74] V. V. Efimov, E. A. Efimova, K. Iakoubovskii, S. Khasanov, D. I. Kochubey, V. V. Kriventsov, A. Kuzmin, B. N. Mavrin, M. Sakharov, V. Sikolenko : EXAFS, X-ray diffraction and Raman studies of $(Pb_{1-x}La_x)(Zr_{0.65}Ti_{0.35})O_3$ ($\boldsymbol{x}$=0.04 and 0.09) ceramics irradiated by high-current pulsed electron beam, *Journal of Physics and Chemistry of Solids*

67 (2006) 2007

[75] A. N. Valyaev, M. K. Kylyshkanov, A. D. Pogrebnjak : Modification of mechanical and tribological properties of R6M5 steel and Be by intense pulsed-ion and Pulsed-electron beams, *Vacuum* 58 (2000) 53

[76] A.B. Markov, V. P. Rotshtein : Calculation and experimental determination of dimensions of hardening and tempering zones in quenched U7A steel irradiated with a pulsed electron beam, *Nucl. Instr. and Meth. in Phys. Res. B.* 132 (1997) 79

[77] A. D. Pogrebnjak, S. Bratushka, V. I. Boyko, I. V. Shamanin, Yu. V. Tsvintarnaya : A review of mixing processes in Ta/Fe and Mo/Fe systems treated by high current electron beams, *Nucl. Instr. and Meth. in Phys. Res. B.* 145 (1998) 373

[78] G. E. Ozur,; D. I. Proskurovsky, V. P. Rotshtein, Production and application of low-energy, high-current electron beams, *Laser and particle beams* 21 (2003) 157

[79] C. Dong, A. M. Wu, S. Z. Hao, J. X. Zou, Z. M. Liu et al. : Surface treatment by High-Current Pulsed Electron Beam, *Surface and Coatings Technology*, 163-164 (2003) 620

[80] Y. Qin, J. X. Zou, C. Dong, X. G. Wang, S. Z. Hao, A. M. Wu, Y. Liu : Temperature stress field and related phenomena induced by a high current pulsed electron beam, *Nucl. Instr. & Meth. In Phys. Res. B* 255 (2004) 544

[81] J. X. Zou, Y. Qin, C. Dong, A. M. Wu, S. Z. Hao, X. G. Wang : Numerical simulation of Thermal-mechanical process during High Current Pulsed Electron Beam (HCPEB) treatment, *J. of Vac. Sci. and Tech. A* 22 (2004) 545

[82] D. B. Williams, C. B. Carter : Transmission Electron Microscopy : A Textbook for Materials Science, Springer, 1st edition (Aug 31 2004)

[83] J. F. Sun, J. J. Huang, J.S. Zhang, A. C. Qiu : Simulation calculation for the energy deposition profile and the transmission fraction of intense pulsed electron beam at various incident angles, *High power laser and particle beams* 5 (2002) 87

[84] S. Z. Hao, B. Gao, A. M. Wu, J. X. Zou, Y. Qin, C. Dong, J. An, Q. F. Guan : Surface modification of steels and magnesium alloy by high current pulsed electron beam, *Nucl. Instr. & Meth. In Phys. Res. B* 240 (2005) 646

[85] S. Z. Hao, S. Yao, J. Guan, A. M. Wu, P. Zhong, C. Dong : Surface treatment of Al by high current pulsed electron beam, *Current Appl. Phys.* 1 (2001) 203

[86] P. Baeri, S. U. Campisano, G. Foti, E. Rimini : A melting model for pulsing-laser annealing of implanted semiconductors, *J. Appl. Phys.* 50 (1979) 788

[87] Z. D. Yan, H. L. Wang : Thermal stress (Chinese) Beijing: High Education Press, 1993, 275

[88] R. Q. Jiang : Transient impact effects in thermal conductivity, mass diffusion and moment transition (Chinese). Beijing: Sci. Press, 1997, p110

[89] X. Y. Le, S. Yan, W. J. Zhao, B. X. Han, Y. G. Wang, J. M. Xue : Computer simulation of thermal–mechanical effects of high intensity pulsed ion beams on a metal surface, *Surface and Coating Technology* 128-129 (2000) 381

[90] I. C. Noyan, J. B. Cohen : Residue Stress, Springer, 1987

[91] H. X. Che : Anisotropic elasticity of metals, Beijing: matellugical industry press, 1996, p74

[92] A. D. Pogrebnjak, et al. : Evolution of vacancy defects and dislocations in surface layers of iron as a result of pulsed electron beam treatment, *Physics letters A* 241 (1998) 357

[93] A. D. Pogrebnjak, V. S. Ladysev, N. A. Pogrebnjak : A comparison of radiation damage and mechanical and tribological properties of a-Fe exposed to intense pulsed electron beam, *Vacuum* 58 (2000) 45

[94] T. L. Warren, M. J. Forrestal : Effect of strain hardening and strain rate sensitivity on the

penetration of aluminium targets with spherical-nose rods, *Int. J. Solids and structures* 35 (1998) 3737

[95] Z. M. Liu, S.Z. Hao, W.D. Shi, L. Chen, C. Dong : Post-treatment of Ti-implanted 9Cr18 steel using pulsedhigh current electron beam (HCPEB), *Nucl. Technol.* 23 (2000) 447

[96] Y. Bo, D. W. Wang, C. T. Ying : Numerical analysis of metal melting and evaporating with liquid surface depression, *Acta Physica Sinca* 53 (6) (2004) 1887

[97] J. X. Zou, T. Grosdidier, K. M. Zhang, C. Dong : Mechanisms of nanostructures and metastable phase transformations in the surface melted layer of a HCPEB treated D2 steel, *Acta Materialia* 54 (2006) 5409

[98] K. M. Zhang, J. X. Zou, T. Grosdidier, C. Dong, D. Z. Yang : Improved pitting corrosion resistance of AISI 316L stainless steel by high current pulsed electron beam treatment, *Surface and Coatings Technology* 201 (2006) 1393

[99] Q. P. Meng, Y. H. Rong, T. Y. Hsu : Nucleation barrier for phase transformations in nanosized crystals, *Phys. Rev. B.* 65 (2002) 174118

[100] Q. Meng, N. Zhou, Y. Rong, S. Chen, T. Y. Hsu, X. Zuyao : Size effect on the Fe nanocrystalline phase transformation, *Acta Materialia*, *Volume 50, Issue 18*, *28 October 2002*, *Pages 4563-457*

[101] T. Y. Hsu : Martensitic transformation under stress, *Materials Science and Engineering A 438-440 (2006) 64*

[102] Q. F. Guan, H. Zou, A. M. Wu, S. Z. Hao, J. X. Zou, Y. Qin, Q. Y. Zhang, C. Dong, Nanostructure and amorphous state in low carbon steel induced by HCPEB treatment, *Surface and Coatings Technology* 183 (2005) 261

[103] J. X. Zou, T. Grosdidier, K. M. Zhang, C. Dong, Y. Qin, S. Z. Hao, Q. F. Guan : Surface nanostructures induced by high current pulsed electron beam irradiation. CISGM 4 2006, May 4-7, Algiria. *Algerian Jounal of Advanced Materials* 3 (2006) 401

[104] J. X. Zou, T. Grosdidier, C. Dong, Surface treatment of carbon steels by HCPEB, In preparation

[105] T. Grosdidier, E. Gautier, Y. Combres, M. J. Philippe : Effect of microstructure variation on the formation of deforemation induced martensite and associated tensile properties in metastable Ti alloy, *Metall. Mater. Trans. A.* 31 (2000) 1095

[106] G. K. Kariofillis, G. E. Kiourtsidis, D. N. Tsipas : Corrosion behaviour of borided AISI H13 hot work steel, *Surf. Coat. Tech.* 201 (2006) 19

[107] M. Ueda, C. Leandro, H. Reuther, C.M. Lepienski : Plasma immersion ion implantation of nitrogen into H13 steel under moderate temperatures, *Nucl. Instr. and Meth. in Phys. Res. B.* 240 (2005) 204

[108] K.A. Chiang, Y. C. Chen : Laser surface hardening of H13 steel in the melt case, *Materials Letters* 59 (2005) 1919

[109] X. B. Hua, L. Lia, X. C. Wu, M. Zhang : Coarsening behavior of $M_{23}C_6$ carbides after ageing or thermal fatigue in AISI H13 steel with niobium, *International Journal of Fatigue* 28 (2006) 175

[110] J. X. Zou, T. Grosdidier, C. Dong, Mechanisms of heterogeneous structure formation induced by high current pulsed electron beam (HCBED) surface treatment in an AISI H13 steel, Submitted

[111] K. M. Zhang, J. X. Zou, T. Grosdidier, N. Gey, S. Weber, D. Z. Yang, C. Dong : The mechanisms of structural evolutions associated with high current pulsed electron beam treatment of a NiTi shape memory alloy, *Journal of Vacuum Science and Technology A* 25 (2007) 28

[112] K. M. Zhang, D. Z. Yang, J. X. Zou, T. Grosdidier, C. Dong : Improved in vitro corrosion resistance of a NiTi alloy by high current pulsed electron beam, *Surface and Coatings Technology* 201 (2006) 3096

[113] K. M. Zhang, J. X. Zou, T. Grosdidier, N. Gey, S. Z. Hao, C. Dong, D. Z. Yang : Surface modification of Ni(50.6at%)Ti alloy by high current pulsed electron beam treatment, *Journal of Alloys and Compounds* 434-435 (2007) 682

[114] J. X. Zou, K. M. Zhang, C. Dong, Y. Qin, S. Z. Hao, T. Grosdidier : Selective surface purification via crater eruption under pulsed electron beam irradiation, *Applied Physics Letters* 89 (2006) 041913

[115] V. A. Shulov, N. A. Nochovnaia, G. E. Remnev : The effect of crater creation on the fatigue strength and corrosion resistance of steels and titanium alloys irradiated by high-power pulsed ion beams, *Surface and Coatings Technology* 158-159 (2002) 488

[116] S. Yan, X.Y. Le, W. J. Zhao, J. M. Xue, Y.G. Wang : A possible thermodynamic mechanism of craters formation on metal surfaces caused by intense pulsed ion beams, *Surface and Coatings Technology* 193 (2005) 69

[117] J. X. Zou, K. M. Zhang, T. Grosdidier, C. Dong, D. Z. Yang : Orientation dependent deformation on 316L stainless steel induced by high current pulsed electron beam irradiation, *Materials Science and Engineering A*, 2007, Accepted

[118] J. X. Zou, T. Grosdidier, K. M. Zhang, C. Dong : Deformation related microstructure modifications on 316L stainless steel induced by high current pulsed electron beam irradiation, In preparation

[119] T. Thordarson, G. Larsen : Volcanism in Iceland in historical time: Volcano types eruption styles and eruptive history, *Journal of Geodynamics* 43 (2007) 118

[120] O. Dirksen, M.C.S. Humphreys, P. Pletchov, O. Melnik, Y. Demyanchuk, R. S. J. Sparks, S. Mahony : The 2001–2004 dome-forming eruption of Shiveluch volcano, Kamchatka: Observation, petrological investigation and numerical modeling. *Journal of Volcanology and Geothermal Research* 155 (2006) 201

[121] Y. Qin, C. Dong, X. G. Wang, S. Z. Hao, A. M. Wu, J. X. Zou, Y. Liu : Temperature profiles and crater formations induced in high-current pulsed electron beam processing, *Journal of Vacuum Science & Technology A* 21(6) (2003) 1934

[122] B. Gao, S. Z. Hao, J. X. Zou, T. Grosdidier, L. M. Jiang, C. Dong, J. Y. Zhou : High current pulsed electron beam treatment of AZ31 Mg alloy, *Journal of Vacuum Science & Technology A* 23 (6) (2005) 1548

[123] B. Gao, PhD Thesis of Dalian University of Technology, 2006

[124] M. P. Ryan, D. E. Williams, R. J. Chater, B. M. Hutton, D. S. McPhail : Why stainless steel corrodes, *Nature* 415 (2002) 770

[125] R. C. Newman : Beyond the kitchen sinks, *Nature* 415 (2002) 743

[126] V. Hays, R. Le Gall, G. Saindreman, D. Roptin : Use of AES to Determine Low Solubilities of Impurities: Case of MnS in Austenitic Stainless Steel, *Scrip. Mater.* 38 (1998) 391

[127] R. Hambleton, H. Jones, W.M. Rainforth : Effect of silicon additions on structure and stability of Al-7.5wt.%Mn alloy melt-spun ribbons, *Materials Science and Engineering A* 226-228 (1997) 157

[128] M. J. Aziz : Model for solute redistribution during rapid solidification, *J. Appl. Phys.* 53 (2) (1982) 1158

[129] C. Cayron, E. Rath, I. Cher, S. Launois : Microstructural evolution of Y_2O_3 and $MgAl_2O_4$ ODS EUROFER steels during their elaboration by mechanical milling and hot isostatic pressing *J. Nucl. Mater.* 335 (2004) 83.

[130] T. Grosdidier, E. Suzon, F. Wagner : Primary recrystallization in an ODS FeAl alloy: an effective way to modify texture and microstructure, Intermetallics 12 (2004) 645.

[131] U. F. Kocks, C. N. Tome, H. K. Wenk : Texture and Anisotropy, Cambridge University Press, 1998, p232-235

[132] W. J. Boettinger, S. R. Coriell, A. L. Greer, A. Karma, W. Kurz, M. Rappaz, R. Trivedi : Solidification microstructure: recent developments, future directions, *Acta Mater.* 48 (2000) 43

[133] R. Willnecker, D. M. Herlach, B. Feuerbacher : Grain refinement induced by a critical crystal growth velocity in undercooled melts, *Appl. Phys. Lett.* 56(4) (1990) 324

[134] Q. L. Jin, J. P. Eom, S. G. Lim, W.W. Park, B. S. You : Grain refining mechanism of a carbon addition method in a Mg-Al magnesium alloy, *Scrip. Mater.* 49 (2003) 1129

[135] J. Bratberg, K. Frisk : An experimental and theoretical analysis of the phase equilibria in the Fe-Cr-V-C system, *Metal. Mater. Trans. A.* 35 (2004) 3649

[136] S. Henry, P. Jarry, M. Rappaz : <110> dendritic growth in Aluminum feathery grains, *Metall. Mater. Trans. A* 29 (1998) 2807

[137] T. Haxhimali, A. Karma, F. Gonzales and M. Rappaz : Orientation selection in dendritic evolution, *Nature Materials* 5 (2006) 660

[138] J. X. Zou, T. Grosdidier, B. Bolle, K. M. Zhang, C. Dong : Texture and microstructure at the surface of an AISI D2 steel treated with high current pulsed electron beam, *Metallurgical & Material Transaction A* 2007, In press

[139] H. Jones : Rapid solidification of metals and alloys, institution of metallurgists, London, 1982

[140] A. Semoroz, Y. Durandet, M. Rappaz : EBSD characterization of dendrite growth directions, texture and misorientations in hot-dipped Al–Zn–Si coatings, *Acta Mater.* 49 (2001) 529

[141] E. Ben-Jacob, P. Garik : The formation of patterns in non-equilibrium growth *Nature* 343 (1990) 523

[142] S. Lenhard, F. Wagner, T. Grosdidier, S. Revol, R. Baccino : Proceedings of the 12th international conference on textures of materials (ICOTOM 12), Ottawa, 1 (1999) 683

[143] F. J. Humphreys, M. Hatherly : Recrystallization and Related Annealing Phenomena, Second Edition (Pergamon Materials Series), Pergamon; 2 edition (February 2, 2004)

[144] B. V. Reddy, S. C. Deevi : Thermophysical properties of FeAl (Fe-40 at.%Al), *Intermetallics* 8 (2000) 1369

[145] V. Saravanan, A. Khantachawana, S. Miyazaki : Texture Analysis and Properties of Rapidly Solidified $Ti_{52}Ni_{38}Cu_{10}$ Shape Memory Alloy, *Mater. Trans.* 45 (2004) 208

[146] W. Huang, E. Arimondo : Expansion for cooling an atomic beam, *J. of physics D: Appl. Phys.* 31 (1998) 3218

[147] H. Wu, P. Xu, W. Luo : Application of droplet evaporation model to the expansion cooling of an atomic an atomic uranium beam, *J. of physics D: Appl. Phys.* 26 (1993) 1351

[148] S. Barrat, E. Bauer-Grosse: Prediction of the feasibility of oriented diamond films by microwave plasma-assisted CVD, *Diam. and Relat. Mater.* 4 (1995) 419

[149] V. P. Rotshtein, Yu. F. Ivanov, A. B. Markov, D. I. Proskurovsky, K. V. Karlik, K. V. Oskomov, B.V. Uglov, A.K. Kuleshov, M.V. Novitskaya, S.N. Dub, et al. : Surface alloying of stainless steel 316 with copper using pulsed electron-beam melting of film–substrate system, *Surface and Coatings Technology* 200 (2006) 6378

[150] V. P. Rotshtein, D. I. Proskurovsky, G. E. Ozur, Yu. F. Ivanov, A. B. Markov : Surface modification and alloying of metallic materials with low-energy high-current electron beams, *Surface and Coatings Technology* 180-181 (2004) 377

[151] V. P. Rotshtein, Yu. F. Ivanov, D. I. Proskurovsky, K. V. Karlik, I. A. Shulepov, A. B. Markov : Microstructure of the near-surface layers of austenitic stainless steels irradiated with a low-energy, high-current electron beam, *Surface and Coatings Technology* 180-181 (2004) 382

[152] Yu. Ivanov, W. Matz, V. Rotshtein, R. Günzel, N. Shevchenko : Pulsed electron-beam melting of high-speed steel: structural phase transformations and wear resistance, *Surface and Coatings Technology* 150 (2002) 188

[153] A. J. Perry, J. N. Matossian, S. J. Bull, D. I. Proskurovsky, P. C. Rice-Evans, T. F. Page, D. E. Geist, J. Taylor, J. J. Vajo, R. E. Doty : The effect of rapid thermal processing (RTP) on TiN coatings deposited by PVD and the steel-turning performance of coated cemented carbide, Surface and Coatings Technology, Volumes 120-121, November 1999, Pages 337-342

[154] L.L. Meisner, A.I. Lotkov, V.P. Sivokha, V.P. Rotshtein, E.G. Barmina and Yu.L. Girjakova : Structural-phase condition, unelastic and plastic behavior and nanohardness of the TiNi surface layers modified by an ion- and electron irradiation, *Materials Science and Engineering* A 438-440 (2006) 558

[155] S. Gnyusov, S. Tarasov, Yu. Ivanov, V. Rothstein : The effect of pulsed electron beam melting on microstructure, friction and wear of WC–Hadfield steel hard metal, *Wear* 257 (2004) 97

[156] A. D. Pogrebnjak, N. I. Shumakova **:** Effect of ‘duplex’ treatment on changes of physical and mechanical properties of steel (0.3 wt% C), *Surface and Coatings Technology* 122 (1999) 183

[157] J. An, X.X. Shen, Y. Lu, Y.B. Liu : Microstructure and tribological properties of Al–Pb alloy modified by high current pulsed electron beam, *Wear* 261 (2006) 208

[158] J. An, X.X. Shen, Y. Lu, Y.B. Liu, R.G. Li, C.M. Chen, M.J. Zhang : Influence of high current pulsed electron beam treatment on the tribological properties of Al–Si–Pb alloy, *Surface and Coatings Technology* 200 (2006) 5590

[159] P. W. Wang, K. R. Kimberlin, C. Y. Wang, T. Ying, G. Q. Lin, A. M. Wu, X. J. Jun : Surface cracking of soda lime glass under pulsed high-current electron radiation, *Materials Chemistry and Physics* 94 (2005) 252

[160] S. Z. Hao, P. S. Wu, J. X. Zou, T. Grosdidier, C. Dong : Microstructure evolution occurring

in the modified surface of 316L stainless steel High Current Pulsed Electron Beam Treatment, *Applied Surface Science* 253 (2007) 5349

[161] B. Gao, S. Z. Hao, J. X. Zou, W. Y. Wu, G. F. Tu, C. Dong : Effect of High Current Pulsed Electron Beam Treatment on Surface Microstructure and Wear and Corrosion Resistance of an AZ91HP Magnesium Alloy, *Surface and Coatings Technology* 201 (2007) 6297

[162] J. X. Zou, T. Grosdidier, K. M. Zhang, B. Gao, S. Z. Hao, C. Dong : Microstructures and phase transformations in the surface layer of AISI D2 steel treated with pulsed electron beam, *Journal of Alloys and Compounds* 434-435 (2007) 707

[163] S. Z. Hao, B. Gao, A. M. Wu, J. X. Zou, Y. Qin, C. Dong, Q. F. Guan : Surface treatment of materials with high current pulsed electron beam, *Material Science Forum* 475-479 (2005) 3959

[164] Y. Qin, C. Dong, X. G. Wang, S.Z. Hao, J.X. Zou, A.M. Wu, Y. Liu : Numerical simulation and experimental evidence for surface modification by high current pulsed electron beam, *Material Science Forum* 475-479 (2005) 3673

[165] J. X. Zou, A. M. Wu, C. Dong, S. Z. Hao, Z. M. Liu, H. T. Ma : Oxidation protection of AISI H13 steel by High Current Pulsed Electron Beam Treatment, *Surface and Coatings Technology* 183 (2004) 261

[166] Z. M. Liu, J. X. Zou, A. M. Wu, C. Dong, W. Gao : Oxidation resistance of a hot die steel (H13) with Al coating and High Current Pulsed Electron Beam treatment, *High Temperature Materials and Processes* 21 (6) (2003) 361

[167] K. M. Zhang, D. Z. Yang, J. X. Zou, C. Dong : Surface modification of 316L stainless steel by high current pulsed electron beam Part I Selective purification of surface and its mechanism. *Acta Metal. Sinica* 43 (2007) 64

[168] K. M. Zhang, D. Z. Yang, J. X. Zou, C. Dong : Surface modification of 316L stainless

steel by high current pulsed electron beam Part II Corrosion behaviours in the simulated body fluid. *Acta Metal. Sinica* 43 (2007) 71

[169] Q. F. Guan, C. X. An, S. Z. Hao, Y. Qin, J. X. Zou, C. Dong, Q. Y. Zhang, G. T. Zou : Microstructure induced by stress generated by high current pulsed electron beam, *Acta Physics Sinica* 8 (2005) 3927

[170] Y. Qin, X. G. Wang, C. Dong, S. Z. Hao, Y. Liu, J. X. Zou, A. M. Wu, Q. F. Guan : Temperature field and forming of craters on the surface induced by High Current Pulsed Electron Beam bombardment, *Acta Physics Sinica* 52(12) (2003) 3043

[171] K. M. Zhang, PhD thesis of Dalian University of Technology, 2006

[172] A Kellou, H. Feraoun, T. Grosdidier, C. Coddet, H. Aourag : Energetics and electronic properties of vacancies, anti-sites, and atomic defects (B, C, and N) in B2-FeAl alloys, *Acta Mater.* 52 (2004) 3263

[173] C. Garcia Oca, D. G. Morris, M. A. Muñoz-Morris : The role of carbon and vacancies in the quench hardening and age softening of a Fe-40Al-C alloy, *Scripta Materialia* 44 (2001) 561-568

[174] S. Z. Hao, Y. Qin, X. X. Mei, B. Gao, J. X. Zou, Q.F. Guan, C. Dong, Q.Y. Zhang : Fundamentals and applications of material modification by intense pulsed beams, *Surface and Coatings Technology*, In Press, Available online

Abstract

High-Current Pulsed Electron Beam (HCPEB) is a recently developed technique for surface treatment of materials. The high-density electron pulses of short durations induce dynamic temperature fields in the surface layers giving rise to superfast heating, possible melting and evaporating. This is followed by a rapid solidification and cooling of the material surface. In addition, a dynamic stress field is formed that causes intense deformation in the material sub-layers. The development and research work carried out using the HCPEB technique have been reviewed in this thesis by underlying its effects under the “melting”, “heating” and “evaporating” treatment modes. At first, different physical models for the HCPEB treatment of materials under the three different treatment modes have been proposed. Subsequently, the intriguing surface modifications associated with the HCPEB treatment were detailed. Finally, the potential applications of the HCPEB technique to improve the materials’ properties have been pointed out. Under all the three treatment modes, HCPEB treatment is proved to be an efficient way to modify the surface of metallic and intermetallic materials to taylor their properties. Overall, this review clearly demonstrate that the high potential of the HCPEB technique can be better achieved by a good control of the processing parameter in order to treat the sample surfaces under the most appropriate mode.

Résumé

La technique de « High-Current Pulsed Electron Beam » (HCPEB) a été développée récemment pour le traitement de surface des matériaux. Des impulsions très courtes avec une importante densité d'énergie d’électrons induisent des cycles thermo-mécaniques ultra-rapides en surface. Ces cycles peuvent conduire à la fusion - voir éventuellement à l'évaporation - de la couche superficielle ainsi qu’à la formation d’un champ de contrainte dynamique qui est à l’origine d’une déformation intense en sous-couche. Ce manuscrit propose une revue des développements récents concernant la technique HCPEB qui ont été obtenus dans le cadre de nos travaux. Nous montrons l’importance de la distinction entre les trois différents modes de traitement : le mode ‘chauffage’, le mode ‘fusion’ et le mode ‘évaporation’. Tout d’abord, des

modèles physiques associés à ces modes ont été proposés. L'analyse expérimentale a ensuite été réalisée sur différents métaux et alliages intermétalliques. Les modifications de surface et certains phénomènes spéciaux liés aux différents modes de traitement ont été détaillés. Finalement, nous avons discuté les applications potentielles de cette technique pour améliorer les propriétés des matériaux. Il apparaît clairement que le potentiel de la technique HCPEB nécessite un bon contrôle des paramètres de traitement pour modifier la surface des matériaux en utilisant le mode de traitement le plus approprié.

Appendix

Abstract in Chinese

博士学位论文

强流脉冲电子束材料表面改性基础研究:在金属及金属间化合物上的应用

Foundamentals of Surface Treatments by High Current Pulsed Electron Beam : Application to metallic and intermetallic alloys

作者姓名：邹建新

学科、专业：材料物理与化学

学　　号：10305006

指导教师：董　闯　教授

Thierry Grosdidier 教授

完成日期：2007 年 4 月

大连理工大学

Dalian University of Technology

独创性说明

作者郑重声明：本博士学位论文是我个人在导师指导下进行的研究工作及取得研究成果。尽我所知，除了文中特别加以标注和致谢的地方外，论文中不包含其他人已经发表或撰写的研究成果，也不包含为获得大连理工大学或者其他单位的学位或证书所使用过的材料。与我一同工作的同志对本研究所做的贡献均已在论文中做了明确的说明并表示了谢意。

作者签名：____________日期：____________

摘 要

强流脉冲电子束是近年来发展迅速的一项新兴表面改性技术。高密度脉冲电子束轰击材料可在表层诱发非常快速的动态温度场，引起超快速加热、熔化及可能的蒸发，而之后则伴随着表层的快速凝固和冷却。此外,动态温度场还导致动态应力场的形成，并且在材料深度方向上均具有高的梯度，从而造成材料表层一定范围内的分层次相变及形变。基于以往的实验和理论研究结果以及本文对不同材料表面处理的探索,脉冲电子束材料表面改性可以简单地分为三种模式，即"加热"，"融化"和"汽化"模式，它们分别取决于电子束轰击参数和被处理材料的物理性能。本文建立了材料在三种脉冲处理模式下的物理机制，并揭示了在不同模式下诱发的各种效应及可能的应用。研究结果表明，在各种处理模式下，强流脉冲电子束技术均可有效的对金属及金属间化合物材料进行表面改性从而获得所需性能。总而言之，为了更好的发挥强流脉冲电子束在材料表面改性方面的应用潜力，需要对处理参数进行优化并选择最佳的处理模式。

关键词：强流脉冲电子束；表面改性；未熔处理；熔化处理；汽化处理

Foundamentals of Surface Treatments by High Current Pulsed Electron Beam : Application to metallic and intermetallic alloys

Abstract

High-Current Pulsed Electron Beam (HCPEB) is a recently developed technique for surface treatment of materials. The high-density electron pulses of short durations induce dynamic temperature fields in the surface layers giving rise to superfast heating, possible melting and evaporating. This is followed by a rapid solidification and cooling of the material surface. In addition, a dynamic stress field is formed that causes intense deformation in the material sub-layers. The development and research work carried out using the HCPEB technique have been reviewed in this thesis by underlying its effects under the “melting”, “heating” and “evaporating” treatment modes. At first, different physical models for the HCPEB treatment of materials under the three different treatment modes have been proposed. Subsequently, the intriguing surface modifications associated with the HCPEB treatment were detailed. Finally, the potential applications of the HCPEB technique to improve the materials’ properties have been pointed out. Under all the three treatment modes, HCPEB treatment is proved to be an efficient way to modify the surface of metallic and intermetallic materials to taylor their properties. Overall, this review clearly demonstrate that the high potential of the HCPEB technique can be better achieved by a good control of the processing parameter in order to treat the sample surfaces under the most appropriate mode.

Key Words: High-Current Pulsed Electron Beam (HCPEB); Surface treatment; Heating mode; Melting mode; Evaporating mode

目　　录

1 绪论

1.1 电子束表面改性技术研究发展概况

利用高能量密度的电子束对材料进行工艺处理的一切方法统称为电子束加工。它是利用电子束的能量对材料进行加工，是完全不同于机械加工的一种新型加工方法，包括电子束焊接、打孔、表面处理、熔炼、镀膜、物理气相沉积、切割以及电子束曝光等。其中电子束焊接、打孔、物理气相沉积以及电子束表面处理等在工业上的应用最为广泛，也最具竞争力。

电子束加工作为特种加工方法的一种起源于德国，德国物理学家 Steigerwald 1948 年发明了第一台电子束加工设备（主要用于焊接），经过几十年的发展，目前全世界已有几千台设备在核工业、航空宇航工业、精密加工业及重型机械等工业部门应用，现已完全被工业部门所接受。近年来，该技术不断发展，在大批量生产，大型零件制造以及复杂零件的加工方面都显示出其独特的优越性。世界上电子束加工技术较先进的国家是德国、日本、美国、独联体以及法国等。

国内从 60 年代开始研究电子束焊接，随后开发了电子束熔炼，到 80 年代，电子束表面改性处理的研究与开发也迅速展开，电子束镀膜机、熔炼炉等设备均已投入实际加工或生产。90 年代以后，随着科学技术和制造水平的进步，具有不同参数范围和工作特点的电子束设备大量涌现，从而使电子束加工技术的应用领域不断扩大。

1.2 电子束在表面改性处理中的应用及研究现状

材料表面层的物理、化学及机械等性能始终是构成其整体性能的重要组成部分，尤其是在一些特殊场合，材料的表面性能将起到关键性作用。表面处理技术的实质是通过特殊的工艺方法，或直接改变原来表面的组织和成分，或在原来表面上复合一个具有特殊性能的表面，从而达到表面改性或提高表面性能的目的。

与其他电子束工艺相比，电子束表面改性技术是 70 年代才发展起来的新技术。电子束表面改性处理包括金属材料的表面淬火、表面合金化、表面清洗及熔覆以及半导体材料的退火和掺杂等。目前，电子束表面非晶态处理及冲击淬火等先进处理工艺的研究也已经在世界各国广泛展开。

从电子枪阴极表面发射的电子，经加速后直接轰击需要处理的工件表面，瞬间的能量转换和沉积使“表面层”（几个μm 到几个 mm）温度急剧升高，而“基体”仍保持“冷态”，电子束结束照射时，加热区域的热量迅速向基体扩散，表面层

的温度急剧下降，从而在表面改性层中形成特定的加热、冷却过程，类似于常规的热处理过程。除此之外，快速的升温冷却过程中形成的巨大温度差会在改性过程中同步造成热应力的产生，并形成一定的应力分布状态。以上述过程为基础，通过控制入射电子束的形成、能量幅值及空间分布，同时附以必要合金元素（气体或固体）的添加，就构成了电子束表面改性处理的独特工艺。

1.2.1 应用现状

电子束技术在表面改性领域的应用是在实践中发展起来的，随着这一技术在众多领域所取得的显著成果，受到世界各国的广泛重视。目前，投入使用和正在开发的电子束表面改性技术已有很多。

早在 70 年代初，美、苏两国首先将电子束用于薄带钢、细丝的连续真空退火和研究淬火问题，这标志着电子束技术开始被用于材料表面改性处理。80 年代是电子束表面改性技术蓬勃发展的时期，世界各国关于成功运用该技术的报道屡见不鲜。80 年代初开始，东德焊接技术中央研究所进行了柴油机活塞的活塞环槽电子束熔融淬火处理实验并取得了成果。采用电子束熔融淬火可改变活塞内铝合金基材的表面性能，提高其耐磨性，所以在解决其他材料的此类问题上显示出很大的优越性。到 86 年，大型活塞的电子束熔融淬火装置就已经转入东德国内的活塞厂生产。

80 年代中期，日本开始将电子束表面改性技术应用于汽车零件的加工处理方面。在五十铃 6B 系列发动机的挺杆上成功地使用了电子束淬火法。采用电子束表面淬火处理后，其淬火组织全部为马氏体，硬度显著提高，同时表面粗糙度几乎没有区别。对装配在发动机中的挺杆进行了磨损量检查，为未处理（淬火加回火）的 1/6～1/2，耐磨性有了显著提高。

同期，法国报道了挡环式离合器滚子滑道的电子束处理方法，用电子束处理的滑道表面硬度超过 HRC58，从而改善了耐磨性。意大利学者 Artinger 与 Korach 对高速钢的电子束局部熔化处理进行了深入探讨，研究结果得出：电子束局部重熔可以使高速钢显微组织变为具有 1～3μm 次生枝晶臂间距的细枝晶组织和宽0.5～1μm 的枝晶间共晶碳化物；碳化物的合金元素相对含量比基体要高1.2～1.3倍，分布更为均匀；与基体相比，重熔区的硬度显著提高；重熔区断口均为细晶状，呈韧性特征，而基体材料呈脆性特征。

随着电子束应用领域的扩大及表面改性要求的不断提高，电子束的形式和参数也在不断地发生变化。在一般的电子束表面改性装置中，入射电子束斑的面积均

很小（～1mm^2），电子束流大多在几百毫安，电子束的加速电压在几十千电子伏，工作方式以连续扫描为主。而从目前的报道情况来看，表面改性工艺中所使用的电子束加速电压已经达到 1MeV，功率密度接近 10^9W/cm^2，大面积及短脉冲（ns 量级）打点等新技术不断出现。以本文所采用的强流脉冲电子束装置为例，该设备是由俄罗斯人倡导并研制的一种新型电子束表面改性装置，可产生大面积（～30cm^2）、强束流（可达到 10kA）的电子束。另外，脉冲工作方式使其具有较广泛的应用范围，可以用于金属、半导体材料的表面强化、表面合金化、清洗及熔覆等。

1.2.2 研究现状

强流脉冲电子束源自核聚变的实验研究，近几年才开始在材料表面改性方面获得重视和使用，而且由于设备的原因，只有俄罗斯，德国，美国，日本等的个别科研单位在这方面进行了一些探索性工作。从文献报道来看，目前对强脉冲电子束流入射引起的材料微观结构及性能变化等方面的研究工作开展得还较少，强流脉冲电子束入射引起的材料改性机制还基本建立在简单实验测试及经验理论上，缺乏系统的材料显微结构分析及相应的实验验证结果。

在研究电子束材料表面改性过程时，要涉及到高速载能电子与材料表面的相互作用，即能量转换问题。对于这个问题，早在 40 年代初研制金属电子显微镜的时候就已经开始研究，因为透射或扫描电镜同样是以电子轰击所产生的物理现象为工作基础的。经过半个多世纪的探索，人们已经获得了大量用以描述电子与固体表面相互作用过程的理论及实验结果，这里不再一一赢述。其中，对于电子束表面改性问题来说，准确描述电子进入材料表层的射程、以及射程内电子能量的损失分布函数是确定电子束表面改性范围及相关理论计算的基础。

从材料角度来看，材料的性能，尤其是机械强度、硬度、耐腐蚀性能取决于其化学成分、晶体结构、晶粒的大小、均匀性及应力状态等，而这些特性又直接受到加工制造条件的强烈影响。电子束表面改性时，入射电子束的能量沉积主要集中在材料表面薄层中，特殊的加热、冷却过程及相关的热冲击作用等是使材料表面性能发生变化的根本原因。利用先进的材料观测手段，包括 TEM、SEM、XRD、RBS、SPB 等，可以对处理层的显微组织结构进行观察。在已报道的文献中，材料的微观变化包括以下几个方面：晶体结构变化，主要指新相或特殊相的产生，还包括非晶的形成；晶粒细化；高密度的晶体缺陷，包括位错、层错及空位；残余应力等。但是，由热冲击作用直接引起的材料显微结构变化到目前还没有明确的实验证据。

在对电子束表面改性机理进行深入研究的过程中，理论模拟计算方法始终发挥着重要的作用。众所周知，电子的质量和体积都很小，当大量以很高的速度运动的电子与材料表面相互作用时会引发一系列复杂的物理过程，另外，电子束表面改性层的尺寸一般都很小，经历加热、冷却过程的时间又很短，所以对于上述过程用常规的方法进行观察和测量基本是不可能的。在这种情况下，从理论模型出发，结合实际参数及实验结果，进行理论模拟计算是解释许多相关现象的有效方法，而且正确的模拟计算结果对于电子束表面改性工艺的进一步应用具有指导性的意义。

1.3 强流脉冲电子束的表面改性研究进展

强流脉冲电子束装置如图 1-1 所示，主要分为电子枪、真空系统、电源控制系统、诊断系统四个部分。

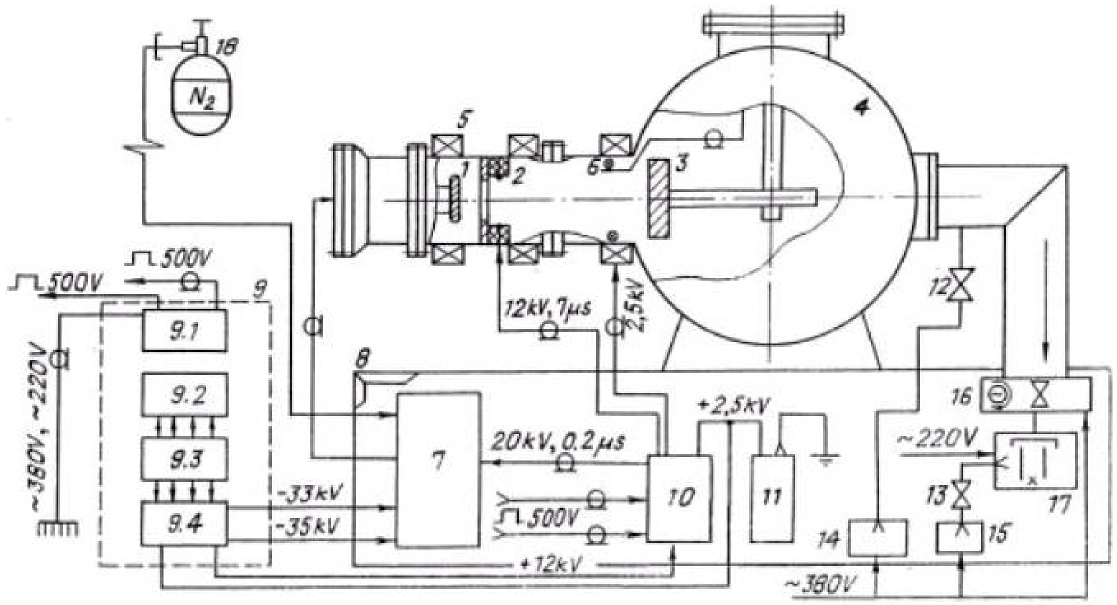

图 1-1 强流脉冲电子束装置示意图

1. 阴极，2. 火花源，3. 工作靶，4. 真空室，5. 线圈，6. 罗戈夫斯基线圈，7. 脉冲高压发生器，8. 支架，9. 电控柜，10. 脉冲触发箱，11. 高压电容，12. 13. 手动真空阀 1，2，14. 15. 机械泵 1，2，16. 电磁阀门，17. 扩散泵，18. N_2气

Fig. 1-1 Schematic diagram of the High Current Pulsed Electron Beam (HCPEB) system

1. cathod, 2. spark source, 3. collector, 4. vacuum chamber, 5. solenoid, 6. rokovsky coil, 7. pulsed high-voltage generator, 8. bracket, 9. electricity controller, 10. pulses trigger, 11. capcitor, 12. 13. manual vacuum valve 1, 2, 14. 15. pump 1，2, 16. electromagnetism valve, 17. diffusion pump, 18. nitrogen.

位于电子枪加速间隙及漂移空间中的等离子体可以由多种物理方法产生，在本实验装置中采用一套独立供电的火花源提供此等离子体，如图 1-2 所示。火花源放置在阳极后面，由按圆周均匀分布的多个石墨阴极火花源组成。多个火花源电极同时产生火花放电，形成稠密的阳极等离子体（$n = 10^{17} / cm^{3}$），等离子体同时会沿横向、纵向进行扩散。电子枪的阴极采用石墨材料，其原因是该材料产生热不稳定性的临界场强比较低，更容易形成一个均匀的阴极等离子体层，因此在石墨表面可以比较快地产生真空表面击穿，从而缩短了阴极的启动时间。阳极由不锈钢制成，中心位置钻有一孔以通过电子束，同时也起到控制电子束截面直径的作用。为了加速等离子体有意义的纵向扩散速度和提高等离子浓度，在放电室外壁加上一个强磁场，可以根据需要调整磁场线圈的位置和选取线圈匝数。另外，这个外加磁场要比电子束自身产生的磁场强得多，从而克服了电子束自身磁压缩导致的束斑面积缩小的问题。

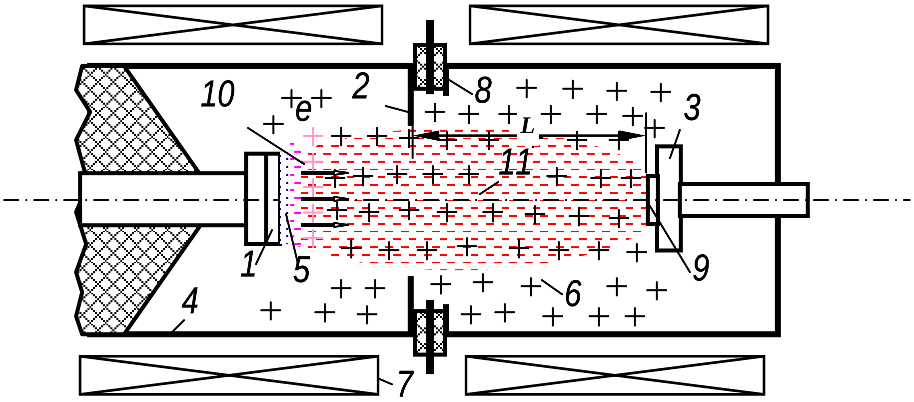

图 1-2 电子束工作原理示意图
1. 阴极 2. 阳极 3. 工作靶 4. 真空室 5. 阴极等离子体 6. 阳极等离子体 7. 线圈 8. 火花源 9. 样品 10. 等离子鞘层 11. 电子束
Fig. 1-2 Schematic diagram of the HCPEB source based on vacuum spark plasma.
(1) cathode (2) anode (3) collector (4) vacuum chamber (5) cathode plasma (6) anode plasma (7) solenoid (8) spark plasma sources (9) specimen(10) plasma sheath (11)electron beam.

Markov等首先建立了强流脉冲电子束轰击在金属材料内引发温度场的物理模型，并且得到了与实验符合较好的数值计算结果。Proskurovsky等在纯铁、膜层体系、钢和合金等材料的表面改性方面作了大量的工作。主要包括对碳钢与合金钢进行表面强化以提高材料表面的耐磨性和耐腐蚀性等，他们发现在材料熔化的外表面层内，原始组织中的第二相被部分或完全熔解，从而形成了过饱和的固溶体以及残余的纳米级第二相颗粒，这些微结构的变化提高了材料表层的强度和电化学性能。为了更好的理解这些现象，他

们进一步发展了Markov等的模型，对温度场和应力场同时进行了数值模拟，给出了材料表层升温、熔化、凝固及冷却的大致过程，结果表明，电子束轰击过程中，加热和冷却的速度达到 10^{8-9}K/s，凝固时结晶前沿移动的速度达到 2~5 m/s。同时，他们也给出了热应力波的数值模拟结果，其幅值大约只有 0.1MPa左右，并且指出材料深层的改性（超过热影响区）是由于热应力波作用的结果，类似于高频振动应力的疲劳过程。

乌克兰Pogrebnjak等人则着重研究了HCPEB对材料结构的影响，以及表面合金化对不同材料表面性能的提高作用。他们采用电子束蒸镀金属薄膜与HCPEB后处理相结合的方法在纯铁表面实现了钽、钼、铬、铝等元素的合金化，同时提高了纯铁的耐磨性和耐腐蚀性。并且使用Nadezhda-2 强流脉冲电子束源，利用RBS、SPB (Slow Positron Beam)以及TEM和SEM等技术，对电子束轰击后的纯铁表面层进行研究，发现了大量的非平衡空位向表面移动，空位的密度达到 10^{-3}，因此在缺陷区域材料的局部密度降低，并且认为这些局部的低密度区域是火山坑在材料表面形成的根源。

在国内，利用俄罗斯Nadezhda-2 强流脉冲电子束（HCPEB）源，大连理工大学三束材料改性国家重点实验室先后进行了大量的实验研究。郝胜智在博士论文研究期间以纯铝为基材，深入研究了不同参数的脉冲电子束轰击处理对试样显微结构和力学性能的影响规律，进而获得了强流脉冲电子束表面改性的一些微观物理机制。他通过深入分析载能电子与固体表面的相互作用过程，建立了较为合理的实际加工中的物理模型，利用二维模型数值计算方法模拟了试样中的动态温度场及应力场分布，并选用 1Cr18Ni9Ti 和GCr15 进行了初步的改性尝试。结果表明：表层快速升降温（10^{8}K/s）与熔凝以及入射束的瞬时热冲击作用是导致表层材料改性的直接原因，表面改性层的抗腐蚀、硬度、抗磨损性能均有明显提高。尤其在对Ti离子注入后的轴承钢表面进行脉冲电子束微熔轰击处理时发现，在实现表面强化效果的同时，注入离子的分布范围得到大幅度提高，显示出明显的增强扩散效应。吴爱民在博士论文研究期间以H13 和D2 两种典型的模具钢为基材，通过脉冲电子束直接淬火和电子束表面合金化等方法进行表面改性处理，结果表明，处理后的模具钢表层硬度、耐磨性，特别是抗微动磨损性能大幅度提高。他在研究中还发现，经过脉冲电子束适当处理后，钢的表层数微米范围内为超细晶甚至纳米晶；而通过纯铝的电子束表面渗碳实验，发现了碳粉在电子束轰击下有向类金刚石结构转变的迹象，这些显示了强流脉冲电子束技术在纳米材料研究领域的应用潜力。秦颖在博士论文研究期间主要用数值模拟的方法研究了脉冲电子束在材料表层诱发的温度场及相关的火山坑形成机制，揭示了亚表层率先熔化从而通过表层向外喷发的火山坑形成机制。同时对脉冲电子束材料表面改性过程中的应力产生及演化过程进行了研究，指出在材料表面未熔化的处理条件下，材料表层应力状态主要是随温度场变化的准静态应力以

及由表面向内部传播的热弹性应力波；材料表面熔化后，由于次表层先熔化而向外喷发，将导致冲击热应力的产生并在材料内传播；当材料由于动态屈服而出现塑性变形后，在冷却过程中将会产生高幅值的应力，当温度降至室温后在材料表层会有残余应力。表面准静态应力以及冷却过程中的应力峰值可达到数百Mpa甚至GPa的量级，而热弹性应力波只有 0.02～0.03MPa左右，冲击热应力的峰值则与准静态应力相当。高波在博士论文研究期间以纯镁以及镁合金为基材，通过脉冲电子束直接轰击及表面合金化等方法进行表面改性研究，结果表明强流脉冲电子束处理能够有效地提高纯镁及镁合金的耐蚀性并达到表面强化的效果。张可敏博士首次将脉冲电子束应用于生物材料表面改性及生物相容性方面。通过 316L医用不锈钢和NiTi合金的脉冲电子束表面改性机理和相关性能的研究，结果显示处理后的样品表面得到强化的同时具有更好的耐蚀性和生物相容性。由此可见，脉冲电子束在生物材料表面改性方面将具有很高科研价值和广阔的应用前景。

电子束在材料表面改性领域的应用研究是 20 世纪 70 年代才开始的。同一时期，也出现了脉冲型电子束发生器研制的相关报道，但其应用在表面改性技术领域的报道则相对较少，直到 20 世纪 80～90 年代才在材料表面改性领域得到快速发展，国际上发达国家从电子枪技术原理的更新换代，到基础理论研究方面的探讨，以及大量的处理过程中的数值模拟计算等方面都得到快速的发展，应用探索性工作也在不断推进。但是，目前在金属或非金属改性方面的研究很多工作还都是探讨性的，更多的应该说是处在对这种技术自身特点和应用潜力进行大范围的探索阶段，而在实际的应用方面的研究则相对缓慢。

1.4 选题依据及研究内容

显而易见，材料经过脉冲电子束表面改性之后的应用性能将取决于处理后表层的成分，微结构，相组成等因素，这些最终状态又同电子束处理诱发的瞬时温度场和应力场密切相关。然而由于这些过程的复杂性，对其进行的系统研究还相当缺乏，而从冶金学角度的研究则更是无人问津。在以往对多种材料处理的经验基础上，我们发现对某一种金属材料的处理效果完全依赖于对脉冲电子束参数的选择，例如每次脉冲的能量密度和使用的脉冲次数。为了获得好的改性效果，通常需要采用多次轰击。从更深层次上看，脉冲电子束诱发的温度场是影响改性效果的最重要因素，它的演化过程决定了耦合的应力场演化过程，从而决定了材料表层发生的形变、相变、熔化、凝固等一系列过程。大量的研究表明，表层诱发的温度场可根据其所达到的最高值与材料熔点及沸点的相对关系大致分为三类。为了更好的说明这一点，图1-3给出了由数值模拟得到的同一材料最表层在不同处理能量下的温度场演化过程。从图中可以看到，当采用的电子束能量很低

时，最表层在整个处理过程中都没有达到熔点，这种处理模式我们称之为未熔模式(Heating mode)。当脉冲电子束能量密度达到一定数值时，最表层在处理过程中可到达或超过熔点，这种处理模式可称之为熔化模式(Melting mode)，其典型特征为温度场出现熔化平台，如图所示。类似地，如果材料最表层温度在处理过程中可达到沸点，则该处理模式可称之为汽化模式(Evaporating mode)。这种对脉冲电子束处理模式的分类很容易理解，并且对于解释脉冲处理过程中诱发的各种效应非常重要。因此，本论文将主要分为三个部分，即1）强流脉冲电子束在熔化模式下对材料的改性处理，2）强流脉冲电子束在未熔模式下对材料的改性处理，3）强流脉冲电子束在汽化模式下对材料的改性处理，并将分别详细讨论不同模式下的物理过程及诱发的不同现象。

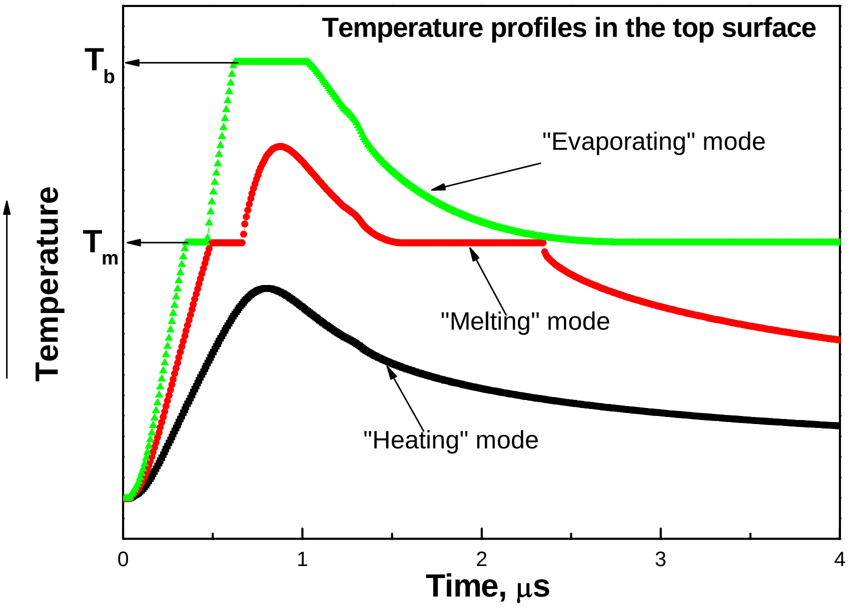

图 1-3 强流脉冲电子束以不同能量轰击在材料最表层诱发的温度场，显示了三种不同处理模式

Fig. 1-3 Typical temperature profiles in the top surface of a material by HCPEB treatment with different energy density, showing the three treating modes.

2 强流脉冲电子束材料表面改性的物理基础

2.1 电子束与材料表面相互作用机理

强流脉冲电子束材料表面改性处理实质上是利用载能电子与固体表面之间特殊的交互作用来实现的。电场中加速的电子，以高能量及高速度与固体相碰撞时，入射电子就和固体中的分子、原子、电子相互作用而损失能量。由于入射电子失去的能量会转变为各种能量形式，所以碰撞就可以引起很多现象，例如引起电磁波（包括 X 射线、阴极荧光等）、电子（包括二次电子、俄歇电子、热电子等）的发射，以及靶材的加热、分子的脱附等等。目前，人们已经利用不同的电子作用效应制造了用于科学研究和生产加工中的各种仪器与设备。其中，对于电子束表面改性处理来说，主要是利用电子束轰击产生的热效应以及由此引发的材料微观组织结构和应力状态变化，最终达到改变材料表面性能的目的。

2.2 温度场与应力场的形成

入射电子经过相互作用区的复杂的散射后，其所携带的能量大部分以热能的形式转移给靶材。这个过程是在瞬间完成的，入射电子的寿命一般在 10^{-10}秒左右，所以电子对材料的加热过程可以近似认为是准绝热过程，其热导效应可忽略不计，因此靶材的加热功率就可以用电子沿入射深度的能量损失分布来进行描述。在加热阶段，能量衰减深度或电子穿透深度控制吸收层的温升。在这里温升包括两层含义：（1）吸收层的最高加热温度，它决定了电子束加热的极限温度；（2）吸收层的温度梯度，它决定了吸收层向其基体内部的热量传递速度。材料的实际升温速率及其所达到的温度，取决于入射电子束的束流强度、加速电压及轰击时间，此外靶材自身的物理性质及其散热条件也将对其产生一定的影响。电子束是一种高能量密度的加热源，材料的表面层在电子的轰击下升温非常迅速，当功率密度达到一定程度时，在微秒的时间内就可以出现熔化，同时随着电子束轰击时间的延长其温度不断上升。电子在靶极中的穿透深度是有限的，在一般的加工条件下，电子的平均穿透深度在微米的数量级，电子相互作用区内温度的迅速升高，将会在材料的内部形成明显的温度差别，即温度梯度。随着电子轰击时间的延长，材料内部的热传导作用会不断加强，从而使加热区域的能量不断地向周围扩散，直至达到平衡态。

当电子束的辐照停止后，靶极材料将迅速地冷却或者凝固，冷却速度取决于加热层的厚度，同时也与靶极材料的热性能和散热条件相关。从上面的分析可以看

到，电子束加工过程中的任一时刻，材料中的不同位置都具有特定的温度分布状态，即形成了温度场的变化。对于这种问题，一般可以通过建立合理的物理模型，然后利用热传导方程进行求解。

材料的温度差别，同样会导致其内部的应力分布不均匀。电子束加热的速度极快，所以材料表层会形成很高的温度梯度，在这种高温度梯度的驱动下，材料内部可以形成很高的应力。应力产生以后，主要沿着垂直方向进行传播和反射，从而在整个材料范围内导致应力的特殊分布，而且该应力分布还将伴随温度场而发生变化，形成所谓的“准静态应力”。对此问题，可采用温度场与应力场非耦合的方法进行计算。

2.3 温度场的数学物理模型

材料表面经强流脉冲电子束轰击处理时，由于加热体积小，温度变化极快，用实验的方法一般很难直接测定处理过程中的温度分布、冷却速度等与改性效果直接相关的具体参数，因此必须通过合理的选取物理模型和数值计算方法，模拟强流脉冲电子束表面改性过程，对此，我们做了以下几点假设：

(1) 电子束流在整个束斑范围内是均匀分布的；

(2) 靶材的厚度和束斑半径远大于电子束的能量沉积深度；

(3) 材料性质均匀，且热物理性能为温度的函数。

于是主导热方程可表示为如下一维带内热源的非稳态热传导方程：

$$\rho c(T)\frac{\partial T}{\partial t}=\frac{\partial}{\partial x}(\lambda(T)\frac{\partial T}{\partial x})+L_v(x,t). \qquad （2\text{-}1）$$

温度T满足初始条件：　$T(x,0)=T_0$　（2-2）

边界条件：.

$$-\lambda(T)\frac{\partial T(x,t)}{\partial x}|_{x=0,x=l}=0. \qquad （2\text{-}3）$$

其中，ρ、c、λ分别为材料的密度、热容及导热系数，L_v为电子束体加热的功率密度，T_0为材料的初始温度，l为工件厚度。

电子束体内加热的功率密度L_v由下式给出：

$$L_v(x,t)=\frac{j(t)E_0(t)}{r(t)e}f(x,r). \qquad （2\text{-}4）$$

其中，$j(t)$为电子束在靶材中的电流密度，$E_0(t)$为电子束接触靶材时的初始能量，$r(t)$为电子的射程，e为电子的电荷，$f(x,r)$为垂直入射电子束在深度方向上的能量损失分布函数，可以近似的描述为如下的三次方程：

$$f(x,r)=0.74+4.7xr^{-1}-8.9(xr^{-1})^2+3.5(xr^{-1})^3, x\in[0,r]. \qquad （2\text{-}5）$$

一定能量的电子在材料中的射程为：

$$r(E_0)=C(E_0/e)^{3/2}/\rho. \qquad （2\text{-}6）$$

其中C= 10^{-4} kg/(m^2・V$^{3/2}$)，E_0是电子的初始能量，单位是千电子伏特 (keV)。

在数值计算过程中，材料的导热系数和热容在不同物相下均采用随温度变化的函数，将物相变化释放或吸收的潜热 H 折算成温度的补偿值，然后再与节点的温度分布进行叠加。单位体积的金属在相变阶段由于潜热的吸收或释放而引起的温度补偿值$\Delta T=H/c$。必须指出的是，当金属表面的温度达到沸点时，一部分材料将发生汽化而离开表面，此时温度场的边界条件必须采用移动边界条件，就是计算时每一位置处的汽化部分都将在下一时刻的计算前被扣除，这样表面实际是在不断向内移动，但坐标原点始终保持在最外表面处。对于任意一节点单元，在达到沸点后一段时间步长τ内的汽化量可以表示为

$$d_k^p=\frac{T_k^{p+1}-T_e}{\Delta T_e}h. \qquad （2\text{-}7）$$

其中T_e为材料的沸点，ΔT_e是汽化补偿温度。在这段时间内靶材总的汽化层厚度应为

$$D^p=\sum_{k=1}^{n}d_k^p. \qquad （2\text{-}8）$$

这样，边界的移动速度V_e就可以表示为：

$$V_e(t)=\frac{D^p}{\tau}. \qquad （2\text{-}9）$$

在总的模拟计算时间 t 内，汽化层的厚度也就是边界的总移动量可用下式来计算：

$$L_e=\int_0^t V_e(t)dt. \qquad （2\text{-}10）$$

2.4 应力波的数学物理模型

脉冲电子束作用于材料表面将产生热应力波。当脉冲能量较小时，材料只经历由固态到液态、液态到固态的状态改变，此时材料的应力状态主要是以热膨胀引起的热应力波为主；当脉冲能量较大时，材料表面强烈汽化形成等离子体并爆炸，结果在靶材表面形成反脉冲，给材料内部一个强压缩，形成冲击波。我们在实验中所采用的强流脉冲电子束装置所能产生的能量密度较小，大约为 1-6 J/cm^2，不足以使一般金属材料产生强烈汽化，因此所产生的应力波强度较小，可以近似采用热弹性微分方程来描述，为了简化模型起见我们假定：

（1）材料由连续介质组成，不考虑微观缺陷的作用。

（2）工件为半无限大物体，且初始温度均匀。

（3）应力波无衰减。

则热弹性微分方程如下：

$$\frac{1}{C_S^2}\frac{\partial^2\sigma_x(x,t)}{\partial t^2}=\frac{\partial^2\sigma_x(x,t)}{\partial x^2}-\frac{1+\nu}{1-\nu}\rho a\frac{\partial^2 T(x,t)}{\partial t^2}. \tag{2-11}$$

其中 v 为材料的泊松比，一般在 0.31-0.35 之间, ρ 、a分别为材料的密度和热膨胀系数，C_s是弹性波在材料中的传播速度。

其中热应力σ满足初始条件：

$$\sigma_x(x,0)=0. \tag{2-12}$$

$$\frac{\partial\sigma_x(x,0)}{\partial t}=0. \tag{2-13}$$

及边界条件：

$$\sigma_x(x,t)|_{x=0,x=l}=0. \tag{2-14}$$

2.5 准静态热应力的数学模型

2.5.1 薄片中的准静态应力

如果将轰击的靶材是比较薄的等厚薄板，则由于在电子束轰击材料表面过程中所形成的温度场分布是非定常的（在深度方向非线性变化），这种情况下薄板由于上下单元的束缚，自由膨胀是不可能的，因此板内必然产生热应力，这种热应力随温度场而变化，因而可以称为准静态热应力。采用补偿法可以求出热应力的大小为：

$$\sigma_y=\sigma_z=\frac{1}{1-\nu}(-\alpha ET(x,t)+\frac{N_T}{l}+\frac{12M_T x}{l^3}). \tag{2-15}$$

其中 v 为材料的泊松比，a为材料的热膨胀系数，E为弹性模量，N_T为一合力，可由下式确定：

$$N_T=\alpha\int_{-l/2}^{l/2}E(T)\bullet T(x,t)dx. \tag{2-16}$$

MT 为合力偶，可表示为：

$$M_T=\alpha\int_{-l/2}^{l/2}E(T)\bullet T(x,t)xdx. \tag{2-17}$$

2.5.2 块体材料表层中的准静态应力

若被轰击的靶材是较厚的块体材料，则轰击后不会产生明显的弯曲现象，但是表面一定范围内随温度场变化的准静态应力仍然存在，根据热应力理论，此时的轴对称准静态应力可以描述为如下方程：

$$\sigma_y(x,t)=\sigma_z(x,t)=-\frac{\alpha E_{<hkl>}}{1-\nu}T(x,t)+\frac{\nu}{1-\nu}\sigma_x. \tag{2-18}$$

由于热应力波幅值较小，因此在式（2-18）中，第 2 项的热应力波影响就可以忽略，从而简化为：

$$\sigma_y(x,t)=\sigma_z(x,t)=-\frac{\alpha E_{<hkl>}}{1-\nu}T(x,t). \tag{2-19}$$

这就是准静态应力，它随温度场的变化而变化，对于半无限大界面的模型来说，这是水平方向完全束缚的情况。在实际处理中样品的中心部位就可以看作是这种情况。因为水平方向是不可能做自由膨胀的，而垂直方向却可以。这里必须指出的是，材料的杨氏弹性模量E通常呈各向异性，因此准静态热应力也将呈现各向异性。这种各向异性在考虑微观单个晶粒的时候会产生显著影响，而在宏观情况下则由于晶粒的统计平均效果可以忽略不计。我们可以根据式（2-19）估算纯铝表层在脉冲电子束轰击下的瞬时静应力，例如在接近熔点时，对于纯铝，$\alpha\approx2.53\times10^{-5}$, $\nu\approx0.33$, $E\approx36$GPa。因此, $P\approx900$MPa，这已经远远超过纯铝的动屈服极限从而必然产生一定的形变而使应力部分释放。Proskurovisky等测量了纯铁在强流脉冲电子束轰击下的准静态应力，结果表明单次轰击下静应力的峰值可达 400MPa左右，这与我们估算的结果数量级相当。

2.6 强流脉冲电子束轰击作用下的扩散过程

通过对 Ti 离子注入 9Cr18 钢采用强流脉冲电子束进行表面后处理，纯铝的电子束表面渗碳，模具钢的表面合金化等实验研究，结果表明，脉冲电子束处理过程中存在着明显的增强扩散效应，仅仅几个脉冲轰击就可以使涂覆或注入的合金元素扩散深度大大增加，从而显著的提高材料的耐磨性和高温抗氧化性，因此有必要对这一过程的机理进行深入的研究。

由于脉冲束流的作用时间极其短暂，而在脉冲电子束作用于材料表面的过程中，质量的迁移又极其复杂，影响因素众多，同时存在浓度梯度、温度梯度和应力梯度，因此必须综合考虑浓度扩散流、温度扩散流和应力扩散流的影响，以下分别是菲克第一定律表示的三种扩散流：

1．浓度扩散流： $J_c=-D\dfrac{\partial c}{\partial x}$ （3-20）

其中 c 是扩散原子的浓度，D 是扩散系数。

2．温度扩散流： $J_T=-\dfrac{DQ_a}{RT^2}c\dfrac{\partial T}{\partial x}$ （3-21）

其中Q_a为每摩尔扩散转移的能量，T为温度，R是普适气体恒量，当Q_a为正时温度梯度使原子向冷端迁移,反之则向热端迁移。

3.　应力扩散流：$J_\sigma = -\frac{DV_a}{RT} c \frac{\partial \sigma}{\partial x}$　（3-22）

其中V_a是每摩尔扩散前后体积变化，σ为应力，当V_a为正时应力梯度使原子向低应力端迁移,反之则向高应力端迁移，由此可见，温度梯度和应力梯度的存在既可能加速扩散的进行，也可能阻碍扩散。

总扩散流：　$J=J_c+J_T+J_\sigma$　（3-23）

根据　$\frac{\partial c}{\partial t} = -\frac{\partial J}{\partial x}$　（3-24）

我们可以得到综合的扩散方程:

$$\frac{\partial c}{\partial t} = D\frac{\partial}{\partial x}(\frac{\partial c}{\partial x} + \frac{Q_a}{RT^2} c\frac{\partial T}{\partial x} + \frac{V_a}{RT} c\frac{\partial \sigma}{\partial x}) \quad (3\text{-}25)$$

其中扩散系数$D = D_0 \exp(-\frac{Q+V_a\sigma}{RT})$，初始条件和边界条件要根据具体情况而定。

2.7 模拟计算结果

综上所述，本文建立了强流脉冲电子束表面改性过程中的温度场与应力场的数学模型，该模型适用于各种材料（纯金属、合金、非金属等），因此对强流脉冲电子束表面改性的实际应用具有重要的指导意义。采用数值方法对多种材料表层的温度场、应力场及扩散过程进行了模拟计算并对比相应的实验结果可得出以下一些结论：

1.　采用非线性、非稳态的热力学方程可以对强流脉冲电子束表面改性的机理做出正确的描述，从而得出材料内部的温度场与应力场分布及其基本变化规律，其中熔化深度的计算结果与实验基本吻合。

2.　由于电子束在材料内部能量的特殊分布，处理过程中熔化最先发生在材料次表层。

3.　对应力波的产生与传播过程进行了初步的模拟，从而得出热应力波的幅值较小，约在0.1MPa量级，与脉冲的能量密度基本成正比而与脉冲宽度成反比。

4.　电子束轰击过程中，材料表面会产生随温度场变化的准静态热应力，其大小在~100MPa量级，远大于材料在高温下的动屈服强度而使材料发生形变。准静态热应力具有各向异性。

5.　纯金属在强流脉冲电子束轰击下，表层的硬化是一种快速应变下的加工硬化，应变速率可达$10^{4\sim5}s^{-1}$。

6.　在温度场和应力场计算的基础上，对强流脉冲电子束轰击金属表面时的扩散行为进

行了数值计算，结果表明，浓度扩散流仍然是影响扩散的主要因素；而轰击超过一定次数后，扩散的作用将减弱；当边界条件为表面扩散时，扩散进行较快，这是表面涂覆加脉冲快速扩渗工艺的理论基础。

7. 对实验结果和理论结果的对比分析表明，在脉冲轰击下，扩散激活能会随空位浓度增加而下降，从而加速扩散过程；在表面有熔化的情况下，液态时的混合作用是主导因素。

3 强流脉冲电子束在材料表层诱发的特殊现象

强流脉冲电子束与材料表面的相互作用是极为复杂的，即使对于没有相变的纯金属也是如此，除了快速升降温、熔凝、蒸发等过程，还会引起热应力、冲击波等现象。在前一章中我们建立了这些宏观过程的物理模型并采用数值模拟对上述的现象进行了描述，但是这些还远远不足以概括电子束轰击过程中的所有宏观和微观过程。以往的研究结果表明，脉冲电子束轰击产生的超快速动态温度场和应力场可以大大改变表面相组成，微结构，成分等，从而提高处理材料表面物理，化学及机械性能。例如，经过脉冲电子束处理后的多种钢材，其耐磨性或耐腐蚀性能可以得到很大提高。这里我们将详细讨论脉冲电子束轰击所诱发的一些特殊现象，包括未熔化，熔化和蒸发三种处理模式。

3.1 亚稳态结构的形成

脉冲电子束轰击处理可在材料表层诱发快速加热、冷却及快速凝固。这些非平衡过程为微观亚稳相的形成提供了可能性。然而，目前对于脉冲电子束诱发的亚稳态结构仍然缺乏详细的分析。尤其是在快速凝固过程中的相选择和随后冷却期间的固态相变路径选择等一些过程都需要详细和系统的研究，因为这些过程决定了材料表面处理层的组织和性能。当然，脉冲电子束的三种处理模式都可诱发亚稳态结构的形成。这里只讨论在熔化模式下的亚稳态结构，因为这是最重要的处理模式。

3.1.1 AISI D2 钢

这里选择AISI D2 （Cr12Mo1V1）钢作为脉冲电子束诱发亚稳态结构一个典型例子。D2 钢是一种合金含量较高的典型冷作模具钢。在进行HCPEB处理前D2 钢样品经过常规淬火回火处理，即 1040℃下淬火 30 分钟，200℃回火 3 小时。然后用 3 J/cm^{2}的脉冲电子束轰击 5 次和 25 次。

图 3-1a 是 5 次轰击样品表面典型的扫描电镜（SEM）形貌。可以明显观察到一些由于凝固而造成的缩孔。另外，还可以清楚地看到许多针状组织，如图中箭头所示。这些针状组织互相连接呈局部聚集分布。电子束背散射衍射（EBSD）结果显示，这些针状组织为马氏体，而其余表面为奥氏体。马氏体与其母相奥氏体之间的晶体关系为 NW 型。25 次脉冲处理样的高倍 SEM 图像显示于图 3-1b。它揭示了非常细小的奥氏体晶粒或亚晶粒覆盖整个样品表面，尺寸大约在 50 到 150 纳米之间。

D2 钢在脉冲电子束轰击下亚稳相的形成可以通过碳化物在处理过程的熔解及液相的均匀化来理解。经过 5 次轰击，由于液相存在时间极其短暂，熔化层的化学成分不能

达到均匀，这导致凝固形成的奥氏体成分不均匀。在随后的冷却过程中，马氏体相变将发生在贫 Cr 和 C 的区域。因此，重熔层的微观组成为残余奥氏体，马氏体和未熔碳化物。经过 25 次轰击后，大部分的碳化物熔解，液相成分趋于均匀并逐渐接近共晶点。此时的凝固组织则为超细晶奥氏体和纳米碳化物。这使得随后冷却过程中马氏体相变受到完全抑制。总之，奥氏体的稳定化可规因于快速凝固下的晶粒细化以及熔化过程中 Cr 和 C 元素的合金化。

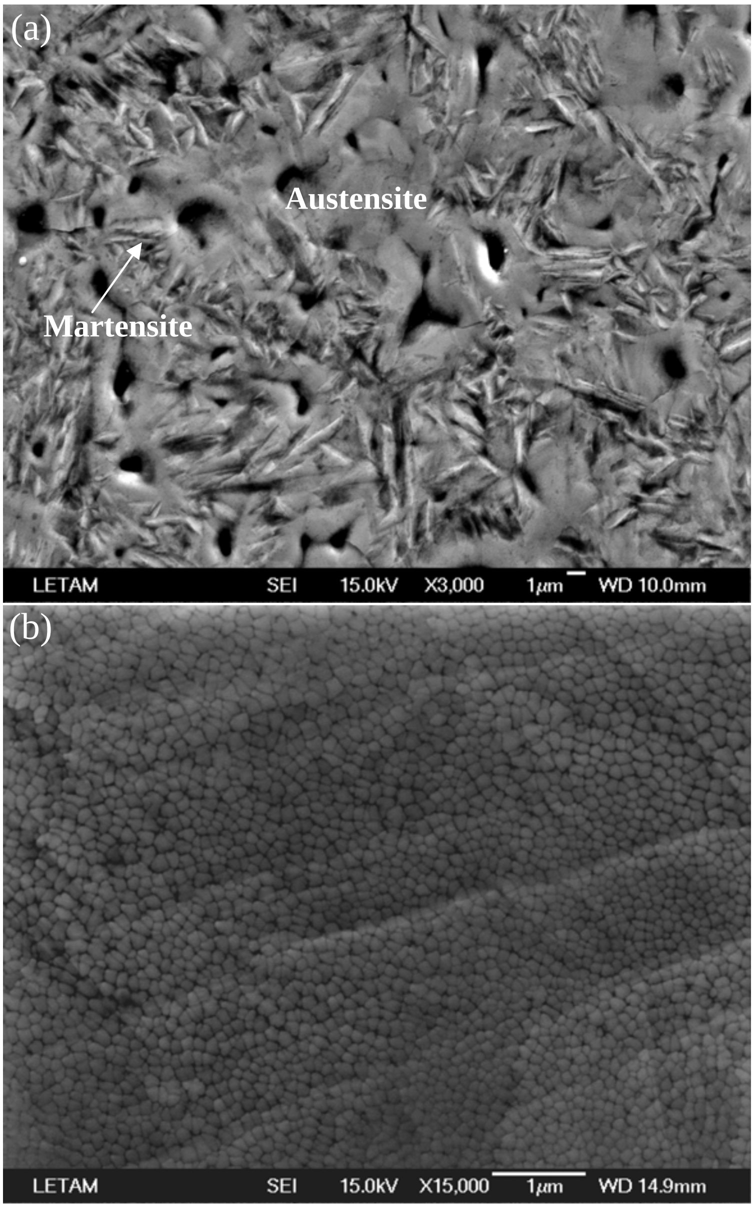

图 3-1 5 次（a）及 25 次（b）轰击 D2 钢表面的典型 SEM 形貌像

Fig. 3-1 A typical SEM surface micrograph on the 5 pulsed D2 sample (a) and high magnification SEM surface micrograph of the sample treated with 25 pulses (b).

3.1.2 NiTi 形状记忆合金

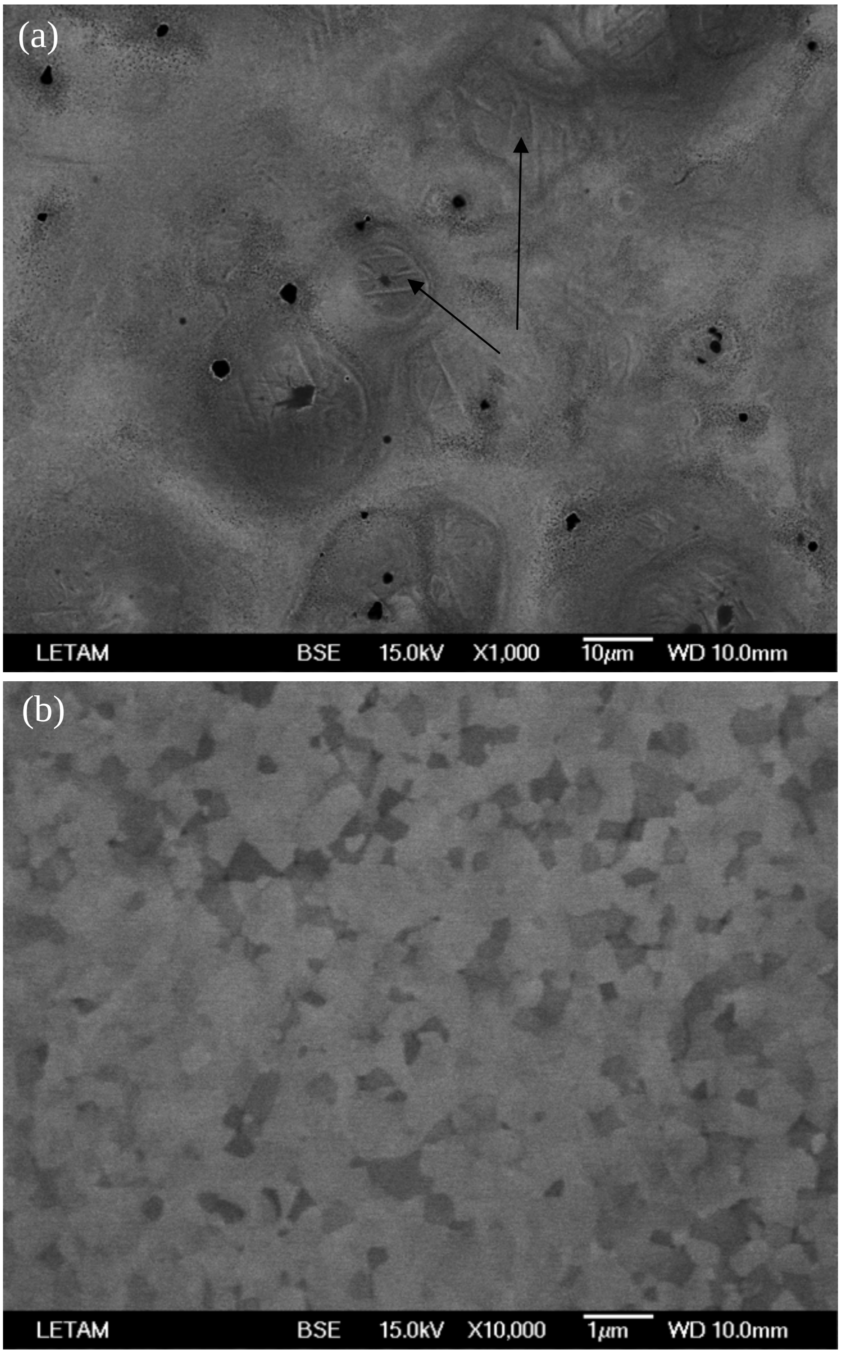

图 3-2 5 次（a）及 25 次（b）轰击 NiTi 合金表面的典型 SEM 形貌像

Fig. 3-2. Typical BSE surface morphology on the 5 pulsed NiTi sample (a) and high magnification BSE (b) surface morphology of the sample treated with 20 pulses.

另一个脉冲电子束诱发亚稳态结构的典型例子是表面改性处理后的镍钛(50.6 at% Ni)形状记忆合金。原始样品在750°下热轧具有B2型结构的奥氏体，其原始织构状态为弱<110>纤维织构平行于轧制方向。晶粒尺寸约为10~50微米。采用熔化处理模式对样品进行处理，加速电压固定在27千伏而脉冲次数不同，分别为5次和20次轰击。

图3-2a为5次脉冲处理样品表面典型的SEM形貌。可以明显观察到很多带状组织，主要存在于接近火山坑的区域。这是因为在轰击处理过程中火山坑附近地区可形成幅值较高的冲击应力场，从而有利于诱发马氏体相变。表面还可以看到一些黑色颗粒，而且往往位于火山中心。它们是原始样中的$NiTi_2$析出相，是形成火山坑的根源。其余表面被细小晶粒和缩孔所覆盖。图3-2b为25次处理样品表面典型的SEM形貌。从图中可以明显看到整个表面均为超细晶粒，这类似于25次轰击处理的D2钢表面形貌。

脉冲电子束在材料表层引发熔化后，由于基体的热传导作用，熔化层发生超快速凝固10^7 K/s。这导致了表层超细晶的形成。与此同时，伴随温度场的准静态热应力与应力波幅值可达数百MPa，从而诱发了马氏体相变。这里我们注意到，NiTi合金与D2钢处理过程中的相变非常相似。马氏体相变发生在轰击次数较少的情况下，例如5次轰击。而轰击次数较多时，由于熔体成分的均匀化以及凝固后的超细晶粒，马氏体相变受到完全抑制。这里，马氏体相变对晶粒细化也有所贡献。它可以将原始的晶粒逐步分化成独立的区域。这一过程在每个脉冲中不断重复，直到晶粒足够细小或成分足够均匀以至于马氏体相变不能再发生。

3.2 特殊表面形貌

以往的大量研究已经揭示材料表面经脉冲电子束轰击后通常会出现特殊形貌。例如表面火山坑的形成是许多材料经过表面轰击处理后的一个共同特点，这同样发生在脉冲激光束和脉冲离子束的处理过程。然而对不同材料表面火山坑的形成机制仍然缺乏详细的分析。这里，我们将讨论不同处理模式下材料表面的典型形貌。

3.2.1 未熔处理模式下的表面形貌

图3-3 是Fe(40 at%)Al样品在未熔处理模式下经20次轰击后表面典型SEM形貌。可以清楚看到表面已不再平整。某些晶粒的表面低于其他晶粒，以至于可以明显分辨出不同的晶粒。这种表面形貌是由于轰击过程中产生的热应力具有各向异性，这造成不同的晶粒形变过程与程度不同。在未熔模式处理下的316L不锈钢样品上也观察到这种各向异性的形变，其中某些晶粒表面出现大量滑移线而其他一些晶粒表面则出现孪晶。总之，在未熔处理模式下，材料表面形貌的显著特征就是由各向异性形变留下的痕迹。

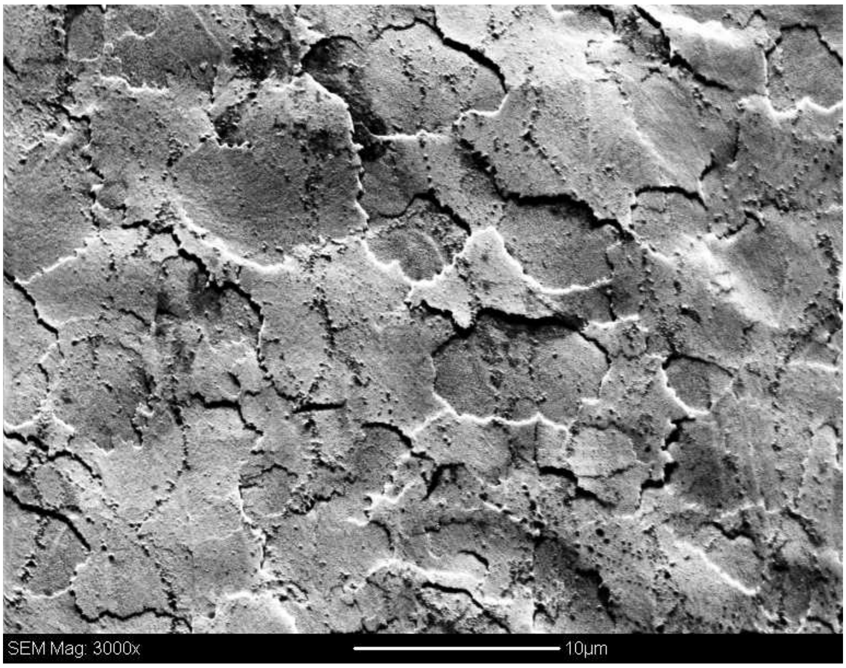

图 3-3 未熔模式下 20 次轰击 FeAl 合金表面的典型 SEM 形貌像

Fig. 3-3 Typical SEM micrograph on the 20 pulsed FeAl sample under heating mode.

3.2.2 熔化处理模式下的表面形貌

火山坑是熔化处理模式下的典型形貌特征。在某些情况下火山喷发还对表面均匀化起着重要作用。图 3-4 显示了 5 次轰击处理下 D2 钢样品表面的背散形貌。可以明显观察到表面形成了大量火山坑。首先，所有的火山坑内都显示出由中心向边缘的辐射状结构。这表明火山坑的形成是从心部喷发。其次，火山坑内部的衬度比其周围区域深，这表明在样品表面存在成分差异。最后，在火山坑心部或内部可以发现被喷发出来的呈灰白色衬度的碳化物。同时，表面还分布着一些未完全熔化的呈黑色衬度的碳化物，它们的形状接近圆形。这表明在 5 脉冲轰击下：(一)碳化物是火山喷发形成的原因 (二)不涉及火山坑喷发的碳化物发生了部分液相熔解。碳化物具有校低熔点，其导热性远远低于金属基体。因此，在脉冲处理过程中，碳化物将发生过热喷发，而随后的快速凝固和冷却使得喷发的形貌保留下来，从而在表面形成火山坑。这种喷发还能起到分裂碳化物的效果。随着轰击次数的增加，越来越多的碳化物被喷发或熔解，使得火山坑得以形核的位置大大减少，形成效率降低。本文及以往的研究结果表明，对某种材料的脉冲处理过程中，增加轰击次数在处理初期使得火山坑密度大大增加。进一步提高轰击次数则导致火山坑密度下降。这是由于多次轰击使表层均匀化。

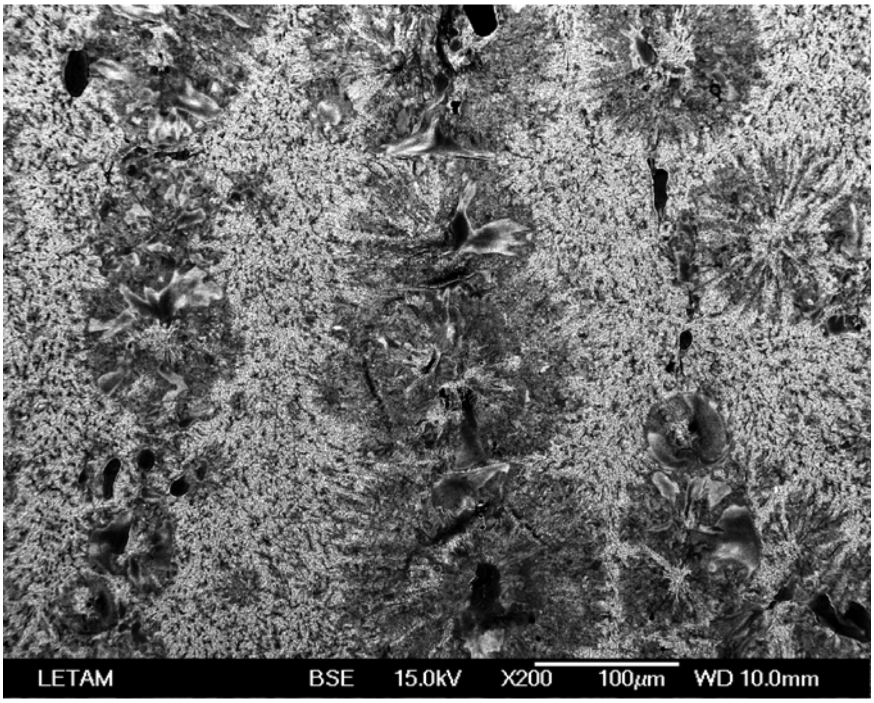

图 3-4 5 次轰击 D2 模具钢表面典型的背散射电子（BSE）形貌像
Fig. 3-4 Typical BSE surface micrograph of the D2 sample treated with 5 pulses.

3.2.3 汽化处理模式下的表面形貌

如前所述，当电子束能量密度足够高时，将使轰击材料表层达到沸点，产生汽化。图 3-5 显示了纯镁在汽化处理模式下的典型表面形貌。此时的表面形貌显著地不同于熔化处理模式下的火山口形貌，而是由分立的近圆形突起物以及分布在其上和其间的大量小颗粒组成。小颗粒的尺寸约在微米至亚微米量级，呈扁平状而不是球状，暗示着这些颗粒是以一定速率落在表面之上的。对小颗粒进行能谱分析，结果表明这些颗粒不含氧，均为纯镁。对于这种形貌的形成机制，可以用以下过程来描述。当表面达到沸点后，汽化同时在表层一定范围内进行，液体中将产生大量气泡。这些气泡达到表面之后就会破裂，对周围产生一定的冲击，并在表面以上凝结出大量小液滴，类似于水的剧烈沸腾，这也使得液体的表面起伏不平，呈叠加的波纹状。由于处理时，靶材的表面是与重力方向平行的，因而蒸发出的小液滴不会在重力作用下回到表面，但此时脉冲电子束流还没有结束，小液滴就会在电子束流作用下充上负电。带负电的小液滴将在电子束的电场力作用下被排斥回阳极，与此同时，固液界面也在很快向表面方向移动，速率约为 3～5m/s，达到表面附近时，由于液体起伏不平，凹下的部分将首先凝固，而凸起的部分后凝固，并在表面张力作用下收缩成近圆形。最后，小液滴将以一定速率落在整个表面之上。在

汽化处理模式下的 NiTi 合金表面也观察到了这种表面起伏加小颗粒的特殊形貌，而表层成分随深度方向的特殊变化也证实了以上的蒸发和沉积过程。

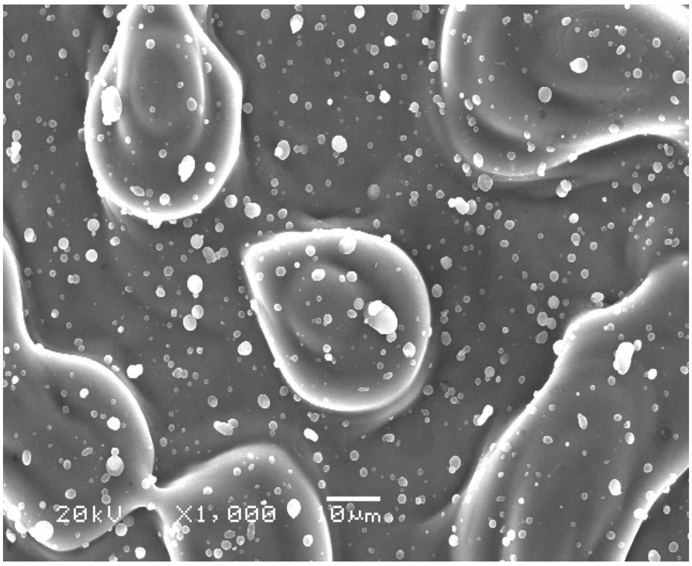

图 3-5 纯镁在汽化处理模式下表面典型的 SEM 形貌像

Fig. 3-5 Typical surface SEM micrograph of pure Mg after HCPEB treatment under evaporation mode.

3.3 表面选择净化与均匀化

3.3.1 未熔处理模式下的表层净化

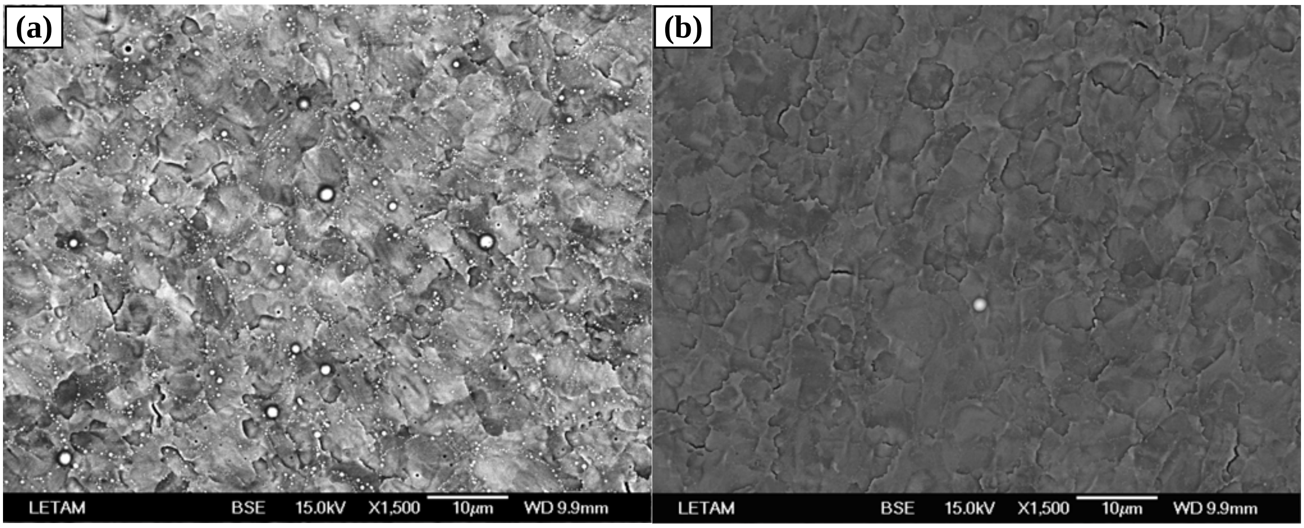

图 3-6 FeAl 合金在未熔处理模式下 5 次（a）及 20 次（b）轰击表面典型的 SEM 形貌像

Fig. 3-6 Typical BSE micrographs observed on the surface of the 5 pulsed (a) and 20 pulsed (b) samples.

图 3-6 显示了在未熔处理模式下氧化物弥散强化铁铝（Fe(40at%)Al＋1wt％ Y_2O_3）样品典型的表面背散射形貌。经过 5 次强流脉冲电子束轰击，表面明显可见许多突出的球形颗粒。经过 20 次轰击后，这些氧化钇颗粒几乎完全被清除。进一步的透射电镜观察证实了选择性净化可在未熔处理模式下发生。这是由于氧化物的导热性很差，在处理过程中发生了局部熔化并在后续的脉冲中被溅射掉。

3.3.2 熔化处理模式下的表层净化

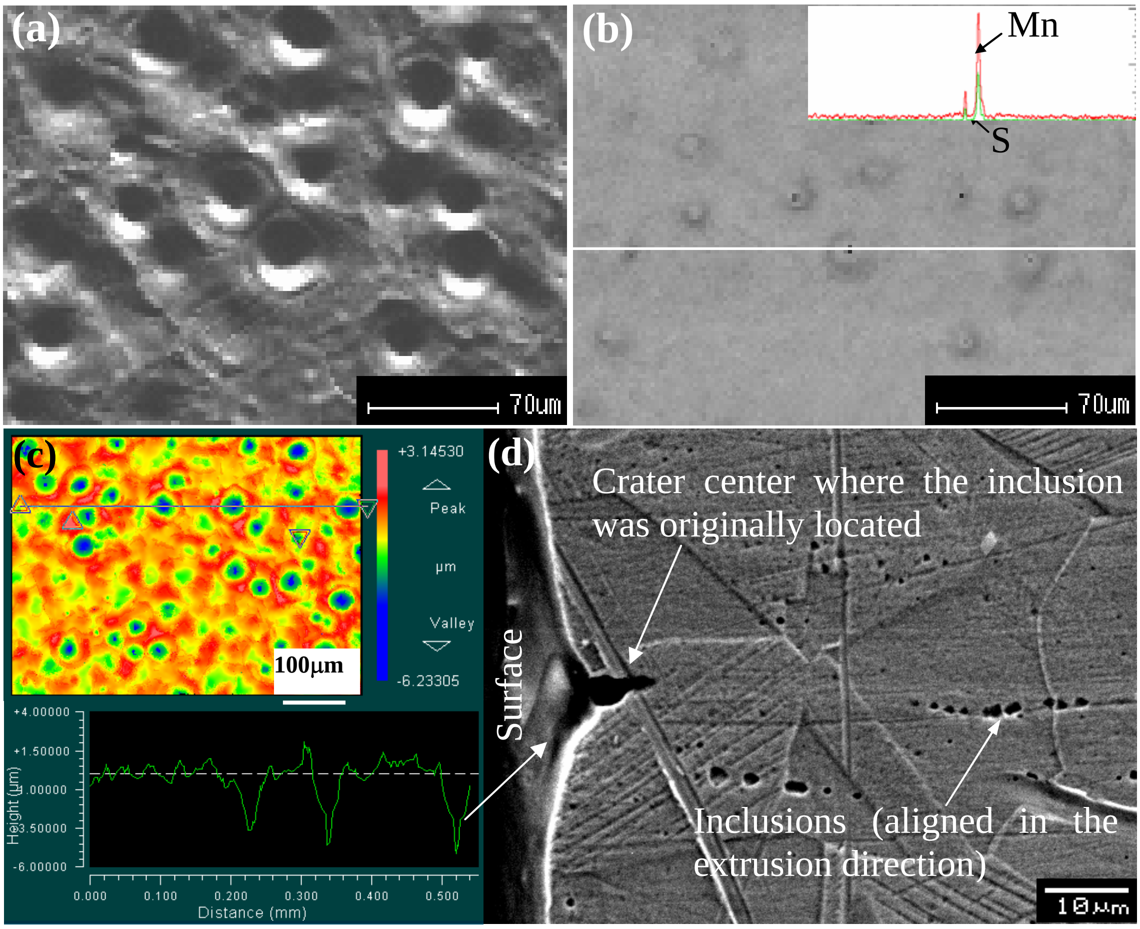

图 3-7 316L 不锈钢 5 次轰击后表面典型的 SEM（a）及对应的背散射像（b）。图 b 中的线扫描表明火山坑中心为 MnS 夹杂。图 c 为 5 次轰击后表面典型的三维形貌像，而图 d 则为火山坑截面的典型形貌

Fig. 3-7 Secondary electron images (a) and its corresponding backscattered electron images (b) of the 316L sample treated for 5 pulses. The line scans show that the black spots are remnants of MnS. Fig. c shows a typical laser 3 dimensional morphology on the 5 pulse treated 316L sample and a line scan of relative height which crosses 3 craters. Fig. d is a SEM image showing the typical aspect of a crater viewed on cross section of the 316L sample treated for 5 pulses.

在熔化处理模式下材料表面形成的火山坑通常被认为是一种缺陷，不利于处理后的表面性能，尤其是耐蚀性。这里我们以 316L 不锈钢为例研究火山坑的形成机制，并显示火山坑形成的有利方面。图 3-7a 是 5 次轰击后样品的二次电子像，图 3-7b 为相应的背散射像。图 3-7a 中可以观察到样品表面在轰击后生成许多火山坑。在图 3-7b 中，一些黑点存在于样品表面。对比图 3-7a 与图 3-7b，可以发现这些黑点总是位于火山坑的中心位置。为了确定火山坑中心处黑点的成分,对其做了线扫描及面成分分析。图 3-7b 中白线上的线扫描分析结果表明黑点为富 Mn 和 S 的 MnS 相。与原始态相比，MnS 的数量已经大大降低。上述结果表明在电子束轰击的过程中，MnS 夹杂物是轰击过程中诱发火山坑的核心。图 3-7c 为 5 次轰击后 316L 不锈钢样品的典型表面激光三维形貌投影图，从中可以更直观的看出表面火山坑（蓝色区域）的形貌。火山坑的直径大约在 50 微米左右，心部向下凹陷。对图中穿过三个火山坑的一条横线进行了相对高度的线扫描分析，结果示于图 3-7c 下部。从线扫描结果中可以清楚的观察到火山坑的实际形状非常接近于漏斗，其中心近似垂直延伸到表层之下数微米深，这种形貌暗示着在火山喷发过程中其心部有条状固态物质被携带喷发出表面。采用扫描电镜对 5 次轰击后的样品截面进行分析，结果如图 3-7d。其中包含一个火山坑。其形貌与激光三维测量结果吻合，由此可以进一步推断这种特殊的形状是由液态物质从次表层喷发并携带部分固体而形成的。正是这种在夹杂物处的火山喷发实现了材料表层的选择性净化。

3.4 应力状态与深层改性

前文中已经指出，脉冲电子束诱发的热应力具有各向异性。当轰击次数较多时，可以从不同晶粒上观察到累积的各向异性形变。这里我们通过 316L不锈钢来显示各向异性形变。由于其层错能较低，因而可通过孪晶和位错滑移两种方式变形。图 3-8a为 316L 不锈钢在 10 次轰击下表面典型的EBSD取向图。图中可以明显发现轰击后形成的大量条带状孪晶粒，其宽度在几百纳米到几个微米之间。它们多出现在蓝色晶粒中，而晶粒呈蓝色表明其<110>晶向接近平行样品法向（ND）。这表明在这些晶粒中的主要变形机制是孪生。所有孪晶片呈红色或近红色是由于孪生过程中发生的 60^{o}的切变((111)面与(100)面的夹角是 54.7^{o})。图 8b是图 3-8a中标“A”的晶粒的极图。从中可以发现 3 个系列的孪晶，其<100>方向均接近平行于ND。那些呈红色的晶粒内则不出现孪晶，但是内部颜色略有区别。对应的扫描形貌显示这些晶粒表面存在大量滑移线。这表明，在这些取向的晶粒中位错滑移是主要的变形模式。在图 3-8a中对一个红色晶粒中所示的白线进行了取向差线扫描，结果示于图 3-8c。可以看到在同一晶粒中的取向差可高达 12 度。

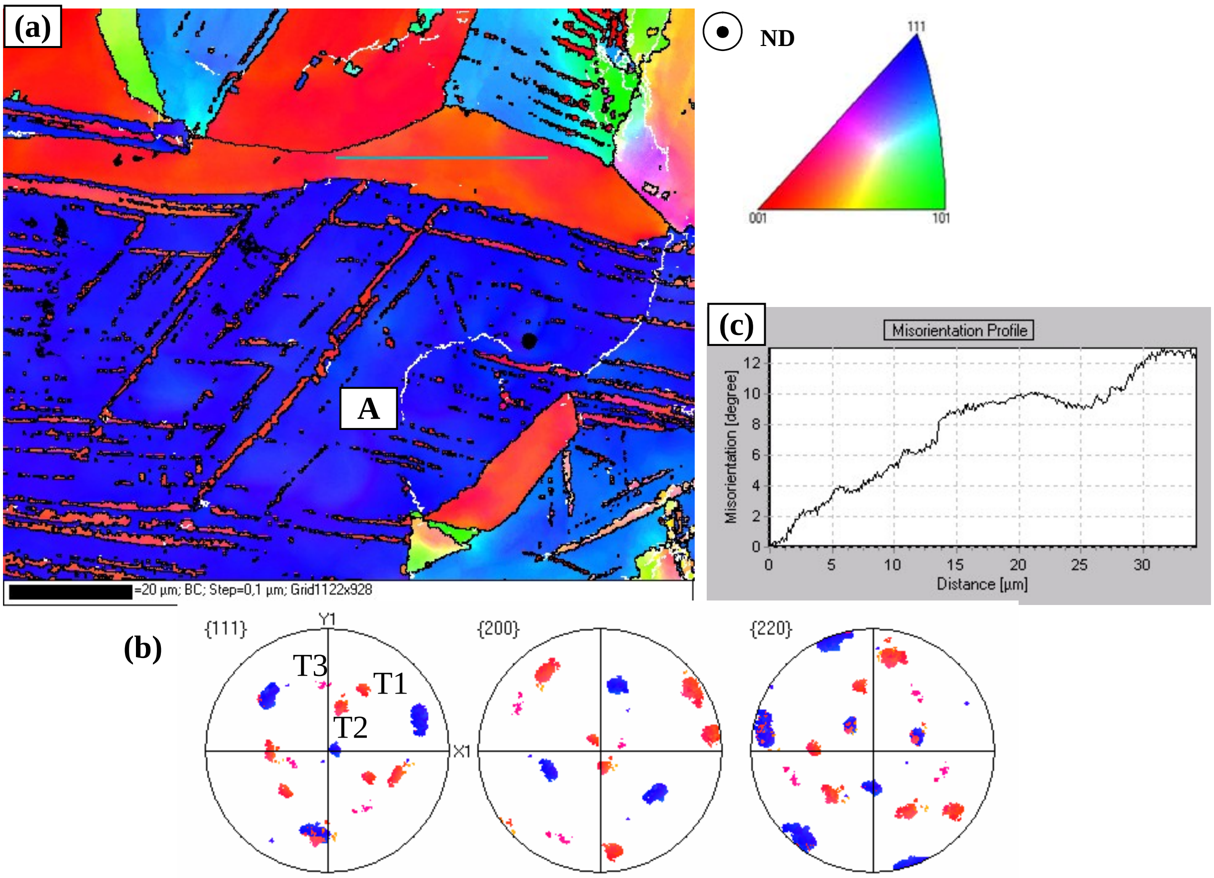

图 3-8 316L 不锈钢在未熔模式下 10 次轰击后表面典型的 EBSD 取向图（a），其中 A 晶粒对应的极图（b）及白线上的取向差分布（c）

Fig. 3-8 Typical EBSD OIM map measured on the 10 pulsed 316L sample (a), pole figures corresponding to a grain marked ‘A’ and a line scan of misorientation along the marked line (b).

3.5 表层织构改变

在不同的处理模式下，强流脉冲电子束轰击可能引发材料表层超快速加热、变形、熔化、蒸发和凝固。从晶体学的观点来看，以上任一过程都可能会改变表层的晶粒取向，从而改变表层的织构。而对脉冲电子束诱发的表层织构变化只是在最近才得到研究。这里，我们将显示并讨论三种处理模式下可能的表层织构变化及其相应的机制。

3.5.1 熔化处理模式下的表层织构变化

我们用 XRD 方法测量了 D2 钢经 25 次轰击后表层奥氏体的织构。结果表明快速凝固而成的奥氏体存在弱而分散的<200>纤维织构。此外，还同时存在着一个相对尖锐的<220>纤维织构。然而总体来说，这两种纤维织构非常弱，最高强度只略高于 2 倍随机取向，其形成都是以牺牲<111>取向晶粒为代价的。

在脉冲电子束处理下形成的这种特殊混合纤维织构可由如下过程来解释。通常，凝固过程可以分为两个阶段，即开始凝固过程的形核和晶粒的进一步生长。由于重熔层是在未熔化的亚表层上凝固，形核过程将可能受到未熔化基体晶粒取向的影响。XRD 测量表明，D2 钢轰击前后铁素体基体均不存在择优取向。也就是说，奥氏体的形核应为随机过程。通常，晶粒应沿着热梯度方向按特定的晶体学方向进行生长，因此，晶粒的生长方向应为〈200〉方向，在快速凝固条件下也是如此。在随机形核的条件下，生长过程将抑制非〈200〉取向晶粒的生长。同时又由于重熔层非常薄(2~3 微米)，这种选择生长过程不能充分进行，从而不难理解存在弱而分散的〈200〉纤维织构。然而，同时存在的〈220〉纤维织构却很难解释，因为（100）面与（110）面间的夹角高达 45°。在对铝合金快速定向凝固的研究过程中，EBSD 分析显示晶粒生长的择优取向可随合金成分改变，这一过程被规因于溶质的饱和度对原子动力学附着的改变。Henry 等人还发现，在铝合金凝固过程〈220〉方向生长的枝晶是通过孪生方式从〈200〉方向生长的枝晶上长出的。对 D2 钢表层奥氏体进行了 EBSD 分析，结果也发现奥氏体晶粒间存在较高比例的孪晶界。这些孪晶界通常存在于两个〈220〉取向的晶粒间。对应于已往的研究结果，本文的结果揭示出在非常不同的凝固条件下，晶粒生长方向的转变不仅可能发生在铝基合金里〔32,40-42〕也能发生在铁基合金中。而最近的理论与实验分析表明，熔体的成分和晶体各向异性参数可以连续改变凝固过程中晶体生长的择优取向。对于 D2 钢，25 次脉冲轰击后，由于碳化物的大量熔解，熔体中 Cr 与 C 均为过饱和状态，同时凝固过程非常迅速，这可大大改变原子动力学附着过程及晶粒择优生长取向。以上过程也显示，强流脉冲电子束技术可以成为一种有效控制金属材料表面织构的方法。

3.5.2 未熔处理模式下的表层织构变化

这里我们以FeAl金属间化合物为例研究脉冲电子束在未熔处理模式下对表层织构的改变。原始样为 1250^{o}C下热挤压成棒状的氧化物弥散强化铁铝（Fe（at%）Al＋1 wt% Y_2O_3）金属间化合物。垂直于轴向将棒切成圆片，然后在未熔模式下采用强流脉冲电子束对样品进行处理。图 3-9a为原始样品典型的EBSD取向图，标准颜色三角形示于图右上角。 可以明显看到，大部分晶粒呈绿色。对应的反极图（图 3-9b）显示，原始样存在较强的<110>纤维织构//ND，强度约为 6.5 倍随机取向。图 3-9c为原始样的晶界取向差分布，接近于完全退火状态下的分布，只在小角晶界处比例略高。图 9d为 20 次脉冲处理样品典型的EBSD取向图。晶粒的颜色相对原始样发生了明显改变，表明织构有所变化。对应的反极图（图 3-9e）显示，处理后样品表层的织构为弱而分散的<321>纤维，其强度最高约 3 倍随机取向。20 次脉冲处理后晶界取向差分布也大大改变，其中小角晶界比例大幅上升。

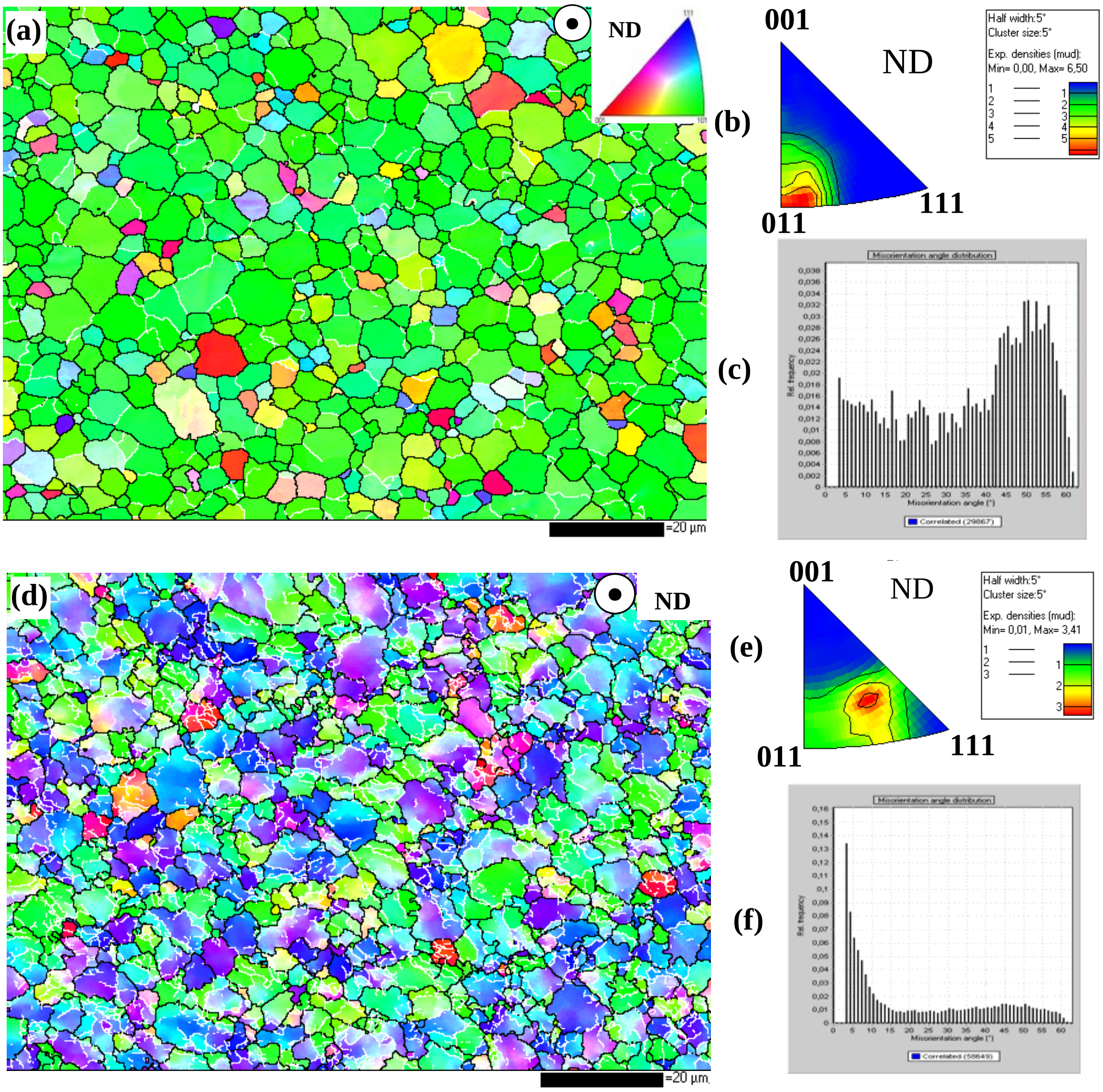

图 3-9 FeAl 合金原始样（a）及在未熔模式下 20 次轰击后表面典型的 EBSD 取向图（d），对应的反极图（b,e）和晶粒取向差分布（c,f）

Fig. 3-9 EBSD orientation map on the surface of the treated FeAl samples (a – initial sample, d-20 pulsed sample), corresponding inversed pole figures (b,e) and grain boundary misorientation distributions (c,f).

采用前一章中建立的物理模型和数值计算方法，我们模拟计算了在本实验条件下Fe（40at%）Al样品表层的瞬时热循环过程。计算结果显示，表层在处理过程中 0.7 微秒时达到最高温度，约 1510 K，而Fe（40at%）Al的熔点为 1653 K。计算结果确认此时所用的能量不足以导致表面熔化。在表面发生熔化之前，热弹性应力波由于幅值很小可以忽略，而准静态热应力则起着主要作用。Fe（40at%）Al合金的杨氏模量是随温度变化的，例如室温下E＝170 GPa，而在 773 K时E=110 GPa。计算表明热应力的最高幅值可

达 2 GPa，这远远高于合金的屈服强度从而使表层发生形变。Fe（40at%）Al的线膨胀系数α是温度的函数，$\alpha \approx 1.483\times10^{-5}+6.7\times10^{-9}T$ m/m•K，体膨胀系数为 3α，可以估算在限制水平方向膨胀的情况下，在温度到达 1510 K时的总热变形量约 7.6%左右，这是理论上单次轰击所能达到的最大变形量。经过 20 次轰击, 总变形量可高达 152%。这样大的形变量结合热循环过程中的回复和再结晶过程足以显著改变材料表层的织构。大量小角晶界的形成正是快速形变与回复和再结晶过程的结果。

3.5.3 汽化处理模式下的表层织构变化

图 3-10a 与 3-10b 分别为 10 次轰击后 NiTi 合金样品表面的 EBSD 取向图以及对应的极图。表面所有晶粒都可以标定为 NiTi 奥氏体相（B2 结构），而图中黑色带状区域内的晶粒取向无法标定，这是由马氏体相变造成的。图 10a 中可以明显发现表层存在大小两种晶粒。小晶粒绝大多数晶粒呈绿色，并附着在大晶粒之上。这些绿色晶粒的{110}晶面垂直或接近垂直于样品表面法向。仔细观察可以发现，小晶粒的取向（颜色）与其下方的大晶粒取向（颜色）并无关系。这表明小晶粒并不是在大晶粒上外延生长而成的。同时，在取向图上还随机地分布着一些红色小晶粒。图 10b 的极图中包含了若干个圆环，说明 10 次轰击后样品表面形成的织构为纤维型织构。该纤维织构主要由平行于法向的强〈110〉织构和弱〈100〉织构组成。

在熔化和蒸发之后，冷凝的蒸汽将沉积在样品表面，并以 10^7 K/s的速率发生快速凝固，这将导致在合金的外表面形成超细的B2 晶粒。沉积的晶粒形核与生长可能受到基体大晶粒原有取向的影响。然而EBSD分析显示表层的小晶粒并不是简单的外延生长。无论其下的大晶粒是什么取相，小晶粒都呈近〈110〉或〈100〉的取向。通常，晶粒应沿着热梯度方向按晶体学方向进行生长，因此， NiTi（立方晶系）晶粒的生长方向应为〈100〉方向，在快速凝固条件下也是如此。例如，在甩带的 NiTi 合金中,$\langle100\rangle_{B2}$ 织构就是平行于热梯度方向进行生长的。在一些透明材料及铝合金中已有报道，尤其在沿高热梯度方向凝固的铝合金中，生长方向可直接通过孪晶方式由〈100〉变为〈110〉，这与过饱和固溶度提高后原子的附着动力学的改变有关。然而在 10 次轰击的NiTi表层，很多小晶粒是独立存在的，聚集存在的小晶粒间通常也没有孪晶关系。因此，蒸发和冷凝沉积可能是产生〈110〉织构的原因。在处理过程中的某一时间点，凝固和蒸发两种机制必将同时起作用。在凝固作用下，原子不断从液态迁移出来堆垛凝成固体。同时，蒸发过程在反方向上产生了原子流。在蒸发模式下，原子以几百m/s的速率运动，这比凝固前沿的移动速率要大的多，因此晶粒的生长在很大程度上受到蒸发的影响。蒸发模式引起大量原子沿固/液界面进行迁移，从而彻底改变凝固过程中的原子附着情况。蒸发

在影响凝固过程的同时，一些蒸汽中的小液滴又重新沉积到表面上形成单个的小晶粒。蒸汽沉积过程的分析表明多种因素影响着晶粒的择优生长方向，比如蒸汽压，基体取向，沉积温度等，这些还需要进一步的详细研究。

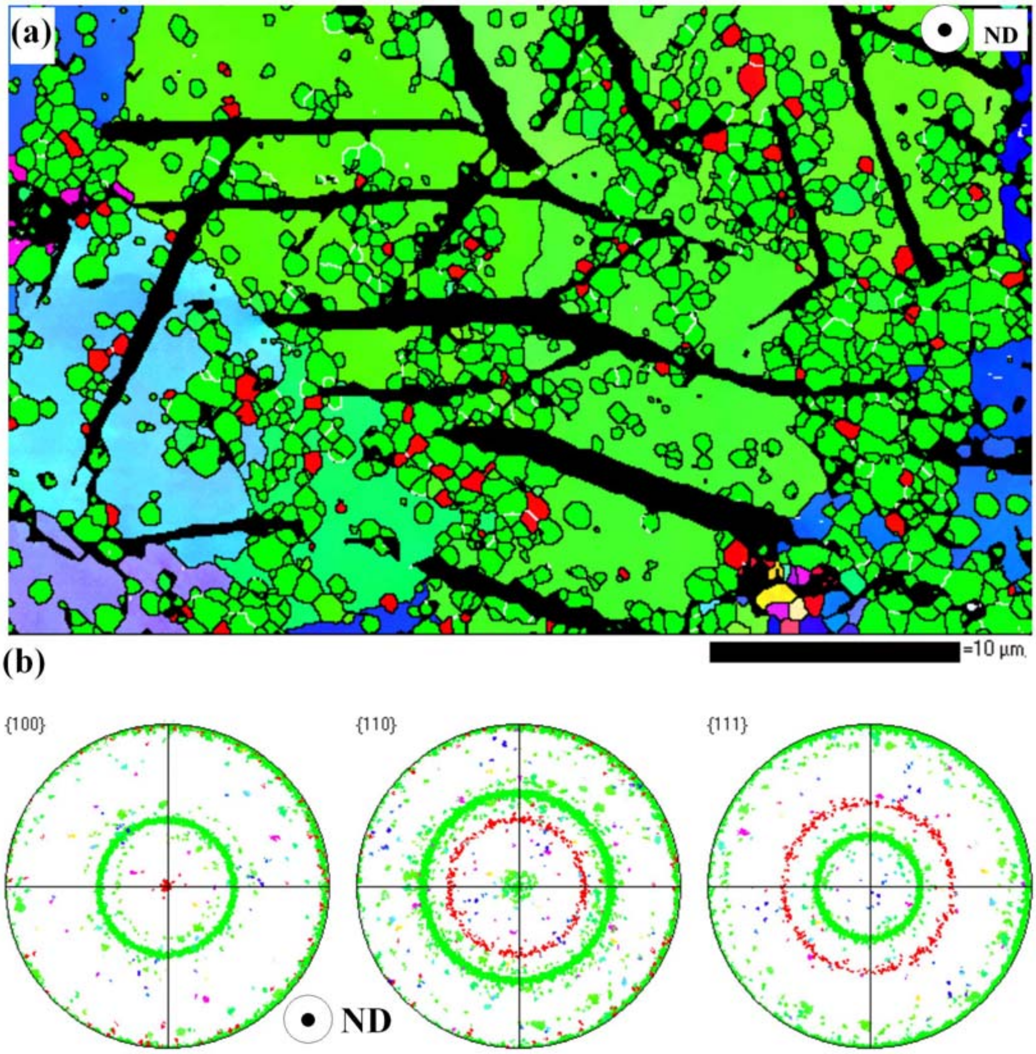

图 3-10 NiTi 合金在汽化模式下 10 次轰击后表面典型的 EBSD 取向图（a）和对应的极图（b）

Fig. 3-10 Typica EBSD OIM map (a) and the pole figures (b) of the surface of the 10 pulsed NiTi sample under evaporating mode.

4 强流脉冲电子束材料表面改性的应用

开发和研究强流脉冲电子束技术的最终目的是将其应用于工业生产中的材料表面处理环节。过去十年中的研究已经清楚表明，脉冲电子束轰击材料表面可导致表层形成快速变化的非稳态温度场以及高强度应力场，冲击波等。在前两章中我们已经讨论了这些复杂的物理过程以及由这些过程所诱发的各种特殊效应。经过脉冲处理的材料表面可形成一层改性层，其特殊的成分，相组成与微结构使材料往往具有常规表面处理技术所无法达到的物理、化学和机械性能。 以往的研究显示，脉冲处理可使许多钢、合金的耐磨损和耐腐蚀性大大提高。而处理后材料的最终结构和性能都强烈依赖于电子束能量密度、脉冲次数和材料的物性参数。本章中，我们将讨论强流脉冲电子束在前述的三种处理模式下的可能应用。

4.1 表面硬化及软化

脉冲电子束对材料性能的一个重要的影响作用是可以改变处理材料的硬度。通常一种材料的硬度取决于其微结构和应力应变状态等多种因素，如晶粒尺寸、相组成和残余应力。如前所述，脉冲电子束轰击处理可在很大程度上改变这些因素，从而改变材料的硬度。事实上，脉冲轰击既可能造成材料表层硬化也可以实现软化，这取决于电子束参数的选择与材料物性参数。这里，我们将给出轰击诱发材料表面硬化和软化的例子。

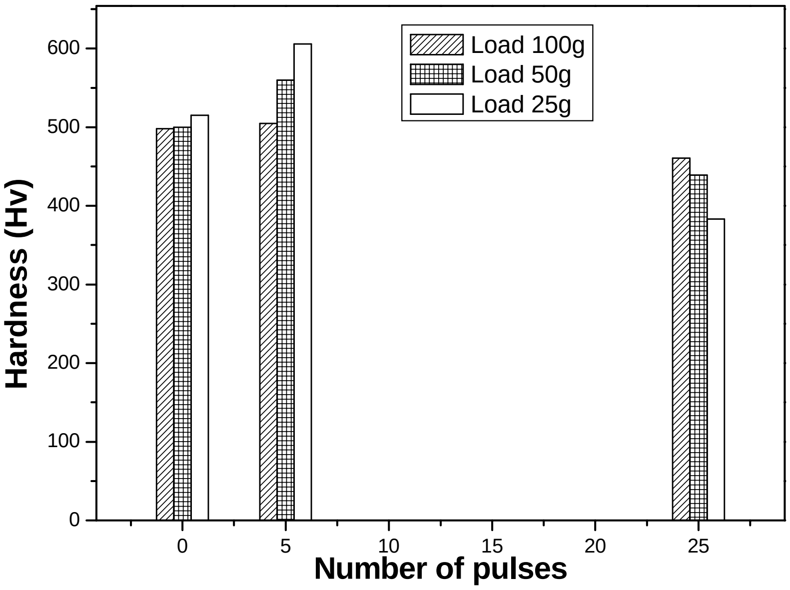

图 4-1 D2 钢脉冲处理前后在不同载荷下的表面维氏硬度

Fig. 4-1 Surface Vicker’s hardness of AISI D2 steel samples before and after HCPEB treatments under different loads.

我们采用不同载荷测量了 D2 钢样品在 5 次和 25 次轰击下的表面硬度，载荷分别为 25 g、50 g 和 100 g。结果归纳于图 4-1 中。原始样品的硬度约为 500 Hv，它不随载荷大小而改变。经过 5 次轰击，硬度明显比原始样有所提高，而载荷增加则导致硬度测量值下降。从微结构分析可知，经过 5 次轰击的 D2 钢，其最表层生成了马氏体，这导致表层硬度提高。而马氏体仅局限于表面层顶部，随着载荷的提高，下方较软基体的影响增大因而硬度测量值下降。 对于 25 次脉冲的样品，其硬度明显下降，并且随载荷的降低其下降愈为明显。显然，经过 25 次轰击后表层硬度下降是由于凝固形成了奥氏体，其硬度较低。而奥氏体也仅存在于表面重熔层中，随着载荷的提高，下方较硬基体的影响增大因而硬度测量值上升。

对多种碳钢、合金钢及不锈钢处理后的硬度测试表明，表面硬度取决于最终的相组成。如果表面生成了马氏体则硬度升高，而生成了奥氏体则硬度下降。当表层不发生相变时，残余应力、表层晶粒大小、空位及位错密度等导致表层硬度改变。

4.2 表面快速合金化

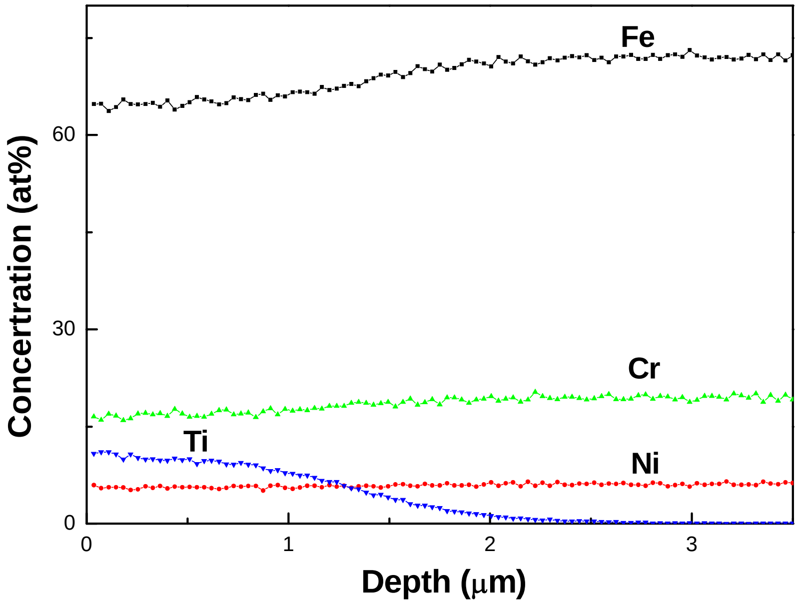

图 4-2 316L 不锈钢表面脉冲电子束 20 次轰击 Ti 合金化后的成分分布曲线

Fig. 4-2 Composition profiles of 316L stainless steel sample after surface alloying by HCPEB with 20 pulses.

高能束表面合金化是近年发展起来的新兴技术，采用高能密度的激光束、电子束在很短时间内在材料表面沉积很高的能量，形成熔化、汽化、应力波、冲击波等物理现象，从而能够快速有效的将预先涂覆的合金元素熔入基体中形成非平衡的过饱和固溶体，使

材料表面具有特殊的物理、化学性能。在以往的实验研究中，我们利用强流脉冲电子束源进行了纯铝表面渗碳，模具钢的表面电子束渗Cr等实验研究，结果表明经过电子束快速表面合金化能够显著提高模具钢的耐磨性。这里，我们以316L不锈钢表面Ti合金化为例显示脉冲电子束合金化过程及其应用。将精细钛粉预涂在样品表面上，采用能量密度~3 J/cm^{2}的脉冲电子束轰击20次。XRD测试结果表明，表面合金化层由α相和γ相组成，这是由于Ti是α相形成元素的缘故。采用SNMS测试了处理后的表层成分，分析结果示于图 4-2。最表层的Ti浓度约为百分之十左右，其含量随深度增加而降低，合金层厚度可达2.5微米。进一步研究表明，表层在熔化过程中的液体混合是促成合金化的主要原因。对未处理样品和钛合金化样品在模拟体液中的腐蚀性能进行了测试，极化曲线显示316L不锈钢经电子束表面合金化后耐蚀性明显改善。

4.3 表面增强扩散

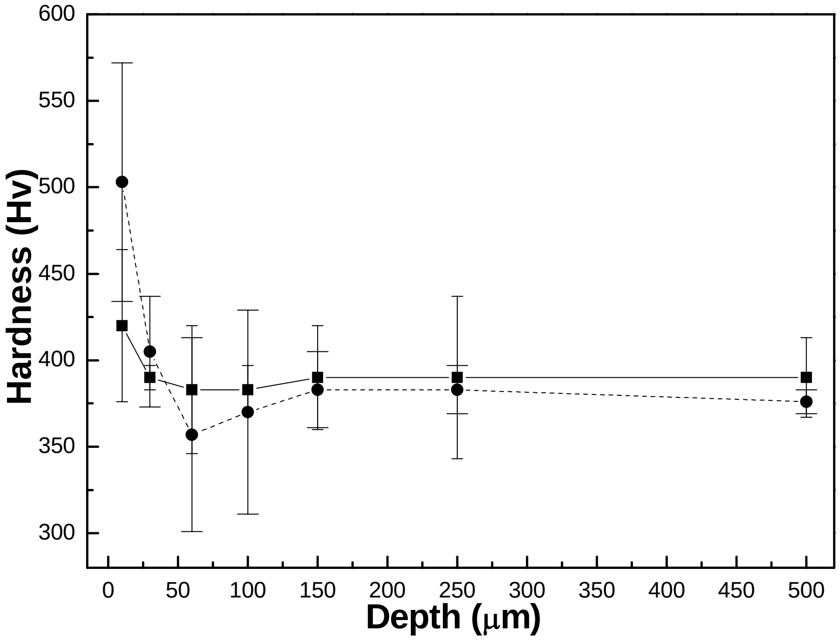

图 4-3 脉冲电子束处理对 Fe-40Al 合金硬度的影响

Fig. 4-3 Effect of the HCPEB treatment on hardening the Fe-40Al intermetallic. Samples treated for 2 pulses with (rounded symbols) and without (squared symbols) the presence of a previously deposited graphite layer.

对Ti离子注入9Cr18钢采用强流脉冲电子束未熔模式下进行表面后处理发现了明显的增强扩散效应，仅仅用几次脉冲轰击就可以使注入元素的分布显著加深。相应的模拟计算显示，在HCPEB表面改性过程中，存在高的非平衡空位浓度和梯度，从而使元素

的扩散激活能下降，因此扩散系数大大增加，从而产生了增强扩散效应。为了显示增强扩散效应对材料性能的影响及可能的应用，我们对 FeAl 合金进行了脉冲电子束表面渗碳处理。将碳粉刷涂于样品表面并在未熔处理模式下用电子束轰击，同时放置并行空白样做对比处理。图 4-3 显示了在 2 次脉冲下渗碳样与直接处理样的截面硬度与深度剖面。很明显，渗碳样品的表面硬度要高于直接处理样，比原始样则高出约 100 Hv 左右。这显示了 C 在脉冲处理中发生了快速的扩散。而 C 对 FeAl 合金的硬化效果则可归因于 C 和 FeAl 合金中空位的相互作用或可能的碳化物析出强化。脉冲电子束诱发的增强扩散效应可提高材料表面硬度，改变表层化学成分，因而可用于提高材料表面的机械及化学性能。

4.4 提高耐蚀性

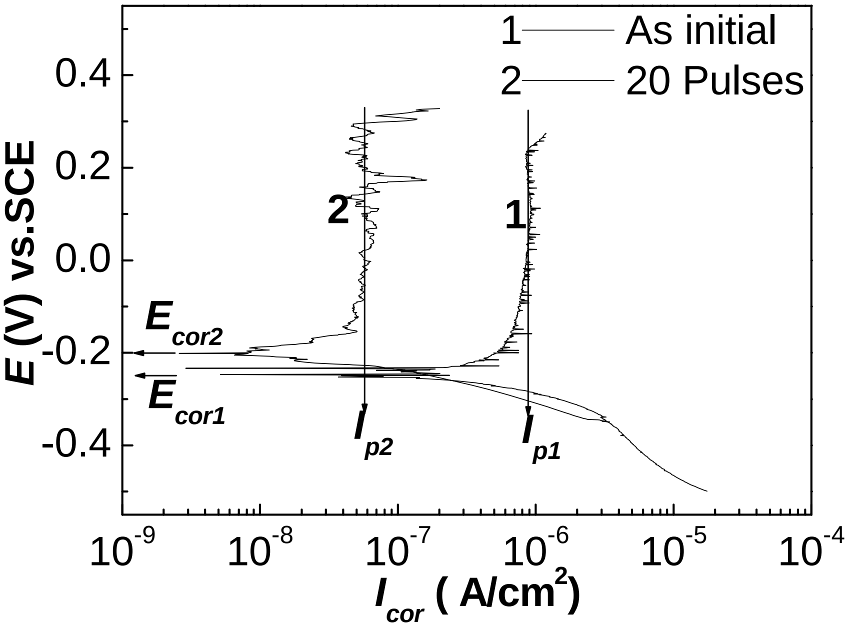

图 4-4 316L 不锈钢脉冲电子束处理前后在模拟体液中的极化曲线

Fig. 4-4 Potentiodynamic polarization curves of 316LSS sample in Tyrode’s simulated body fluid before and after HCPEB with 20 pulses.

在第三章中，我们讨论了脉冲电子束在熔化模式下诱发的表层选择净化作用。由于材料的腐蚀通常优先发生在表层的夹杂物处，特别是不锈钢在卤素离子存在环境中的点蚀，因而表层净化应该能够有效的提高材料的耐蚀性。图 4-4 为电子束处理前后 316L 不锈钢样品在模拟体液中的动态极化曲线。与原始样品相比，20 次脉冲电子束处理后的样品具有大大降低的钝化电流密度(i_p)和更高的腐蚀电位（E_{cor}）。在所考察的整个电位

范围内，20 次轰击后样品的腐蚀电流密度较原始样品低一个数量级。表层钝化膜的击穿电位(E_{brk})也由原始样品的 233 mV增至 20 次轰击后样品的 342 mV。以上结果证明经强流脉冲电子束表面处理后，316L不锈钢的耐蚀性得到了显著提高。详细的研究表明，腐蚀性能的提高与表面MnS夹杂的清除直接相关。

脉冲电子束在汽化处理模式下的选择蒸发效应可以有效改变材料表层成分。对 Mg 合金及 NiTi 合金的汽化处理结构显示，在弱蒸发条件下，材料的耐蚀性可以得到有效提高，这是由于表层对耐蚀性有利的元素，如 Mg 合金中的 Al 以及 NiTi 合金中的 Ti，通过选择蒸发作用在表层富集。

4.5 提高耐磨性

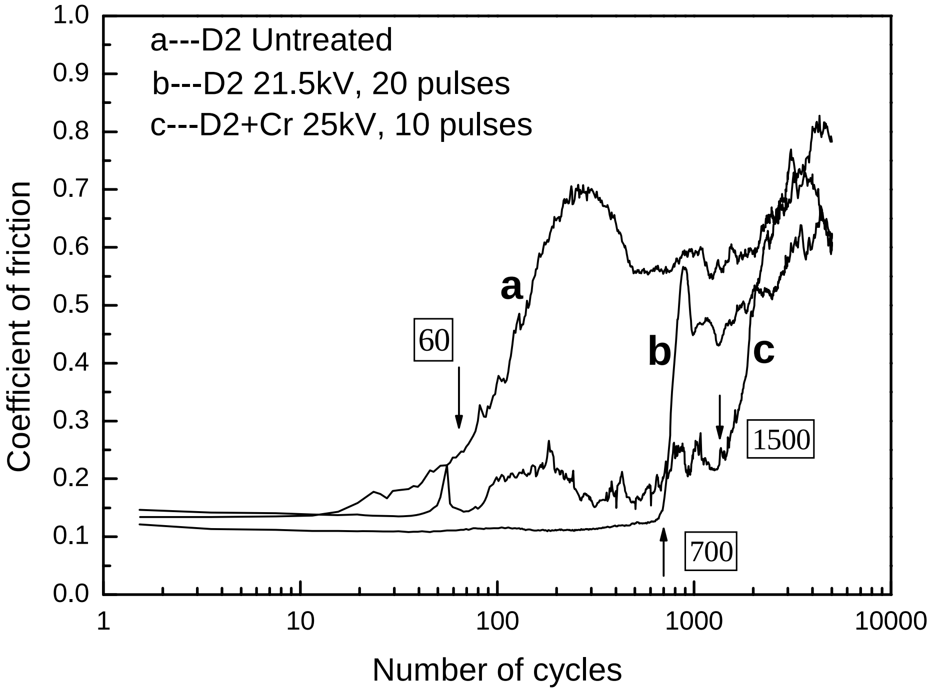

图 4-5 D2 钢脉冲电子束处理前后摩擦系数随循环次数变化曲线，载荷 100 N，位移 150 μm，循环次数 50000 次

Fig. 4-5 Coefficient of friction vs. number of fretting cycles for the samples before and after HCPEB treatments, F_n=100 N, N=5000 cycles, D=150 μm.

对多种钢材的强流脉冲电子束处理结果表明材料的磨损性能可以得到显著提高。一个典型的例子是 D2 模具钢的强流脉冲电子束表面改性处理。图 4-5 显示了处理前后 D2 钢样品的微动摩擦系数随循环次数变化情况。在低滑动位移条件下（30μm）处理后的样品的微动摩擦系数同样比未处理过的 D2 钢要低很多，原始

样品的摩擦系数一开始就迅速升高，在滑动 60 次左右就表现出破坏的特征，滑动 250 次左右就达到最高值，然后就进入稳定磨损阶段，而处理过的样品，比如 21.5 kV 下 20 次脉冲处理试样，其摩擦系数到 700 次左右时才突然升高，在 900 次左右达到最高值以后就稳定磨损。涂覆 Cr 粉的样品，其摩擦系数在滑动到 1500 次左右才开始快速增加。由此可见，脉冲电子束直接处理或合金化均可明显改善 D2 钢的抗微动磨损性能。这可以部分归结于脉冲电子束处理后材料内部特殊的相组成、微结构和高硬度分布。脉冲电子束在汽化处理模式下的选择蒸发效应同样被证明可用于提高镁合金的耐磨损性能。

5 结论与展望

本论文详细探讨了强流脉冲电子束表面改性过程的物理基础，处理过程中所诱发的特殊效应及其可能的应用。

在对多种合金进行表面改性实验结果的基础上，我们发现脉冲处理可以简单分为三种处理模式，即未熔模式、熔化模式和汽化模式。本文建立了三种模式下温度场与应力场的物理模型，并采用数值方法对强流脉冲电子束轰击金属表面时的热、力学过程进行了研究。结果表明：由于电子束在材料内部能量的特殊分布，处理过程中熔化最先发生在材料次表层；热应力波的幅值较小，约在 0.1MPa量级，与脉冲的能量密度基本成正比而与脉冲宽度成反比；电子束轰击过程中，材料表面会产生随温度场变化的准静态热应力，其大小在数百MPa量级且具有各向异性，远大于材料在高温下的动屈服强度而使材料发生形变；纯金属在强流脉冲电子束轰击下，表层的硬化是一种快速应变下的加工硬化，应变速率可达 $10^{4\sim5}s^{-1}$；在温度场和应力场计算的基础上，对强流脉冲电子束轰击金属表面时的扩散行为进行了数值计算，结果表明，浓度扩散流仍然是影响扩散的主要因素；对实验结果和理论结果的对比分析表明，在脉冲轰击下，扩散激活能会随空位浓度增加而下降，从而加速扩散过程；在表面有熔化的情况下，则液态时的混合作用是主导因素。

本文深入研究并分析了脉冲电子束在三种模式下所诱发的多种特殊效应，如表层亚稳结构的形成、表面特殊形貌、表面选择净化、表层特殊应力状态以及表面织构化等。这些特殊现象可以在文中所建立的物理基础上来理解。在三种处理模式下，脉冲电子束轰击均被证明是一种有效改善金属材料表面特性的处理方法。其诱发的多种效应可应用于材料的表面硬化与软化、快速表面合金化、提高材料腐蚀性和耐磨性等等。

通过本文的研究结果来看，强流脉冲电子束表面改性技术无论在应用研究还是在基础研究方面均有很大潜力，而很多研究工作还尚待进一步深入，这包括如下一些方面：

1) 本文中对 FeAl 在未熔模式下的处理结果显示，这是一种非常独特的处理方式，其诱发的各种效应及性能改变的机制有待进一步研究并应用于其他材料。

2) 本文揭示，在三种处理模式下，脉冲电子束处理均可诱发表层织构的改变。其机制随处理模式不同差别很大。深入的探讨将考虑多种影响材料织构的因素，从而能够预测并控制脉冲轰击后表层织构的形成。

3) 脉冲电子束技术可以与其他表面改性技术相结合从而具有更广泛的应用前景，例如脉冲轰击在材料表面诱发的火山坑可以用来提高后续镀膜的结合力。

4) 在理论研究方面，对脉冲束诱发的应力场所建立的模型还有待于进一步完善，例如考虑高温下的塑性形变与高速形变下材料的特殊响应。另外，温度场与应力场的模型还有待于扩展到二维甚至三维的情况下，这样就可以更好的模拟并解释一些由材料自身不均匀而导致的温度场及应力场不均匀分布。

创新点摘要

1. 首次按照改性效果对不同金属材料的强流脉冲电子束表面改性进行了分类。分别建立了材料在“未熔”、“熔化”及“蒸发”三种脉冲处理模式下的物理机制，并揭示了在不同模式下诱发的各种效应及可能的应用。
2. 利用 EBSD 技术定量分析了脉冲电子束轰击在不同材料表层诱发的织构转变，根据不同处理模式给出了相应的解释。

致　　谢

本论文是在大连理工大学董闯教授和法国梅斯大学 Thierry Grosdidier（高泰瑞）教授的共同悉心指导下完成的。导师们渊博的知识、敏锐的眼光、严谨的态度和孜孜以求的精神令我受益匪浅。导师的严格培养，使我的知识水平、科研能力和创新意识都得到了很大的提高，为今后的工作打下了坚实的基础。

本文的实验工作是在大连理工大学三束材料表面改性国家重点实验室和法国梅斯大学材料织构的研究与应用实验室（LETAM UMR CNRS 7078）完成的。感谢郝胜智、吴爱民、秦颖博士在论文的计算与实验工作中卓有成效的讨论和无私的帮助与指导。感谢三束实验室关心和帮助过我的各位老师和同学们！在梅斯大学的学习与生活过程中，与嵇罡、张宇东，从道永、王珏、佟伟平、Daniel、Juan、Lionel、Suhash、Ananthi、Francois 等同学和老师结下了深厚的友谊。在此向他们致以诚挚的感谢。同时非常感谢 Nathalie Gey，Bernard Bolle 在实验及数据分析过程中给予的指导与大力协助。感谢南锡矿业学院 Weber 教授在 SNMS 成分分析方面的大力协助。

感谢准晶室陈宝清、吕传花、刘振民、王英敏、王清和羌建兵老师在生活和学习方面给予的深切关怀和帮助，感谢大工材料系金相实验室王德和教授、邹龙江教授、宋美丽、徐卫平、袁力江等老师对论文分析工作提供的帮助和指导。

感谢同组张向东、王彦芳、赵彦辉、刘天伟、高波等师兄弟师姐妹们给予我的无私帮助，在共同的学习生活中结下深厚的友谊，让我感受到研究工作中的许多乐趣。

特别感谢我最亲爱的父亲、母亲，爱人张可敏和关心爱护着我的家人们，他们的理解、关心和支持是我工作和生活中最大的原动力！

再一次向所有指导、关心、支持、帮助和鼓励过我的人表示最衷心的感谢！

大连理工大学学位论文版权使用授权书

本学位论文作者及指导教师完全了解“大连理工大学硕士、博士学位论文版权使用规定”，同意大连理工大学保留并向国家有关部门或机构送交学位论文的复印件和电子版，允许论文被查阅和借阅。本人授权大连理工大学可以将本学位论文的全部或部分内容编入有关数据库进行检索，也可采用影印、缩印或扫描等复制手段保存和汇编学位论文。

作者签名：____________________

导师签名：____________________

_______年____月____日